THE UNIVERSITY OF MICHIGAN

COLLEGE OF LITERATURE, SCIENCE, AND THE ARTS
Department of Physics

Technical Note

THE USE OF THE SHOCK TUBE AS A SPECTROSCOPIC SOURCE WITH AN APPLICATION TO THE MEASUREMENT OF gf-VALUES FOR LINES OF NEUTRAL AND SINGLY IONIZED CHROMIUM

T. Wilkerson
O. Laporte, Project Supervisor

ORA Project 02822

under contract with:

AIR FORCE OFFICE OF SCIENTIFIC RESEARCH
AIR RESEARCH AND DEVELOPMENT COMMAND
CONTRACT NO. AF 49(638)-439
WASHINGTON, D.C.

administered through:

OFFICE OF RESEARCH ADMINISTRATION ANN ARBOR

June 1961

This report was also a dissertation submitted in partial fulfillment of the requirements for the degree of Doctor of Philosophy in The University of Michigan, 1961.

ACKNOWLEDGMENTS

The author wishes to thank Professor Otto Laporte for his thoughtful supervision during the course of the research and the preparation of this manuscript. The author's colleagues, George Charatis and Lowell Doherty, have participated in much of the work reported here, and their help and advice are gratefully acknowledged. The able assistance of David Koopman in experiments and Samuel Ting in computations is greatly appreciated. The author also wishes to thank Harlan Stevens, Harry Willsher and George Prosser for their part in publishing the dissertation.

The draft of the manuscript was prepared by the author's wife, Marilyn Wilkerson; her encouragement and support have been invaluable throughout this work.

The author also wishes to thank the United States Air Force for its generous financial support of the research, under Contract AF-49-(638)-439 with The University of Michigan.

TABLE OF CONTENTS

TABLE OF CONTENTS (Concluded)

LIST OF TABLES

LIST OF FIGURES

LIST OF FIGURES (Continued)

FIGURES Page

LIST OF FIGURES (Continued)

LIST OF FIGURES (Concluded)

ABSTRACT

A shock tube has been used to produce gas samples which are at sufficiently high temperature to emit atomic and molecular spectra. The observed intensities of atomic lines are correlated with the predicted state of the gas to determine gf-values (transition probabilities) for the lines.

The gas initially present in the shock tube has a total pressure of about 1 cm Hg and consists of neon plus a small percentage of a spectroscopic additive, such as methane (CH_4) or chromium carbonyl ($Cr(CO)_6$). The driver gas is hydrogen at pressures of 100 to 700 psi. The ranges of temperature achieved behind primary and reflected shock waves are approximately 3000-5000°K and 7000-10000°K, respectively. Radiation by atoms, ions and molecules is observed under transient, non-equilibrium conditions as well as from steady states in thermal equilibrium.

The duration of any one steady state in the shock tube is limited to about 100 microseconds. Since a succession of events occurs at any place in the tube, the emission spectra and the motions of luminous shock waves are time-resolved by photography on moving films.

The velocities of shock waves and flow particles are not entirely in accord with the usual hydrodynamic theory of the shock tube. Deviations from theory arise from the viscosity and heat conductivity of the gases. Direct measurements are performed on some of the spectroscopically important flow variables. The absolute pressure and the kinetic temperature of the gas near the end wall of the tube are found to be in good agreement with theory.

The presence of organic additives in neon leads to luminosity which is useful for flow visualization. Strong transient emission by C_2 and CN molecules is observed near shock waves and in turbulent boundary layers. A theory is proposed which accounts for many aspects of this phenomenon. The theory considers simultaneous chemical creation and radiative annihilation of molecules in excited electronic states.

With chromium carbonyl as the additive, the gas behind the reflected shock emits intense lines of neutral and singly ionized chromium (CrI and CrII). Line intensities are measured by heterochromatic photometry, using the anode crater of a carbon arc as the primary radiation standard. The state of the gas is computed from shock tube theory, taking account of dissociation, ionization and excitation. Computed atomic populations are used, in conjunction with the theory of radiative

transfer, to derive absolute gf-values of the lines from their observed intensities. The measurements cover twenty lines of CrI and eight lines of CrII in the wavelength region 4500-5000 Å. The relative magnitudes of the CrI gf-values are quite different from the relative values previously found in a furnace experiment. The new values rectify the anomalies attributed to CrI in arcs and the sun on the basis of the previous work. The results of other experiments are compared to a few of the new absolute gf-values of CrI. The new values are three to five times greater. The gf-values for CrII are apparently the first to be measured for this ion.

Observations are made of the ionization relaxation of CrI immediately behind the reflected shock. The delay time for this process is between 1 and 10 microseconds and depends inversely on the computed electron pressure in the primary flow.

Thermodynamic functions governing dissociation, ionization and excitation have been computed for several atoms, ions and molecules and are presented in tabular form.

CHAPTER I

INTRODUCTION

1. INTRODUCTION

For the past nine years, the Shock Tube Laboratory at The University of Michigan has been studying the use of the shock tube as a spectroscopic source. Specifically, our experiments have dealt with the emission spectra of gases in the temperature range 3000-15,000°K. The purpose of this work has been to measure transition probabilities and line-broadening coefficients, in the hope of contributing new data for diagnostic studies in plasma physics and astrophysics.

By means of the shock waves generated in a shock tube, any gas can be rapidly heated to a condition of high temperature and luminosity. This method of excitation has, for our purposes, a number of advantages over more familiar light sources such as the arc or the glow discharge. Usually the shock-heated gas is in a well-defined equilibrium state which is uniform along the line of sight. The gas temperature can be computed from a straight forward hydrodynamic theory and can be varied over a wide range by simple changes of the experimental parameters.

We generate shock waves in a low pressure gas (e.g., neon at 1 cm Hg) by subjecting it to the sudden expansion of a gas at much higher pressure (e.g., hydrogen at 100 to 1000 psi). The gases are contained in a long tube of uniform cross section and are initially separated from one another by a diaphragm perpendicular to the tube axis. When the diaphragm is broken, a

shock wave propagates through the low pressure gas (the "test gas") at supersonic speed, compressing and heating the gas and setting it into a trailing motion. The shock wave reflects from the closed end of the tube back into the once-heated gas, compressing and heating it again and bringing it virtually to rest. Though later interactions with the expanded hydrogen cause the gas to cool, its state of rest at high temperature persists for about 100 microseconds. A typical state achieved during this time is a temperature of 11,000°K and a pressure of 2.5 atmospheres.

The hot gas is generally quite luminous, though the character and brightness of its spectrum naturally depend on the initial composition of the test gas and the degree of heating by the shock waves. The radiation that one observes can be classified into two types, one steady, the other transient. Our principal interest lies in that radiation which has a steady intensity during a steady hydrodynamic state. Assuming the condition of thermal equilibrium, we correlate the observed emission with the state of the gas; e.g., the intensities of spectral lines are combined with atomic abundances and level populations to yield transition probabilities. The thermal state is computed from measured shock speeds and the theory of shock wave hydrodynamics; in addition, the state variables are sometimes verified by direct measurement. The theory of radiative transfer is then invoked to convert the line intensities into atomic constants.

The spectrum of the test gas, neutral neon (Ne I), is naturally a prominent feature in the emission we observe. Many other spectra are

easily generated by premixing small amounts of the appropriate gases with the neon. We estimate that the spectra of at least fifty elements may be so generated and studied under conditions of thermal equilibrium. In the work done in this laboratory, the gaseous additive method has yielded the spectra of the following atoms and molecules:

Ne I, A I, H I, C I, O I, Cr I, Cr II,

Kr I, Xe I, Xe II, S I, Cl I, Cl II, Cu I,

C_2, CN, CO, CrO.

We have further studied those in the top row with respect to absolute line intensity.

For this program it is essential to separate out the transient radiation that is often seen in the vicinity of shock waves. The most sudden change in a gas passing through a shock front is the re-establishment of translational equilibrium at the higher temperature; other equilibria, such as dissociation and ionization, require more time to be set up. During these relaxation processes, line intensities are quite unsteady and related to no distribution of level populations which one could easily calculate a priori. Inversely, the shock tube is often used to study the approach to equilibrium. Though this has not been our main concern, we have studied a few transitory processes to relate their rate of completion to the hydrodynamic variables. Fortunately these processes are usually complete in times of the order of 1 to 10 microseconds; i.e., they occupy only 1% to 10% of the total observing time of spectroscopic interest.

For the phenomena described above, it is clear that any experimental

procedure must involve the time display of both radiant intensity and shock wave position. We employ photography on moving films for both purposes. The films are wrapped on rotating drums which spin rapidly enough to perform the necessary resolution of time. A time-resolved spectrogram has wavelength and time as orthogonal axes, while the third "dimension" of intensity, $I(\lambda,t)$, is provided by the degree of blackening at any point of the film. A "world-line" diagram of shock wave motion is easily obtained on moving film when the shock fronts are luminous. Their direction of motion (the shock tube axis) is imaged across the film, so that the film coordinates (x,t) represent the space-time of the laboratory. For a luminous shock of constant velocity, the x-t photograph shows a straight line whose slope is directly related to the laboratory speed of the shock. With moving films one has the advantage of a continuous presentation of data over the maximum number of dimensions. At the expense of generality, one may go to other methods for the purpose of simplifying the data reduction. Spectral line intensities can be studied with high sensitivity and good time resolution by means of photomultipliers in the image plane of a spectrograph. Shock wave velocities are often measured by time-of-flight techniques. The only such method used in our experiments is the recording of pressure histories at certain stations along the shock tube.

2. EARLY HISTORY OF RELATED EXPERIMENTS

Since the present field of study is a combination of hydrodynamics and spectroscopy it is felt to be worthwhile to discuss here the early experi-

ments in both areas which have bearing on our present work. We hope that this may be of some interest to those readers who are more familiar with one field than the other. We will emphasize here those experiments which gave rise to new interpretations of phenomena by means of either their qualitative results or their simplicity of quantitative measurement. For now, the discussions of theory and modern experimentation will be minimized, though we will return to these subjects in following chapters.

Many present day methods were already well developed by 1900 for the study of supersonic waves in closed tubes. The first reports of such phenomena were made independently in 1881 by two groups of workers—Berthelot and Vielle,[1] Mallard and Le Chatelier[2]—who were attempting to understand the thermochemical laws of combustion. They initiated flames in combustible gas mixtures, such as cyanogen and oxygen, and observed the propagation of high pressure waves with speeds as great as ten times the speed of sound. The velocities were measured with smoked revolving drums which were marked when the waves passed various tube stations. Some ingenious transducers were used for this purpose and were later carried to a high level of development by Berthelot and Vielle.

In another direction, Mallard and Le Chatelier soon succeeded with x-t photography of the combustion waves, particularly for such gas mixtures as carbon disulphide and oxygen, "these mixtures yielding highly actinic flames." We quote here from Dixon *et al.*[3] who, in 1903, published a comprehensive review of both the earlier work and their own extensive studies. This article contains some eighty x-t photographs illustrating the various

kinds of combustion waves and their interactions with one another and with different terminations of the tube. Several early spectroscopic studies are also reported here, as well as measurements of high pressure in detonation waves and the marked temperature dependence of molecular specific heats. For a summary of combustion studies to 1951, we refer the interested reader to the book by Lewis and von Elbe.[4]

Vielle[5] was the first to demonstrate, in 1899, that supersonic pressure discontinuities could propagate in non-combustible gases and were not necessarily due to exothermic processes. Vielle's apparatus was the first shock tube per se and operated like the gas-driven tubes used today. In one of his experiments, for example, a shock wave propagated at about twice the speed of sound through several meters of air at atmospheric pressure. The driver gas was air at 27 atmos., and the diaphragm was collodion sheet of 0.3 mm thickness. By means of lightweight pistons which marked a rotating drum, Vielle measured the flight times for shocks between several stations and observed decreases in speed at large distances from the diaphragm.

By the time of Vielle's experiments, the theory of finite amplitude waves in gases had already been well laid down, principally by Rankine (1869) and Hugoniot (1887). Earlier studies by Earnshaw (1858) and Riemann (1860) also contributed to this development. Chapman (1899) had extended the theory of shock waves into the realm of combustion, as Jouget was independently to do in 1905. The year 1910 saw a re-deriving and clarification of the shock conditions by Rayleigh and the development, by Kobes,[6] of a theory which Schardin[7] later applied to the gas-driven shock

tube (1932). Courant and Friedrichs[8] summarize most of this early work in addition to presenting the theory in its modern form.

A significant experimental advance was made by Payman, Shepherd et al.[9] in 1928. They applied Toepler's[10] schlieren method (1866) to the photography of shock waves and detonation waves. In this method, the gases are not required to be luminous since an external light source illuminates the flow field from one side. As in the Foucault test for optical surfaces, knife edges are put in the light path to preferentially block out or pass deviated rays, the deviation in this case arising from refraction at density gradients in the gas. Thus shock fronts may be photographed as dark lines on a light background or vice versa. Payman, Shepherd et al. combined this technique with x-t photography to study shock velocity and wave interactions over a wide range of parameters. In their sixth article (1946) they reported verification of the theory for shock velocity as a function of driver gas pressure, for the case of atmospheric pressure in the test gas.

Muraour and Michel-Lévy[11] (1934) seem to have been the first to recognize the essential role of shock waves in creating the luminous halos near explosions.* They made several experiments ("micropyrotechnics") with rows of lead azide grains laid out on photographic plates, one grain being detonated externally, the others then following in order. Since the detonation of each grain generated an expanding shock, a train of shock waves was

*Dixon[3] et al., report that this phenomenon was photographed by the Austrian artillery in 1896. Two grenades were simultaneously set off near one another, and a distinct zone of luminosity was observed equidistant between them.

led along any row, and interactions between shocks were set up at intersections of the rows. At these intersections, unique halos of light were seen which could not be ascribed to the luminescence of detonated material (or to a deposit of lead azide on the plate). Muraour and Michel-Levy concluded that the halos were due to strong shock-heating of the ambient air itself. They later showed that the intensity of the halo was strongly affected by the choice of ambient gas, being the greatest for argon and diminishing as one went to gases with more internal degrees of freedom.

The present phase of interest in the shock tube began with the second world war. Under Bleakney at Princeton, shock tubes were used to calibrate pressure gauges and to generate gas flows for wave interaction studies. Related work soon began at Michigan and Toronto and, by 1955, many laboratories were using and studying the shock tube for a wide variety of purposes. It is not possible to do justice to all this work here, and we must refer the reader to Turner,[12] Zel'dovich,[13] and Glass and Hall[14] for summaries to the period 1956-58. In Section 3 we will discuss the development of shock tube spectroscopy at Michigan, and we would again have recourse to additional bibliographies—e.g., the article by Laporte and this author[15] and the chapter by Kolb and Griem in Bates' forthcoming book.[16]

The remainder of this section is devoted to the early history of experiments on radiative transfer in gases, particularly the work of Gouy[17] in 1879. By this time, several important results had been reported; we

may refer to White's book[18] for this bibliography. The absorption lines in the solar spectrum were first observed by Wollaston (1802) and later by Fraunhofer (1817). In 1860, Foucault demonstrated that Fraunhofer's D lines could be duplicated in the laboratory by interposing a sodium flame between an arc and a spectroscope. By introducing various elements into flames, Kirchoff and Bunsen discovered many emission lines which could be correlated with the solar absorption lines. Thus several facts were already fairly clear, namely that to every element there corresponded a characteristic spectrum, that the composition of the earth and the rest of the universe were to some extent the same, and that the phenomena of emission and absorption of light were fundamentally interrelated. This last idea was quantitatively set forth by Kirchoff in his famous lectures of 1859-60. In its modern form, Kirchoff's principal law is the following: For any body in thermal equilibrium at the temperature T, and for any frequency ν, the ratio between the coefficients of emission and absorption is equal to the Planck function $B(\nu,T)$, i.e., the brightness in the frequency ν of a black body whose temperature is T.

In 1879, Gouy reported his extensive studies of the transparency of salted flames to their own radiation. He thereby elucidated the application of Kirchoff's law to spectral lines—a problem which Kirchoff himself had not fully understood. On either a monochromatic or "square wave" picture of spectral lines, Kirchoff had asserted that the line intensity would naturally saturate at the black body level appropriate to the flame temperature, as one increased the density or thickness of the flame. Though

agreeing to this saturation in each wavelength, Gouy emphasized that a continuous variation of emission coefficient from very small to large values was customarily hidden well within the width of the slit image, and that one would perforce measure the integrated intensity of this shape, $I = \int I_\lambda d\lambda$, in most cases. For a given slit width, the integrated intensity would continue to grow long after one approached saturation in the center of the line, since the unsaturated wings could still add their increasing brightness to the illumination of the slit image.*

Gouy verified this phenomenon of "growth" by means of a simple and ingenious procedure, an essential part of which was the comparitor-spectroscope he used to relate all intensities to the steady emission of a gas lamp. He studied several lines each for a number of elements whose salts he sprayed into flames. The intensity I_2 of a line emitted by two identical flames viewed in tandem was measured as a function of the line intensity I_1 from either one of the flames alone, and the ratio I_2/I_1 was plotted vs. I_1. As I_1 was varied from small to large values, I_2/I_1 was observed to diminish smoothly from 2 and finally settle at about 1.4. Though the curves varied from one line to another, they all possessed the same asymptotes, none of them leading to the saturation asymptote ($I_2/I_1 = 1$) suggested by Kirchoff.

This sort of measurement constituted a large part of Gouy's work, but

*Gouy brought out the spectral line shapes by keeping the slit width fixed at a reasonable value and passing to exceptional conditions of density in the flame. In this regime, the lines were so wide as to present an essentially constant intensity over the width of any slit image, and Gouy verified Kirchoff's law in this case.

he did much more which we can describe here only briefly. Multiple flames were tried in tandem; mirrors were used with single and double flames to duplicate the above effects. Gouy showed that the optical properties of any flame depended only on the product of flame thickness and atomic abundance, assentially what we now call the optical depth τ. Further, the brightness varied linearly with τ for τ small, and with $\sqrt{\tau}$ for τ large, the asymptote 1.4 (above) representing $\sqrt{2}$. These results anticipated by many years the theory of the curve of growth which we shall treat in Chapter V. Gouy correctly surmised that the ultimate $\sqrt{\tau}$ dependence and the rapidity with which it was achieved must somehow reflect the nature of the line profiles.

Though a satisfying description of atomic radiation had to await the development of wave mechanics in the 1920s, several aspects of radiative transfer were well understood by that time. In particular, two important parameters had been introduced which are still in use today, namely the damping ratio and the f-value of a spectral line. Both of these quantities originated with the electron-oscillator model of atomic emission.

The damping ratio is a measure of the relative contributions of dispersion effects vs. the Doppler effect in giving a shape to spectral lines. The line profile combining both these effects was first derived by Voigt[19] (1912) and Reiche[20] (1913), who showed that the absorption coefficient of a gas of damped oscillators was a convolution integral of the dispersion and Gaussian functions.* Additional contributions to the dispersion width

*The quantum mechanical derivation of this form was given by Weisskopf in 1932.[21]

were known to arise from collisions in the gas, after Michelson[22] (1895) and Lorentz[23] (1905). The evaluation of the integrated intensity from the Voigt function proved, with good reason, to be difficult and generally amenable only to numerical methods We will discuss the up-to-date results (i.e., the curve of growth) in Section 5 of Chapter V. Suffice it to say here that the integrated intensity I of an emission line depends very much on the damping ratio , a , when the line is bright, but very little when the line is faint. For a fixed value of $a > o$, an increase of atomic abundance causes I to first grow linearly with, and later as the square root of, abundance. The cases $a = \infty$ and $a = o$, respectively, were treated by Ladenburg and Reiche[24] (1913) and Ladenburg and Levy[25] (1930). Schütz[26] computed curves of growth for intermediate cases in 1930 and gave a complete explanation of Gouy's results in 1931. This year also saw the first application of the curve of growth to the Fraunhofer lines by Minnaert and Slob.[27]

The f-value is a measure of the inherent strength of a spectral line. Once it was realized that the intensity of each line was directly related to the number N of atoms in the appropriate state, the f-value was introduced as that fraction of N which brought the line intensity into agreement with the electron-oscillator theory. This method of specifying line strength is still the most common today, particularly so in the astronomical literature. The concept was apparently introduced by Ladenburg circa 1910, since one sees a continual emphasis on the "number of dispersion electrons" in his work and that of his colleagues and students during suc-

ceeding years. The work of Füchtbauer and Hofmann[28] (1914) and of Senftleben[29] (1915) are good examples of the spectroscopic studies of this period. Following Einstein's (1917) derivation of the transition probability,[30] Ladenburg (1921) demonstrated the simple connection betwen the f-value and the Einstein A coefficient.[31]

For the purpose of connecting this history to the present time, we may refer to a number of useful sources. The most complete and modern description of wave mechanics and atomic spectroscopy is Condon and Shortley's book.[32] The subject of transition probability is treated here much more fully than in other similar texts. The book by Mitchell and Zemansky[33] unifies most of the work to 1934 on resonance radiation. Hinnov and Kohn[34] (Duke University) describe their experiments on f-values, damping constants and line-reversal and cover much of the related work to 1956. Doherty[35] (Michigan) surveys the various methods used to measure f-values. An extensive review of f-value results to 1960, with particular application to determining the abundances of elements, is given by Goldberg, Müller and Aller.[36] Further references on radiative transfer will be given in Chapter V.

3. DEVELOPMENT OF THE SPECTROSCOPIC PROGRAM AT MICHIGAN

This work dates from Hollyer's observation (1952) of luminosity near the end of a hydrogen-driven shock tube he had been using for purely hydrodynamic experiments in nitrogen. Krypton and xenon were subsequently used to intensify the phenomenon, and preliminary reports of emission spec-

tra and shock velocities were communicated to the American Physical Society[37] and to Nature.[38] Simultaneously, related studies were also being carried out and reported on by three other laboratories. Taken altogether, the four means of generating strong shocks at that time comprise a set of methods which is still today the principal one. At Cornell University, Kantrowitz[39] et al. employed the combustion of hydrogen-oxygen mixtures to drive ionizing shocks through low pressure argon. Shreffler and Christian[40] at Los Alamos used solid explosives to create luminous shocks in argon at atmospheric pressure. At the University of Oklahoma, Fowler[41] et al. generated luminous shocks in low pressure hydrogen and helium by discharging a capacitor bank through a portion of the test gas.

The next phase of the Michigan work was begun in 1953 by Turner who designed and built the shock tube currently in use. Turner's principal experiment[12] consisted of measuring the first-order Stark effect broadening of H_β as a function of computed ion density behind the reflected shock. For $n_i \sim 10^{16}/cm^3$, the observed half-width of H_β was about 10 Å. The profiles were wider by 20(±10)% than predicted by the Holtsmark theory. The test gas in these experiments was neon with an additive of 1% hydrogen. Using other gases, Turner also measured the relaxation time for ionization behind primary shocks in xenon and qualitatively studied the second-order Stark effect broadening of the lines of argon, krypton and xenon.

In 1956, Doherty initiated a program of intensity measurements on spectral lines of astrophysical interest. The operating temperature, as in Turner's case, was around 12,000°K. By including such additives as CH_4,

O_2 and argon with the neon test gas, Doherty[35] was able to measure f-values for a few lines of CI and OI and many lines of AI and NeI.

Midway in Doherty's work, the success of the program was cast in doubt by the discovery of inadequacies in the usual shock tube theory. Charatis,[42] Doherty[43] and this author[42] observed discrepancies between theory and experiment for the reflected shock speed and other hydrodynamic observables. Other laboratories began reporting similar effects, and it was then clear that they were of a general nature rather than peculiar to our shock tubes. None of this work, however, dealt directly with pressure or temperature, and it was necessary for us to examine the possibility of errors in these variables. The temperature is particularly important because of the dependence of atomic level populations on the Boltzmann factor. Doherty's method of dealing with this problem was to attribute the new effects to "sinks" of momentum and energy not allowed for in the usual theory. Hollyer[44] had previously found that sink calculations were useful for treating the attenuation of primary shocks. In Doherty's work, the failures of theory led to values for the sinks and to empirical corrections for the shock tube state variables. Doherty showed that the temperature error was at most only a few percent and would not obviate the intensity measurements. Further he showed that the ion density had to be increased by 20%, thereby resolving the puzzle which still remained from Turner's work on H_β. Doherty's H_β profiles are consistent with his corrected ion densities and the newer Stark broadening theory of Griem, Kolb and Shen.[45] This theory gives results which are similar to Holtsmark's for the range of

conditions in the shock tube experiments and, in addition, has been tested in the water-stabilized arc.

Taken together, the studies of H_β by Turner and Doherty demonstrate that collisional equilibrium can indeed be attained in the shock tube. Further, this condition is shown to be (1) capable of rapid establishment, (2) recognizable from the end of relaxation processes and the onset of steady emission, and (3) reproducible with the composition of the test gas and the speed of the primary shock.

These favorable conclusions had not been firmly established when the present author s work was begun. It was decided to attempt a verification of excitation temperature by means of relative spectral line intensities. For this, an element was required for which relative f-values were known over a range of excitation potential, so that measurements of intensity could be reduced to the Boltzmann distribution of atoms over their energy levels. Neutral chromium was chosen as the thermometric element since its line spectrum is not too densely packed, many of its f-values had been measured (relatively) by Hill and King,[46] and it could be put into the shock tube in the gas phase as chromium carbonyl, $Cr(CO)_6$.* The lines of Cr I and Cr II were easily brought out, and the relative intensities of the appropriate Cr I lines were measured.

---

*Due to their stability at room temperature, the carbonyls serve this purpose very well (see Appendix B). Doherty reports unsuccessful attempts to generate titanium (Ti I) lines using $TiCl_4$ as an additive. Unless extreme care is taken to avoid water vapor and (hence) hydrolysis, $TiCl_4$ yields only HCl as the additive. Doherty observed a rich spectrum of Cl I and Cl II in this case.

Charatis and the writer reported the first results[47] of this study in late 1959. We found an apparent discrepancy between the measured excitation temperature T_e(~6000°K) and the computed kinetic temperature T(~10,000°K) behind the reflected shock. It will subsequently be shown that, though these experiments still stand, their interpretation with regard to temperature was in error. The fault lay in the set of relative f-values employed at the time. A systematic error in the determination of these values had indeed been suspected by other workers for some time. However, this interpretation was not then readily believed by us because of our previous observations of non-ideal shock tube behavior.

A number of alternatives were considered and later abandoned. In particular, the author proposed an "atmospheric" model[48] of the shock tube gas wherein heat conduction set up a thermal boundary layer in the line of sight. Because of strong Cr I ionization in the main body of gas, the principal Cr I emission was supposed to originate in the cooler layer. This model appeared to succeed at first, because of overestimates of the main stream ionization, but was discarded when the simultaneous ionization equilibria of all constituents (Cr I, C I, O I, Ne I) became better understood. Non-equilibrum distributions of the electrons and Cr I were also considered and discarded on the basis of density and excitation cross sections.

The chromium experiments were re-interpreted as valid determinations of the f-values on the strength of two developments. The first of these was Doherty's demonstration of near-ideal equilibrium conditions for atoms whose excitation and ionization potentials are much higher than in the case

of chromium. Secondly, we had directly shown in the meantime that the pressure and kinetic temperature were very close to the computed values. We report these latter measurements here. Our principal task, then, has been the determination of chromium f-values using line intensity measurements together with the theories describing shock waves and radiative transfer. The dissertation is organized according to the plan given in the following Section.

4. OUTLINE OF THE DISSERTATION

The theory of the changes of state caused by shock waves is treated in Chapter II. We consider the effects arising from ionization, dissociation, etc., particularly for the case of neon with a chromium carbonyl additive. The thermodynamic functions we have computed for a number of atoms and molecules are tabulated in Appendix A. The last section discusses the use of simultaneous measurements of shock velocity and flow velocity for determining the change of state across a shock wave.

Chapter III describes various experiments of a thermo-hydrodynamic nature. The vapor pressure of chromium carbonyl was remeasured to insure our knowledge of the chromium abundance in the shock tube. The non-ideal behavior of the shock tube flow was observed by means of the luminosity which organic additives induce in neon. The results of other workers bearing on our experiments are discussed. The last two sections describe our direct measurements of pressure and kinetic temperature, which support the use of the shock tube as a spectroscopic source.

Chapter IV considers (primarily theoretically) the transient molecular luminosity observed with organic gases added to neon. A non-equilibrium theory was previously proposed for this phenomenon, and we examine it further here via a chemical-kinetic calculation.

The theory of radiative transfer through a uniform atmosphere in thermal equilibrium is given in Chapter V. The dependence of the integrated intensity of a spectral line on its f-value and its shape is discussed and illustrated by means of the curve of growth.

The experiments on chromium line intensity are described in Chapter VI. The hydrodynamic effects observed with chromium carbonyl as the additive are summarized here rather than in Chapter III. The ionization relaxation of chromium at the reflected shock is studied as a function of primary flow conditions. By means of photographic photometry, absolute f-values are found for neutral and singly ionized chromium lines emitted from the gas behind the reflected shock. We also discuss the previous chromium f-value results of other workers.

Chapter VII summarizes the results of our investigations and assesses the utility of the shock tube for spectroscopic studies in the future.

CHAPTER II

HYDRODYNAMIC THEORY

1. INTRODUCTION

A complete theory of shock tube flow can be constructed under the assumptions that the gases are inviscid and undergo one-dimensional motion. The theory gives the velocity and thermodynamic state of the gases as functions of distance and time, and it consists of a piecing together of the various simple solutions of the Euler equations. These equations express the conservation of fluid mass, momentum and energy, in terms of first-order time and space derivatives alone. The class of solutions includes both continuous and discontinuous waves.

The first wave to propagate into the low pressure section of a shock tube is a shock wave, a surface across which all the flow variables change abruptly. In discussing the subsequent phenomena, we will consider this primary shock wave as the essential one and treat most of the other waves as incidental, though they are all interrelated. The primary shock travels entirely within the low pressure gas, setting the gas into motion and increasing its pressure and temperature. When the primary wave arrives at the closed end of the shock tube, a reflected shock is sent back into the primary flow field. This wave brings the gas to rest and further increases its pressure and temperature.

The general theory for these changes of state is outlined in Section 2. Section 3 treats the simple theory for gases of constant

specific heat, particularly the rare gases. The flow variables are shown to follow from the primary shock speed. In Section 4, we consider the modifications which are required by the variability of specific heats due to excitation, dissociation and ionization. Computed thermodynamic functions for several substances are given in Appendix A. In Section 5, numerical results are given for a test gas consisting of neon and chromium carbonyl. Even when the fractional abundance of the carbonyl is less than 1%, large effects are predicted for the state variables behind strong shocks. Section 6 discusses the principles of measuring thermodynamic state variables by observing the flow velocities on both sides of a shock transition.

Since much of the pertinent theory is now well known, we have abbreviated its presentation wherever possible. A good source reference on the compressible flow of simple gases is the book by Courant and Friedrichs.[8] Turner's dissertation[12] contains computation of wave interactions and the effects of variable specific heat. A concise derivation of the general conditions on fluid discontinuities is given in an appendix of Johnson's dissertation.[49]

2. THE GENERAL SHOCK RELATIONS

A diagram showing the ideal wave motion in a shock tube is shown in Figure 1. This x-t diagram shows the space-time loci of the waves and (superposed) the pressure profiles along the tube at three different times. Until the time t_o, a diaphragm separates the high pressure (p_4)

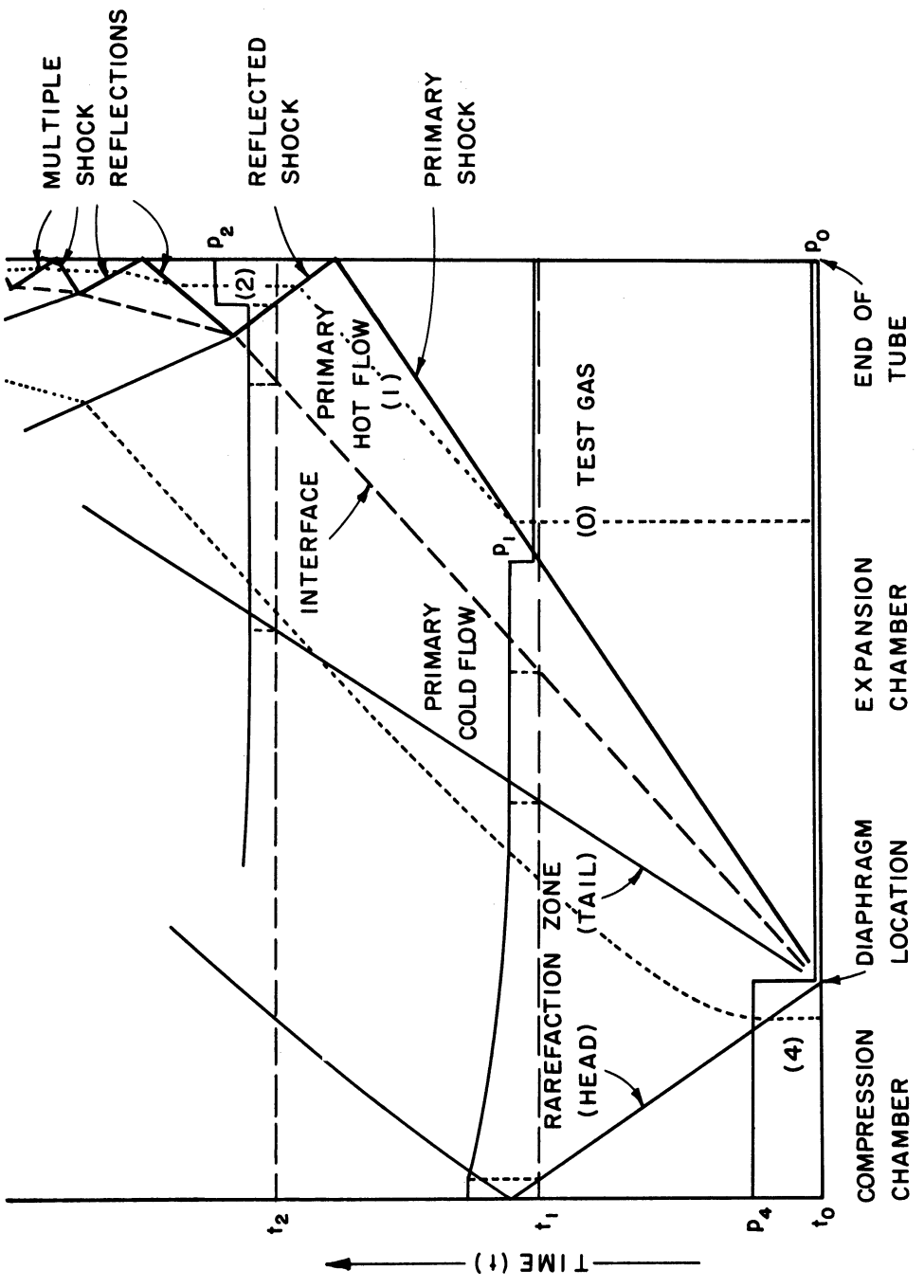

Figure 1. x-t diagram of entire shock tube flow, according to ideal theory.

and low pressure (p_o) sections. The flow processes begin when the diaphragm opens at time t_o. The primary shock wave moves to the right with constant speed U, setting all the test gas into motion with constant velocity $u_1 < U$ and increasing its pressure and temperature from (p_o, T_o) to (p_1, T_1). The shock speed is greater than than the speed of sound in the test gas. The dotted line represents the motion of a particular element of fluid. The increase of fluid density ρ caused by the shock is shown by the greater proximity of the dotted line to the end of the tube when the shock arrives there than when the shock overran the element. The gas is further compressed to the state (p_2, T_2) when it is brought to rest again by the reflected shock, whose speed we will denote by V.

Assuming that no fluid is lost in this process of double compression, one can easily derive the kinematic relations

$$u_1/U = 1 - \frac{\rho_o}{\rho_1},$$

$$V/U = \left(1 - \frac{\rho_o}{\rho_1}\right)\Big/\left(\frac{\rho_2}{\rho_1} - 1\right). \qquad \text{(II.1)}$$

These relations will emerge later as part of the general treatment of shock transitions. Here they serve to illustrate the connections between thermodynamic quantities and the speeds of signals and mass motion.

The shock phenomena in the test gas are "driven" by the expansion of high pressure gas (4) from the chamber on the left of Figure 1. The

removal of the diaphragm sends a rarefaction signal into region (4) at the speed of sound. From the "head" to the "tail" of this wave, the gas is gradually accelerated, cooled and rarefied. The x-t history of a particular fluid element is again shown by a dotted path. Ultimately, the driver gas achieves a constant state in the primary cold flow; here the pressure and velocity are equal to the values (p_1, u_1) describing the primary hot flow. The interface between the expanded driver gas and the compressed test gas is a surface of discontinuity for the density and temperature.*

The meeting of the interface with the reflected shock wave gives rise to a new set of waves. Only in exceptional cases are the properties of the cold flow such that it can be brought to rest at the same pressure as the hot gas behind the first reflected shock. The general problem of this interaction has been treated by Turner.[12] In Figure 1, the ensuing wave pattern represents the case of low pressure neon driven by hydrogen at sufficiently high pressure. One shock is transmitted into the cold hydrogen, and another is reflected back into the hot neon. Between these two shocks the flow speeds of both gases (and thus of the new interface) are the same. The neon is subjected to several shock reflections, each of which increases the pressure and temperature of the gas. In Section 5 of Chapter III, experiments will be described

*The expansion of gas (4) takes place at constant entropy, while the shock compression of (0) is irreversible. The interface may be considered as an entropy discontinunity supporting the initial difference across the diaphragm plus the increment arising from the shock transition.

which show that the theory of these interactions is qualitatively correct. However, the actual interface is a zone of turbulent mixing, and the interactions of shocks with it cannot proceed according to the simple theory. Therefore we will not further discuss these interactions here, and will confine our attention to the gas behind the primary and first reflected shock waves.

The conditions on a normal shock discontinuity are that the fluxes of mass, momentum and energy into the surface are balanced by the corresponding fluxes outward. Johnson has shown how these conditions follow directly from the Euler equations.[49] The shock conditions are most simply written for the frame of reference in which the shock is at rest. For the primary shock, the incoming fluid has the velocity $v_0 = U$, and the speed of the outgoing fluid is $v_1 = U - u_1$. In the above order, the conservation equations are

$$\rho_1 v_1 = \rho_0 v_0$$

$$\rho_1 v_1^2 + p_1 = \rho_0 v_0^2 + p_0$$

$$h_1(\rho_1, p_1) + \frac{v_1^2}{2} = h_0(\rho_0, p_0) + \frac{v_0^2}{2} \qquad \text{(II.2)}$$

where $h(p, \rho)$ is the enthalpy per unit mass. Under the appropriate substitutions, similar equations describe the reflected shock transition. These conditions are valid <u>locally</u>; i.e., they apply at any normal shock no matter what the form of the flow field away from the shock. We will assume in addition that the flow fields of interest are uniform and are

thus described throughout by these equations.

Assuming the initial fluid state (ρ_0, p_0, v_0) to be known, these conditions completely prescribe the state (ρ_1, p_1, v_1) behind the shock. For gases in which the enthalpy is a simple function of pressure and density, the relations may be so rearranged as to present the flow variables in very simple forms. We will return to this topic in the following section after laying the necessary groundwork here.

The first equation and its reflection-analogue lead to the laboratory-coordinate Equations (II.1). The relation for the reflected shock speed V follows from the assumption that the primary flow is brought to rest by the reflected shock. In the frame of reference of this shock, we denote by v_3 the speed of the incoming primary flow, and by v_2 the speed of the denser outgoing gas (which is at rest in the laboratory frame). From the mass flux equation

$$\rho_2 v_2 = \rho_1 v_3 ,$$

and the relation

$$v_3 = u_1 + V = u_1 + v_2 ,$$

it follows that

$$V = u_1 \Big/ \left(\frac{\rho_2}{\rho_1} - 1 \right) .$$

We will later use the equivalent relation

$$u_1 = v_3 \left(1 - \frac{\rho_1}{\rho_2}\right) .$$

(II.3)

Together with the conservation of mass, the dynamical condition on the momentum flux leads to a general connection between the primary and reflected shock transitions. From the first two shock conditions,

$$v_1^2 = \frac{\rho_0}{\rho_1} \cdot \frac{p_1 - p_0}{\rho_1 - \rho_0} = \frac{p_0}{\rho_0} \cdot \frac{(y_{10} - 1)}{x_{10}(x_{10} - 1)}$$

$$v_0^2 = \frac{\rho_1}{\rho_0} \cdot \frac{p_1 - p_0}{\rho_1 - \rho_0} = \frac{p_0}{\rho_0} \cdot \frac{x_{10}(y_{10} - 1)}{(x_{10} - 1)} .$$

(II.4)

where $x_{10} = \rho_1/\rho_0$ and the "shock strength" $y_{10} = p_1/p_0$. The reflection-analogue to the second of these equations is

$$v_3^2 = \frac{p_1}{\rho_1} \frac{x_{21}(y_{21} - 1)}{(x_{21} - 1)} ,$$

which may be written in terms of u_1 by Equation (II.3). Also, u_1 is given by both Equations (II.4), and can thus be eliminated. The resulting thermodynamic relation is

$$\frac{(y_{10} - 1)(x_{10} - 1)}{y_{10}} = \frac{(y_{21} - 1)(x_{21} - 1)}{x_{21}} .$$

(II.5)

The thermodynamics of each of the shock transitions is determined by all three conservation laws. Substituting Equations (II.4) into the third (energy) shock condition, one derives the Hugoniot relation

$$h_1(p_1, \rho_1) - h_0(p_0, \rho_0) = \frac{(p_1 - p_0)}{2}\left(\frac{1}{\rho_1} + \frac{1}{\rho_0}\right). \tag{II.6}$$

Again, an analagous equation holds for the reflected shock. Through the equation of state for the gas, the Hugoniot relation determines the number of possible states behind a shock. For most gases there are (in principle) two available states which differ in that the shock is compressive in one case and rarefying in the other. The rarefaction shock is usually disallowed by the restriction of increasing entropy; i.e.,

$$S_1 > S_0 \Rightarrow \rho_1 > \rho_0 \Rightarrow v_1 < v_0 . \tag{II.7}$$

3. THE SHOCK RELATIONS FOR GASES WITH A CONSTANT NUMBER OF DEGREES OF FREEDOM

The equation of state for an ideal gas is

$$p/\rho = RT/\sigma \tag{II.8}$$

where R is the gas constant (8.314×10^7 ergs/mole °K), T is the temperature, and σ the molecular weight. The enthalpy per gram of an ideal gas is

$$h = \frac{f+2}{2}\frac{p}{\rho} = \frac{\mu+1}{2}\frac{p}{\rho}, \tag{II.9}$$

where f is the (fixed) number of degrees of freedom of the gas particles, and $\mu = f+1$. Substitution of this form into the Hugoniot relation (II.6) leads directly to two consequences.

In the first instance, the Rankine-Hugoniot equation expresses the density ratio as a function of the shock strength alone.

$$x_{10} = \frac{\mu y_{10} + 1}{\mu + y_{10}} \qquad \text{(II.10)}$$

Even for very large shock strength, the density ratio is limited to the value μ(4 for the rare gases). Thus the temperature ratio

$$T_{10} = T_1 / T_0 = y_{10} / x_{10} \qquad \text{(II.11)}$$

may grow without bound for successively stronger shocks in gases with a fixed number of degrees of freedom. The efficacy of shock heating is much greater than that of adiabatic heating where no such limitation on ρ_1/ρ_0 exists. It is the density-pressure relation of Equations (II.10) which enables the association (in Equation II.7) between increasing entropy and density.

The second consequence of combining Equations (II.9) and (II.6) may be seen by rewriting ρ_1 and p_1 in terms of the unknown velocity v_1. The Hugoniot relation then becomes a quadratic polynomial in v_1, the coefficients being combinations of the "influx variables" (ρ_0, p_0, v_0). Of the two solutions, one is $v_1 = v_0$ and is extraneous to the shock problem.

It is easily shown that the other solution satisfies Equation (II.7) only if the incoming flow is supersonic; i.e., the Mach number of this flow is

$$M_0 = v_0/c_0 > 1,$$

where $c_0 = (\gamma RT_0/\sigma)^{\frac{1}{2}}$ is the speed of sound, and $\gamma = (f+2)/f = (\mu+1)/(\mu-1)$. Thus the laboratory speed $U = v_0$ of a primary shock wave is always greater than the speed of sound in the test gas.

The connection between the strength of a shock and its speed is derived by substitution of the Rankine-Hugoniot Equation (II.10) into the second of Equations (II.4). The various forms which result are

$$\begin{aligned} y_{10} &= \frac{\mu-1}{\mu}\,\frac{\rho_0 v_0^2}{p_0} - \frac{1}{\mu} \\ &= \frac{\mu-1}{\mu}\,\frac{\sigma \mathcal{U}^2}{RT_0} - \frac{1}{\mu} \\ &= \frac{\mu-1}{\mu}\,\eta_0 - \frac{1}{\mu} \\ &= \frac{\mu+1}{\mu}\,M_0^2 - \frac{1}{\mu}. \end{aligned}$$

(II.12)

The parameter $r_0 = \sigma U^2/RT_0$ is particularly useful for shock waves in gas mixtures.

In turn, the strength y_{21} of the reflected shock follows from y_{10} via Equation (II.5) and the Rankine-Hugoniot equations for both transitions:

$$y_{21} = \frac{(\mu+2)\, y_{10} - 1}{\mu + y_{10}} \tag{II.13}$$

The other state variables behind the reflected shock are calculated from this quantity. This completes the program of computing all the flow variables from the primary shock speed and the initial conditions of the test gas. In terms of the parameter r_0, we have compiled the appropriate identities for the rare gases ($f = 3$) in Table I.

We note here the asymptotic behavior of some of the quantities for large shock strength (large r_0), since the violation of these limits forms the basis of the experimental discussion of Chapter III. In discussing a limiting number n, we will denote it by $n^{(+)}$ or $n^{(-)}$, according as the limit is approached from above or below. We have already mentioned $x_{10} \to 4^{(-)}$. Correspondingly, the primary flow speed $u_1 \to .75^{(-)}U$. For the reflected shock, the strength $y_{21} \to 6^{(-)}$ and thus the density ratio $x_{21} \to 2.5^{(-)}$. Thus the over-all density ratio $x_{20} = \rho_2/\rho_0$ is no greater than 10. The reflected shock speed $V \to .50^{(+)}U$.

The previously mentioned theory for the entire shock tube flow predicts the primary shock strength from the initial pressures in the tube.

TABLE I

IDENTITIES FOR SHOCKS IN THE RARE GASES (NO IONIZATION)

$$r_0 \stackrel{d}{=} \frac{\rho_0 v^2}{p_0} = \frac{\sigma v^2}{R T_0} \quad ; \quad \mu = 4$$

$$y_{10} = \frac{3r_0 - 1}{4} \qquad x_{10} = \frac{4 r_0}{r_0 + 5} \qquad T_{10} = \frac{y_{10}}{x_{10}}$$

$$y_{21} = \frac{18 r_0 - 10}{3 r_0 + 15} \qquad x_{21} = 2.5 \left(\frac{3 r_0 - 1}{3 r_0 + 5} \right)$$

$$T_{21} = \frac{y_{21}}{x_{21}} \qquad T_{20} = T_{21} \cdot T_{10} = \frac{(3r_0 + 5)(9r_0 - 5)}{60 r_0}$$

$$u_{10} = \frac{u_1}{v} = \frac{3}{4} - \frac{5}{4 r_0} \qquad v_{20} = \frac{V}{v} = \frac{1}{2} + \frac{5}{6 r_0}$$

Defining $z = p_4/p_0$, the Taub equation* is

$$z = y_{10}\left[1 - \frac{c_0(\mu_0 - 1)(y_{10} - 1)}{c_4(\mu_4 - 1)\sqrt{(\mu_0 + 1)(1 + \mu_0 y_{10})}}\right]^{-(\mu_4 + 1)} \qquad \text{(II.14)}$$

The possibility of using different gases in the two chambers is allowed by the subscripts on μ and c. As one would expect, y_{10} increases monotonically with z for any combination of gases. In addition, this equation predicts that the strongest shocks are obtained in a gas of low sound speed driven by a gas of high sound speed, as long as the values of μ are not too different. Except for these trends, the Taub equation is generally not borne out by experiment (see Section 6 of Chapter III). The flow variables are usually inferred from direct measurements of the primary shock speed.

4. THE SHOCK RELATIONS FOR GASES WITH A VARIABLE NUMBER OF DEGREES OF FREEDOM

For shock transitions to states of high temperature, the simple theory outlined in Section 3 is not adequate. At sufficiently high temperature, a fraction of the total thermodynamic energy of an atomic gas appears in electronic excitation and ionization; molecules demonstrate electronic, vibrational, and rotational excitation as well as ionization and dissociation. The extent to which these degrees of freedom come into play under a given set of conditions is determined by the quantum-

*See References 12 and 14 for discussions of this equation.

mechanical properties of the particles such as the degeneracies and term values for bound states and the potentials for ionization and dissociation. If these properties are known, the enthalpy per unit mass may be computed in any situation, and the Hugoniot relation (II.6) allows a complete analysis of shock transitions in the given substance. The difficulty of such calculations arises from the transcendental relation between the state variables and the added contributions to the enthalpy. For many purposes, a useful method is iteration, starting with the state variables predicted via the simple relations of the previous section. Ionization, dissociation, etc., are computed in this zeroth state. The implied consumption of energy is then included in the Hugoniot relation, and a new state behind the shock is calculated, etc. Computations of this sort have been performed by many workers in the shock tube field, the most recent being those of Faneuff, Anderson, and Kolb[50] for helium, Alpher and Greyber[51] for N_2 and O_2, and Turner[52] for H_2. The case of interest to this author is that in which the shock tube test gas is a mixture of neon with a small amount of $Cr(CO)_6$ vapor. Following a survey of the pertinent energy-consuming processes, the modified shock relations are derived. Their application is discussed for the example of a nitrogen impurity in neon. The effects of a chromium carbonyl additive are discussed in Section 5.

A. Ionization

Let α_{AI} represent the extent of the ionization reaction

$$A\,I \overset{\chi}{\rightleftharpoons} A\,II + e^- \tag{II.15}$$

for a neutral atom AI of ionization potential χ.

$$\alpha_{AI} \overset{d}{=} n_{AII} / n^o_{AI} \tag{II.16}$$

where n^o_{AI} is the number density of atoms if no ionization were to take place, and n_{AII} is the number density of ions resulting from the establishment of the ionization equilibrium. α_{AI} is the degree of ionization and is given by the Saha equation,

$$\frac{\alpha_{AI}}{1-\alpha_{AI}} p_e = f_{AI}(T)$$

$$\overset{d}{=} 2 \frac{(2\pi m_e k)^{3/2}}{h^3} kT^{5/2} \frac{Z_{AII}}{Z_{AI}} e^{-\chi/kT}$$

$$= \frac{T^{5/2} e^{-\chi/kT}}{1.5002\, Z_{AI}/Z_{AII}} \quad (c.g.s.). \tag{II.17}$$

p_e and m_e are electron pressure and mass, h and k are the Planck and Boltzmann constants, and Z_{AII} and Z_{AI} are the internal partition functions for the ion and the atom. $Z = \Sigma g_n e^{-E_n/kT}$, the quantum numbers

n labeling the stationary states whose degeneracies are g_n and energies above the ground state are E_n. Tables of $f_{AI}(T)$ computed by S.C.C. Ting and the writer are given in Appendix A for the first ionization equilibria of:

neon,	chromium,	cobalt,
carbon,	molybdenum,	caesium,
nitrogen,	tungsten,	and
oxygen,	nickel,	mercury.

Also included are partition functions and internal energies for the atoms and ions.

If (II.15) is the only electron-producing reaction, then $pe = \alpha_{AI} p^o_{AI}$, where $p^o_{AI} = n^o_{AI}\, kT$, and (17) becomes

$$\frac{\alpha^2_{AI}}{1-\alpha_{AI}} = f_{AI}(T) \Big/ p^o_{AI}$$

To compute the ionization equilibria for a mixture of Cr, C, O and Ne in any given state, one must simultaneously solve four equations of type (II.17) subject to the condition

$$p_e = \sum_{i=1}^{4} \alpha_i p^o_i$$

This is most easily done by rewriting the equations as

$$p_e = \sum_{i=1}^{4} \frac{p_i^{\circ} f_i(T)}{p_e + f_i(T)} \quad ; \quad \alpha_i = \frac{f_i(T)/p_e}{1 + \frac{f_i(T)}{p_e}}$$

(II.18)

By trial and error, a solution pe may be found for the first equation; the second then gives each α_i directly.

B. Dissociation of Diatomic Molecules

Consider the isolated reaction

$$AB \underset{\leftarrow}{\overset{\chi}{\rightleftharpoons}} A + B \, .$$

(II.19)

Defining α_{AB} (as in the case of ionization) by

$$n_A = n_B = \alpha n_{AB}^{\circ} \, ,$$

(II.20)

the analogous equilibrium condition is

$$\frac{\alpha_{AB}^2}{1 - \alpha_{AB}} = \frac{f_{AB}(T)}{p_{AB}^{\circ}} \, ,$$

$$f_{AB}(T) \overset{d}{=} \left(\frac{2\pi m_A m_B}{m_{AB}} \right)^{3/2} \frac{k^{5/2}}{h^3} T^{5/2} \frac{Z_A Z_B}{Z_{AB}} e^{-\chi/kT} \, .$$

(II.21)

Z_A and Z_B are electron-excitation partition functions.

In the Born- Oppenheimer approximation, one considers separately the electronic, vibrational, and rotational "degrees of freedom" of a molecule. Thus

$$Z_{AB} = Z_{AB,E} \cdot Z_{AB,V} \cdot Z_{AB,R} \cdot \tag{II.22}$$

The excited electronic terms of the molecules of interest (CO and N_2) are all many electron-volts above the $^1\Sigma$ ground state, so that $Z_{AB,E} \sim 1$ for T as high as 10,000°K (~1 ev.). Also the approximation will be made that the vibration is simple-harmonic and the rotation is rigid. Thus

$$Z_{AB,V} = \left(1 - e^{-\frac{\omega hc}{kT}}\right)^{-1} = \left(1 - e^{-\frac{\omega(cm^{-1})\ 1.4385\ cm\,{}^\circ K}{T({}^\circ K)}}\right)^{-1},$$

$$Z_{AB,R} = \frac{kT}{Bhc} = \frac{T({}^\circ K)}{B(cm^{-1})\ 1.4385\ cm\,{}^\circ K}, \tag{II.23}$$

where ω and B are the vibrational and rotational term-constants, respectively. These approximations are sufficiently accurate for the present purposes because the inpurity level of interest is quite low.

The dissociation equilibrium for a homonuclear diatomic molecule

$$A_2 \rightleftarrows 2A \tag{II.24}$$

differs in some respects from the previous case because of the indistinguishability of the constituent (and therefore product) atoms. If α_{A_2}

is analogously defined by

$$n_{A_2} = (1 - \alpha_{A_2}) n^{o}_{A_2} ,$$

(II.25)

then $n_A = \alpha_{A_2} n^{o}_{A_2}$. Also $m_{A_2} = 2mA$. Therefore

$$\frac{\alpha^2_{A_2}}{1-\alpha_{A_2}} = \frac{f_{A_2}(T)}{p^{o}_{A_2}} ;$$

$$f_{A_2}(T) \stackrel{d}{=} \frac{1}{4} (\pi m_A)^{3/2} \frac{k^{5/2}}{h^3} T^{5/2} \frac{Z^2_A}{Z_{A_2}} e^{-\chi/kT}$$

(II.26)

With regard to the partition functions, everything goes through as before except that the rotational phase space of the molecule must be reduced by half because of the symmetry of the rotator; i.e.,

$$Z_{A_2,R} = \frac{1}{2} \frac{kT}{Bhc} .$$

(II.27)

This is of course not true for a molecule AA* in which A* is an isotope of A.

Dissociation equilibria for CO and N_2 were computed with the above approximation and the results are included in Appendix A.

C. Energies Associated With Various Degrees of Freedom

The translational energy <u>per particle</u> is $\epsilon_T = \frac{3}{2} kT$. For the temperatures of interest, rotational energy may be derived classically. Thus

$$\epsilon_R / kT = f_R / 2 , \tag{II.28}$$

where f_R is the number of rotational degrees of freedom. Vibrational energy level spacings for N_2 and CO are roughly equivalent to 3000°K, so one must use the quantum-mechanical partition function in computing

$$\epsilon_V = kT^2 \frac{\partial}{\partial T} \ln Z_V \tag{II.29}$$

Define $f_V = \epsilon_V / kT$; then

$$f_V = \frac{u}{e^u - 1} \quad ; \quad u = \frac{\omega(cm^{-1})\, 1.4385\ cm°K}{T(°K)} . \tag{II.30}$$

The average electronic excitation energies per particle (ϵ_E) must generally be computed from the defining equation, and we write the corresponding "degree of freedom" as

$$f_E \stackrel{d}{=} \frac{\epsilon_E}{kT} = \frac{\sum E_n g_n e^{-E_n/kT}}{kT \cdot Z_E} . \tag{II.31}$$

In Appendix A, f_V is given for CO and N_2, and f_E is given for several atoms and their ions.

D. Equations of State

It is advantageous for computing purposes to retain the form

$$p/\rho = RT/\sigma \tag{II.32}$$

of the equation of state. For multi-component gases σ is now the effective molecular weight; i.e.,

$$\sigma = \sum_i \sigma_i \eta_i \,. \tag{II.33}$$

For the species i, σ_i is the molecular weight and η_i is the fractional abundance. This equation is equivalent to the representation $p/\rho = (1+\alpha) RT/\sigma_A$ often used as the equation of state for a partially ionized gas.

E. The Generalized Hugoniot Relation

The foregoing processes are entered into the theory of shock transitions simply by computing the total enthalpy per gram and substituting into the Hugoniot relation (II.6). By definition, the enthalpy $h = e + \frac{p}{\rho}$; e is the internal energy <u>per gram</u> and may be subdivided according to the various degrees of freedom.

$$e = e_T + e_R + e_V + e_E + e_D \,, \tag{II.34}$$

where e_D is the energy per gram that has gone into ionization and dissociation. $e_T = 3kTN^\circ/2\sigma$, where N° is Avagadro's number.

Therefore, by Equation (II.32),

$$e_T = \frac{3}{2}\frac{p}{\rho} \,. \tag{II.35}$$

Also,

$$e_R = \frac{N^\circ kT}{2\sigma} \sum_i f_{Ri} \eta_i = \frac{p}{2\rho} \sum f_{Ri} \eta_i \,, \tag{II.36}$$

$$e_V = \frac{p}{\rho} \sum_i f_{iV} \eta_i ,$$

(II.37)

$$e_E = \frac{p}{\rho} \sum_i f_{iE} \eta_i .$$

(II.38)

The dissociation energy per gram can be written

$$e_D = \sum_i \chi_i \alpha_i \delta_i ,$$

(II.39)

where χ_i is dissociation energy or ionization potential, α_i is the fractional dissociation or ionization, and δ_i is the number of particles per gram available for dissociation or ionization, all for the i^{th} species. Summing all these contributions enables the enthalpy to be written as

$$h = \frac{1}{2} \frac{p}{\rho} \mathcal{L} + \frac{1}{2} \mathcal{D} ;$$

$$\mathcal{L} = 5 + \sum_i \eta_i \left(f_{iR} + 2 f_{iV} + 2 f_{iE} \right)$$

$$\mathcal{D} = 2 \sum_i \chi_i \alpha_i \delta_i .$$

(II.40)

Substitution into the Hugoniot relation (II.6) yields

$$x_{10} = \frac{(\mathcal{Q}_1 - 1)\, y_{10} + 1}{y_{10} + \left\{ (\mathcal{Q}_0 - 1) - (\mathcal{D}_1 - \mathcal{D}_0) \frac{\rho_0}{p_0} \right\}} , \tag{II.41}$$

where again $y_{10} = p_1/p_0$ and $x_{10} = \rho_1/\rho_0$. This relation, when abbreviated as

$$x_{10} = \frac{\beta_1 y_{10} + 1}{y_{10} + \kappa_{10}} , \tag{II.42}$$

is quite similar to the Rankine-Hugoniot Equation (II.10), but in the place of μ we now find the general unequal numbers β_1 and κ_{10} which depend in a complicated way on the gas conditions. As before $y = y(U)$ is derived from the third Equation (II.12) with the result that

$$2\beta_1 y_{10} = (\beta_1 - 1)(n_0 + 1) + \sqrt{(\beta_1 - 1)^2 (n_0 + 1)^2 + 4\beta_1 (1 + n_0 - n_0 \kappa_{10})} . \tag{II.43}$$

An expression for the strength of the reflected shock which brings the primary flow to rest is again derivable from Equation (II.5), only now it is more convenient simply to define

$$n_1 = \frac{\rho_1 u_1^2}{p_1} = \frac{(y_{10} - 1)(x_{10} - 1)}{y_{10}} = \frac{(y_{21} - 1)(x_{21} - 1)}{x_{21}} . \tag{II.44}$$

In analogy with (II.42), the appropriate Rankine-Hugoniot equation is

$$x_{21} = \frac{\beta_2 y_{21} + 1}{y_{21} + K_{21}}, \qquad \text{(II.45)}$$

whence

$$2(\beta_2 - 1) y_{21} = \left[K_{21} + \beta_2 + r_1 \beta_2 - 2\right] + \sqrt{[\cdots]^2 - 4(\beta_2 - 1)(K_{21} - r_1 - 1)}. \qquad \text{(II.46)}$$

The reflected shock speed follows from the density ratios x_{10} and x_{21} as in Equation (II.1).

As an example, consider a shock of speed U moving into a mixture of neon and molecular nitrogen whose temperature is T_0 and total pressure is p_0. The initial fractions of the components are $\eta_0(Ne)$ and $\eta_0(N_2)$. By Equation (II.33), the initial effective molecular weight is $\sigma_0 = \sigma(Ne)\eta_0(Ne) + \sigma(N_2)\eta_0(N_2)$, and thus $r_0 = \sigma_0 U^2/RT_0$ is known. From the collection of simple shock identities in Table I, zeroth-order y_{10} and T_{10} are computed, and thus approximate values for p_1 and T_1 are known. The partial pressures of Ne and N_2 available for dissociation ionization follow from their initial fractional abundances, and all the equilibria can be computed from the zeroth-order conditions. Assuming the neon to be truly permanent, the only such fractions to be considered behind the shock are $\alpha_1(N_2)$ and $\alpha_1(NI)$. Their computation at any temperature is allowed by graphical presentation of the thermodynamic tables given in Appendix A. In front of the shock, $\alpha_0(N_2) = \alpha_0(NI) = 0$; therefore

(in reference to Equation (II.40)) $\vartheta_0 = 0$.

$$\vartheta_1 = 2 \sum_i \chi_i \alpha_i' \delta_i'$$

$$= 2 \left[\chi(N_2) \alpha_1(N_2) \frac{N^0}{\sigma_0} \eta_0(N_2) \right.$$

$$\left. + \chi(NI) \alpha_1(NI) \frac{N^0}{\sigma_0} \eta_0(N_2) 2\alpha_1(N_2) \right].$$

Therefore

$$\frac{\vartheta_1 \rho_0}{p_0} = \frac{2\eta_0(N_2) \alpha_1(N_2)}{kT_0} \left\{ \chi(N_2) + 2\chi(NI) \alpha_1(NI) \right\}.$$

Thus the dissociation-ionization contributions to the Hugoniot relation are spelled out in quantities which can be computed from the zeroth-order approximations.

In order that the effective degrees of freedom be computed behind the shock, the fractional abundances of the various species must be known. Aside from their obvious dependence on the associated dissociation-ionization equilibria, each of these fractions depends on all the reactions through the net change in the number of particles per gram. The ratio of effective molecular weights is

$$\sigma_{10} = \sigma_1 / \sigma_0 = \left(1 + \eta_0(N_2) \alpha_1(N_2) \left\{ 1 + 2\alpha_1(NI) \right\} \right)^{-1},$$

and the fractional abundances for the various species behind the shock wave are

$$\eta_1(Ne) = \sigma_{10}\,\eta_0(Ne),$$

$$\eta_1(N_2) = \sigma_{10}\,\eta_0(N_2)\left\{1 - \alpha_1(N_2)\right\},$$

$$\eta_1(NI) = 2\sigma_{10}\,\eta_0(N_2)\,\alpha_1(N_2)\left\{1 - \alpha_1(NI)\right\},$$

$$\eta_1(NII) = 2\sigma_{10}\,\eta_0(N_2)\,\alpha_1(N_2)\,\alpha_1(NI).$$

These fractions, together with the numbers $f_V(N_2)$, $f_E(NI)$, etc., tabulated in Appendix A, completely determine the sums $\sum_i f_i\eta_i$ which enter as the degree-of-freedom contributions $\mathcal{R}$ in the enthalpy (II.40) and the Rankine-Hugoniot Equation (II.41). Together, $\mathcal{R}$ and $\mathcal{D}$ determine β_1 and κ_{10}, the generalized μ-values. Then the combination $(r_0, \beta_1, \kappa_{10})$ implies the first-order value of y_{10} from (II.43). With this, the pair (β_1, κ_{10}) determines a first-order x_{10} from (II.42). Finally, the first-order value of T_{10} is given by

$$T_{10} = T_1/T_0 = \sigma_{10}\,y_{10}/x_{10}.$$

Thus the thermodynamics of the gas mixture in the zeroth-order state leads, through the generalized shock relations, to an evaluation of a corrected first-order state. If the state variables have changed so markedly that even the newly-derived state is suspect, then the process

may be repeated until the change per iteration is within some specified limit. Once the primary shock flow field has been thus computed, then one can enter into a similar analysis of the reflected shock transition via Equations (II.44) through (II.46).

5. SHOCK WAVES IN MIXTURES OF NEON AND CHROMIUM CARBONYL

This section gives numerical results for the temperature T_2 and pressure p_2 behind reflected shock waves when the test gas is a mixture of neon and chromium carbonyl. Two fractional abundances are considered, namely $\eta_o[Cr(CO)_6] = 3 \times 10^{-4}$ and 3×10^{-3} (3/100% and 3/10%). The initial temperature of the test gas is taken to be $T_o = 300°K$, and the total initial pressure $p_o = 1.027 \times 10^4$ cgs.* The range of assumed shock strengths is such as would ordinarily cover a range of T_2 from 4200 to 11,600°K for a permanent rare gas ($\mu = 4$). These choices are appropriate to the spectroscopic experiments described in Chapter VI.

A small contamination of air was also common to these experiments (Section 3, Chapter III), but in no case contributed more than 1/10% to p_o. The thermodynamic effects of this level of air impurity were evaluated by means of the N_2-in-neon theory given in the preceding section. The largest perturbation on T_2 was a drop of only 2% in the highest value, and the air impurity was thenceforth neglected in the calculations of the much stronger effects of chromium carbonyl.

---

*We will use this abbreviation for dynes/cm^2. This value of p_o is approximately 1/100 atmosphere ~ 7.5 mm Hg ~ 100 mm dibutylphthalate.

The equations specific to the perturbations by $Cr(CO)_6$ on neon are obvious extensions of those given in Section 4 and will not all be written out here. They run on into many terms since one must in general consider the dissociation of $Cr(CO)_6$ and CO, the ionization of Cr, C, O and Ne, the vibrational excitation of CO, and the electronic excitation of the four types of atoms and their ions. For example, the molecular weight ratio across the primary shock is given in general by

$$\sigma_{10} = \left[\begin{array}{l} 1 + 6\eta_0(Cr(CO)_6) \\ \\ + \eta_0(NeI)\,\alpha_1(NeI) + \eta_0(Cr(CO)_6)\,\alpha_1(CrI) \\ \\ + 6\eta_0(Cr(CO)_6)\,\alpha_1(CO)\left\{1 + \alpha_1(CI) + \alpha_1(OI)\right\} \end{array} \right]^{-1},$$

since the carbonyl is completely dissociated* behind the shock. The occurence of thermodynamically significant amounts of the molecules C_2, O_2, and CrO is ruled out by their low dissociation energies. Spectroscopic observations of small concentrations of C_2 and CrO are discussed in succeeding chapters.

*The dissociation equilibrium for $Cr(CO)_6$ is discussed in Appendix B. In spite of its stability at room temperature and its moderately high dissociation energy (8 ~ eV), the carbonyl is completely dissociated at 700°K for the pressures of interest.

We will also illustrate how the dissociation contribution to the enthalpy is computed for the reflected shock transition. With reference to the modified Rankine-Hugoniot Equations (II.41, 42, 45), we compute

$$(\Theta_2 - D_1)\frac{\rho_1}{p_1} =$$

$$2\frac{\sigma_{10}}{kT_1}\,\eta_0(NeI)\;\chi(NeI)\;\alpha_2(NeI)$$

$$+2\frac{\sigma_{10}}{kT_1}\,\eta_0(Cr(CO)_6)\left[\begin{array}{l}\chi(CrI)\left\{\alpha_2(CrI)-\alpha_1(CrI)\right\}\\ +6\,\chi(CO)\left\{\alpha_2(CO)-\alpha_1(CO)\right\}\\ +6\,\chi(CI)\;\alpha_2(CO)\;\alpha_2(CI)\\ +6\,\chi(OI)\;\alpha_2(CO)\;\alpha_2(OI)\end{array}\right],$$

where χ is the energy of dissociation or ionization and k is the Boltzmann constant. The carbonyl dissociation does not enter here because of its completion behind both the primary and reflected shocks. The lack of symmetry in this relation is due to the low primary flow temperatures of interest (2,000 to 5,000°K) whereby α_1(NeI, CI, OI) = 0. Table II gives the various binding energies used in our computations. The ionization potentials were taken from Charlotte Moore's[53] compilation of atomic-energy levels. We assumed the dissociation energy of CO to be 11.11 eV.*

*For a review of the problem of χ(CO), we refer the reader to the publications by Toennies and Greene.[71]

Appendix B discusses our derivation of $\chi[Cr(CO)_6]$ from thermochemical data.

TABLE II

BINDING ENERGIES

Process	Species	χ/k
Molecular Dissociation	$Cr(CO)_6$	8.61×10^4 °K
" "	CO	12.89 "
Atomic Ionization	CrI	7.8492 "
" "	CI	13.073 "
" "	OI	15.800 "
" "	NeI	25.020 "

Figures 2, 3, and 4 present the computed conditions behind the reflected shock as functions of the parameter r_o which characterizes the primary shock. The curves are drawn to connect smoothly the points computed for seven values of r_o spanning the range from 30 to 85. In order, these figures show the temperature, the pressure and the degrees of dissociation and ionization. The zero-impurity curves for T_2 and p_2 were calculated from the relations given in Section 3. These states (and those for the primary flow) were the starting points for the iteration procedures required by the carbonyl additive. All of the iterations were carried out until the change in temperature from one to the next had diminished to 1/2% or less. At this stage the corresponding fluctuation in pressure was usually about 1/5%. The term "fluctuation" is

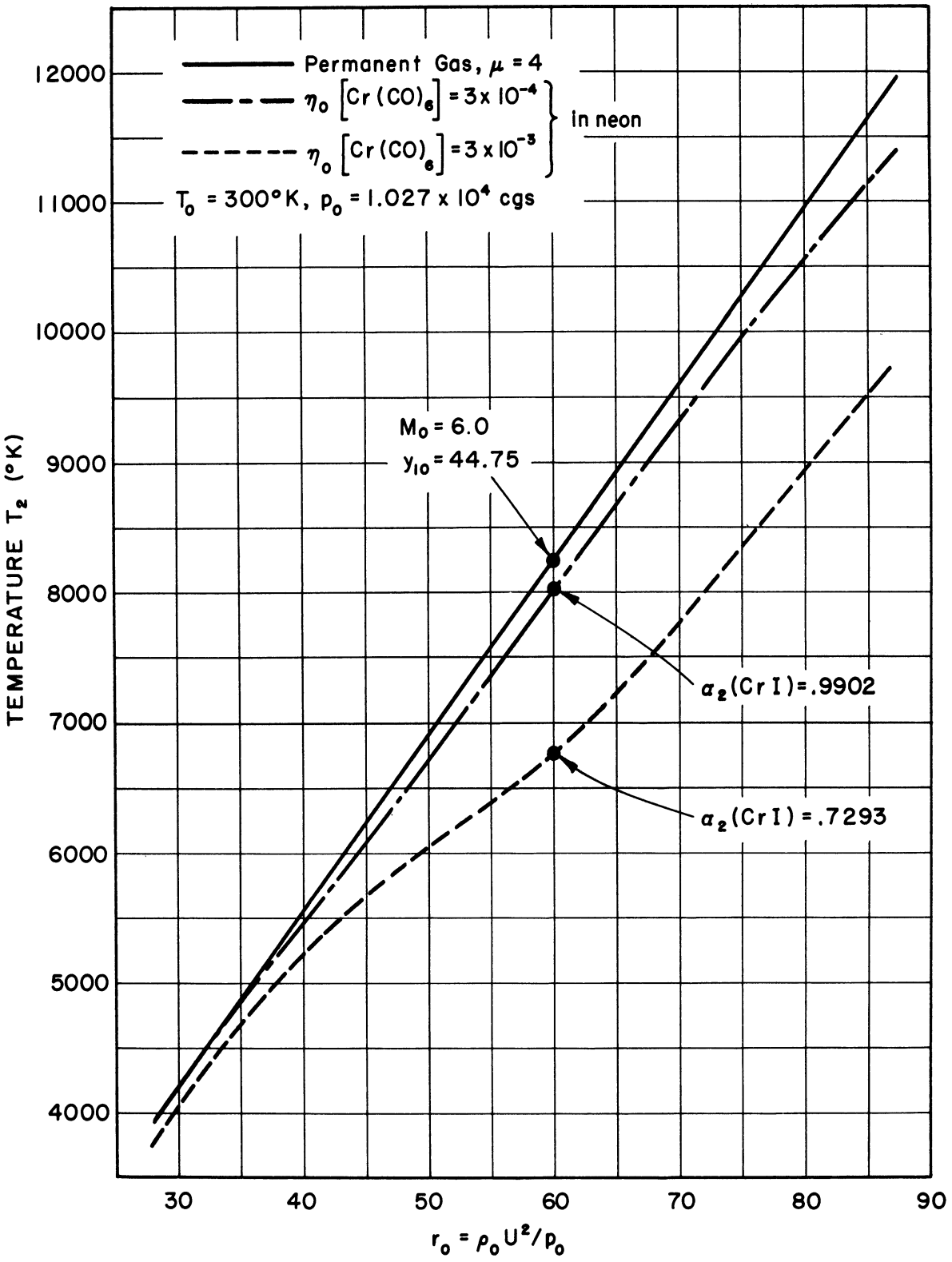

Figure 2. Temperature behind reflected shock vs. r_0-value of primary shock, for a permanent gas and two mixtures of $Cr(CO)_6$ in neon.

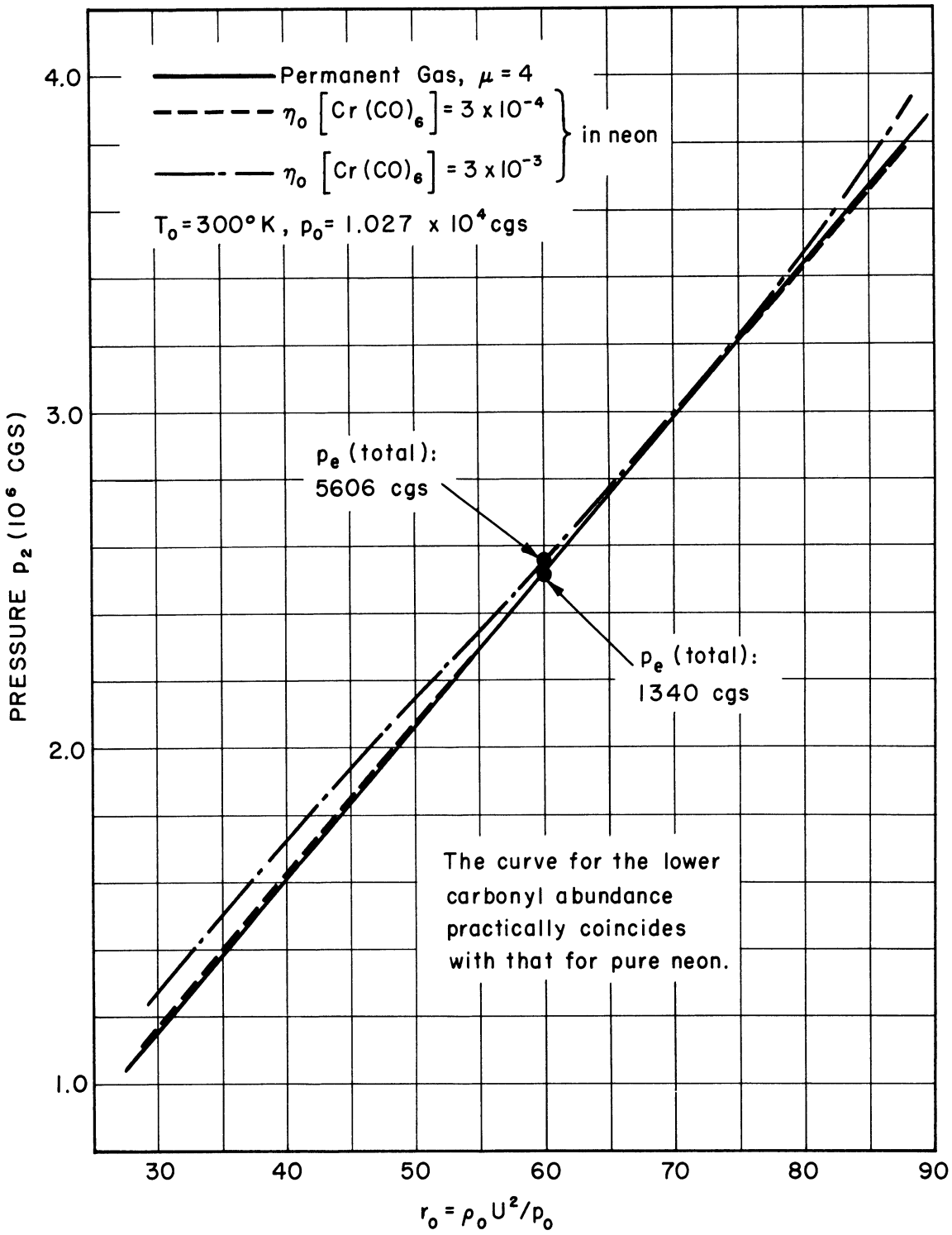

Figure 3. Pressure behind reflected shock vs. r_o-value of primary shock, for a permanent gas and two mixtures of $Cr(CO)_6$ in neon.

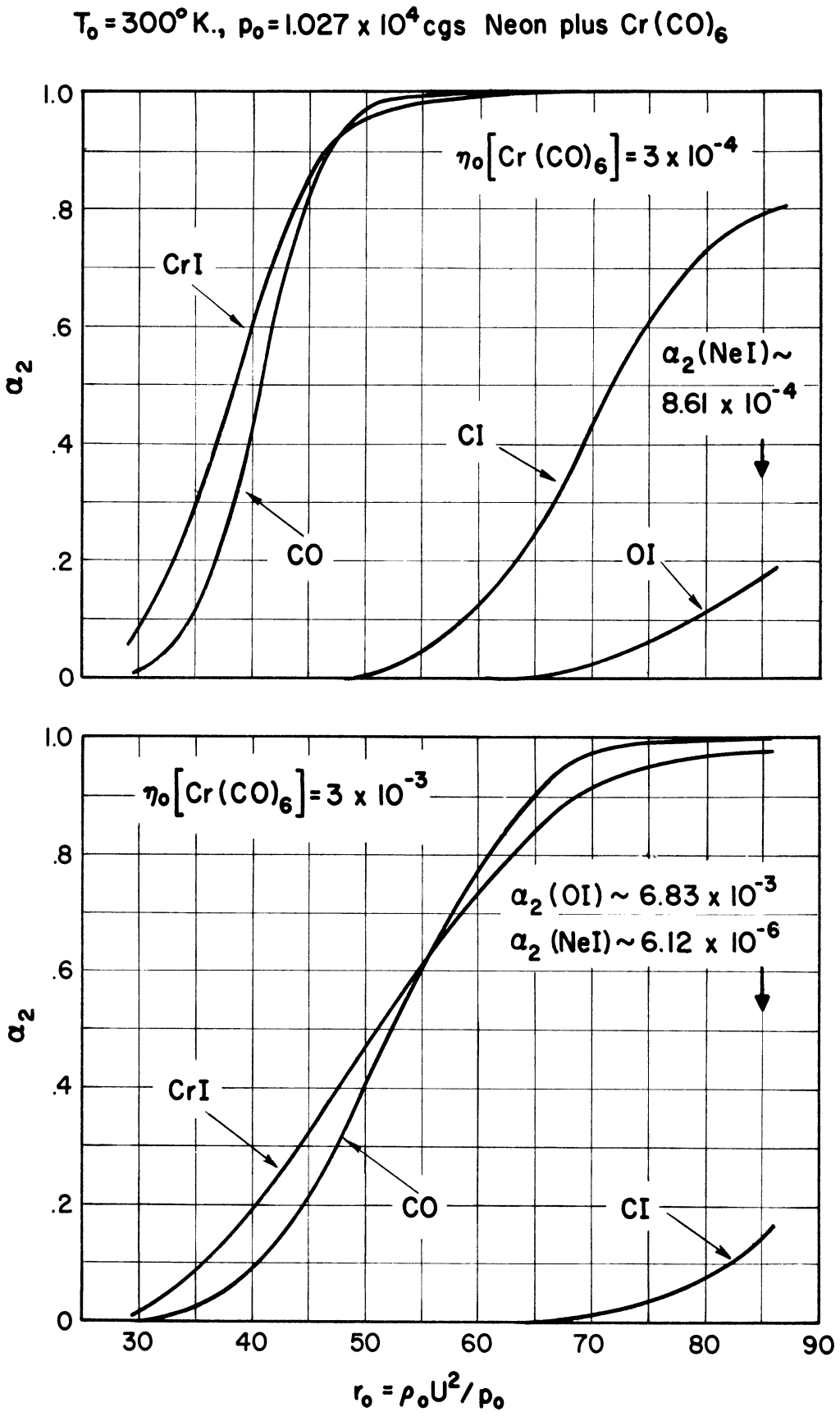

Figure 4. Degrees of dissociation and ionization behind reflected shock vs. r_0-value of primary shock, for two mixtures of $Cr(CO)_6$ in neon.

appropriate since the iteration procedure typically yields successive over- and under-estimates to the true state. When finally this oscillation fell within the above limits, the final state (p_2, T_2) was chosen to be midway between the last two iteration results. The equilibria shown in Figure 4 were computed in this final state.

In Table III, we list the maximum number of iterations required by the above criterion for the two impurity levels of interest and the primary and reflected shock transitions.

TABLE III

ORDER OF ITERATIONS REQUIRED FOR COMPUTING STATE VARIABLES BEHIND SHOCKS IN TWO MIXTURES OF NEON AND $Cr(CO)_6$

Shock Transition	$\eta_o[Cr(CO)_6] = 3 \times 10^{-4}$	$\eta_o[Cr(CO)_6] = 3 \times 10^{-3}$
0 → 1	2	3
1 → 2	4	6

These numbers apply strictly to the higher temperature cases ($r_o = 70$ above); the required number was generally one less for r_o as low as 30 or 40. For the reflected shock transition (1 → 2) at $\eta_o[Cr(CO)_6] = 3/10\%$, the carbonyl effects were so strong that the usual procedure had to be by-passed by some judicious guessing. The first two iterations from the permanent gas states showed fluctuations so large that 10 or

or 15 customary steps appeared likely. This was particularly marked for r_o = 50 and 60 where the fractional dissociation of CO was very sensitive to the assumed temperature. Fortunately, the new states chosen at this stage were sufficiently good that the number of subsequent iterations had only to be about half what it might have been with the straight forward procedure.

From Figures 2 and 3, one can see that the chromium carbonyl affects the temperature far more than the pressure. For r_o = 80($T_2 \sim$ 11,000°K for a permanent rare gas) the temperature decrements are about 500 and 2,000°K for additive fractions of 3/100% and 3/10%, respectively. By contrast, the corresponding pressures are all within 1% of each other. This kind of behavior of the state variables is typical for real gases when they are sufficiently heated that their latent impermanence comes into play. The temperature decrease is due primarily to the binding energies χ which must be drawn from the gas to establish the dissociation and ionization equilibria.* The extents of these reactions appear (together with their energies) as subtractive terms in the denominator of the generalized Rankine-Hugoniot Equation (II.41). Thus, for a given shock strength, the density can be significantly greater than for a permanent gas, and the temperature correspondingly less.

In our case, the details of this effect are somewhat clouded by our having to treat two successive shock transitions. Nonetheless, our com-

*Roughly speaking, these energies are of the order of 10 eV, compared to the nominal values of 1eV for the mean translational energy of the particles and 1/10 to 1 eV for their internal excitation.

putations indicate that the major part of the T_2 - decrement comes from the increased density ratio (x_{21}) across the reflected shock. This is due, in turn, to the considerable break-up of atoms and molecules behind the reflected shock, of which the most effective is CO dissociation. For stronger shocks, the fractional ionization of neon (the principal constituent) would become large enough to induce even larger temperature decrements. A hint of this already appears in Figure 2 as a dip in the upper end of the middle curve. For $r_o = 85$ and $\eta_o[Cr(CO)_6) = 3 \times 10^{-4}$, the ionization of neon is already contributing about 3/10 of the total electron pressure, compared to contributions of 1/10 each by chromium and oxygen and 1/2 by carbon.

In Chapter VI we will discuss the use of our calculations in spectroscopic experiments whose conditions are very close to those we have considered here. One may also use the curves in Figures 2-4 to make good guesses of the state variables in other situations and thus be able to shorten the iteration procedure in computing accurate states. For the chosen value of p_o(~ 1/100 atoms), any value of $\eta_o[Cr(CO)_6]$ up to about 1% could be thus accommodated. For higher values of p_o, the percentage effects of a fixed <u>fraction</u> of the carbonyl will be reduced, since the extents of dissociation and ionization will be suppressed by the higher absolute pressure of the carbonyl fragments. Also for higher p_o, a fixed initial <u>partial pressure</u> of $Cr(CO)_6$ is equivalent to a reduced η_o, and the curves can again provide upper bounds on the percentage changes of p_2 and T_2 from their permanent gas values. The effects with other car-

rier gases, such as helium and argon, could similarly be estimated except for ionization of the carrier at high temperature (e.g., argon at 10,000°K). The effects of other metallic carbonyls (see Appendix B) would be similar to those of $Cr(CO)_6$, since the principal cooling agent is CO for this range of shock strength, and these other compounds have similar metal-to-CO ratios.

6. THEORY OF ADDITIONAL VELOCITY MEASUREMENTS

We close this chapter by discussing the utility of simultaneous measurements of wave and particle velocities. Some workers have used this technique to determine (via the Hugoniot relation) the equation of state of a particular gas. For example, Christian, Duff and Yarger[54] have measured the dissociation energy of N_2 by observing the velocities of both the primary shock and the flow behind it. The relevant theory has been given in the previous section.

The simple shock relations of Section 3 allow a different sort of measurement on an ideal gas of unknown temperature. The pressure and density ratios across a shock wave and the absolute temperatures on either side of it may be computed from both flow velocities in the shock-stationary frame. Since this frame of reference is usually not the one in which laboratory experiments are performed, an additional measurement of the absolute shock speed is required. In Section 7 of the next chapter we describe such experiments with the reflected shock transition; the pertinent theory is given here.

Figure 5 is an x-t diagram for the flow near the end of a shock tube as it would be viewed by an observer moving with the reflected shock velocity. In this frame, the primary flow speed is denoted by v_3. Somewhat in anticipation of the experiments of Chapter III, we have relaxed the assumptions as to the uniformity of the primary flow and the state of rest behind the reflected shock. In general, $v_2 \neq V$. The reflected shock conditions for an ideal gas are

$$\rho_1 v_3 = \rho_2 v_2 ,$$

$$\rho_1 v_3^2 + p_1 = \rho_2 v_2^2 + p_2 ,$$

$$(\mu+1)\frac{p_1}{\rho_1} + v_3^2 = (\mu+1)\frac{p_2}{\rho_2} + v_2^2 .$$

(II.47)

Regarding the velocities as known, these conditions constitute a system of three equations in the four unknowns (ρ_1, p_1, ρ_2, p_2). Ratios of three of these to a fourth (e.g., ρ_1) can be found, and one derives

$$x_{21} = \rho_2/\rho_1 = v_3/v_2 ,$$

$$y_{21} = p_2/p_1 = (\mu v_3 - v_2)/(\mu v_2 - v_3) ,$$

$$T_1 = \sigma v_3 (\mu v_2 - v_3)/R(\mu+1) ,$$

$$T_2 = \sigma v_2 (\mu v_3 - v_2)/R(\mu+1) .$$

(II.48)

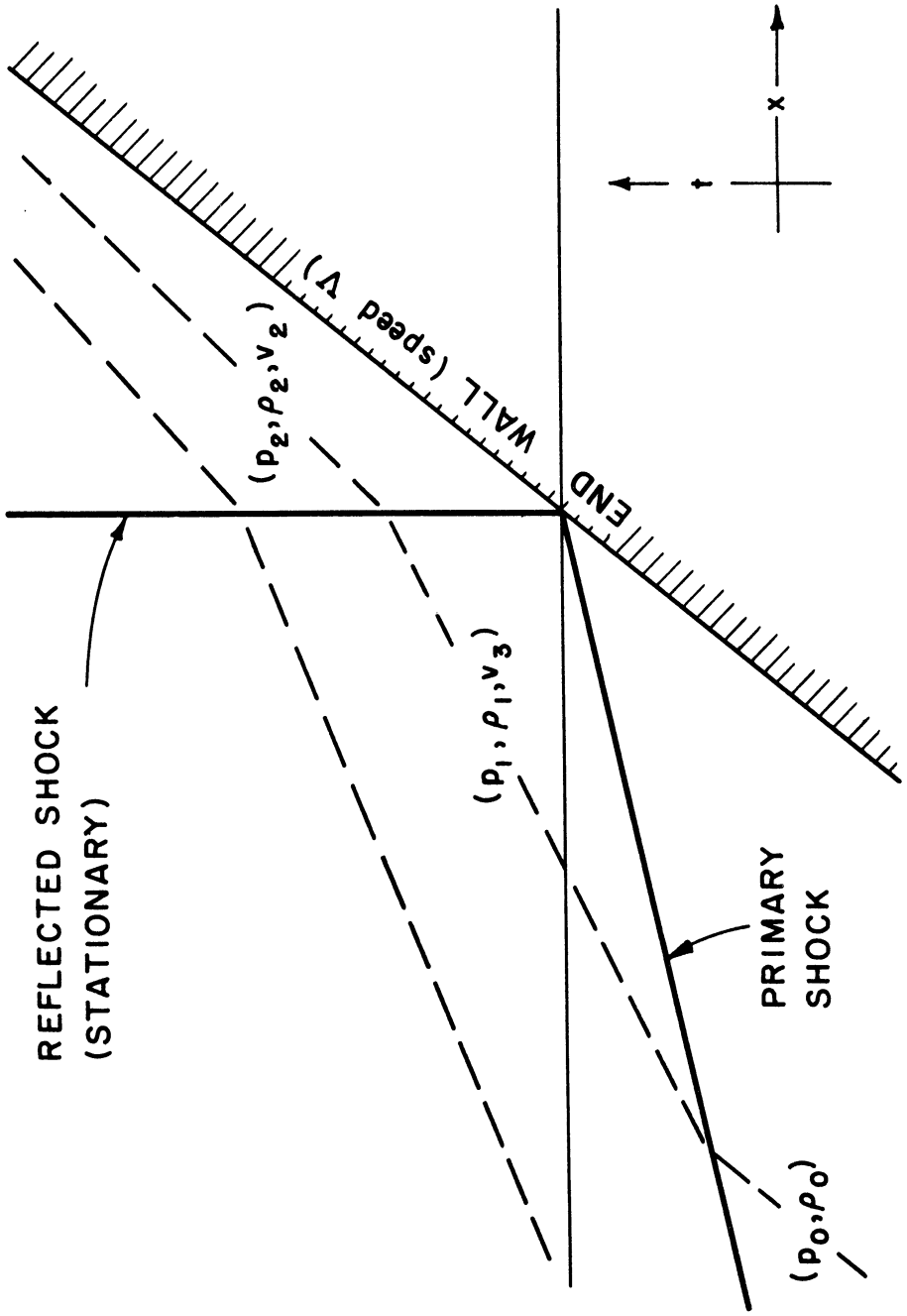

Figure 5. x-t diagram of flow near the end wall with the reflected shock stationary.

The velocities follow from laboratory measurements of the reflected shock speed V, the primary flow speed u_1, and the (small, positive) flow speed u_2 behind the reflected shock.

$$v_3 = V + u_1 ,$$

$$v_2 = V + u_2$$

This method enables a direct check on the temperatures computed from the primary shock speed alone. The method may be supplemented (as in Section 8, Chapter III) by measurements of absolute pressure in both regions of flow. A consistency check is provided by comparison of the y_{21} as computed from the velocity measurements (second of Equations (II.48)) and derived from the pressure measurements.

CHAPTER III

HYDRODYNAMIC EXPERIMENTS

1. INTRODUCTION

At the Michigan Shock Tube Laboratory, the majority of the observations of high temperature rare gas flows is made by photographing the luminosity which results from the addition of contaminants to the rare gases. Following the discussion of equipment and techniques in Sections 2, 3, and 4, Section 5 describes the space-time visualization of shock waves, interfaces and boundary layers by means of molecular emission. This emission differs markedly from steady, thermal equilibrium radiation, which is the topic of Chapter V. We will discuss the origins of transient molecular emission in Chapter IV.

The self-luminosity of the gases makes immediately evident several departures of shock tube behavior from the simple theory of the previous chapter. These departures and their relation to viscosity are discussed in Section 6. The quantitative understanding of shock tube viscosity effects is as yet incomplete, and we have had to inquire whether the ideally-computed state variables are significantly in error.

Sections 7 and 8 describe the direct measurements of flow velocity and pressure which were made to test the adequacy of the observed primary shock speed as an indicator of the flow variables near the end of the shock tube. We have paid particular attention to the thermodynamic conditions behind the reflected shock because of our interest in this gas as a

spectroscopic source.

The measured state of this gas is in good agreement with ideal theory in spite of the non-ideal effects observed in the primary flow.

2. GENERAL DESCRIPTION OF EQUIPMENT

The shock tube used for our measurements has already been described in large part by Turner,[12] and the reader is referred to his dissertation for those details omitted here. Figure 6 shows the present experimental arrangement. The shock tube is supported above a long table which is also a platform for most of the gas-filling and evacuation accessories. From right to left, the shock tube sections are first the compression chamber (120 cm long) and then the expansion chamber (265 cm long) of which the test section is the terminal part. Manometers and McLeod gauges are mounted on the tall vertical panels near the diaphragm breech between the high and low pressure sections. Behind these gauges are the lines used in filling the expansion chamber with gas from flasks and bottles. Not visible are the common manifold to which these lines run, the flush valve* between the manifold and the expansion chamber, and the oil diffusion pump connected to this manifold. The mechanical pump on the floor provides rough vacua for the diffusion pump exhaust, the manometer reference, and the initial pumping of the entire tube. In use, the high pressure

*Contrary to what one might expect, this name derives not from a procedure but rather from the mechanical design. The valve may be described as a very blunt right-angle needle valve whose seat is an O-ring on the outer side wall of the shock tube. The "needle" is so shaped that when the valve is closed the inner wall is practically continuous.

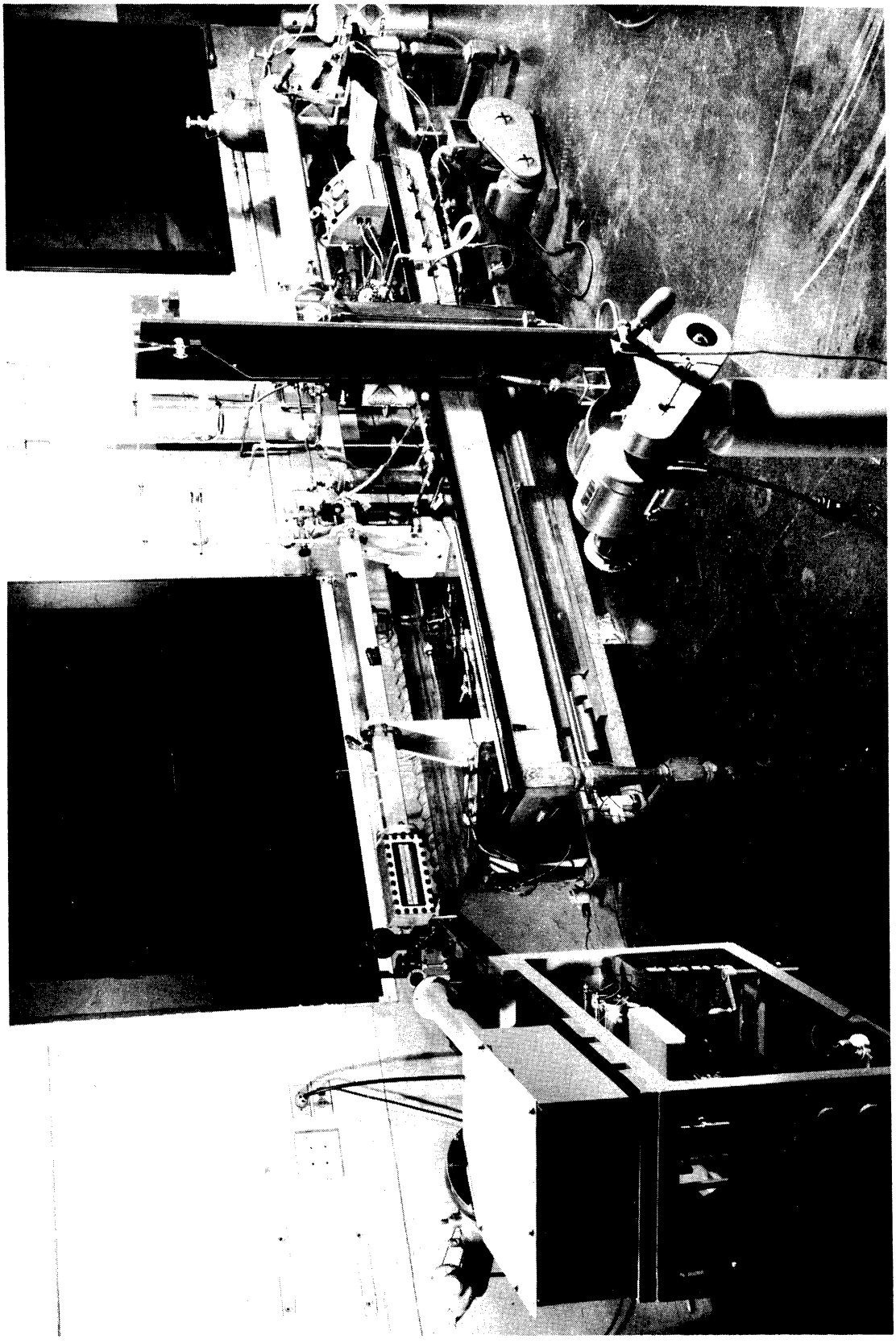

Figure 6. The high temperature shock tube.

section is filled with hydrogen from the tank at the right. The main body of the test section was machined from an aluminum forging and has the internal cross-section of 4.13 (horizontal) by 6.67 cm (vertical) which is common to the entire tube. The side walls of this section are 1" thick Plexiglas windows which are held in place by retaining rings with double O-ring seals. These windows allow an unobstructed view of the top, bottom, and end walls of the section. In Figure 6, all of the front window is covered except for a narrow slit which is parallel to the direction of gas flow. This slit is imaged across a moving film in the rotating-drum camera (foreground) for x-t photography of luminous phenomena. At the extreme left is a spectrograph with another rotating-drum camera. The spectrograph is illuminated by means of a mirror which collects light from the gas in the test section through the back Plexiglas window. This arrangement enables the simultaneous recording of x-t data and time-resolved spectra.

3. GENERAL OPERATIONS WITH GASES AND VAPOR PRESSURE MEASUREMENTS ON $Cr(CO)_6$

For all experiments the gas in the compression chamber is high pressure hydrogen at room temperature. This chamber is first evacuated to 100 microns and then filled directly from a 2000 psi tank; the high pressure is then read with a Bourdon gauge. The diaphragms used to separate the high and low pressure sections are cellulose acetate sheets of various thickness. For this particular cross-section of tube, a .060" diaphragm holds 400 psi for several minutes but ruptures in a few seconds under a 600 psi

load. These diaphragms always break out over the entire tube cross-section. A solenoid-driven prod is sometimes used to break the diaphragm at a predetermined driver pressure. The gas-dynamic phenomena take place very rapidly as soon as the diaphragm breaks, and certainly within 5 seconds the tube is simply a pipe containing primarily hydrogen (at roughly 1/3 the driving pressure) and diaphragm particles of various sizes. The hydrogen overpressure is released through a pipe to the atmosphere outside the building. The tube is again closed up and the residual hydrogen is pumped outside with the mechanical pump. Air is let into the tube which is then opened for cleaning and diaphragm replacement. The diaphragm fragments are removed by swabbing with a dry-or alcohol-soaked cloth. In each shot some damage is done to the test section windows by high speed diaphragm particles. So far this has been tolerated by buffing or (eventually) replacing the windows. Metal diaphragms are now being tried with some success. An aluminum sheet, .050" thick and milled with an X pattern of grooves .015" deep, breaks under a 350 psi load in this cross-section of tube. The four petals flap out violently against the inside walls of the expansion chamber, but do not tear away from the rest of the diaphragm.

The low pressure side of the shock tube (consisting of the expansion chamber, manifold, and gas-delivery lines) can be pumped down with the diffusion pump to a pressure of less than 1/10 micron (10^{-4} mm Hg). For all parts of this sytem, the static leak rate can be made as low as 4/10 micron per minute if some care is taken in the cleaning of the tube, assembly of ground glass joints, etc. The running of an experiment is generally preceded

by a 5-minute interval during which the diffusion pump is closed off and the appropriate gases are loaded in the tube. The temperature of the test gas is read to an accuracy of 1/10°C on a thermometer strapped to the expansion chamber. The test gas pressure is usually of the order of 10 mm Hg, so that the impurity level due to leaks is always less than 1/10%. The range of gas pressures from 10^{-4} to 10^{3} mm Hg is covered by coarse and fine McLeod gauges (gauge constants of 5.25×10^{-4} and 5.16×10^{-6} mm^{-1}), a dibutyl phthalate manometer, and a mercury manometer. In addition a thermocouple gauge is used as a continuous, qualitative pressure monitor. All of these gauges are connected to a common manifold through which gases are loaded into, and evacuated from, the expansion chamber. The flush valve connecting this chamber to the manifold is closed just before the tube is fired to prevent the flow of high pressure hydrogen into the manifold.

The test gases used in these experiments were usually mixtures of Linde "mass-spectrometer-checked" neon with small amounts of contaminants added for spectroscopic purposes. In qualitative work with additives such as CH_4 and NH_3, the mixtures were made in the shock tube just before firing. For the quantitative studies with $Cr(CO)_6$, mixtures were made up in separate flasks several days prior to their use. In either case the neon (or argon) was taken directly from the Linde bottle. The vapor pressure of an additive determined the method by which it could be introduced. CH_4 and NH_3 (Matheson, CP grade) were obtained directly from their supply bottles. Less volatile liquids, such as pyridine (C_5NH_5) and carbon disulfide, were frozen with liquid air in vacuum test-tube flasks. After

the air was pumped out, the flasks were closed off and allowed to return to room temperature. The resultant liquid-vapor equilibrium in the flasks provided a more than adequate gas supply. The required pressures of these additives in the shock tube were low enough that they could be read on the McLeod gauges without fear of condensation.

Considerable discussion will be given here to the handling of the metal carbonyls because of the difficulties involved on the one hand and, on the other, the great promise which these compounds hold for spectroscopic studies in gas-dynamic devices. Gifts of various carbonyls were made to this laboratory by Dr. Leslie Brimm* of Linde Air Products and Dr. Irving Wender of the U. S. Bureau of Mines. Most of the carbonyls are highly toxic, primarily because of the valence states in which the metals occur; also these compounds are flammable and yield large amounts of carbon monoxide upon decomposition. With respect to volatility at room temperature, $Ni(CO)_4$ and $Fe(CO)_5$ can be classed with the liquids discussed above, but $Cr(CO)_6$, $Mo(CO)_6$, and $W(CO)_6$ are crystalline substances which sublime to pressures of the order of 100 microns. Because of condensation, these pressures cannot be read on a McLeod gauge. It proved possible to control and measure the abundance of $Cr(CO)_6$ by means of the temperature variation of its vapor pressure. We have not yet worked with the other solid carbonyls, but the similarity of their physical properties implies that they can be handled by identical methods.

---

*We are particularly grateful to Dr. Brimm for a discussion of vapor pressure data for the carbonyls.

A reservoir of $Cr(CO)_6$ vapor was obtained in a vacuum test-tube flask (as above). This flask was then connected to a larger flask, and the two were allowed to come to vapor equilibrium over a period of an hour. During this time the room temperature was held constant at a few degrees below the normal condition. Finally, a predetermined amount of neon was added to the larger flask which then constituted a reservoir of pre-mixed neon and $Cr(CO)_6$ of known composition, and was subsequently used to fill the shock tube.

It proved necessary to re-determine the $Cr(CO)_6$ vapor pressure curve, for which two rather different results had previously been published. This was done by the writer and David M. Brown* of the Mass Spectroscopy Laboratory, Chemical and Metallurgical Engineering Department, The University of Michigan. The vapor pressure was measured at four temperatures with a Consolidated Electrodynamic micromanometer. Each of these pressures was null-checked by providing the manometer with non-zero reference pressures of air which were read on a McLeod gauge. Our results agree with the 1935 determinations[55] by Hieber and Romberg** and are listed in Table IV. The

*We are greatly indebted to Mr. Brown for his assistance in these measurements. This study was materially aided by the low temperature vacuum-distillation technique developed by him for growing large, flawless crystals of $Cr(CO)_6$ and thereby ridding the solid of occluded gases.

**The paper referred to here is the twenty-first in a series, "Uber Metallcarbonyle," by Hieber and co-workers at the Technische Hochschule, Stuttgart. These publications contain much useful information on the properties, preparation and handling of the carbonyls. The 1934 determinations by Windsor and Blanchard[56] yield room-temperature vapor pressures of $Cr(CO)_6$ which are too high by a factor of two. Their data apparently were affected by partial decomposition of the carbonyl into carbon monoxide (see Appendix B).

heat of sublimation implied by our measurements is

$\Delta H_S)_{Cr(CO)_6}$ = 17.2 kilocalories per mole = 8650°K per particle.

TABLE IV

MEASURED VAPOR PRESSURE OF $Cr(CO)_6$

T	$p_V(Cr(CO)_6)$
0.17°C	13.4 ± 1 microns
12.8	51.1 ± 1
21.4	121 ± 2.5
26.5	195 ± 4

These measurements were also used by Brown to make standard neon-$Cr(CO)_6$ mixtures which were analyzed in the mass spectrometer. The mass spectrum of the various carbonyl fragments was reproducible within the accuracy of the above data, and was used for calibrating the"cross check" analyses of mixtures made up later at the Shock Tube Laboratory. In all cases the predicted abundances of neon and $Cr(CO)_6$ were verified by these checks. Therefore the absolute amount of the carbonyl was known with at least 2% accuracy in all the shock tube experiments, and the abundance of chromium in the various portions of shock tube flow was subject to good control. Precautions were always taken to insure that neither the vapor pressure measurement nor the making of mixtures was subject to contamination by air, water vapor, or carbon monoxide. Prior to freezing the carbonyl for removal of air, the test-tube flask was pumped on for several minutes to remove condensible vapors, and the freezing was done at dry-ice temperature. A cold trap was required to keep the carbonyl out of the vacuum pumps.

4. PHOTOGRAPHIC METHODS

Space-time photographs of the shock tube flow are taken with the revolving-drum camera. The addition of contaminants to neon causes many portions of the flow to be self-luminous* and there is no pressing need for the optical accessories (e.g., schlieren systems and external light sources) required in low temperature shock tube studies. In all cases the field of view of the camera is restricted to a narrow slit which runs in the space-direction of interest. This slit is formed by ruled metal straight-edges screwed onto the outside of the test section window. The rest of the window is covered with black paper. The slit is imaged across a 35-mm film wrapped once around a drum inside the camera. Time resolution is achieved by rotating the drum at high speed with an external motor. The "writing rate" of this camera (in microseconds per millimeter of film length) is W = 89,960/drum rpm. The rpm is measured to 1/4% with a Hasler-Tel speed indicator. Usually the rpm is about 13,000 and the corresponding W is roughly 7 μsec/mm. The camera lens has an aperture of f/4.5 and a focal length of 8.5". With the camera placed 6' from the test section, the reduction factor M from slit to slit-image is approximately 7; thus the image of a 20-cm long slit is easily fit into the 35 mm width of the film.

For measuring the velocities of shock waves moving along the tube axis (x-direction), the slit is horizontal. The trace of a luminous

*As will be shown in following sections, there is a wealth of information contained in the kinematic diagrams which this method provides. Naturally, some care must be taken in identifying the features in the diagrams.

shock front on a x-t film is a black line cutting diagonally across the film. For a shock whose speed is 3×10^5 cm/sec, the angle between its trace and the direction of film motion is about 70°. For accurate computation of shock speed, various calibrations of the x-t picture are required. The drum rpm (and therefore W) is measured just as the shock tube is fired. Prior to each experiment, still pictures are taken of the slit to determine its angle with respect to the direction of film motion. The reduction factor M is obtained from the images of the slit-jaw rulings; this is suitably corrected for the difference between (optical) camera distances from the slit and from the luminous gas inside the test section. The time axis on the film is determined by spinning the drum with the camera shutter open, thereby exposing the film to the image of a point light-source temporarily mounted in front of the slit. The resulting "time-line" is the base against which all image angles are later measured with a Gaertner protractor microscope. These angle measurements yield the shock speed v_f in film coordinates, and the application of M and W converts v_f to the laboratory shock speed U. The net accuracy to which U can be measured is between 1/2% and 1%.*

Space-time photographs are also taken through a vertical slit. These pictures record the time variations of luminosity <u>across</u> the flow channel (y-direction). Accessible to this method are such determinations as the relative planarity of a luminous shock, the shape of the driving interface,

---

*The alignment precautions necessary for this kind of photography are fully discussed by Doherty in Chapter II of his dissertation.[35]

and the nature of wall luminosities.

Emission spectra of luminous portions of the flow are obtained with an f/7 grating spectrograph. This instrument will be described more fully in Chapter VI. For the experiments relevant to this chapter, a small portion of the test section is imaged on the spectrograph slit. The (x,y) location of this portion is easily varied. The succession of fluid-dynamic events at any particular place in the tube requires time-resolution of the spectra, and this is accomplished by the rotating-drum camera in the image plane of the spectrograph. The 35-mm film in the drum takes the place of the customary spectrographic plate. The wavelength "direction" runs across the film and, again, time runs along the length of the film.

All black and white pictures are taken with the Eastman Kodak 103 emulsion in the spectral classes D, F, and O. The films are unperforated and anti-halation backed. Most of the processing is done with D-19 developer (5 minutes) and F-6 hypo. A few films were developed with Ethol UFG, but no significant improvement was observed in the blackening of faint images. By taking some snapshots in the laboratory, we have estimated the ASA speed of the 103-D emulsion to be between 2500 and 3000. This high speed is apparently not seriously reduced for the short exposure time (1 to 100 μsec) encountered in the moving-film photography.

We have taken x-t and y-t pictures in color with the Anscochrome and Super-Anscochrome emulsions developed for ASA 128 and ASA 200/400, respectively. Comparison of these pictures with time-resolved spectra indicates that the color rendition is much more faithful than one might expect for

the short exposure time. It proved possible to identify and locate in space-time some of the more characteristically-colored emitters.

5. FLOW VISUALIZATION VIA ORGANIC ADDITIVES

The luminosity of moderately strong shock fronts in the rare gases was a puzzle for several years following its discovery in 1951 by Petschek.[57] In x-t photographs, this luminosity is recorded as a thin diagonal line across the film. In 1955, Turner,[12,58,59] and Rosa[60] identified the emission as primarily the Swan bands of C_2 and the violet bands of CN. The presence of carbon and nitrogen was attributed to small amounts of air and pump-oil vapor in the test gas. When the vacuum system of the Michigan shock tube was later improved, the primary shock luminosity vanished. Charatis, Doherty and the writer then undertook a study of how the luminosity might systematically be restored with organic additives.[61] The resulting photographs enabled the direct visualization of many portions of the flow. Simultaneously, several phenomena were observed which were inconsistent with the one-dimensional, inviscid flow theory of the shock tube. Most of these will be discussed from a hydrodynamic standpoint in Section 6. This section describes the method of generating the luminosity and the hydrodynamic objects which may then be seen.

A. We found that many organic additives would lead to luminosity at and behind shocks that would otherwise have been invisible. For photography with the equipment described above, the required shock strength was

$y_{10} \geq 40$ ($M_0 \geq 5.5$, $T_1 \geq 3300°K$) and the partial pressure of the contaminant was between 10 and 100 microns. With the additives, CH_4, CS_2, C_2H_2, C_2H_4, C_2H_6, and C_6H_6, the primary shock luminosity in the visible spectrum consisted of the C_2 Swan bands. In addition, the CN violet bands appeared with the additives $CH_4 + NH_3$, C_5NH_5 (pyridine), and $C_4N_2H_4$ (pyrimidine). A typical x-t picture is shown in Figure 7. The conditions for this particular experiment are listed in Table V. We have computed the flow variables

TABLE V

COMPUTATIONS FOR THE EXPERIMENT OF FIGURE 7

Driver pressure:	$p_4 = 645$ psi
Initial test gas pressure:	$p_0 = 15.5$ mm Hg neon + $CH_4(40\mu)$
Initial temperature:	$T_0 = 297°K$
Primary shock speed:	$U = 3.07 \times 10^5$ cm/sec
Primary shock strength:	$p_1/p_0 = y_{10} = 57.5$
Primary shock Mach number:	$M_0 = 6.80$
Behind primary shock	
Pressure:	$p_1 = 891$ mm Hg
Temperature:	$T_1 = 4550°K$
Behind reflected shock	
Pressure:	$p_2 = 4990$ mm Hg
Temperature:	$T_2 = 10{,}500°K$

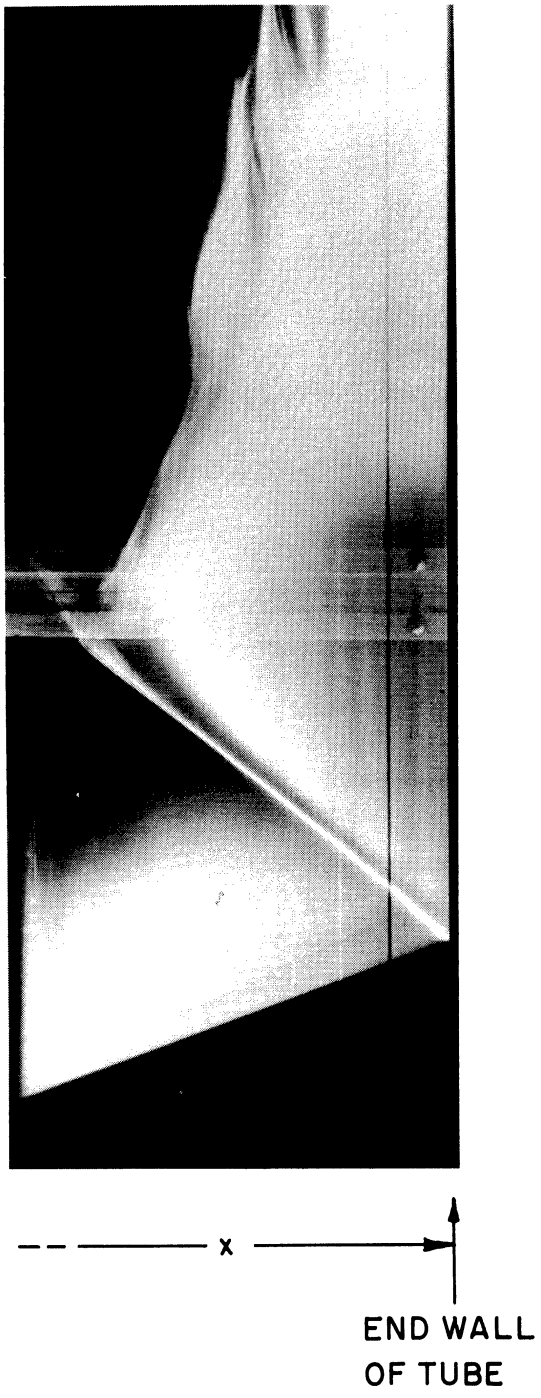

Figure 7. x-t photograph taken through horizontal slit.

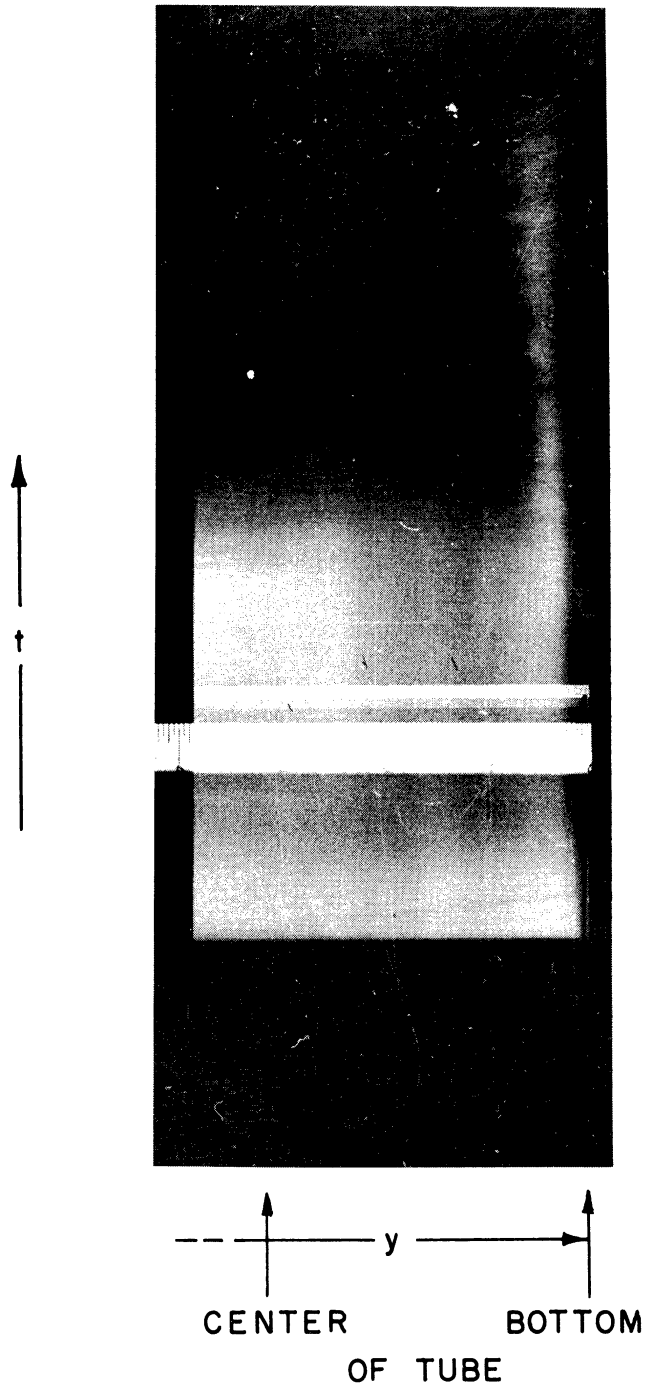

Figure 8. y-t photograph taken through vertical slit.

from the shock speed and the initial conditions, neglecting CH_4 dissociation and all possible ionizations.

Strong C_2 emission occurs in much of the primary flow and in the reflected shock front; these regions are a rich blue in a color photograph. During the "dark time" following the reflected shock, the relaxation to equilibrium ionization is occurring. Its completion is signalled by a sharp increase in luminosity consisting primarily of the red lines of neon and Stark-broadened Balmer lines of hydrogen. Faint C_2 bands are also emitted from this region. The color of the light is a vivid pink. The subsequent wave pattern shows repeated shock passages between the cold hydrogen interface* and the end wall. Each passage increases the pressure and temperature of the gas and the intensity and broadening of the emitted spectral lines.

B. For the experiment of Figure 7 and all similar experiments, the original x-t films showed many faint streaks of exposure in the region between the luminous front of the primary flow and the apparent locus of the non-luminous interface. For lower initial pressure p_o, the primary flow field was shorter and smoothly luminous throughout. We discovered the cause of the streaks by taking y-t pictures through a vertical slit[42] placed far enough from the end wall of the tube that the reflected shock was not seen. Figure 8 is such a photograph of an experiment similar to

*Apart from turbulence and mixing at this surface, we regard it as the interface and not some counterfeit arising from strong waves entirely within the driven gas. The hydrogen content of the mixing region was verified by Turner. Even when the test was pure neon, he observed strong Balmer line emission from the region following its interaction with the first reflected shock. Moreover, the subsequent flow and shock lines match reasonably well with a one-dimensional theory of the interface-reflected shock interaction; e.g., see Turner, p. 30.

the one of Figure 7. Only the lower half of the flow is visible, since the camera had purposely been aligned so that its line of sight grazed the floor of the tube. The luminosity behind the primary shock separates gradually from the floor of the tube. The growth of the dark intervening zone suggests the development of a cool laminar boundary layer. As the main stream luminosity fades, an increasingly thick layer of ragged luminosity develops near the wall. It appears that the assumed laminar layer undergoes a transition into turbulence. All luminosity disappears when the driving interface passes the slit about 150 μsec later than the shock. Time-resolved spectra were taken at various y positions behind the vertical slit and showed that the erratic boundary layer emission also consisted of the C_2 Swan bands. Both the main stream and boundary layer luminosities were blue in color y-t photographs. For most experiments of this type, the original y-t films showed some randomly distributed patches of C_2 emission up above the layer. These apparently were luminous eddies of the turbulent layer on the side walls of the tube. It was these patches which, by their motion down the tube, had made the streaks on the x-t films. For experiments with lower p_o, the C_2 turbulence-luminosity did not appear in the y-t pictures and thus the associated streaks did not occur on the x-t films. The emission did not occur in any experiment with pure neon.

The identification of the luminous and non-luminous gases with the customary boundary layer zones is supported by comparison of our data with other experiments and with theories of viscous flow. Such comparison proceeds from the Reynolds number

$$\mathcal{R}_e = \frac{\rho v L}{\eta} ,$$

where η, ρ, and v are respectively the viscosity coefficient, density, and speed of the gas, and L is a characteristic length of the flow process. The definition of Reynolds numbers appropriate to the shock tube problem is discussed in a recent Lehigh University report by Chabai.[62] This report gives an excellent set of references to theoretical and experimental studies of shock tube boundary layers. The Reynolds number which seems most appropriate for the primary flow is given by the main stream values of viscosity, density, and laboratory flow speed, and the length ℓ over which the gas moves after being set in motion by the shock, i.e.,

$$\mathcal{R}_e = \frac{\rho_1 u_1 \ell}{\eta} . \qquad \text{(III.1)}$$

If observations of the flow are made at a fixed station (e.g., the vertical slit in the case of y-t photography), this Reynolds number is zero at the moment of shock passage and increases with time as gas originating from further and further upstream comes into view. This is expressed by setting ℓ equal to

$$\Delta t \cdot U \left(\frac{\rho_1}{\rho_0} - 1 \right) ,$$

where Δt is the time interval elapsed since shock passage, and the multiplier is the kinematic factor expressing the conservation of mass. This substitution and the simple shock relations of the previous chapter enable

the Reynolds number to be written

$$\mathcal{R}_e = \frac{(\mu-1)\rho_0 \Delta t}{\eta_1} \left[\frac{(\mu y_{10}+1)(y_{10}-1)^2}{(\mu + y_{10})^2} \right] . \qquad \text{(III.2)}$$

From the classical theory of the incompressible boundary layer on a flat plate, one may derive the approximate boundary layer thickness $\delta = L/\sqrt{Re}$. With the previous relations, this becomes

$$\delta = \sqrt{\frac{\eta_1 \Delta t}{\rho_0}} = \sqrt{\frac{\eta_1 \Delta t}{\rho_1}} \cdot \sqrt{\frac{\rho_1}{\rho_0}} , \qquad \text{(III.3)}$$

where the second radical varies only from 1 to 2 in the rare gases as y_{10} is varied from 1 to large values. As shown by Duff,[63] the size of the compressible laminary boundary layer is not qualitatively different. Essentially his result is that $(\rho/\rho_0)^{\frac{1}{2}}$ above should be replaced by a constant of the order of 2.5, over a wide range of shock strength.

We found that the thickness of the non-luminous layer in the primary flow agreed with these predictions. The measured size for Δt = 50 μsec was

$1 \pm 1/2$ mm for $p_0 \sim$ 15 mm Hg of neon, and

$2 \pm 1/2$ mm for $p_0 \sim$ 4 mm Hg of neon.

The corresponding values predicted from Equation III.3 above were 0.8 and 1.6 mm, respectively.

The Reynolds number describing the laminar-turbulent transition was estimated by measuring the onset time for ragged C_2 luminosity in experiments with $p_0 \sim$ 15 mm Hg. Our derived value of 3.0 ($\pm$ 1.0) x 10^5 is certainly of the right order. According to Chabai's heat gauge measurements

behind weaker shocks in air ($y_{1_0} \sim 2$ to 10), the critical Reynolds number is 7.5 ($\pm$ 2.5) x 10^5.

The absence of turbulence-luminosity in lower pressure experiments ($p_0 \sim 4$ mm Hg) was due partly to the correspondingly lower Reynolds number given in Equation III.2. Maintenance of the transition condition in experiments of successively lower pressure (but of the same shock strength) would have required a compensating increase in Δt and hence in the length of the shock tube. Moreover, it is now well known that, in low pressure shock tube flows, gas which is set in motion from positions far upstream does not reach the observing station as part of the primary hot flow. Equivalently one may say that the effective length of a shock tube decreases strongly with decreasing p_0, this effective length being measured either by the length to which the primary flow column grows or the duration of the primary flow at a downstream station. This marked deviation from ideal shock tube theory is among those discussed in Section 6.

In the next section, we will also discuss the theory by Mark[64] for the interaction between the reflected shock wave and the boundary layer of the primary flow. Following the publication of Mark's thesis, Charatis and the writer attempted to see the details of such an interaction by the C_2 emission method. A resulting vertical slit picture is shown in Figure 9. In order to make the laminar boundary layer thick enough that the interaction zone could be photographed, we had to use a fairly low initial pressure (~4 mm Hg neon). The primary shock speed was ~3 x 10^5 cm/sec. In Chapter IV, we will demonstrate that, for most of

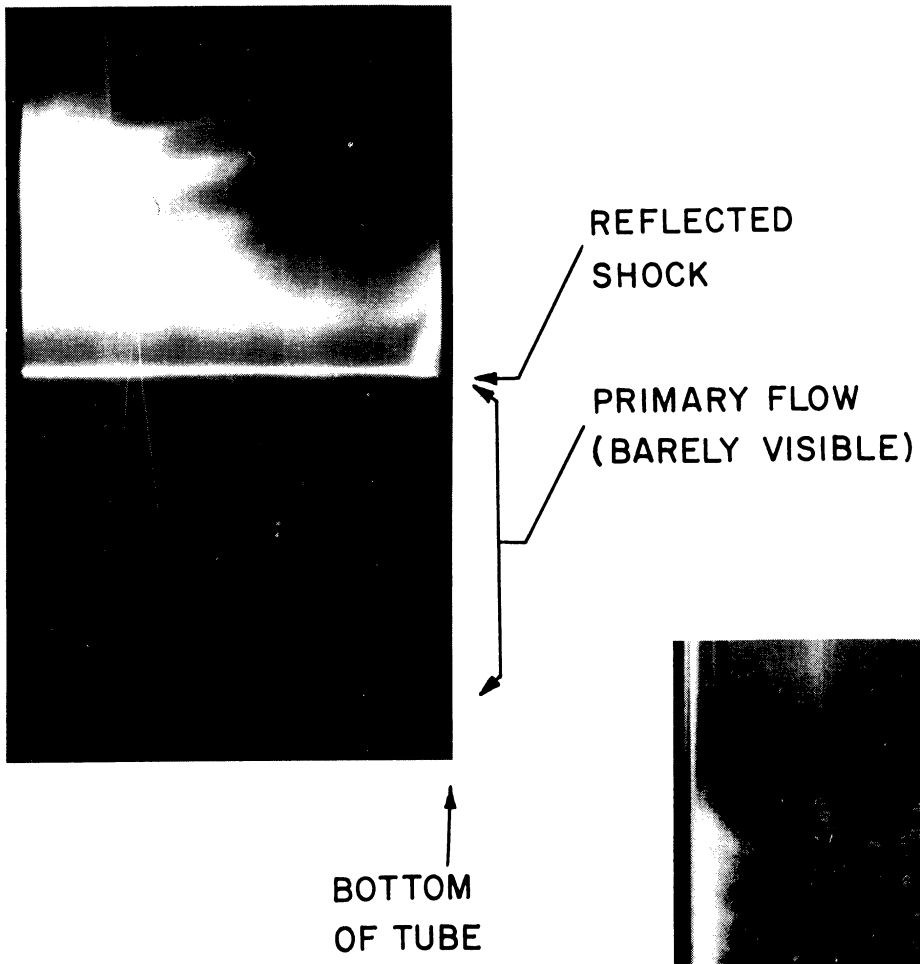

Figure 9. y-t picture showing effect of laminar boundary layer on reflected shock. Only half of the flow is visible.

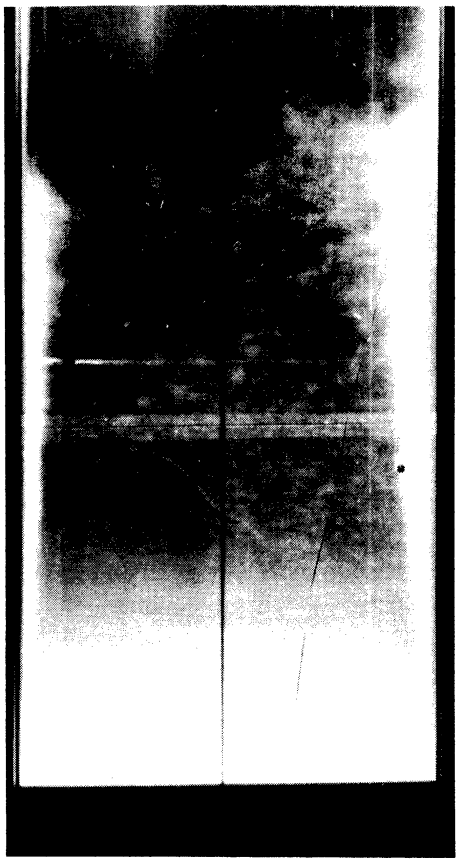

Figure 10. y-t picture of primary flow boundary layer. Camera views entire flow channel (asymmetrically).

our experiments, C_2 emission by the reflected shock arises from CH_4 in the boundary layer. Here, the reflected shock shows a slight wavy distortion and does not quite reach the floor of the tube. Figure 9 indicates that the boundary layer fluid flows under the "foot" of the reflected shock and expands somewhat before its CH_4 is dissociated by the hot gas behind the shock. The expansion is consistent with Mark's prediction that the stagnation pressure of the boundary layer gas would be greater than the pressure behind the reflected shock. The arrival soon afterward of the hydrogen interface is due to the placement of the vertical slit at a considerable distance from the end wall of the tube.

Figure 10 shows a very striking C_2 picture of turbulent boundary layers. For this film, the drum camera was moved farther away from the test section so that both the top and bottom walls of the tube were seen, although not symmetrically. The test gas was argon ($p_o \sim 15$ mm Hg) with CH_4 contaminant (~80 microns) and was driven by hydrogen (580 psi). The shock strength was $y_{10} \sim 74$ and the primary flow temperature was $T_1 \sim 5800°K$. A time-resolved spectrum of the boundary layer showed the same history of C_2 emission as in the lower temperature neon experiment of Figure 8. For this high temperature argon case, we also observed the sodium D lines (5890, 5896 Å) and the H and K lines of singly-ionized calcium (3968, 3934 Å). These faint lines appeared earlier than the strong C_2 turbulence emission but were confined to the wall layer, being recorded only when the spectrograph was "looking edge on" to the entire layer. Thus it appears that this wall layer was responsible for these lines as observed near very strong shock fronts by

Rosa and Turner. The impurity lines were not seen by us in either neon or argon experiments when the primary flow temperature was less than 5000°K. At lower temperatures, we assume that our luminosity phenomena are not influenced by these impurities. For higher temperatures, they may prove to be valuable adjuncts to the flow visualization by organic additives.

C. The ease with which shock waves and boundary layers are seen by their luminosity contrasts with surrounding gases suggests that the molecular (and atomic*) emission method may find useful application in studies of a more aerodynamic nature. In this connection, C_2 emission by reflected shock waves will be further investigated at this laboratory for the purpose of visualizing stationary shock waves in the vicinity of models.

Also we believe that the general method should be investigated for measuring the viscosity coefficients of high temperature gases by observing (1) the rate of laminary boundary layer growth behind the primary shock and (2) the extent of the reflected shock-primary boundary layer interaction. Even a factor-of-two estimate of the transport properties of partially ionized gases (e.g., hydrogen and helium) would be of considerable interest in present studies of low pressure, electrically-driven shock tubes.

---

*Evidences of boundary layer growth also appeared in the vertical slit pictures taken by Turner[12] in his studies of ionization-relaxation behind strong primary shocks in xenon. The intense main-stream luminosity (continuum and neutral xenon lines) was separated from the top and bottom walls of the tube by fuzzy dark zones which became 2 to 5 mm thick near the driving interface.

6. NON-IDEAL HYDRODYNAMIC EFFECTS IN SHOCK TUBES

One of the principal values of flow luminosity is to make readily visible the shortcomings of the simple theory of shock tube flow. The failure of the Taub equation to predict the primary shock speed is immediately evident, and so also are the failures of what we will call the "ideal" theory of the flow. This theory assumes that the flow field behind the shock is uniform; the principal datum for its application is the observed shock speed, rather than the initial pressures in the tube. Deviations from this ideal theory often take the form of excesses or defects which put the observables well outside the bounds of even the asymptotic, or strong-shock, relations. For the experiments discussed in this chapter, the effects of ionization and dissociation are not so great as to liberalize significantly either these bounds or the exact equations. The inadequacy of the ideal theory is further highlighted by observations of flow velocities which are greater even than the Taub equation would allow, while the shock speed is usually less in the same sense. This section describes such effects as they have been observed by us and many other workers. We also discuss here some theoretical treatments of real shock tube flows. The failure of the simpler theory can usually be traced to the viscosity of the gases and the concomitant three-dimensionality and time-dependence of the flow fields.

A. To illustrate the kind and amount of information which may be derived from a luminous flow picture, we will first discuss the measurements made on the original x-t film of Figure 7. The conditions for this

experiment were previously listed in Table V. All velocities here are given either as fractions of the primary shock speed U or in units of mm/μsec = 10^5 cm/sec. The effects of ionization and dissociation are subsumed under the name of "real gas" effects.

(1) The measured shock speed (3.07) is much less than the value 3.41 predicted from the initial pressures p_4 and p_0 via the Taub equation.

(2) The distance from the interface-reflected shock interaction to the end wall is only 13 or 14 cm. This is about 1/2 of the minimum value (26.5 cm) which one would expect from the expansion chamber length (265 cm) and the strong shock limit (10) on the density ratio $x_{20} = \rho_2/\rho_0$.

(3) The flow speed associated with the streaks near the interface is about 2.70 = .879 U. This value exceeds all the velocities which the simple theory might predict. In order of decreasing magnitude these predicted values are the Taub velocity 2.51, the asymptotic velocity, .750 U, and the computed velocities .743 U (real gas) and .734 U (permanent gas).

(4) The reflected shock speed is V = 1.43 = .466 U. This value is less than all the speeds predictable from the ideal theory and the primary shock speed. The asymptotic speed is .500 U and the computed speeds are .502 U (real gas) and .511 U (permanent gas).

At lower initial pressures the deviations from theory were even more

pronounced. For p_o = 1.82 mm Hg of neon, we observed a shock speed U = 2.66 while the Taub prediction was 3.53. The maximum length of the gas column behind the reflected shock was about 6 or 7 cm or roughly 1/4 of the theoretical value. The short primary flow was entirely luminous, and the speed of its back edge was equal to the shock speed and slightly greater than the flow speed predicted by the Taub equation. The reflected shock speed was .475 U and about 9% less than expected.

B. The failure of the Taub equation is well known and is due to a combination of imperfect diaphragm opening and viscous losses at the walls of the shock tube. For summaries of the many studies of the problem to 1958, the reader is referred to Sections 3 and 4 of the shock tube compendium by Glass and Hall[14] (University of Toronto) and to the article on wall effects by Emrich and Wheeler[65] (Lehigh University). The relevant data for the strong-shock tube at Michigan are the most extensive for the case of hydrogen-driven neon at initial pressures $p_o \sim 7.5$ mm Hg ($\sim 10^4$ dynes/cm^2). The driving pressure p_4 has been varied from 100 to 1000 psi, the highest values arising in Turner's work, and the lowest in the recent work on chromium spectra (see Figure 26, Section 5, Chapter VI). The data are satisfactorily represented by setting y_{10} at 25($\pm$5)% below the values predicted by the Taub equation. Since this equation may, then, not be relied upon, the point of view taken in most applications of the shock tube is that the separate measurement of shock speed is necessary for defining every experiment. That this is also sufficient is an assumption which, in view of the other non-ideal effects, must have its limitations.

C. Already in 1953, the outlines of this reservation had been sketched by Glass, Martin, and Patterson at Toronto.[66] They made x-t schlieren records of the entire primary flow history, and found that the shock speed had a maximum, and the interface speed a minimum, at a certain "formation distance" x_f from the diaphragm. These extrema were, respectively, less and greater than the Taub predictions. The shock acceleration for $x > x_f$ was attributed to the catch-up of compression waves from the gradually opening diaphragm. Viscosity and heat conduction were held responsible for the subsequent shock attenuation ($x < x_f$) and for the defect ("formation decrement") in shock strength at $x = x_f$. That the interface accelerates beyond this point (while the shock is attenuated) clearly implies that the flow field near the interface cannot correctly be described by simply wedding the observed downstream shock speed with the uniform flow theory. Various experiments have demonstrated the time-dependent character of this flow field; early examples are the measurements by Curtis, Emrich, and Mack[67] of increased density near the interface and the measurements by Hollyer[44] of increased flow Mach number and decreased length of the primary flow column.

We will not cite here all of the more recent literature which describes, in one context or another, the failure of the primary flow to achieve its ideal length. For most of this information, we must refer the reader to the bibliographies of our previous and immediately following references. The defect in the flow length is variously represented as an acceleration of the interface behind an attenuating shock, a short duration of the primary flow past a downstream station, or a decreased

"age" of the flow near the interface.* The phenomenon is due to the loss of material from the primary flow through boundary layers on the walls. The engulfing of these layers by the driver gas consumes much of the gas that ideal theory would predict to reside in the primary hot flow. Even a thin boundary layer may cause considerable mass transport and thereby strongly perturb the main primary flow. Further disturbances arise from interactions with the viscous flow field of the driver gas. The primary flow column is prevented from growing to its ideal size and is made non-uniform along its length and over any cross-section. These phenomena also dictate the attenuation of the primary shock which forms the flow field. The two effects are not separable. We will describe here the attenuation theory by Mirels and Braun[68] which seems to classify the observed flow-shortening effects. We consider a few experimental observations, particularly some which indicate the existence of a quasi-steady viscous flow behind shock waves in low pressure gases. Also discussed is the model advanced by Duff[69] to explain this state of flow.

D. The report by Mirels and Braun (NACA, Cleveland) is a good example of the existing theories of shock tube flows with boundary layers. Shock attenuation and the primary flow variables are computed by a perturbation method for Mach 1.25 to 6 shocks in air (constant $\mu = 6$) driven by

---

*In our early studies of the effect, it was named the "anomalous compression" by virtue of the high flow density apparently implied. Though certainly an anomaly in terms of the ideal theory, the effect is more nearly the rule rather than the exception in actual shock tube flows. Neither does this "customary anomaly" truly represent a compression of all the test gas into the primary flow column.

high pressure air. Since most of the experiments discussed below were made with neon and argon, it is perhaps an oversimplification to present them in the context of this theory. However, the comparison is justified by the similarities of the thermodynamic functions and the transport coefficients,* and the theory of the boundary layer itself is apparently insensitive to the small differences which do exist.** Moreover, the specificity of the results for air is further reduced by their presentation in a normalized form; i.e., the deviations of the primary flow field from the predictions of the Taub equation are given as functions of the computed attenuative effects on the primary shock.

According to Mirels and Braun, the non-ideal effects of the completely laminar layer are less than those of the completely turbulent layer, but the variation with shock strength is roughly the same in both cases. We will discuss (for the turbulent case) the predicted time-variations of pressure and flow speed as the attenuated shock wave, the primary flow and, finally, the interface move past a fixed observing station.

(1) Behind the weak shocks, the pressure rises in time almost to the value predicted by the Taub equation, while the flow speed increases to values considerably above the Taub prediction.

---

*See the recent computations by Amdur and Mason,[70] particularly for the viscosity and thermal conductivity of neon, argon, and nitrogen (N_2) at temperatures of 1000 to 15,000°K.

**Duff has initiated a program of boundary layer computations for argon.[63] His preliminary results are in good agreement with earlier approximate calculations for air.

(2) For successively stronger shocks, the time increase of the pressure becomes less and less rapid and, for $M_o \geq 4.5$ reverses to a decrease before the arrival of the interface. For the wholly turbulent boundary layer and $M_o \geq 5$, the decrease is so strong as to overcome the mild rise occurring earlier in time, and the pressure at the interface falls below the pressure at the shock. The pressure rise is the least for the highest shock Mach number ($M_o = 6$), and the decrease is the most definite and occurs earliest. The flow speed increases monotonically with time as before, except that for M_o as high as 5 or 6, the highest speed (i.e., the speed at the interface) is roughly equal to the Taub prediction.

With regard to pressure, the usual experimental finding is the monotonic increase of case (1) above. In Section 8 of this chapter, we report what appear to be the first observations of the extreme type of pressure decrease predicted for case (2).

By means of the luminosity induced with additives, we have observed the time-increase of flow velocity behind the primary shock. This work is reported in Section 7 of this chapter.

In either of the Mirels-Braun cases, the motion of the interface relative to the (attenuated) shock amounts to a "shortening" of the flow column with respect to its ideally predicted length. The Toronto measurements demonstrated the absolute interface acceleration of case (1). Toennies and Greene[71] (Brown University) observed shock attenuation, flow-

shortening, and the case (2) equality between actual interface speeds and those predicted from the Taub equation. These experiments were done with M_o = 7 shocks in 10 mm Hg of argon; at least some portion of the boundary layer must have been turbulent. Toennies discusses the flow-shortening in considerable detail in his dissertation.

The pertinent data for our neon experiments was given at the beginning of this section. The interface speeds slightly exceed the Taub predictions, the moreso for the higher Mach number experiment at higher initial pressure. Recall (Section 5) that this flow possessed a mixed boundary layer , 1/3 laminar and 2/3 turbulent. In the quoted experiment at lower initial pressure, the boundary layer was thick and entirely laminar, and the result seemed to be a purer example of the case (2) equality between actual interface speed and the Taub prediction. To our surprise, the low pressure experiments showed a further equality between the speeds of the interface and the primary shock. This condition obtained for all initial pressures below 3 mm Hg. In this range of p_o, the maximum length of the gas column behind the reflected shock was roughly proportional to p_o, decreasing to 1/10 and 1/35 the ideal length for p_o = 0.50 and 0.17 mm Hg, respectively. The primary shock seemed to have decelerated to the point where a constant amount of gas was maintained between it and the interface, the spacing between the two depending solely on the initial pressure. Doherty suggested that this configuration might represent some sort of a terminal state into which the flow naturally developed after having been subjected to sufficient attenuation.

E. In 1958, Duff (Los Alamos) independently made an extensive study[69] of the extreme "shortening" effect with M_o = 1.2 to 7 shocks in argon at initial pressures of 0.25 to 5.0 mm Hg. This study was made with an electron-beam densitometer whose distance (d) from the diaphragm of the tube could be varied from about 0.5 to 7.5 meters. With a driver pressures of 2 psi (absolute) of argon and p_o = 0.5 mm Hg, it was found that the primary shock had a fairly constant speed (M_o = 1.6) from d ~ 2.5 to 5.5 meters. Over this distance the duration of the primary flow remained constant at about 230 μsec compared to the 5750 to 12650 μsec predicted by ideal theory. The obvious corollaries are the equality between shock and interface speeds, the constant length of the flow column, and the "shortness" of the column compared to the ideal length. For M_o = 1.6, the flow duration varied linearly with p_o for p_o up to 5 mm Hg. This dependence is identical with that we observed for the flow length in neon at high Mach numbers.

Duff's view of the primary flow in this regime is that the mass continually being added through the moving shock is lost at the same rate by compression into the laminar boundary layer and is ultimately consumed by the driver gas. Duff has shown that this model is consistent with several observations. The assumption of an adiabatic acceleration from shock to interface gives satisfactory limits on the failure of the Taub equation. The increase of mean density with distance behind the shock agrees with laminar boundary layer theory. The mass transport of which the computed boundary layers are capable is indeed adequate for consuming the mass flux through the shock.

It is clear that such effects may preclude some spectroscopic and aerodynamic applications of shock tube flows at very low pressure. In this connection, we paraphrase here the conclusions of Duff's article.

> "... shock-tube performance at low initial pressures is more nearly approximated by a complicated pipe flow than by one-dimensional shock tube theory. ... Probably the most important (implication) is that the testing time for a given tube diameter is a function of initial pressure and not of expansion chamber length. Large tube diameters must be used if long testing times are needed. Also, if a knowledge of the state and history of the hot flow is important for a given experiment, the actual flow must be examined critically; in particular, the age of hot flow in the vicinity of the contact surface is not as prediced by shock-wave theory."

We considered the possibility that the flow-shortening was somehow due to the shock formation process. White[72] at General Electric recently studied the influence of diaphragm opening time on shock formation and found strong shocks which were still accelerating some 20 to 40 feet from diaphragm. The opening time for White's thin steel diaphragms was about 600 microseconds, a time comparable to the typical transit time of the primary shock over the length of the Michigan shock tube. No direct measurement has yet been made of the opening time for the diaphragms in the Michigan tube; however, several pieces of indirect evidence indicate that the formation process is <u>not</u> the cause of the observed non-ideal effects. In view of this

negative conclusion, we have relegated the discussion of the evidence to an extended footnote.*

---

*(1) The variation of flow length with the initial pressures p_0 and p_4 does not fit any hypothesis which one might make about variations in diaphragm opening time. The picture is complicated somewhat by the impossibility of varying these pressures and the initial pressure ratio (z) independently. For a fixed p_0 (2 to 20 mm Hg of neon) the flow length was independent of z, though z was varied by an order of magnitude for each p_0. This independence thus extends to p_4 and hence to diaphragm thickness, since p_4 was usually determined by the self-bursting pressure of the plastic diaphragms. As previously shown, the flow length was strongly dependent on p_0. Interpreting the data in terms of a fixed p_4 (fixed diaphragm thickness) one would have reluctantly to conclude that the diaphragm opening time depended on the very small p_0 and, indeed, in an inverse fashion.

(2) The mean speed of the primary shock over the entire length of the tube was derivable from the electronic pressure measurements described in Section 8. The time interval between diaphragm breakage and arrival of the shock at a transducer in the test section was measured with electrical signals generated by both events. In most cases, the mean shock speed was about 10% higher than the test section shock speed computed from the x-t film, indicating that the "formation distance" lay upstream of the test section. In one experiment (with an under-loaded diaphragm) the mean speed of the shock was 10% less than its speed in the test section, implying that the primary flow field had never become free of formation signals. This was verified by the x-t picture of this shot which showed irregular luminosity in the rear two-thirds of the primary flow and considerable distortion of the reflected shock during its interaction with the perturbed flow. Nonetheless, the flow length in this unusual experiment was the same as the flow length in all the usual experiments of the same p_0.

(3) Preliminary experiments with scored aluminum diaphragms demonstrate the same flow lengths as in the plastic diaphragm experiments for $p_0 \sim 10$ mm Hg of neon, whereas one expects differences in the rupture processes of the two types. White has succeeded in extending the diaphragm opening time by loading the petals with small weights. It is intended that this and similar methods of control be applied in the Michigan tube with the hope of ascertaining the possible influences of the formation process. To this end, a test section is being designed which will enable photography of the flow adjacent to the diaphragm. Various systems are being considered for measuring the times of arrival of the primary shock at several stations along the tube.

F. The failure of the uniform flow theory far from the shock leads one to the more restricted viewpoint that the observed primary shock speed predicts the flow variables only in a region which is, in some sense, near the shock. Thus one expects that near the end wall of a shock tube the speed of the reflected shock should be correctly predicted from the primary shock speed. That even this is not strictly true was realized in 1957 by Mark[64] at Cornell, Strehlow and Cohen[73] at the Ballistics Research Laboratories, and Doherty[35,43] at Michigan. The extensive analysis and experiments by Mark showed that the hot gas (2) behind the reflected shock can be strongly affected by its contact with the cold dense gas is the laminar boundary layer of the primary flow. Sound waves move into the gas (2) from all sides; the reflected shock is distorted and the main stream gas which it "processes" is not generally brought to rest. Strehlow and Cohen found a significant decrement in reflected shock speed even in the case of argon where the boundary layer is thin compared to those in polyatomic gases. They pointed out that this effect was a source of possible error in earlier attempts by Toennies and Greene[71] to measure the dissociation energies of N_2 and CO by means of the ratio (U_{2_0}) between reflected and primary shock speeds. At this time Doherty had found a 5% to 10% reflected shock speed decrement in neon; he has since developed a method whereby this decrement can be used to evaluate empirical corrections of the zeroth order (ideal) state which the primary shock speed predicts to exist behind the reflected shock.

The direct measurements described in the following two sections were performed to determine the cumulative effects on pressure and temperature

of all the non-ideal processes described above. The measurements also provided further evidence (if more were needed) of some of the effects we have discussed. The number of useful experiments was limited by several developmental difficulties. We therefore concentrated our effort on the hydrodynamic situations appropriate to the spectroscopic measurements of Chapter VI. The range of initial pressures included the lowest p_0 of interest, so as to reveal the worst possible effects of viscosity. For sufficiently high initial pressure, the conclusions are very favorable to the spectroscopic use of the gas behind the reflected shock. The deviations from ideal theory are certainly less than 10% for the pressure p_2 and less than 2% for the kinetic temperature T_2, for initial neon pressures as low as 7.5 mm Hg and temperatures T_2 up to 10,000°K. We surmise that even better agreement may be found in shock tubes for which a higher initial pressure and a lower surface-to-volume ratio are available.

7. FLOW VELOCITY MEASUREMENTS

The ability of organic additives to "light up" various regions of the shock tube flow suggested the possibility of measuring flow speed with spatially restricted luminosity. When the primary flow column was luminous throughout, only the shock speed and the interface speed could be measured from x-t photographs. In this section we describe three luminosity methods of measuring the flow speed between the shock and the interface. Each method demonstrates an excess of primary flow speed over the predictions of ideal theory. The first two techniques are only briefly reported here

because of the limited information which they provided about the thermodynamic state behind the reflected shock. Though the third technique has not yet been fully developed, we report here the details of our results so far. For a few experiments, this method has allowed us to measure the absolute temperature on both sides of the reflected shock and the pressure and density ratios across this shock. These quantities are in reasonably good agreement with the predictions of ideal theory, and particularly so if one takes literally the indications of residual gas motion immediately behind the reflected shock. The ideal assumption of zero velocity is not in accord with either our present understanding of the non-ideal primary flow or the pressure measurements discussed in Section 8. We believe that slight improvements in this method will enable its application in various hydrodynamic experiments at high temperature.

A. The first technique grew directly out of the work with organic additives discussed in Section 5. The slopes of the x-t streaks in the primary flow were measured. These streaks had been shown to arise from patches of C_2 turbulence-luminosity, and it was assumed that these glowing samples of gas were blown along with the flow speed. In all cases, the streak velocities were significantly in excess of the flow speed computed from U. Again using the experimental conditions of Figures 7 and 8 as an example, the excess was usually 10% for the streak nearest the shock and then rose to 20% or 25% near the interface. It was felt that if the streaks did not give the actual speed they at least provided a lower bound. Therefore, the gas velocity in the primary flow was most everywhere in excess of the value

computed from the shock speed, the excess probably being zero very near the shock* but certainly becoming large near the interface.

Doherty's analysis[35] of the organic flow streak data ascribes a mean speed excess of 5% to the gas in the first 5 cm behind the primary shock. Following a method of Hollyer,[44] Doherty has allowed for the high velocity by adding momentum and energy "sinks" to the conservation equations. The resulting perturbation theory contains adjustable parameters which are determined by physical arguments and an evaluation of reflected shock speed data. There also results a set of perturbations on the state variables behind the reflected shock. Doherty's predictions are in accord with the direct measurements described in this section and in Section 8. He predicts a residual gas velocity behind the reflected shock and demonstrates this motion by means of isophotometer tracings of x-t pictures taken in the light of the Balmer line H_β. Doherty also shows that his corrected state variables behind the reflected shock are consistent with the observed line-shape of H_β and the recent line-broadening theory of Griem, Kolb, and Shen.[45]

B. In the second method, atomic emission was used to create luminosity interfaces in the primary flow. The motion of these interfaces demonstrated that the flow was at least roughly brought to rest by the reflected shock. Further, the observed excess of the primary flow speed substantiated the flow-streak measurements made with organic additives. We separated the expansion chamber into two volumes with a thin foil or film,** the 1/4 volume near the end wall being filled with neon (plus methane) and the remaining

*Recent interferometric measurements by Alpher and White[74] on strong shocks in argon ($p_o \sim 3$ mm Hg) indicate that the density near the shock agrees with the ideal theory. One need only apply the principle of mass conservation to arrive at the same conclusion for the flow velocity.

**In most experiments, the separator was aluminum foil of .00075-inch thickness. Imperfect breaking of the foil caused strong perturbations of the late primary flow. We failed in the attempt to make impermeable films of lacquer and plastic which were properly weak but yet strong enough to withstand the rigors of evacuating and filling the shock tube. Our vacuum requirements prevented the use of a double-slide device which was made for inserting films into the prefilled tube.

3/4 volume with the same pressure of a xenon-helium mixture whose effective molecular weight was equal to that of neon. A few experiments were run at $y_{10} \sim 63$ to 74 ($M_o \sim 7.1$ to 7.7) with initial pressures of 5 to 10 mm Hg. The associated primary flow temperatures were 5000 to 5800°K, high enough to ensure C_2 emission at the shock front and xenon luminosity in the late primary flow. This latter luminosity was separated from the shock, but extended back to the interface and was considerably striated throughout. The x-t streaks nearest the primary shock had speeds in excess of the predicted values by 10% to 15%. These streaks intersected the reflected shock at about 3 or 4 cm from the end of the tube and were thereupon turned approximately parallel to the time axis on the film with a considerable increase in luminosity.

C. The final method employed a solid powered contaminant, $CsNO_3$. This material was easily vaporized and dissociated in the hot flow and thereby provided strong, localized caesium emission behind primary and reflected shock waves. Prior to an experiment, a very small amount of $CsNO_3$ dust was picked up on a fine silk thread, the ends of which were then tacked with vacuum wax to the top and bottom walls inside the shock tube. Thus the thread was mounted vertically in midstream at an x position which was either in, or upstream from, the test section. With the thread in the field of view of the x-t camera, we observed the onset of luminosity when the thread was overrun by the primary shock wave. As soon as the shock passed, a few faint x-t streaks came straight off the thread. These "flow markers" were followed by strongly luminous ones which emanated from the

(now moving) thread. Ultimately the thread was blown into the gas behind the reflected shock, all the caesium emission having preceded it.

In most of the experiments, the thread was mounted upstream from the test section, and CH_4 was added to the neon to make the shock waves visible. The viewing of flow lines by Cs emission and the shock waves by C_2 emission posed a serious observational problem. An experiment was considered a complete success if one could measure (in addition to the primary shock speed) the instantaneous speeds of the reflected shock and the incoming and outgoing flow lines at their common x-t intersection. The CH_4 content had to be just large enough to make the primary shock visible without making the reflected shock so intense that a flow line immediately behind it was obscured. The requisite amount of CH_4 varied with the shock strength. A complete measurement could be made only with the first one or two Cs-streaks to intersect the shock. However, the clarity of the few good films that were obtained warranted a thorough reduction of the data, and it is these results which we present here.

For improving the method, we suggest that the shock luminosity be eliminated and the shock speeds measured by probe or schlieren methods. Also it would be better to introduce the $CsNO_3$ as a gas, provided it remains confined to a small "bubble." This would allow greater control of the emission intensity and impurity level and would also minimize flow disturbances. A possible method is to replace the thread with a No. 40 copper wire with a few small beads of $CsNO_3$ melted onto it, and quickly heat the wire electrically to 600 or 700°C just before the shock tube is fired.

The caesium flow-markers in the main stream enabled us not only to compare the primary flow speed with its ideally predicted value but also to study the reflected shock transition independent of the primary shock which had created it. Flow velocities relative to the reflected shock were derived from measurements of the (laboratory) speeds of the reflected shock surface and the gas on both sides of it. The shock strength y_{21}, the density ratio x_{21}, and the absolute temperature T_1 and T_2 were computed via the relations (II.48) in Chapter II, without recourse to prior knowledge of the primary shock speed U. Thus the usual technique of measuring U and then predicting all other flow variables was subject to direct test.* Comparison of T_1 and T_2 as derived by these two independent methods shows remarkable agreement in spite of the 5% to 10% variance between predicted and observed speeds of primary flow and reflected shock.

An x-t picture of one of the caesium flow-streak experiments is shown in Figure 11. The initial pressure here was 15.74 mm Hg neon with organic impurity, and the primary shock speed was $2.98(3) \times 10^5$ cm/sec. The streaks of caesium emission in the primary flow are straight and have parallel edges, and thus meet the conditions required of a gaseous indicator of the flow speed. The earliest streaks strike the reflected shock at roughly that distance (2.5 to 3 cm) from the end wall which is expected from the location of the dusted thread and the strong

*The direct method is likewise independent of the previously mentioned perturbation theories of the flow, since one relies only on the validity of the conservation equations at the reflected shock surface.

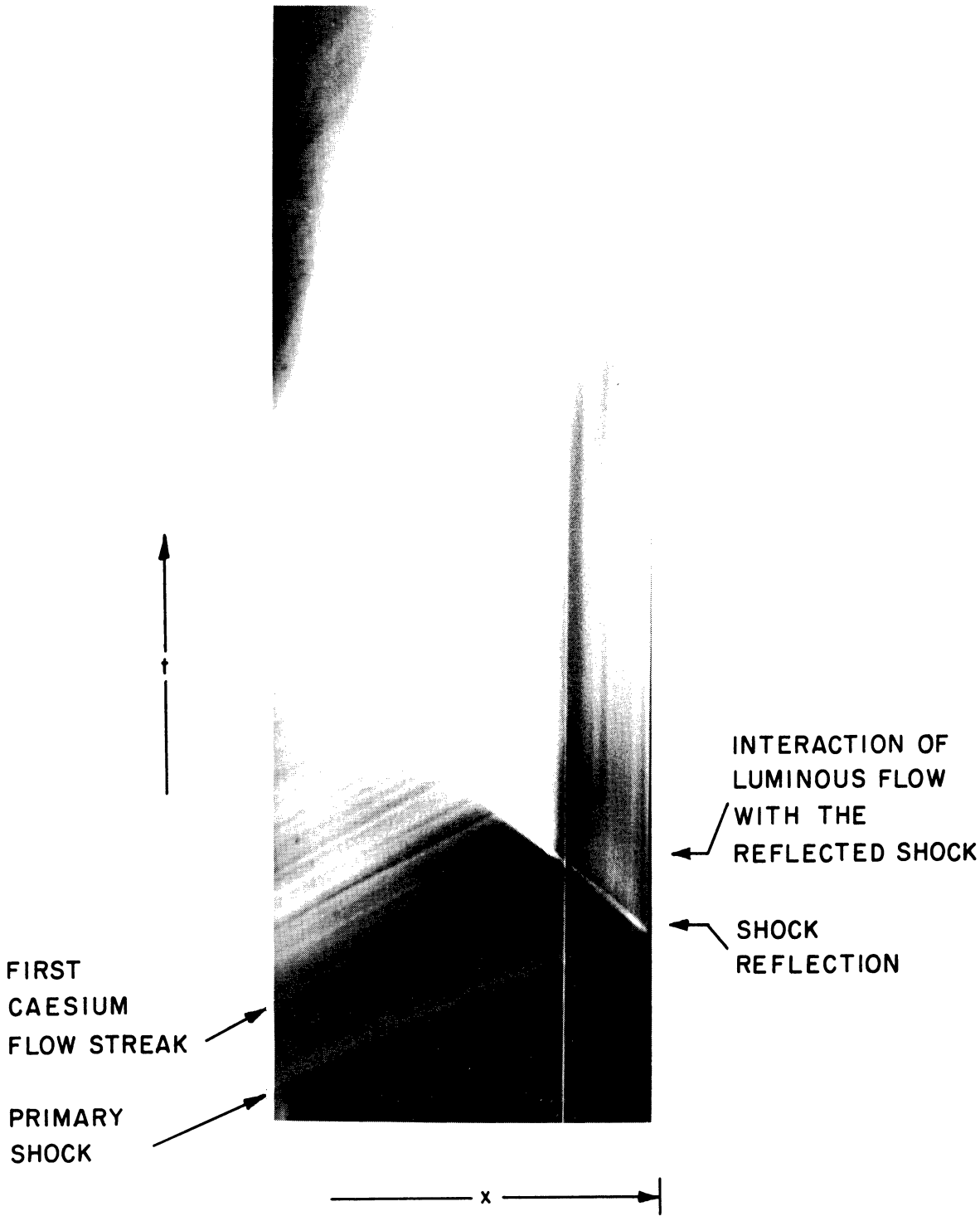

Figure 11. x-t picture for flow velocity measurement with caesium emission.

shock limit of 10 on the density ratio x_{20}. To zeroth order, the Cs luminosity is brought to rest at the reflected shock. However, a closer examination of the x-t films shows a residual motion of this glow toward the end wall with a velocity of about 3% or 4% of the reflected shock speed. The strong effect of this speed on the computations will be shown below. It is possible that the speed is only apparent and represents a finite deceleration-time for small ablating $CsNO_3$ particles. However, the calculations by Doherty have indicated the necessity of a residual gas speed of this order of magnitude, and Mark's work (discussed in Section 6) suggests that such motion is always to be expected.

The computed flow variables for the experiment of Figure 11 are given in Table VI as a representative example of the results of this work. All

TABLE VI

COMPUTATIONS FOR EXPERIMENT OF FIGURE 11

$U = 2.98(3) \times 10^5$ cm/sec
$u_1 = 2.27(3) \pm .045$
$V = 1.46(8) \pm .015$
$u_2 = 0.061(9) \pm .0036$

$p_o = 15.74$ mm Hg
$T_o = 297.1°K$
$u_{1o} = u_1/U$
$U_{2o} = V/U$

	A	B	C
y_{1o}	$54.33 \pm .77$	---	---
u_{1o}	$.7323 \pm .0003$	$.762 \pm .015$	$.762 \pm .015$
$T_1(°K)$	4309 ± 60	4320 ± 30	3869 ± 35
y_{21}	$5.571 \pm .008$	$5.65 \pm .18$	$6.34 \pm .22$
x_{21}	$2.433 \pm .002$	$2.46 \pm .03$	$2.55 \pm .03$
$T_2(°K)$	9868 ± 138	9978 ± 132	9616 ± 126
U_{2o}	$.5115 \pm .0002$	$.492 \pm .004$	$.492 \pm .004$

calculations were performed assuming $\mu = 4$. Column A lists the results which follow from the ideal shock wave theory and the observed U. Column B gives the results from u_1, V, and u_2 as observed, and column C differs from B only insofar as u_2 is assumed to be zero. An error of 1% was assumed for U, and the other observables were

$$u_1 = 2.27(3) \pm .045,\ V = 1.46(8) \pm .015,\ \text{and}\ u_2 = .061(9) \pm .0036\ ,$$

in units of mm/μsec or 10^5 cm/sec. For the sake of again emphasizing the variances with asymptotic ideal theory, some of the results are given in ratio form. $u_{10} = u_1/U$ and $U_{20} = V/U$.

In addition to this particular experiment, three partially successful shots were made in the $T_2 \sim 10{,}000°K$ range, one at the same pressure, the others at half the pressure. For these, the view of Cs emission immediately behind the reflected shock was obscured by other strong luminosity, and it was therefore possible only to assume $u_2 = 0$. The numbers thus computed stood in relation to the predictions from U very much as in the above table, save for the relative sizes of $T_2)_A$* and $T_2)_C$. The observed primary flow velocity ratio $u_{10})_{B,C}$ was between 4% and 7% greater than the ideal ratio $u\ )_A$ for that segment of the flow which was ultimately brought to "rest" within 3 cm from the end wall.

For the experiments above, the assumption $u_2 = 0$ implies that

(1) $T_1)_C$ is 7% to 10% <u>less</u> than $T_1)_A$, and

(2) $y_{21})_C$ is 11% to 14% <u>greater</u> than $y_{21})_A$.

---

*This notation will be used in the remainder of this section only. By $T_2)_A$ is meant "T_2 as computed by the method appropriate to column A."

These implications are not consistent with the currently accepted picture of low pressure shock tube flows, and we therefore conclude that $u_2 \neq 0$. As Duff and Mirels-Braun have pointed out, T_1 should increase as the gas near the shock is gradually compressed and accelerated. Thus T_1 as measured here should be slightly greater than the value computed from the primary shock speed. The implied high values of y_{21} are not borne out by the pressure measurements discussed in the next section. As an example, consider one of these latter experiments which is comparable to that of Table VI; $p_0 = 15.51$ mm Hg of neon and the ideally predicted pressure ratio is $y_{21} = 5.58$. The observed pressure ratio was 5.42 ± 0.43, far less than the value 6.34 required by setting $u_2 = 0$ in Table VI. At all events, the temperature T_2 apears to be quite close to that predicted from the primary shock speed. The difference is only about 2% assuming $u_2 = 0$ in each of the three experiments, and is about 1% using the observed u_2 in the one experiment for which it seemed to be measurable.

The same trend was observed in three successful experiments with initial pressure $p_0 \sim 31$ mm Hg of neon and $y_{10} \sim 45$ ($T_2 \sim 8500°K$). The excess of the actual u_{10} over the ideal value was between 4% and 6%. The observed u_2 implied temperature T_1 and T_2 which were within 2% of the ideal values and pressure ratios y_{21} which were consistent with separate pressure measurements. Unrealistically high values of y_{21} resulted from assuming $u_2 = 0$.

The following statements may then be made for experiments under our conditions:

(1) In spite of all the non-ideal effects, the gas behind the reflected shock (near the end wall) has a kinetic temperature very close to the ideally-predicted value. Spectroscopic experiments with this gas sample are therefore justified insofar as the ideal temperature may be used in the data reduction.

(2) The ideal assumption of zero flow speed behind the reflected shock is inconsistent with our measurements, the experiments of other workers, and the present understanding of viscosity effects on shock tube flows.

(3) The primary flow column is quite non-uniform with respect to flow velocity, and this nonuniformity probably extends to other flow variables such as pressure and temperature. The importance of these effects should be evaluated for (a) spectroscopic experiments which use the emission (or absorption) by the entire primary flow, (b) aerodynamic experiments involving the passage of the primary flow over a model, and (3) chemical kinetic experiments performed at low initial pressure in order that the reaction zones become stretched out over the whole flow column.

By means of the simplifications discussed earlier, the caesium emission method may be extended to cover wider ranges of both the hydrodynamic conditions and positions in the shock tube. Measurements can be made both of the primary flow velocity as a function of distance behind the shock and of the residual velocity of the "rest gas" as a function of distance from the end wall of the tube. In conjunction with pressure measurements, such a program could lead to an empirical picture of the actual flow throughout the strong-shock tube, and comparison with existing theories

would then be possible. Of particular interest to us are the consequences for the entire temperature field behind the reflected shock. In many experiments, the ionization delay time and steady luminosity behind this wave are fairly constant as the wave recedes from the end wall. This may indicate that the state variables for the "rest gas" are much less dependent on x than one would expect from the non-uniformity of the incoming primary flow.

8. PRESSURE MEASUREMENTS

We have measured the absolute gas pressure behind strong shock waves by means of a piezoelectric transducer. Our experiments cover a pressure range of 0.5 to 10 atmospheres, and the measurement accuracy is between 3% and 8% with the system in its present form. To this level of accuracy, the pressure in the primary flow near the shock is in all cases consistent with separate measurements of the shock speed and ideal shock tube theory. The pressure near the interface is significantly less than the ideal prediction. Behind the reflected shock, both agreement and slight disagreement are observed. The principal experimental difficulty has been the mechanical response of the gauge to the sudden pressure jump across a shock wave. The accuracy of the present system is allowed only by a detailed analysis of the ensuing signal. The gauge mounting is now being improved so that more and better observations can be made of the phenomena we have briefly studied.

The pressure measurement system consisted of a piezoelectric SLM quartz

transducer (type PZ6-S), a Kistler amplifier-calibrator (type PT6), and a 150-A Hewlett-Packard oscilloscope. The transducer was plugged into a Plexiglas test section window at x-locations of either 17.7 cm or 2.3 cm from the end wall, the choice depending on whether the primary flow or the gas behind the reflected shock was the principal object of interest. A larger fitting held the transducer so that its active face was flush with the inside wall of the flow channel. A pressure force against this face is transmitted to the internal pre-stressed quartz crystals and induces a voltage across the electrodes attached to the crystals. A coaxial cable connects the electrodes to the amplifier which is used primarily to match the high internal impedance of the transducer to that of the oscilloscope input. The overall sensitivity of this system is about 8 millivolts per psi. The high impedance of quartz enables the system to be calibrated with static pressures.

The measurement of pressure was coordinated with the hydrodynamic events in the shock tube by means of an aluminum-coated mylar fuse taped to the diaphragm inside the tube. Prior to the diaphragm breakage, the fuse was an integral part of a circuit which held the grid of a 2D21 thyratron below cutoff potential. The grid voltage rose rapidly above cutoff when the fuse was broken by the rupture of the diaphragm, and the resultant cathode-to-ground potential was a 250 volt pulse of about 1/10 microsecond rise time. This pulse was fed into a variable-delay phantastron circuit which later triggered a single oscilloscope sweep slightly in advance of the arrival of the primary shock at the transducer. A 1.6-mega-

cycle Potter chronograph monitored the delay time induced by the phantastron, and a Dumont camera recorded the oscilloscope trace.

After each experiment, the pressure trace was absolutely calibrated against the known pressure of the atmosphere. When the tube had been pumped out preparatory to cleaning, the storage capacitor in the amplifier was grounded out and a "vacuum trace" was photographed. One, two, and four minutes later, "atmospheric traces" were obtained with the tube at atmospheric pressure. These traces were required by the slow drift in signal level due to gradual accumulation of charge in the transducer-amplifier system. The drift effect was calibrated out by extrapolation of the atmospheric traces back to the time at which the vacuum trace had been recorded. We prevented the charge accumulation from affecting the position of the experimental pressure trace by grounding out the amplifier just before the experiment was run. All the pressure trace data were reduced by measuring the oscilloscope pictures with a traveling microscope.

The transducer mounting proved to be very important in determining the character of the output signal caused by shock wave. None of these pressure traces was a simple step-function; all showed a 7 μsec ringing period in the gauge. We successfully dealt with this problem by averaging the ringing-extremes on each half-cycle to determine the mean signal during that time. This method demonstrated the inadequacy of the Teflon transducer mounting that was tried at first.* The amplitude of the 7 μsec

*It was hoped that a soft mounting such as this would provide desirable insulation of the transducer from compression waves in the Plexiglas window surrounding the Teflon holder. This view reckoned without the importance of coupling the gauge to a substance which would damp the elastic waves induced in the gauge itself.

ringing was about 60% of the mean signal; in turn, the mean signal smoothly oscillated about its time-average with a 20% amplitude and 50 μsec period. The x-t pictures of the same experiments showed no evidence of perturbing waves of such strength as a literal interpretation of the pressure traces would indicate. The ring-frequencies were independent of the predicted shock tube conditions, and appeared to be characteristic only of the gauge and its mounting. For experiments in which the ideally predicted pressure ratios vere $y_{10} \sim 55$ and $y_{21} \sim 6$, the Teflon-mounted transducer indicated $y_{10} \sim 62 \pm 9$ and $y_{21} \sim 6.2 \pm 1$.

The quality of the pressure signal was considerably improved with an adaptation of the mounting developed by Kaegi, Warren, and Vitale[75] of General Electric. The transducer (~1/4" dia.) is sealed inside a larger flanged cylinder of brass which is mechanically isolated from the Plexiglas window by O-rings and flat rubber shock-mounts. Figure 12 is a photograph of the mounting, its accessories, and the test section window. The window has two holes, either of which may receive the mounting or a brass filler-plug. On the back of the mounting is a short bolt (not visible) which holds the transducer tightly in the mount. The coaxial cable passes through a hole in this bolt. Examples of the pressure records obtained with this mounting are shown in Figs. 13 and 14. When the gauge is subjected to a sudden change in pressure, the ringing-amplitude is initially about 50% of the mean signal but drops to 10% or 15% of the signal by the third cycle. The later surges of the signal and the random re-establishment of ringing are believed to represent genuine hydrodynamic noise.

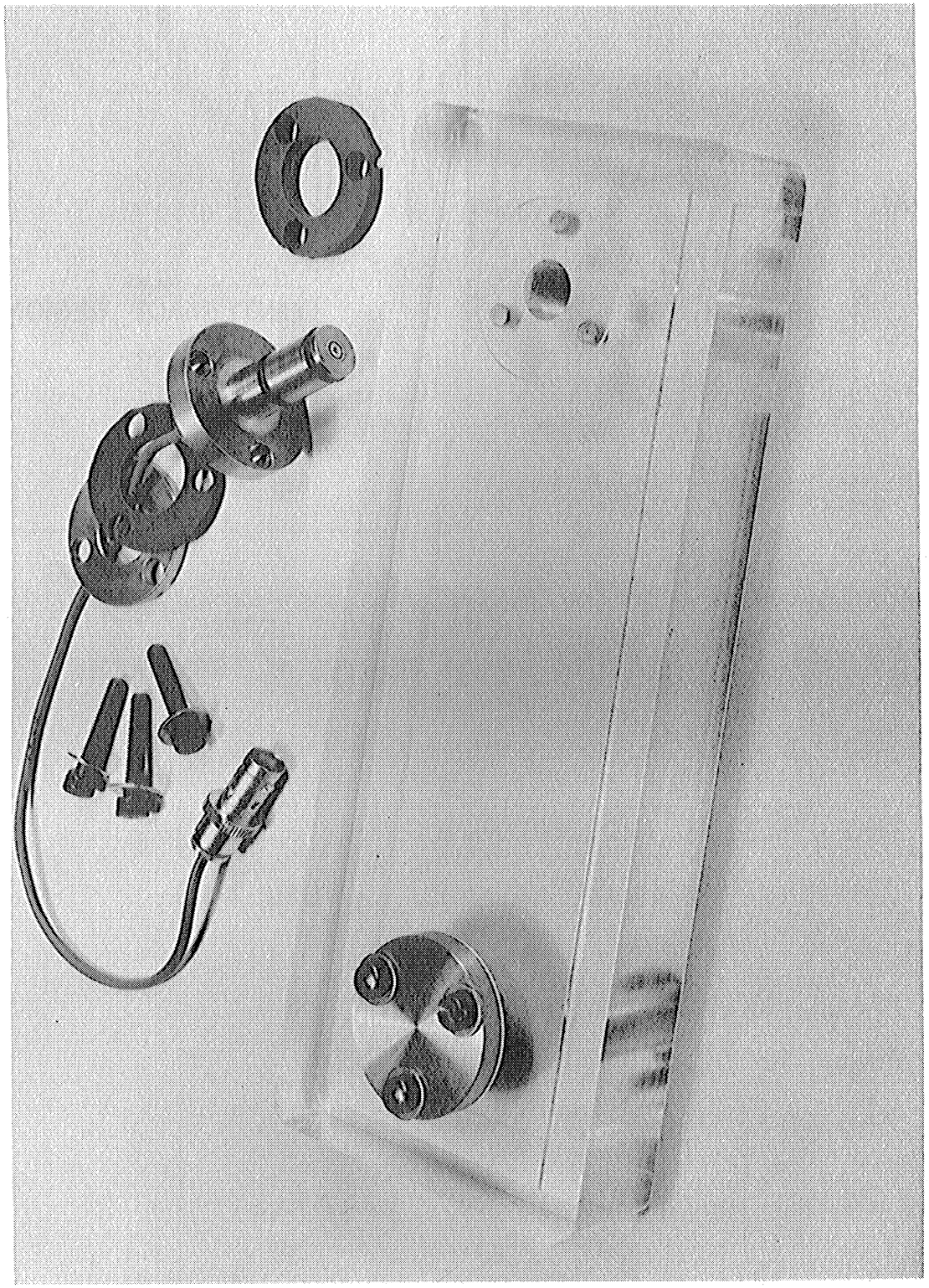

Figure 12. Brass plug-in mounting for PZ6-S pressure transducer, shown with test section window (1" thick Plexiglas).

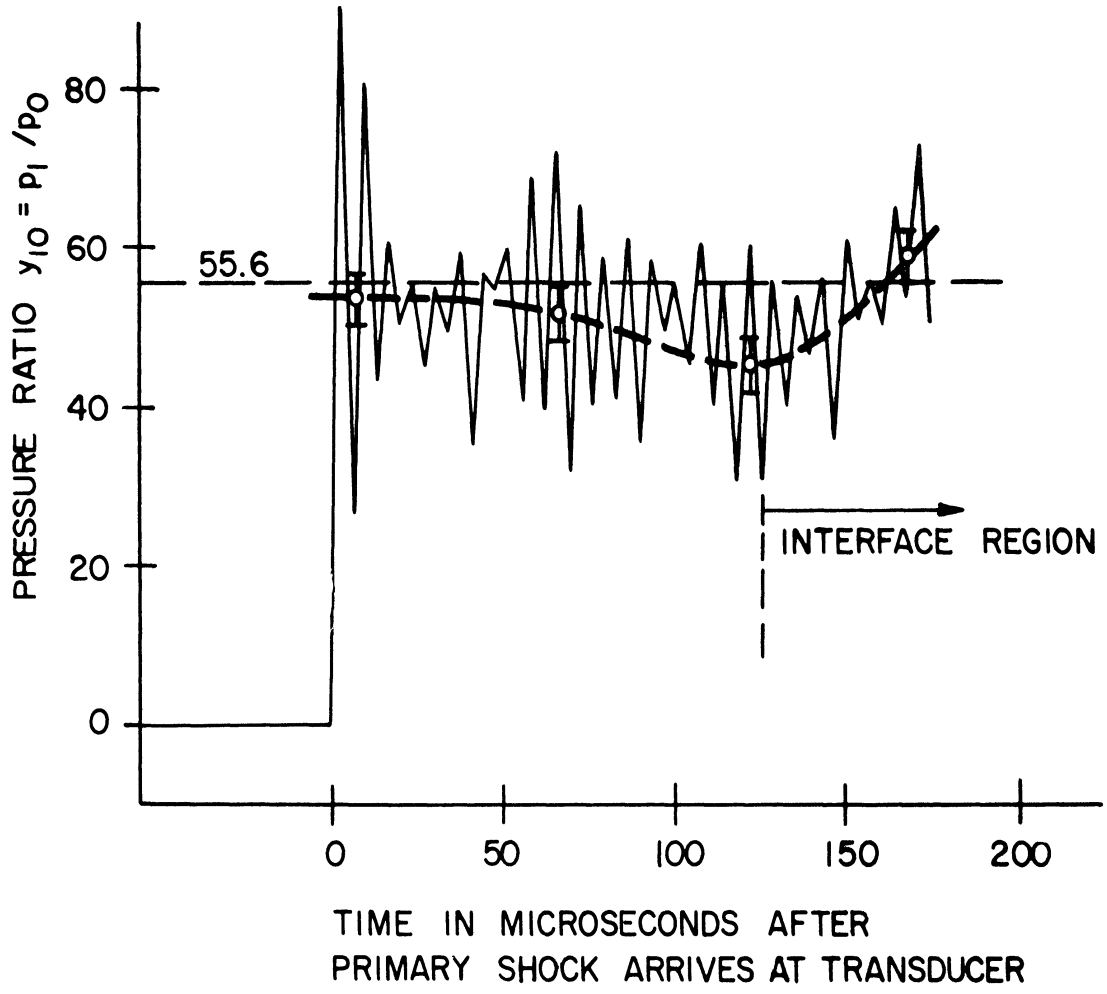

FOR THE FIRST 50 MICROSECONDS,

THE OBSERVED PRESSURE RATIO IS $y_{10} = 53.1 \pm 3.5$.

THE PREDICTED PRESSURE RATIO IS $y_{10} = 55.6$,
ACCORDING TO IDEAL SHOCK TUBE THEORY
AND THE OBSERVED SHOCK VELOCITY.

$p_0 = 7.676$ mm Hg OF NEON. $x = 17.7$ cm

Figure 13. Upstream pressure record with PZ6-S transducer.

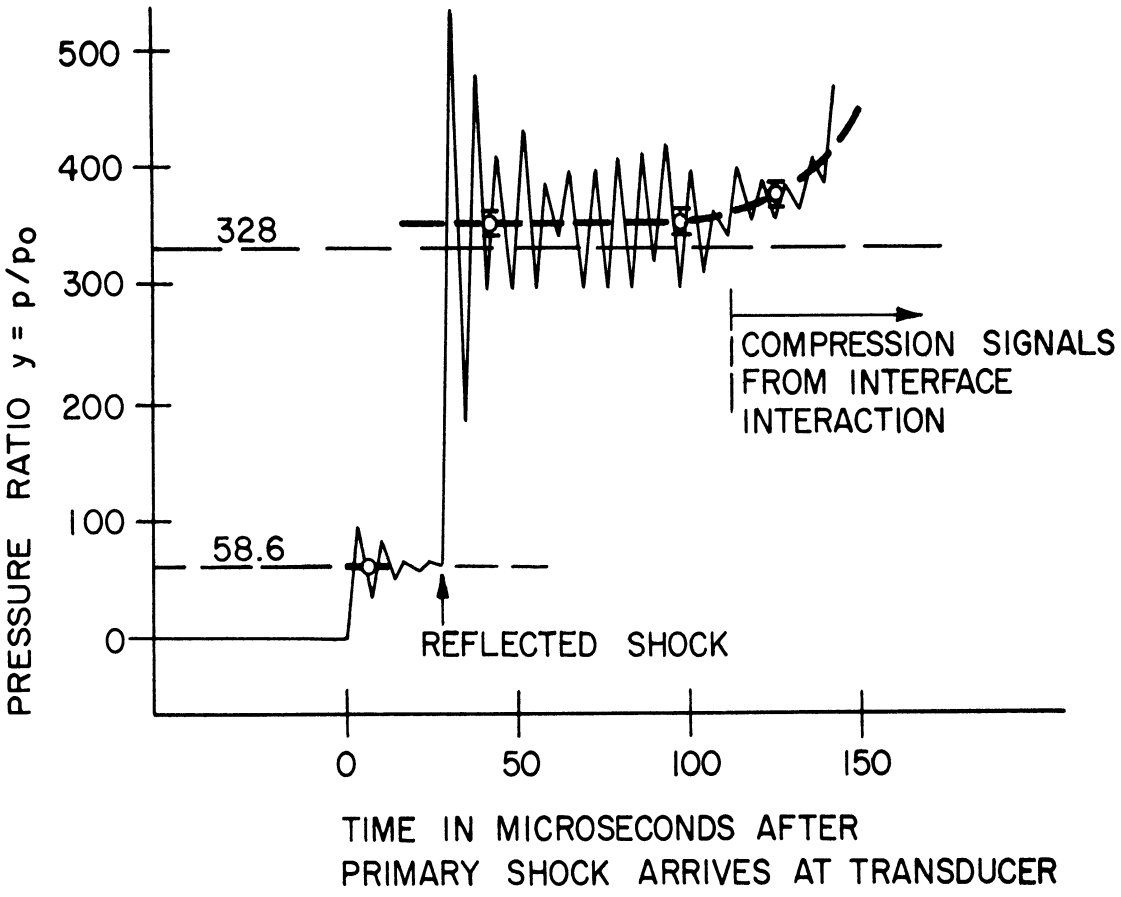

OBSERVED PRESSURE RATIOS: $\begin{cases} y_{10} = 58.9 \pm 4.5 \\ y_{20} = 349 \pm 11 \end{cases}$

PREDICTED PRESSURE RATIOS: $\begin{cases} y_{10} = 58.6 \\ y_{20} = 328 \end{cases}$

p_0 = 7.695 mm Hg OF NEON $\qquad$ x = 2.3 cm

Figure 14. Downstream pressure record with PZ6-S transducer.

None of these traces show the long-period oscillations encountered with the Teflon mounting. Pending further improvements* in the mounting, we felt that the signal quality warranted a limited number of quantitative experiments in the strong-shock tube. We will first describe the required method of data analysis and then discuss the results.

The oscilloscope traces represented in Figs. 13 and 14 were drawn by plotting the traveling-microscope readings of the ringing-extremes of the signal. Let E_i^+ and E_i^- be the maximum and minimum of the signal on the i^{th} half-cycle. The corresponding average signal was defined as

$$A_i = \frac{E_i^+ + E_i^-}{2}$$

For a number (n) of consecutive half-cycles, the mean signal

$$M_n = \overline{A_i}^{(n)}$$

and the mean deviation

$$\Delta_n = \overline{M_n - A_i}^{(n)}$$

were derived. The signal level during the n half-cycles was represented as

$$M_n \pm \Delta_n ,$$

which was converted to the pressure

---

*Kaegi et al. used a dense, machinable tungsten alloy, Hevimet, to hold the gauge. Our brass holder was made for testing the design, and will soon be replaced by Hevimet We are indebted to Donald L. Upham for his excellent design of this mounting. We also wish to thank Alan L. Cole and Alfred C. Hunting for the loan of the electronic components of our pressure measurement system. The present form of the gauge has been used extensively by Cole in his study of cylindrical shock waves.

$$p \pm \Delta p$$

via the atmospheric pressure calibration previously discussed. This number could then be reduced to the pressure ratio form; e.g.,

$$y_{10} = \frac{p_1 \pm \Delta p_1}{p_0} .$$

Such values of the pressure ratios are represented by points and error flags in Figs. 13 and 14. Also shown for comparison in the figures are the ideal shock strengths predicted by simultaneous x-t measurements of the primary shock velocity. A graph summarizing the data will be given following a discussion of the illustrations.

The pressure record in Fig. 13 shows mostly the neon primary flow column since the gauge was located 17.7 cm from the end of the tube. The interaction between the reflected shock and the interface region occurred slightly downstream ($x \sim 12$ to 14 cm) of the gauge. Thus neither the reflected shock nor much of the (initial) cold hydrogen flow was recorded, the latter limitation arising from the shock sent upstream by the aforesaid interaction. During the first 50 μsec of flow behind the shock, the measured pressure agrees with the ideal pressure to within the experimental error of 7%. With the passage of time, the pressure first decreases and then increases to roughly its original value. The minimum pressure is about 20% less than the pressure near the shock and is achieved when the x-t film indicates that the leading edge of the interface region passes the gauge. The pressure decrease was observed in other experiments with the

same and twice the initial pressure. This effect is discussed at the end of the section.

Figure 14 duplicates the pressure record obtained with the gauge placed 2.3 cm from the end of the tube. For about 25 or 30 μsec, the primary flow pressure is registered and agrees with the ideally predicted value to within the available accuracy of 7.5%. Except for some dandom noise, the pressure behind the reflected shock is quite steady until such time as the x-t film indicates that the first signals come back from the reflected shock-interface collision. The measurement accuracy of the pressure is 3%, and the central value of the pressure is 6.4% in excess of the value computed from ideal theory. This small excess was observed in another experiment at the same p_o. For higher initial pressures, we observed agreement with ideal theory to within the measurement error.

The results of the usable experiments with the brass mounting are shown in Figure 15. The pressures indicated by the transducer are graphed against the pressures computed from the primary shock speed. The lowest pressures were measured behind primary shocks with $p_o \sim 7.5$ mm Hg and the highest behind reflected shocks with $p_o \sim 31$ mm Hg. The only observable deviations from ideal theory are shown by the circled points which were recorded behind reflected shocks with the lowest initial pressure.

These results, together with the flow speed data in the previous section, indicate that the thermodynamic conditions behind a reflected shock in neon can be satisfactorily inferred from the primary shock speed in the range of conditions we have investigated. The importance of the pressure

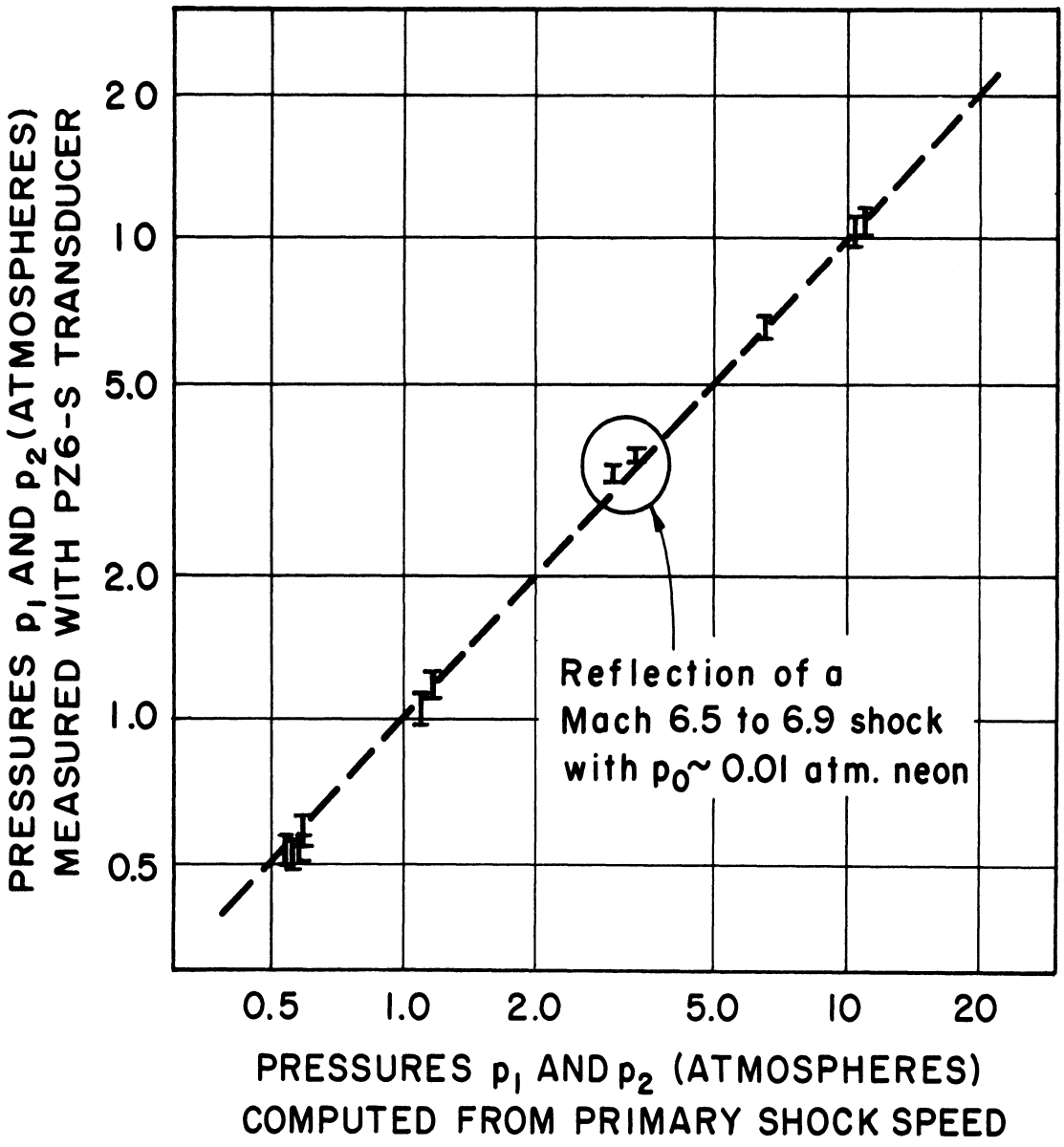

Figure 15. Absolute pressures: transducer measurements vs. predictions of ideal theory.

excess at the lowest initial pressure would have to be evaluated from its effect on the ionization equilibria of spectroscopic additives.* The excess appears to vanish for $p_o \sim 15$ mm Hg and above, and probably occurs at lower pressure because of the increased attenuation effects.

When these measurements were undertaken, we did not expect to see large pressure variations in the primary flow. However, all the upstream records show the pressure minimum at the interface as illustrated in Figure 13. The decrease of pressure behind the shock confirms our conclusion (Section 6) that the shock formation process is usually completed upstream of the test section. The strong noise signals in the late primary flow probably reflect the turbulence that was visualized by the C_2 emission method. We tentatively identify the pressure decrease as an extreme form of the decrease predicted by Mirels and Braun (Section 6) for strong shocks attenuated by turbulent boundary layers.

The magnitude of this prediction for air is less than we observe in neon driven by hydrogen. The Mirels-Braun results are given as a ratio of pressure decrements which we write as

$$\delta_{t,o} = \frac{\Delta p_{1,t}}{\Delta p_{o,t}}$$

$\Delta p_{1,o}$ is the amount by which the pressure at the shock is below the Taub prediction when the shock arrives at the observing station. $\Delta p_{1,t}$ similarly represents the failure of the Taub equation for the portion of the

*For example, Doherty[35] discusses the effects of such phenomena on the electron pressure behind reflected shocks for a temperature range (11,000 to 14,000°K) higher than the range covered here.

flow which arrives at the station at a later time t. The maximum (i.e., interface) value for $\delta_{t,o}$ given by Mirels and Braun is about 1.1. By comparison, we compute the value

$$\delta_{t,o} = 1.4$$

for shocks of the same observed strength ($y_{10} \sim 55$) at two different initial pressures ($p_o \sim 7.7$ and 15.7 mm Hg neon). The required values of $z = p_4/p_o$ were quite different, being 2670 and 2080, respectively. Though this agreement may be only fortuitous, it would appear that the derived $\delta_{t,o}$ (like its analogue in the Mirels-Braun theory) is capable of describing experiments of rather different absolute amounts of attenuation.

A program is now being planned for further pressure measurements with the new transducer mounting. The range of reflected shock measurements will be extended, and the late primary flow will be examined over a considerable length. A short "straight-through" test section has been inserted in the expansion chamber about 70 cm from the end wall. This section accommodates two small windows, the pressure gauge and other apparatus. The anticipated improvement in the transducer signal will simplify the data reduction for each shot and enable more experiments to be run. The nature of the "noise" in the flow fields can perhaps be clarified. The hydrogen cold flow may be particularly interesting, since the present records indicate a strong pressure increase in this region. Some understanding may be possible regarding the effects of driver gas attenuation and mixing, both on the driver itself and the primary hot flow.

CHAPTER IV

TRANSIENT MOLECULAR EMISSION

1. INTRODUCTION

In Section 5 of the preceding chapter, we have described the luminosity induced in the shock tube gas by organic contaminants. For gas temperatures as low as 3500°K, the intense emission of the C_2 and CN bands enables the direct photography of rare gas flow which would be non-luminous were it not for the contaminant. In this chapter we will discuss the mechanism which seems to underlie the strong molecular radiation by various portions of the flow.

In 1957, Charatis, Doherty, and the author[61] proposed a non-equilibrium theory for the transient C_2 and CN emission observed behind strong shock fronts. This theory and the deductions leading to it are reviewed in Section 2. Section 3 presents chemical-kinetic calculations which lend support to the proposed mechanism. Differential equations are written to express the chemical creation and radiative anihilation of excited C_2 moleclues. The solutions of these equations possess strong maxima very near the shock front. In Section 4, we demonstrate the origin of C_2 and CN emission from turbulent boundary layers. Section 5 discusses the implications of our mechanism for radiation by other molecules under similar circumstances.

2. DEDUCTION OF THE NON-EQUILIBRIUM MECHANISM

In most of the situations previously described, the strength and history of the C_2 and CN radiation were at first very puzzling. The only exception was the steady molecular emission following the ionization relaxation time behind the reflected shock (again, see Figure 7). In this case, the pressure and temperature of the electron gas were manifestly high enough that the excited electronic states of atoms and molecules were populated by collision processes. Except for this situation, the molecular emission was quite transient in regions of constant hydrodynamic state and occurred with greatest strength in the vicinity of violent hydrodynamic change. The maximum light intensities were often 100 or 1000 times greater than one would expect from equilibrium calculations of the abundance of excited C_2 molecules. Yet these same calculations would predict recordable intensities in some regions of the flow where little or no light was seen. Thus we assumed that the observed emission was the manifestation of one or more non-equilibrium processes.

The most extenisvely studied phenomenon was the C_2 emission from the main stream of the primary flow. Many x-t and y-t films were traced with a recording densitometer. The x-profile of the light was generally smooth, rising quickly to a maximum very near the shock and then decreasing more slowly. The rates with which the profile rose and fell depended both on the organic additive and on the shock strength. For all the additives, a shock strength of 70 was sufficient to put the maximum

within a millimeter of the shock surface.* By decreasing the partial pressure of an additive in this situation, the "tail" of the luminosity profile could be so reduced in intensity as not to expose the film. In this way, the generally broad swath of exposure on the x-t films could be reduced to a very thin line, the same sort of line which had resulted from impurities in the experiments of Petschek,[57] Rosa[60] and Turner.[12] By holding the additive partial pressure at, say, 40 microns and decreasing the shock strength so that the primary flow became just barely luminous, we could "shift" the peaked profile of strong C_2 emission into the gas behind the reflected shock. This gas was then at a low enough temperature that ionization-relaxation (and the associated onset of steady emission) was prevented from occurring within the available time. Invariably, the regions of transient molecular emission were disjoint from the regions of appreciable ionization.

These observations led to some hypotheses about the radiation mechanism. The creation of electronically excited molecules did not require electron collisions, nor were such collisions available for re-exciting the molecules once they had radiated. The chemical reactions induced by a shock transition produced the excited molecules from an organic additive. The history of the excited molecule concentration (and

*The identification of luminosity fronts as the primary and reflected shock waves was clear from the common x-t intersection of them with the end wall of the tube and their unperturbed appearance away from the end wall. In all cases, a decision on this point was possible up to the 1 μsec resolving-time on the x-t films and on microdensitometer tracings of the films.

hence of the emission) depended both on the rates of these reactions and on the rate of radiative extinction. The reaction rates increased with increasing temperature, so that the rise and fall of molecular emission occurred most rapidly behind the strongest shocks.

The experiments with CH_4 showed that the reactions need not proceed by the analysis of poly-carbon molecules. The absence of carbon-carbon pairs in the methane clearly implied that the C_2 molecules were very rapidly synthesized and, moreover, in an excited electronic state. A similarly fast creation of excited CN was observed when the additive was a mixture of CH_4 and NH_3. The synthesis of C_2 in the excited state ($A\ ^3\Pi_g$) responsible for the Swan bands required the combination of $C(^3P)$ with $C(^1D)$* in the presence of a third (probably neon) body. In the absence of electron collisions, $C(^1D)$ must result from the dissociation of CH_4. It is known from calculations of Voge[78] that a considerable admixture of ^5S, ^3P, ^1D, and ^3D states of atomic carbon is required for describing the valence of carbon in CH_4. Therefore the sequence of non-equilibrium events which accounts for the transient molecular emission is the following:

(1) CH_4 and NH_3 are rapidly destroyed when exposed to energetic neon collisions.

(2) Appreciable fractions of the resulting atoms are electronically

*Herzberg[76] discusses combination rules in Chapter VI of his book on diatomic molecules. He also gives several specific examples in Chapters VII and VIII. See also the review article by Van Vleck and Sherman.[77]

excited by virtue of the mixtures of atomic states in the parent compound. In particular, the species $C(^3P)$, $C(^1D)$, and $N(^2D)$ exist of higher concentrations than equilibrium calculations would indicate.

(3) $C(^3P)$ and $C(^1D)$ combine into the excited molecule $C_2(A\ ^3\Pi_g)$ whose transition to the $^3\Pi_u$ ground state is accompanied by emission of the Swan bands. Similarly, the combination of $C(^3P)$ and $N(^2D)$ into $CN(B\ ^2\Sigma^+)$ is followed by radiation of the CN violet bands as the molecule decays to its ground state.

(4) Neither the molecules nor their ground state dissociation products, $C(^3P)$ and $N(^4S)$, are re-excited because of the absence of electrons at sufficiently high energy and concentration. Thus the concentration of excited molecules drops below the equilibrium value and, eventually, to zero.

3. SEQUENTIAL REACTIONS

The following calculations by the author show that the above sequence of events does lead to luminosity profiles of the observed type. The concentration n(t) of excited molecules in a certain gaseous volume element is computed as a function of the "proper time" for the fluid element, once it is overrun and set in motion by a shock wave. We will assume here that the observed band intensity is directly proportional to n(t).

In surveying the literature preparatory to writing this section, we find that Hammerling, Teare and Kivel[79] have recently made similar com-

putations for the transient emission by N_2^+ behind very strong shocks in N_2. The reaction chain for this case is very complicated, and numerical integration is apparently required. The computed results are thus specific to each experimental situation and reaction rate assumption. For the simpler case of C_2(or CN) produced by association in an unionized rare gas atmosphere, the theory presented here admits of some analytical solutions whose dependence on the reaction constants is quite clear. The influence of successive reactions can be systematized by reduction of the equations to certain well known problems of classical analysis.

A. Neglecting collisional excitation and de-excitation,* the time-variation of n(t) is determined by the rates of chemical creation and radiative extinction of the excited molecules; i.e.,

$$\frac{dn}{dt} = \left.\frac{dn}{dt}\right)_{reac.} + \left.\frac{dn}{dt}\right)_{rad.}$$

We will denote the reaction term by g(t). The radiative term equals $-n\alpha$, where α is the Einstein coefficient for spontaneous emission. Therefore,

$$\frac{dn}{dt} + \alpha n = g(t),$$

which is solved by

$$n(t) = n(0)\, e^{-\alpha t} + e^{-\alpha t}\int_0^t e^{\alpha \xi}\, g(\xi)\, d\xi .$$

If no chemical reactions occur, one is left only with the exponential

*This assumption is justified by the composition and temperature of the gases of interest.

decay of the molecular concentration initially present. We will assume the opposite case, namely that the concentration is initially zero and is built up by subsequent reactions; therefore,

$$n(t) = e^{-at} \int_0^t e^{a\xi} g(\xi)\, d\xi \qquad \text{(IV.1)}$$

Any process (such as the spontaneous emission "reaction") in which the concentration and its time-rate-of change are linearly related is said to be a first order reaction. The dissociation of CH_4 is most likely such a process; i.e.,

$$-\frac{d\,n(CH_4)}{dt} = \gamma\, n(CH_4)\,, \qquad \text{(IV.2)}$$

where γ (the rate constant) depends on the conditions under which the reaction is taking place. This reaction alone cannot describe the function g(t) for excited C_2 molecules, since it yields only carbon atoms which must combine in some intervening process.*

The rate of this combination depends on the product of the concentrations of $C(^3P)$ and $C(^1D)$, and the reaction is thus of second order. For

*If we had observed the C_2 Swan bands only with more complicated organic additives, then one might assume that the excited molecules came directly out of the compound in a first order process. For such a case, $g(\xi)$ would be proportional to $\gamma e^{-\gamma\xi}$, and n(t) would be determined by two sequential first order reactions, one chemical and the other radiative. This case was first studied for purely chemical processes by Harcourt and Esson[80] in 1865, and is among the various sequential reactions discussed in the books by Laidler[81] and Glasstone.[82]

the purpose of simplification, we assume that the reaction

$$C(^3P) + C(^1D) \rightarrow C_2(A\,^3\Pi_g) \tag{IV.3}$$

is the only reaction in which either species takes part, and that neither type is regenerated by later events. We also suppose that the numbers of both species having been set free from CH_4 are equal to the same function $\Gamma(t)$. Under these conditions, $\left(d/dt\right)_{\text{reac.}} n\,(C_2A\,^3\Pi_g)$ is

$$g(t) = \epsilon \left\{ \Gamma(t) - \int_0^t g(\xi)\, d\xi \right\}^2, \tag{IV.4}$$

where ϵ is the second order rate constant. In principle, this equation may always be solved by reduction first to a Riccati equation and then to the linear, second order form

$$G_1''(t) - \epsilon\, \Gamma'(t)\, G(t) = 0, \tag{IV.5}$$

where

$$G_1 = e^{\sqrt{\epsilon} \int \sqrt{g(\xi)}\, d\xi}$$

Assuming a solution g(t) can be found, it is substituted into Equation (IV.1) which yields n(t) in closed form. Clearly the atomic "creation function" $\Gamma(t)$ determines the character of these solutions.

B. To examine the simplest case, we suppose all the methane to be dissociated immediately upon passing through the shock front. We will de-

note by n_o the resulting initial concentration of both types of carbon atoms. Therefore,

$$\Gamma(t) \equiv n_o \quad ; \; t > 0 \,, \tag{IV.6}$$

and the second order reaction occurs in its most elementary form (e.g., see Glasstone,[82] pp. 1054 et seq.).

$$g(t) = \frac{\epsilon n_o^2}{(\epsilon n_o t + 1)^2} \,. \tag{IV.7}$$

Substitution of this "forcing function" into Equation (IV.1) yields the concentration of excited C_2 molecules; i.e.,

$$n(t) = n_o \lambda \, e^{-\lambda(\tau+1)} \int_{\lambda}^{\lambda(\tau+1)} d\xi \left(e^{\xi} / \xi^2 \right) \,,$$

where $\lambda = a/\epsilon n_o$ expresses the relative speeds of the radiative and chemical processes, and $\tau = \epsilon n_o t$ is the dimensionless "time" in terms of the speed of the chemical process alone. After partial integration, we may write

$$\phi(\lambda, t) \stackrel{d}{=} n(t)/n_o$$

$$= e^{-\lambda\tau} - \frac{1}{\tau+1} + \lambda \, e^{-\lambda(\tau+1)} \left\{ E_i\left[\lambda(\tau+1)\right] - E_i\left[\lambda\right] \right\} \,,$$

(IV.8)

where

$$E_i(x) = \int_{-\infty}^{x} d\xi \left(e^{\xi}/\xi \right)$$

is the exponential-integral function. Figure 16 shows a graph of $\phi(\lambda,t)$ for $\lambda = 1$; the time is here represented in units of a^{-1}, the radiative lifetime of an excited molecule. The concentration of these molecules goes through a smooth maximum at $t = 0.9\ a^{-1}$ and then drops to about 1/10 the maximum value for $t = 6.5\ a^{-1}$. Thus the sequence of reactions we have imagined does lead to luminosity profiles which are qualitatively similar to those that we observed behind shock waves.

Also shown in Figure 16 is a table of the times required for $\phi(\lambda,t)$ to reach its maximum for different values of λ. For $\lambda = 10^3$, the time of greatest intensity is about $7a^{-1}$. The meaning of such a large λ is that the chemical formation of excited molecules takes place much more slowly than their radiative extinction. The peak intensity is rapidly attained in spite of the comparative slowness of the underlying reaction.

The case of large λ seems the most reasonable for our experiments. By means of the collision theory of reaction rates, we have estimated the rate constant ϵ for C_2 formation at 5,000°K. We will not give the details here because the theory is very simple and is discussed in detail by Laidler[81] and by Glasstone.[82] Assuming two body collisions, $10^7 < \epsilon n_o(\text{sec}^{-1}) < 10^8$. These numbers are also of the order of a, the Einstein emission coefficient for the Swan bands of C_2. Therefore $\lambda = a/\epsilon n_o$ is certainly no less than 1. It is actually much larger, since ϵn_o must be

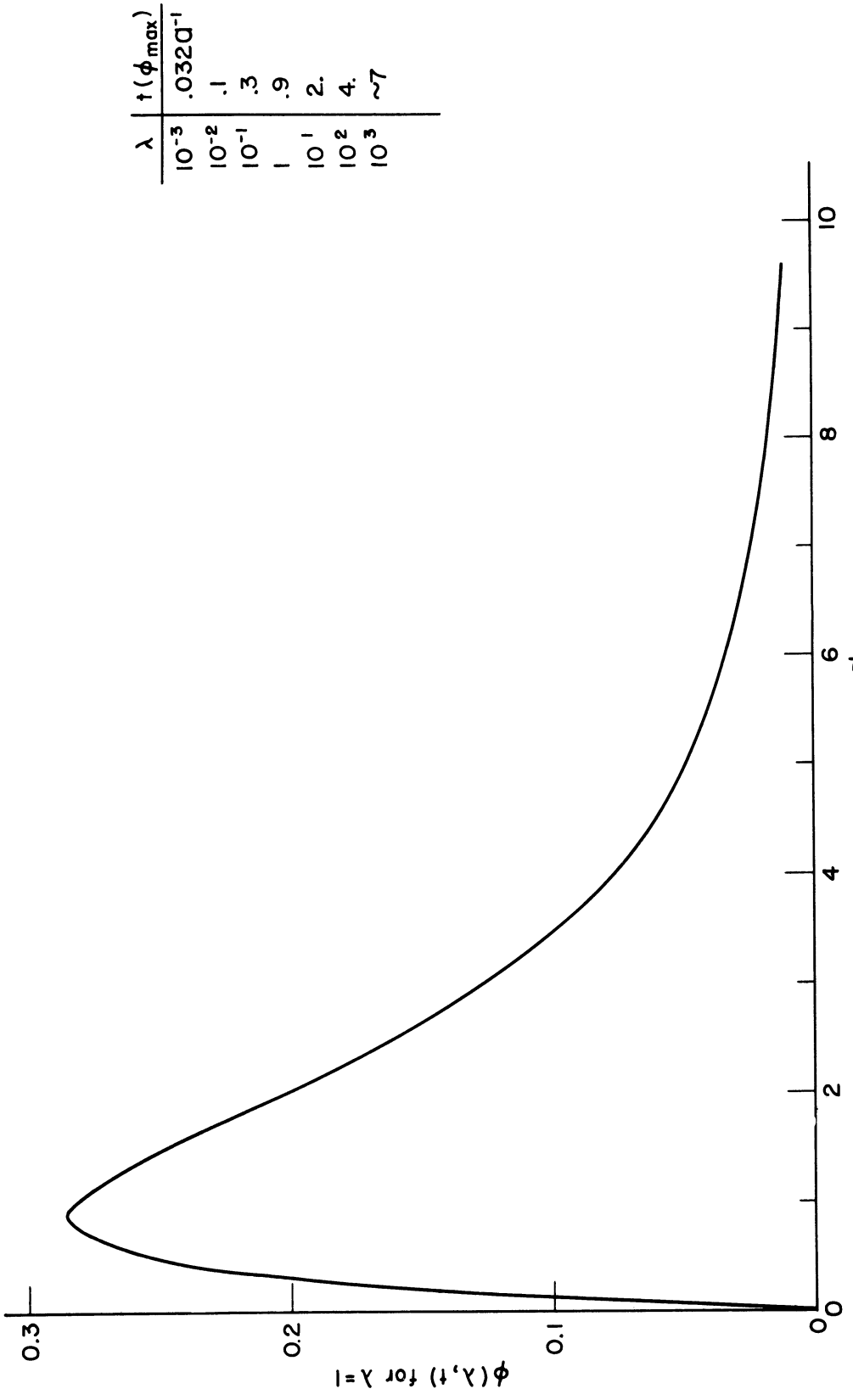

Figure 16. Time variation of the concentration of excited C_2 molecules, according to simple reaction-kinetic theory.

reduced by a factor which is the fraction of carbon-carbon collisions which occur in the presence of a third body. For our typical primary flow pressure, $1000 < \lambda < 10{,}000$.

In the case of $\lambda = 10^3$, the times required for the intensity to fall to 1/2 and 1/10 its maximum value are about $400\alpha^{-1}$ and $2200\alpha^{-1}$, respectively. The latter time is roughly 20 μsec if $\alpha = 10^8$ sec^{-1}; this corresponds to a 2 cm laboratory distance behind the shock for most of our experiments. Thus the predicted luminosity profiles decay over lengths which are within an order of magnitude of all the observed decay lengths. Further, the maximum value of $\phi(10^3,t)$ is about .001, and the corresponding excited C_2 concentration is between 1×10^{12} and 5×10^{12} cm^{-3} in our experiments. For this predicted abundance, the total intensity in the C_2 Swan bands is consistent with the high photographic densities of the shock wave images we observed.

C. An obvious objection to the foregoing calculation is that the dissociation of methane cannot take place instantaneously at the shock front as assumed in Equation (IV.6). This equation is approximately true if the first order dissociation (Equation IV.2) takes place at a rate γ which is much greater than α and ϵn_0. In general, the supply of free carbon atoms must be given by

$$\Gamma(t) = n_0 \left(1 - e^{-\gamma t}\right)$$

and Equation (IV.5) therefore becomes the equation for the modified Bessel functions* (of zero order) in the variable

*See Magnus and Oberhettinger,[83] p. 19.

$$\left[\frac{4\epsilon n_o}{\gamma}\, e^{-\gamma t}\right]^{1/2}$$

Thus the chemical derivative g(t) and the net concentration n(t) of excited molecules are complicated integrals of these functions and their derivatives. Rather than pursuing this difficult analysis further, we numerically integrated Equations (IV.1) and IV.4) together for the one case in which all rates were set equal. In the case of instantaneous dissociation, this assumption had resulted in $n(C_2A^3\pi_g)$ achieving its maximum in about 0.9 radiative lifetimes. Now, with $\alpha = \gamma = \epsilon n_o$, the maximum concentration is delayed to 2.3 radiative lifetimes. At this time, 9/10 of the CH_4 is dissociated but less than 1/2 of the potential C_2 molecules have been formed. Thus the constraint imposed by the methane reaction can be appreciable, even if the reaction rate is comparable to the others. It may have been the dissociation rate of CH_4 which was responsible for the visible "rise time" of the luminosity profiles behind weaker shocks. Further complications must arise from the regeneration of $C(^3P)$ via the dissociation of C_2 out of its ground state and the consumption of both $C(^3P)$ and $C(^1D)$ in reactions other than (IV.3).

Our assumption of equal abundances for $C(^3P)$ and $C(^1D)$ may be replaced by another which is, in a sense, the opposite extreme. If the dissociation of CH_4 leads initially to a great preponderance of $C(^3P)$

over all the other carbon species, then the concentration of this type of atom will change very little as the terminal equilibrium,

$$C(^3P) + C(^3P) \rightleftarrows C_2(^3\Pi_u),$$

is established. In this event, one might consider the concentration of $C(^3P)$ as roughly constant during the course of all other reactions. Reaction (IV.3) would then be of the pseudo-first order type, its progress depending primarily on the diminishing amount of $C(^1D)$. n(t) would then be described by the equations for two first order reactions, which we previously mentioned in the footnote following Equation (IV.2). The associated luminosity profiles would be qualitatively similar to the ones discussed above.

Clearly, extensive experimentation will be required to unravel all the processes which underlie the transient emission phenomenon. Our calculations serve primarily to illustrate some of the characteristics of the chemical-radiative sequences which must occur.

4. BOUNDARY LAYER EMISSION

The mechanism given in Section 2 was also able to account for the strong C_2 emission from turbulent boundary layers under the assumption that the cold layer near the wall contained methane, the emission arising from turbulent mixing of this material with the hot main stream gas. The opposite process, namely the recombination-by-cooling of carbon atoms from the main stream gas, could not so account for the emission. The

late primary flow adjacent to the turbulent layer was non-luminous presumably because of its lack of those atomic species necessary for the formation of excited molecules. We settled the matter in favor of the first assumption by using the luminosity of the reflected shock wave to indicate those regions of the primary flow containing residual methane.

The x-t films gave the first evidence of the CH_4 distribution across the primary flow. The x-t camera was usually set so that its optic axis intersected the axis of flow perpendicularly at an x location of 2 or 3 cm from the end wall of the tube. A shock wave at this position was viewed "edge-on" and measurement of its speed here was unambiguous. However when a shock was 10 or 15 cm from the end wall, its intersections with the near and far walls of the tube subtended a significant angle at the camera. Thus the x-t image of a luminous primary shock front was not a line of constant width but, rather, a narrow wedge whose width was greatest when the shock was farthest from the point of zero parallax.

Examination of reflected shock waves in the same context gave quite another result which, though barely visible in Figure 7 , was clearly shown in the original films of this and similar experiments. The image of the reflected shock was observed to split into two distinct lines as the shock moved upstream from the zero parallax position. These lines represented the near and far wall intersections of the reflected shock. Clearly the wall layers contained methane which gave rise to C_2 emission when subjected to the reflected shock transition. The lack of exposure between the lines showed that the reflected shock surface was non-luminous

over most of the tube cross section and, therefore, that the main stream of the late primary flow was devoid of methane. A few x-t films were taken with the zero parallax position set 10 cm from the end wall. These pictures enabled a similar search for "parallax splitting" of the reflected shock image near the end wall of the tube. Here we found that the shock luminosity was again strong at the walls but was also present to a lesser degree over the entire tube cross section. In this case, the reflected shock was moving through that portion of the primary flow which was still luminous and which, by our chemical kinetic view, was likely still to contain some methane in the main stream.

The same conclusions were drawn from vertical-slit photographs taken close enough to the end of the tube that the reflected shock could be observed as it interacted with either the laminar or turbulent boundary layer portions of the primary flow. In one case, the parallax effect was heightened by so setting the camera that its line of sight was still in the horizontal plane but made an angle of 20° with the normal to the tube axis. The reflected shock was seen as two distinct line images whose separation on the film coresponded to the expected time difference for passage of the wall intersections of the shock across the line of sight. With the camera viewing the tube perpendicularly, we saw a layer of strong C_2 emission on the floor of the tube immediately behind the reflected shock. In most cases, this layer was only as thick as the oncoming wall layer in the primary flow. Again it was evident that the laminar and turbulent boundary layers were carrying considerable amounts

of methane into the gas behind the reflected shock. In this connection we recall Figure 9 (described in Section 5, Chapter III). This film provided an "edge-on" C_2 emission picture of the surface where the methane came into contact with the hot gas behind the reflect shock.

5. FURTHER CONSEQUENCES OF THE NON-EQUILIBRIUM THEORY

The Ångström and Third positive bands of CO were never observed by us in experiments with additives such as O_2+CH_4 and O_2+C_2H_4. The similar but more extensive experiments by Fairbairn and Gaydon[84] (Imperial College, London) gave the same results.* The absence of transient CO emission in such cases is apparently due to a failure of the physical processes to satisfy the essential step (2) in our non-equilibrium theory (Section 2). The dissociation of O_2 does not provide oxygen atoms which can combine (with carbon) into the excited state of CO appropriate to the emission of the Ångström and Third positive bands. These states require $O(^1D)$ and $O(^1S)$, respectively, whereas the $^3\Sigma_g^-$ electronic ground state of O_2 dissociates into $C(^3P)$ and $O(^3P)$. For such experiments, an allowed mode of CO emission (in principle) would be the Cameron bands (~ 2000 to 2600Å). These bands originate with the first $^3\Pi$ excited state of CO. This state is connected with $C(^3P)$ and $O(^3P)$, both of which should result from the

*Fairbairn and Gaydon studied C_2, CH, and OH emission behind shocks and detonations in a wide variety of mixtures of oxygen, organic compounds and rare gases. They specifically remark on the absence of those spectra (such as the visible bands of CO) which are commonly associated with electron collisions in discharge tubes. We feel that this is additional justification for discussing the transient flow luminosity without reference to collisional excitation by electrons.

dissociation of the original molecules. However, this state is metastable with respect to the $^1\Sigma^+$ ground state which is the terminal state for the Cameron bands. This radiation is therefore quite improbable and has so far been observed only at gas pressures much lower than those encountered in shock tubes. (See Pearse and Gaydon[85] for references to these experiments.)

Some other shock tube experiments are suggested by the work with C_2 and CN.

(1) With additives which are mixtures of NH_3+O_2, transient NO emission should be observed in the β bands but not in the γ bands. Our CN experiments demonstrate the release of $N(^2D)$ from NH_3. This nitrogen species, together with $O(^3P)$ from O_2, can combine into the first $^2\Pi$ excited state of NO which gives rise to the β bands. On the other hand, the "γ-band-state" of NO requires $O(^5S)$, which is not produced by the dissociation of O_2 from its ground state.

(2) By analogy with C_2 and CN, it may be possible to produce the silicon molecules Si_2 and SiN in electronically excited states if monosilane (SiH_4) is used as an additive in place of CH_4. The known spectrum of SiN is a proper analogue of the violet bands of CN. Of particular interest here is the possibility of verifying the existence of Si_2. A tentative identification has been made by Downie and Barrow[86] from visible bands emitted by a H_2+$SiCl_4$ flame.

(3) We surmise that similar experiments with the volatile compounds of boron (such as diborane, B_2H_6) could provide information about the

electronic states of boron in these molecules. Their decomposition in the presence of NH_3 and O_2 would likely lead to emission of some of the bands of BN and BO, which are isoelectronic analogues of C_2 and CN. Currently there is considerable interest in the similarities between the -CC- and -BN- groups as molecular "building blocks."

We will close this discussion with an experimental remark. Our work with transient radiation was hindered by the dependence on photographic observation alone. The early work by Greene[87] and the more recent studies by Roth[88] show the uses to which electronic methods may be put. Even very low intensity processes may be followed in detail by means of photomultipliers in the image plane of a spectrograph. This technique, however, provides data only at a few wavelengths in any one experiment, and it should be supplemented by time-resolved photographic spectroscopy.

CHAPTER V

RADIATION THEORY FOR GASES IN THERMAL EQUILIBRIUM

1. INTRODUCTION

The shock tube emission spectra to be discussed in the next chapter consist of isolated atomic lines. Following a definition of specific radiative intensity in Section 2, the transport theory for line radiation is given in Section 3. Local thermodynamic equilibrium is assumed to obtain in the shock tube gas. Section 4 presents the simple results which one expects with radiation sources which are optically thin. In particular, the measurement of excitation temperature is shown to follow from observed integrated line intensities suitably reduced with the relative gf-values of the lines. The complications arising from appreciable optical thickness are discussed in Section 5. For self-absorbed lines which are subject to both Doppler and dispersion broadening, the theory of the curve of growth enables a systematic study of the integrated intensity. Some numerical illustrations pertaining to the use of the curve of growth are given in Section 6. This chapter constitutes the necessary groundwork for the chromium line intensity measurements of Chapter VI.

For more extensive treatments of the theory of radiative transfer, the reader is referred to the books by Unsöld,[89] Chandrasekhar,[90] and Aller,[91] and to the articles by Milne[92] and by Cowan and Dieke.[93] The broadening of spectral lines emitted by ionized gases has recently been

reviewed by Margenau and Lewis.[94] Most of the available data on line strengths and the coefficients governing line broadening are to be found in Allen's book[95] and in the articles by Joos, Saur, and Biermann in the Landolt-Börnstein tables.[96] We also recall some of the bibliography of Section 2, Chapter I, particularly the applications of radiative transfer theory by Mitchell and Zemansky,[33] Hinnov and Kohn,[34] Doherty,[35] and Goldberg et al.[36]

2. SPECIFIC INTENSITY

In Figure 17, we show a simple device whose operation illustrates the principles of radiation measurements. This "erg collector" looks into the radiation field at the left and, by means of the energy deposited on its collecting surface, enables the radiant energy distribution to be measured. The collector is a truncated right-conical shell of entrance area $d\sigma$ and internal solid angle $d\omega$. The filter passes only those frequencies between ν and $\nu+d\nu$. The energy deposited in the collecting surface in a time dt is

$$dE_\nu = I_\nu \, dt \, d\nu \, d\sigma \, d\omega \tag{V.1}$$

where I_ν is the specific intensity of the radiation field under examination. The radiation field is said to be isotropic if examination by such a machine shows that I_ν is not a function of the angle Θ between the axis of the machine and some space-fixed axis. In this case an equivalent statement is that an interposed control surface (of elemental area

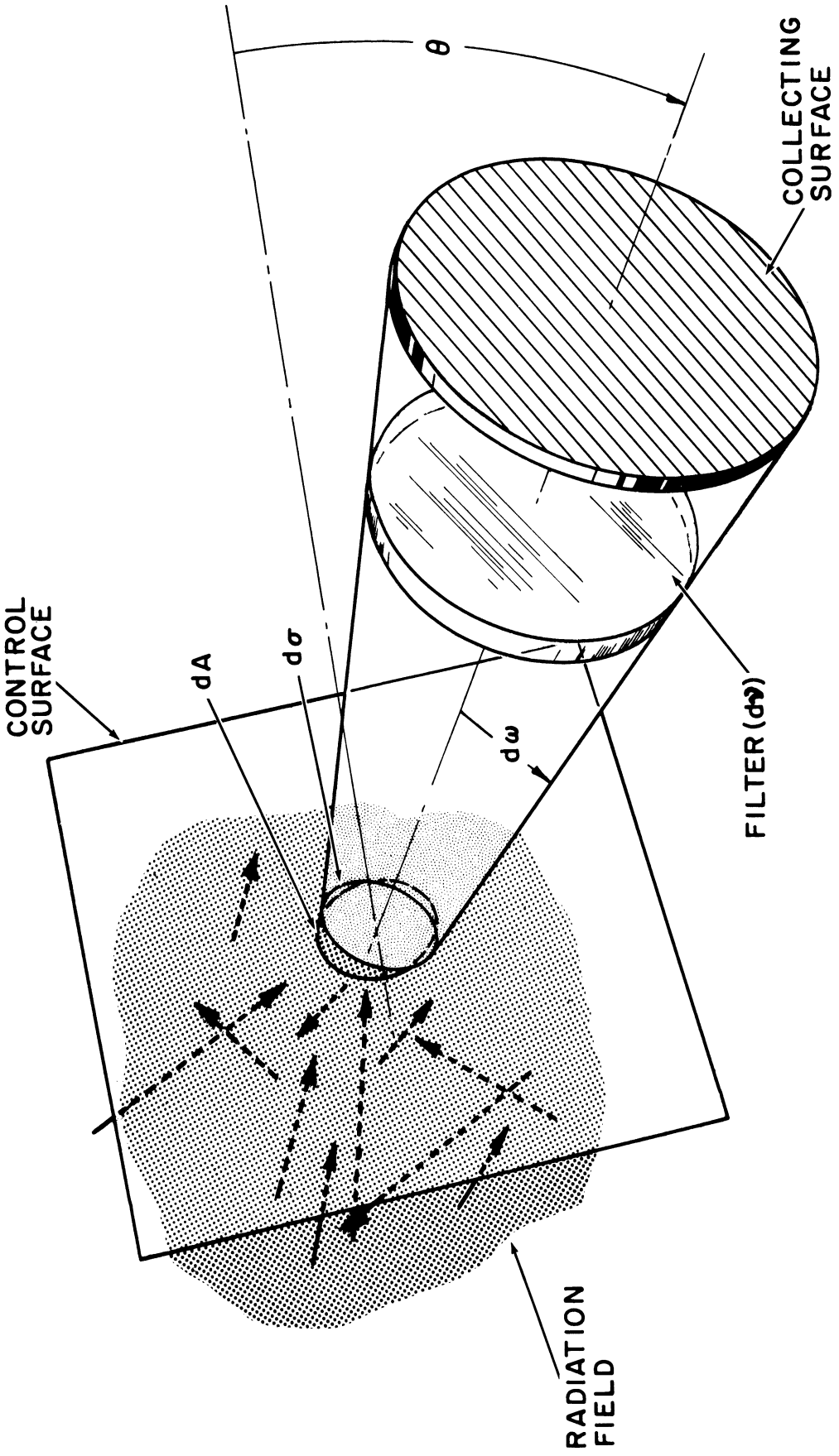

Figure 17. Abstract "machine" for measuring the specific intensity of a radiation field.

dA) is a "Lambert's law radiator"; i.e.,

$$\frac{dE_\nu / dt\, d\nu\, d\omega}{dA\, \cos\theta} = I_\nu \quad ; \quad I_\nu \neq I_\nu(\theta). \tag{V.2}$$

For surfaces which are themselves emitters, the terms luminance or surface brightness are often applied to I_ν.

Measurements of the energy emitted by radiating sources are carried out with systems which measure I_ν or integrals of I_ν over one or more of the variables t, ν, σ, and ω. Therefore the principal task of a theory of radiative transfer through a gas is to predict the I_ν which is ultimately to be seen by the measurement apparatus. In the following sections we discuss the theory which is appropriate to the spectroscopic experiments usually performed in the Michigan shock tube. The prominent features in the emission spectrum of the shock tube gas are the isolated lines of atoms and molecules.

3. SOLUTIONS OF THE RADIATIVE TRANSFER EQUATION

Consider a gaseous volume element whose length along the line of sight is ds. Over this length, the rate of change of the specific intensity I_ν at a frequency ν associated with the atomic emission transition $i \to j$ is

$$\frac{dI_\nu}{ds} = \left[n_i A_{ij} - I_\nu (n_j B_{ji} - n_i B_{ij}) \right] h\nu\, P(\nu), \tag{V.3}$$

where n_i is the number of atoms per unit volume in the state i, and $P(\nu)$ is the "shape function" of the spectral line.

$$\int_0^\infty P(\nu)\, d\nu = 1.$$

A_{ij}, B_{ji}, and B_{ij} are the Einstein coefficients for spontaneous emission, absorption, and induced emission, respectively, defined in terms of intensity. The relations among these quantities are

$$\frac{c^2}{2h\nu_{ij}^3} g_i A_{ij} = g_j B_{ji} = g_i B_{ij}, \qquad (V.4)$$

where g_i is the degeneracy of the state i of energy E_i, and $h\nu_{ij} = E_i - E_j$. We assume that the spectral lines are narrow, so that $\nu \simeq \nu_{ij}$ except when expressions involving the line shape $P(\nu)$ are to be evaluated. For convenience, Equation (V.3) considers the induced emission as "negative absorption."*

The Einstein relations (V.4) are derived by imagining the medium to be in complete thermodynamic equilibrium, so that

$$\frac{dI_\nu}{ds} = 0, \qquad (V.4)$$

the atomic levels are populated according to Maxwell-Boltzmann statistics,

*Many authors use the original Einstein coefficients $\mathcal{A}$, $\mathcal{B}$ defined in terms of the radiation energy density u_ν. In this representation, the analogue to (V.3) is

$$\frac{du_\nu}{dt} = \left\{ n_i \mathcal{A}_{ij} - u_\nu \left(n_j \mathcal{B}_{ji} - n_i \mathcal{B}_{ij} \right) \right\} h\nu\, P(\nu),$$

where $\mathcal{A} = 4\pi A$ and $\mathcal{B} = cB$.

$$g_i n_i = g_j n_j e^{-h\nu_{ij}/kT} \tag{V.5}$$

and the specific intensity is equal to the Planck expression for black body radiation,

$$B_\nu(T) = \frac{2h\nu^3}{c^2} \frac{1}{e^{h\nu/kT} - 1} \cdot \tag{V.6}$$

Making these substitutions in the equation of transfer (V.3), one finds a relation between the Einstein coefficients and the temperature. However, the coefficients are required to be independent of the thermodynamic state and characteristic only of the radiating species. This circumstance is allowed only by the set of relations (V.4).

With the Einstein relations in hand, one can show that the only radiation field capable of maintaining the equilibrium population of states (V.5) is exactly the Planck function (V.6) of the same temperature. However, in many light sources, the state occupations are determined by mechanisms other than radiative excitation, such as electron collisions. The radiation field may then be regarded as a non-interfering probe with which an observer may deduce the properties of the source along the line of sight. Such sources are said to be in a condition of <u>local thermodynamic equilibrium</u>. This concept was first introduced by K. Schwarzschild in 1906.[97] One retains the description of state occupations given in Equation (V.5) and solves the equation of transfer (V.3) subject to this constraint. Doherty has examined the validity of this procedure

for the case of the shock tube, particularly for the partially ionized gas behind the reflected shock.[35] He finds that this description is correct for the customary experimental conditions, and we will assume it so in the development which follows. Essentially, the assumption is justified by the number density and temperature of the electron gas and the cross sections for collisional excitation of atoms by electrons. A similar conclusion has been made by Keck, Camm, Kivel and Wentink (AVCO) for their shock tube studies of diatomic molecule spectra.[98]

Assuming local thermodynamic equilibrium, the equation of transfer may be written

$$\frac{dI_\nu}{ds} = \kappa'_\nu \left[B_\nu(T) - I_\nu \right] \tag{V.7}$$

where

$$\left.\begin{aligned} \kappa'_\nu &= \kappa_\nu \left(1 - e^{-h\nu/kT}\right) \\ \text{and} \\ \kappa_\nu &= n_j B_{j'} \, h\nu \, P(\nu) \end{aligned}\right\} \tag{V.8}$$

κ'_ν is the ordinary absorption coefficient (κ_ν) corrected for the stimulated emission from the significantly populated upper level. Following Ladenburg,* it is customary to express the total absorption coefficient due to a transition as some fraction f of the absorption coefficient of

*We again recall the discussion in Section 2, Chapter I.

a classical electron oscillator; i.e.,

$$\int k_\nu d\nu / n_j \stackrel{d}{=} f_{ji}\, \pi e^2/mc \qquad (V.9)$$

where e and m are the charge and mass of an electron. This number f is variously called the oscillator strength, the f-value, the f-number, or the number of dispersion electrons effective in the transition. Its relation with the Einstein coefficients is given by

$$f_{ji} = B_{ji}\, h\nu mc/\pi e^2$$

In terms of the quantum theory of atomic transitions,

$$g_j f_{ji} = \frac{8\pi^2 m\nu}{3e^2 h} \sum |(\psi_i, \mathbb{P} \psi_j)|^2, \qquad (V.10)$$

where we understand the sum-of-the-squares of the matrix elements to extend over both sets of magnetic substates (m,m') for the levels involved; i.e., our labels (i,j) include the angular momenta (J,J') of the levels which are degenerate in (m,m'). Except for a few cases, the matrix elements cannot be accurately computed because the radial wave functions are not known. Thus the gf-values must be found experimentally; this is exactly the task we undertake in Chapter VI. The measurement of absolute gf-values is often uncertain because of the difficulties in determining the absolute abundance of the atoms in many spectroscopic sources. As a result, one sometimes measures relative gf-values for a set of lines, one line being given some arbitrary value in hopes that

the absolute scale will be fixed in the future.*

For the general case of plane parallel radiation through the half-space $s = x \geqslant 0$, the transfer Equation (V.7) has the solution

$$I_\nu(x) = I_\nu^\circ \, e^{-\int_0^x \kappa'_\nu(\xi)\,d\xi} + e^{-\int_0^x \kappa'_\nu(\xi)\,d\xi} \int_0^x d\eta \, \kappa'_\nu(\eta) \, e^{\int_0^\eta \kappa'_\nu(\xi)\,d\xi} \, B_\nu(T(\eta)). \tag{V.11}$$

where I_ν° is the specific intensity imposed at $x = 0$ by an external radiation field. If the gas is uniform, this equation becomes

$$I_\nu(x) = I_\nu^\circ \, e^{-\kappa'_\nu x} + B_\nu(T)\left(1 - e^{-\kappa'_\nu x}\right)$$

For a zero-temperature medium,

$$I_\nu = I_\nu^\circ \, e^{-\kappa_\nu x}$$

this is sometimes referred to as Beer's Law. In shock tube emission spectroscopy, the source can usually be considered as uniform, and there is generally no radiation imposed from outside the gas. The specific intensity of radiation emerging normally from the gas is then

$$I_\nu(\ell) = B_\nu(T)\left(1 - e^{-\tau'_\nu}\right), \tag{V.11}$$

*It is easily seen that the gf-value of a line is symmetric in the initial and final states, whereas the f-value alone is not. Hence the gf-value (or, equivalently, the "line strength" S of Condon and Shortley[32]) is now in common use. S is just the sum alone in Equation (V.10)

where

$$\tau_\nu' = \kappa_\nu' \ell \tag{V.12}$$

is called the optical depth of the gas at the frequency ν, and ℓ is the actual thickness of the gas sample. Since $0 \leqslant \tau_\nu' \leqslant \infty$, the specific intensity of this source can never exceed the brightness of a black body at the temperature of the source. This may also be seen directly from the equation of transfer (V.7) by setting $I_\nu = B_\nu(T)$.

If the gas volume is viewed at an angle θ with respect to the normal of the surface $x = \ell$, the specific intensity is

$$I_\nu(\ell, \theta) = B_\nu(T)\left(1 - e^{-\kappa_\nu' \ell \sec\theta}\right)$$

The angular dependence of I_ν is in principle important in treating the radiant energy collected from a source by an optical system of appreciable aperture, since the optical depth is different for each ray. In the case of normal viewing, the optical depth is greatest for the extreme rays, but the effect on the specific intensity does not exceed 2-1/2% for a polar acceptance angle of 13°. This angle is typical of the systems used to conduct the radiation measurements described in Chapter VI. The probable error of these intensity measurements is more of the order of 5%, and the smaller angular effects will not be further pursued here.

4. OPTICALLY THIN SOURCES; TEMPERATURE MEASUREMENT

A source is said to be optically thin at a frequency ν if

$$\tau_\nu' \ll 1$$

In this case, Equation (V.11) becomes simply

$$I_\nu = \tau_\nu' B_\nu(T) = \kappa_\nu' B_\nu(T) \ell ;$$

i.e., the specific intensity increases linearly with the actual thickness of the source as long as the source is not optically thick enough to absorb its own radiation. Equivalently, one may speak of the radiative mean free path* $(1/\kappa_\nu')$ as being much greater than the thickness of the source in this case. By means of Equations (V.4-6, 8-10), the specific intensity may be re-written as

$$I_\nu = n_i A_{ij} h\nu \ell P(\nu). \qquad (V.12)$$

This is indeed the result which one would have derived in the beginning, had only the total spontaneous emission into a unit solid angle been considered.

---

*The analogy with kinetic theory may be further extended by ascribing to κ_ν' a cross section

$$\sigma_\nu' = \frac{\pi e^2}{mc} f_{ji} P(\nu) \left(1 - e^{-h\nu/kT}\right)$$

where

$$\kappa_\nu' = n_j \sigma_\nu'$$

For a spectral line in which the optical depth is much less than 1 throughout, the integrated intensity is

$$I \stackrel{d}{=} \int I_\nu \, d\nu = n_i A_{ij} h\nu \ell$$

$$= \frac{n_i}{g_i} g_j f_{ji} \frac{2\pi e^2 \nu^2}{mc^3} h\nu \ell \, .$$

(V.13)

Setting the wavelength $\lambda = c/\nu$, and writing $n_i = (n/Z) g_i \, e^{-E_i/kT}$, where n is the total number density and Z the partition function for the atomic species under consideration,

$$I = \frac{2\pi h e^2 \ell}{m} \frac{n}{Z} \frac{g_j f_{ji} \, e^{-E_i/kT}}{\lambda^3} \, . \qquad \text{(V.14)}$$

If the spectrum of a source contains many emission lines of a certain element, and if the relative gf-values, gf_r, for these lines are known, then Equation (V.14) may be applied to the measurement of the excitation temperature T. All that is required for this determination is the measurement of relative integrated intensities I_r. The temperature T is determined by plotting E_i vs. $\log_{10} (I_r \lambda^3 / gf_r)$; i.e.,

$$T(^\circ K) = 5041 \left(E_i^n - E_i^m\right) \Big/ \log_{10}\left(\frac{I_r \lambda^3}{gf_r}\right)_m - \log_{10}\left(\frac{I_r \lambda^3}{gf_r}\right)_n \, ,$$

(V.15)

where E_i is in electron-volts, and the letters n,m,... label the various

observed spectral lines. This method of data reduction is very useful for two reasons. A non-Boltzmann distribution is indicated by any departure from a linear relation between the plotting variables, and the temperature describing a Boltzmann distribution is given simply by the slope of a straight line. In Section 8 of Chapter VI, we will describe such temperature measurements for neutral chromium and the way in which they depend on the reliability of the set of gf-values employed.

5. EFFECTS OF SELF-ABSORPTION AND LINE SHAPE ON THE INTEGRATED INTENSITY; THE CURVE OF GROWTH

Though it is desirable, it is not always possible to generate and study spectral lines in the optically thin condition. If the minimum intensity required for detection by a certain measurement apparatus is, say, 1/2 the brightness of a black body at the source temperature, then by Equation (V.11) the optical depth must be at least as large as 7/10 for the line to be seen at all. One might try to avoid this by increasing the source temperature to a point where a line could be detected if its optical depth were only 1/10, but this could imply such extreme ionization of the element of interest that the evaluation of the amount of un-ionized residue would become quite uncertain. Any attempt to suppress the fractional ionization by increasing the absolute atomic abundance would lead to an increase in optical depth. The existence of appreciable optical thickness over some portion of a spectral line complicates the treatment of the integrated intensity which, by virtue of finite resolution, is often the only spectrophotometric observable. The rest

of this chapter is devoted to a discussion of the dependence of the integrated intensity on the details of the spectral line shape.

The normalized "shape function" $P(\nu)$ was introduced in Equation (V.3) in order to take phenomenological account of the various line-broadening mechanisms. In a great many cases, $P(\nu)$ is a convolution of functions of the forms $e^{-k_1(x-x_0)^2}$ and $k_2/[k_2+(x-x_0)^2]$, the first form arising from thermal Doppler broadening, and the second from what are called <u>damping</u> or <u>dispersion</u> effects. These latter names stem from the rôle of damping in the classical electron-oscillator theory of optical dispersion. We may write

$$P(\nu) = H(a,b)\Big/\sqrt{\pi}\,\Delta\nu_D \ ,$$

$$H(a,b) = \frac{a}{\pi}\int_{-\infty}^{+\infty}\frac{e^{-x^2}\,dx}{a^2+(b-x)^2} \ , \qquad \text{(V.16)}$$

$$a = \Delta\nu_S/\Delta\nu_D \ , \quad b = \frac{\nu-\nu_0}{\Delta\nu_D} \ , \quad \Delta\nu_D = \nu_0\sqrt{\frac{2RT}{\sigma c^2}} \ ,$$

where $\Delta\nu_D$ is the 1/e half-width of the Doppler profile, and $\Delta\nu_S$ is the 1/2 half-width of the dispersion profile. Also, R is the gas constant per mole, σ the molecular weight of the radiating atom, c the velocity of light, and ν_0 the frequency at the line center. The finite lifetimes of atomic states contribute a damping width $\Delta\nu_S \sim 10^7$ sec^{-1} which, in shock tube experiments, is usually small compared to the damping widths arising from other causes. These last are discussed in detail in Sec-

tion 6.

The function H(a,b) has been investigated by many authors, the most recent being Penner and Kavanagh[99] to whose article the reader is referred for details and references to earlier computations. It can be shown that

$$H(a,b) = \mathcal{R}\left\{ e^{(a+ib)^2} \frac{2}{\sqrt{\pi}} \int_{a+ib}^{\infty} e^{-z^2} dz \right\}$$

i.e., it contains the error function of complex argument. At the line center, $\nu = \nu_0$ and b = 0; therefore

$$H(a,0) = e^{a^2} \operatorname{erfc}(a)$$

gives the a-dependence of the central line intensity. Values of H(a,0) are listed in Table VII

TABLE VII

CENTRAL LINE INTENSITY FOR THE VOIGT FUNCTION

a:	0	0.2	0.5	1.0	1.5	2.0	2.5
H(a,0):	1.000	.8090	.6157	.4276	.3216	.2555	.2124

For $a \ll 1$, the Doppler effect is dominant and $H(a,0) \sim 1$, while for $a \gg 1$ the damping effects are the most important and H(a,0) is diminished.

The optical depth may now be written as

$$\left.\begin{aligned} \tau_\nu' &= C\,H(a,b), \\ C &= \frac{\pi e^2}{mc}\, n_j f_{ji}\, \ell \left(1 - e^{-h\nu/kT}\right) \frac{1}{\sqrt{\pi}\,\Delta\nu_D} \end{aligned}\right\} \qquad (V.17)$$

The specific intensity is

$$I_\nu = B_\nu(T)\left(1 - e^{-C\,H(a,b)}\right), \qquad (V.18)$$

and the integrated intensity is

$$I \cong B_{\nu_{ij}}(T) \int_{-\infty}^{\infty} \left(1 - e^{-C\,H(a,b)}\right) d\nu$$

$$= B_{\nu_{ij}}(T) \cdot 2\Delta\nu_D \int_0^{\infty} \left(1 - e^{-C\,H(a,b)}\right) db. \qquad (V.19)$$

It is customary to define the equivalent width W_ν by

$$W_\nu = I \,/\, B_{\nu_{ij}}(T). \qquad (V.20)$$

W_ν can be interpreted as the full width (in frequency units) of a fictitious spectral line containing the same energy as the actual line and having a uniform intensity equal to the Planck function of the emitting gas. Comparing the equivalent width to the full 1/e Doppler width, we may write

$$\mathcal{J}(C,a) \equiv \frac{W_\nu}{2\Delta\nu_D} = \int_0^{\infty} \left(1 - e^{-C\,H(a,b)}\right) db. \qquad (V.21)$$

The function $\mathcal{J}(C,a)$ has been computed and graphed by v.d. Held[100] up to a = 0.5 and extended by Penner and Kavanagh[99] to a = 10. Figure 18 summarizes these results in the curve of growth form; i.e., $\mathcal{J}(C,a)$ is plotted vs. $\log_{10} C$ for different values of the parameter a. For C sufficiently small, the curve is linear with slope 1; this is equivalent to the previous result of the optically thin analysis. However for C sufficiently large, $\mathcal{J}(C,a)$ is proportional to $C^{\frac{1}{2}}$ and its absolute value depends on the details of the line shape through the parameter a.

6. FURTHER DISCUSSION OF THE CURVE OF GROWTH

In order to illustrate the uses and consequences of these curves, we have also shown in Figure 18 some representative points for the neutral chromium resonance line at 4254 Å ($z^7P^o_4 \rightarrow a^7S_3$). The most recent* intensity measurement on this line was made by Ostrovskiĭ and Penkin[101] in 1957. Their f-value is 0.15, which is equivalent to

$$gf\,(Cr\,I\;\lambda 4254) = 1.05$$

Using this number and the CrI ionization function given in Appendix A, we have computed the quantity C for T = 10,000°K and various chromium abundances. The length of the source ($\mathcal{L}$) was taken to be 4.13 cm, the horizontal width of the luminous shock tube.

The abundances are specified on the graph in terms of p^o(CrI), the

*We learned of this measurement through Dr. Edith A. Müller of the Astronomy Department, The University of Michigan. We are grateful to Dr. Müller for several informative discussions of line-intensity data.

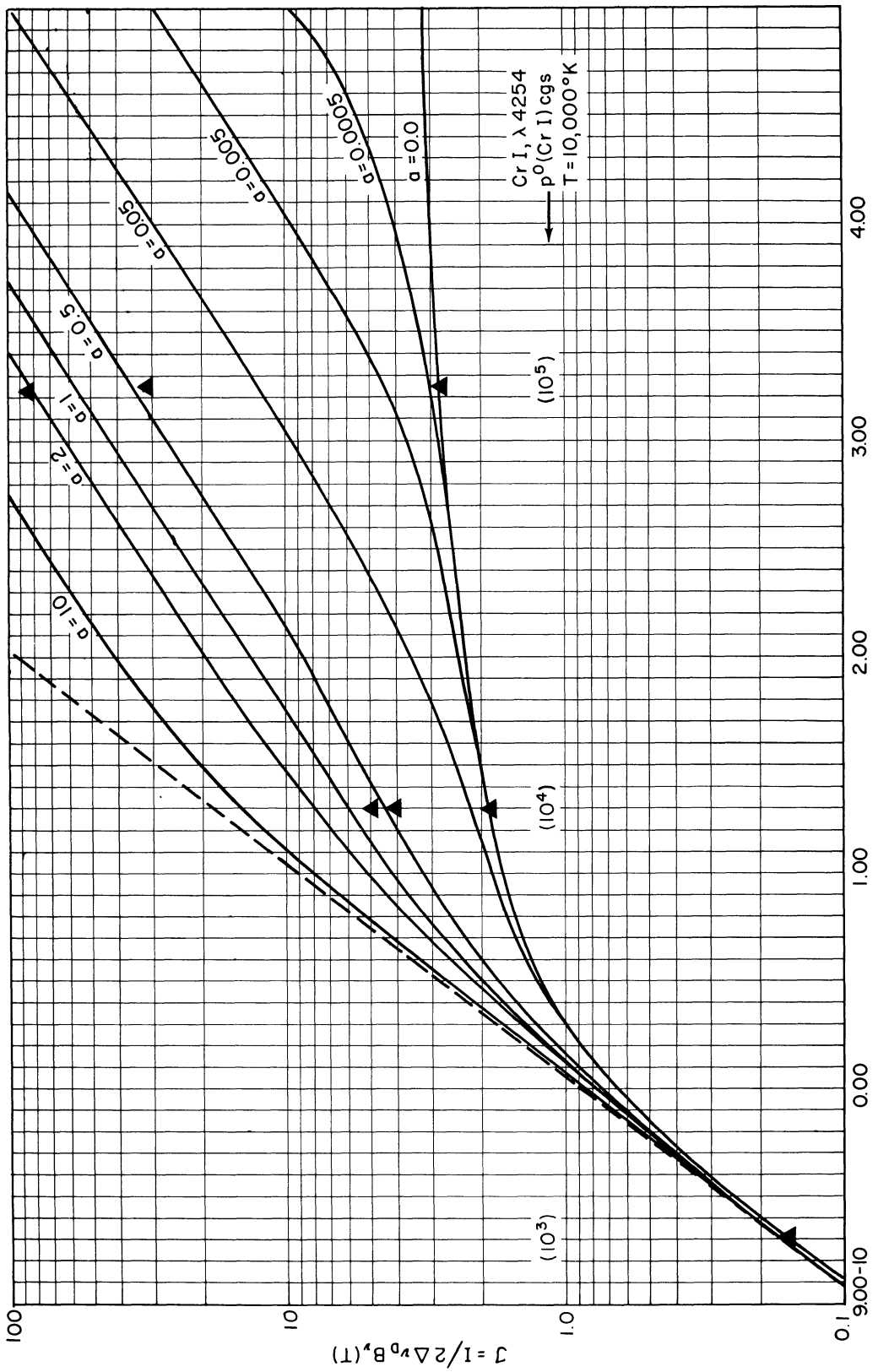

Figure 18. Curves of growth, with representative points for one of the chromium resonance lines in an idealized case.

pressure of chromium (in dynes/cm^2) if no ionization were allowed to take place. The computed quantities are given on the next page in Tables VIII and IX. The extreme degree of ionization (α) is worthy of note here. For this example, the dependence of α on the abundance is such that a ten-fold increase of p^o leads to approximately a hundred-fold increase in the amount of residual neutral chromium.

Given the values of C computed from Table IX, the placement of the points on the various curves of growth depends on assumptions about the line shape. In the case of no damping effects (i.e., pure Doppler broadening) all of the points lie on the lowest of the curves, a = 0.

TABLE VIII

IONIZATION EQUILIBRIA AT 10,000°K FOR CrI ALONE

$CrI \rightleftarrows CrII + e$; $f(10^4\ °K) = 1.52 \times 10^6$ cgs

$p(CrI) = (1-\alpha)\ p^o(CrI)$; $p = nkT$

$p^o(CrI)$ (cgs)	$\alpha(CrI)$	$n(CrI)$ (cm^{-3})	$p(CrI)$ (cgs)	$n(CrII)$ (cm^{-3})
10^3	.99934	4.78×10^{11}	0.66	7.24×10^{14}
10^4	.9935	4.71×10^{13}	65.0	7.20×10^{15}
10^5	.942	4.20×10^{15}	5800.	6.82×10^{16}

The points above this curve (i.e., for $p^o = 10^4$ and 10^5 cgs) have been computed for the damping effects to be expected when this line is excited in an atmosphere of hot un-ionized neon and partially ionized

TABLE IX

THE FACTORS OF C

$$C = \frac{\pi e^2}{mc} \eta_j f_{j'i} \ell \left(1 - e^{-h\nu/kT}\right) \cdot \frac{1}{\sqrt{\pi}\, \Delta\nu_D} .$$

CrI(λ4254): gf = 1.05 ℓ = 4.13 cm, T = 10,000°K

$\Delta\nu_D$ = 42.0×10^8 sec^{-1}	$\Delta\lambda_D$ = 2.54×10^{-2} Å
$\pi e^2/mc$ = 2.66×10^{-2} cm^2/sec	$(1-e^{-h\nu/kT})$ = .966
n_j = g_j n(CrI)/Z(CrI, 10^4 °K)	Z = 33.54
C = .310 p(CrI), if p is in dynes/cm^2	

chromium. The lowest pair of points (both on the curve a = .45) corresponds to the damping from neon-on-CrI collisions. The highest pair (on different a-curves) includes this damping plus the contribution of the quadratic Stark effect due to the presence of ions and electrons. The coefficients governing these effects are not well known for CrI. Using reasonable estimates from experiments on other elements, we have computed the points by means of the simple theories of collision damping. (See Aller,[91] Chapter 8, and Unsöld,[89] Sections 75 through 82.)

The average time t between neon collisions on CrI is given by

$$\frac{1}{t} = \pi \bar{r}^2 n \bar{v} \qquad \text{(V.22)}$$

where n is the number density of neon atoms, and $\bar{r}$ is the effective collision diameter for neon collisions with CrI in the particular electronic

state of interest. v is the average relative velocity in such a collision and is given by

$$v = \sqrt{\frac{8RT}{\pi}\left(\frac{1}{\sigma(Ne)} + \frac{1}{\sigma(Cr)}\right)} \qquad (V.23)$$

where σ is molecular weight. A typical number density for our shock tube experiments is

$$n(Ne) = 2 \times 10^{18} \text{ cm}^{-3} ,$$

and the relative speed at 10,000°K is

$$v = 3.82 \times 10^{5} \text{ cm/sec.}$$

The collision diameter is chosen to be

$$\bar{r} = 7 \text{ Å} .$$

Values of this order are typical* for the resonance lines of metallic atoms diluted by inert atompsheres. By Equations (V.16) and (V.22), we compute the 1/2 half-width of the collision damping profile to be

$$\Delta\nu_S = 1/2\pi t = 18.7 \times 10^{8} \text{ sec}^{-1} .$$

The line shape parameter is therefore

$$a = \Delta\nu_S/\Delta\nu_D = .45 ,$$

*For example, Schütz[102] found $\bar{r}$ = 6.15 Å for the sodium D lines excited in neon. Hinnov and Kohn[34] have recently measured $\bar{r}$ = 6.6 Å for CrIλ4254 as broadened by collisions with N_2.

where $\Delta\nu_D$ is given in Table IX. This number is independent of the chromium abundance and thus describes the middle pair of points on Figure 18 for both $p^o = 10^4$ and 10^5 cgs.

The additional broadening due to the interatomic Stark effect depends on the chromium abundance through the number density of ions and electrons. Assuming the Stark broadening to be quadratic and to be described by the impact theory, the 1/2 half-width of the resulting line profile is

$$\Delta\nu_S = 3.09\, A^{2/3}\, v^{1/3}\, n \qquad (sec^{-1}), \tag{V.24}$$

where n is the number density of charged perturbers, and v is their average velocity relative to the radiating atom. The Stark coefficient A may be written (in cgs units) as

$$A = \Delta\nu\, e^2 / F^2$$

where e is the electronic charge, and $\Delta\nu$ is the observed Stark displacement of the line in the electric field F. Equivalently one may write

$$A = 6.21 \times 10^{-4}\, \Delta\tilde{\nu} / E^2 \tag{V.25}$$

in terms of the electric field E in practical units and the shift in wave number $\tilde{\nu}$. For some visible iron lines of high excitation, the observed Stark displacements are of the order of 10 cm^{-1} in an electric field of 10^5 volts/cm. The corresponding value of A is about 5×10^{-13} cm^4/sec. The effect is generally much smaller for lines arising from deeper levels.

By examining the data for several elements, we estimate the Stark displacement for CrIλ4254, to be no larger than .01 cm^{-1} for an electric field of 10^5 volts/cm; correspondingly,

$$A = 6.21 \times 10^{-16} \text{ cm}^4/\text{sec}.$$

By Equation (V.23), the velocities of perturbers relative to CrI at 10,000°K are

$$v(e) = 6.23 \times 10^7 \text{ cm/sec} \quad \text{for electrons,}$$

$$v(\text{CrII}) = 2.85 \times 10^5 \text{ cm/sec} \quad \text{for chromium ions.}$$

The net broadening effect is given by

$$\begin{aligned} nv^{1/3} &= n(e)v(e)^{1/3} + n(\text{CrII})v(\text{CrII})^{1/3} \\ &= (397 + 65.8)\, n(\text{CrII}) \\ &= 463\, n(\text{CrII}). \end{aligned}$$

With these values and the number densities given in Table VIII, we compute

$$\Delta\nu_s = 7.50 \times 10^8 \text{ sec}^{-1} \quad \text{for } p^o = 10^4 \text{ cgs},$$

$$= 71.0 \times 10^8 \text{ sec}^{-1} \quad \text{for } p^o = 10^5 \text{ cgs}.$$

Adding these half-widths to the collision damping value for neon collisions, and dividing by the Doppler width, the corresponding line shape parameters are, respectively,

$$a = .624 \text{ and } a = 2.14$$

It is these values which are associated with the uppermost points at the two abundances of interest in Figure 18.

For spectral lines of C-value greater than 2, the strong effect of damping on the equivalent width can be a complicating factor in the interpretation of intensity measurements. Such measurements are usually made on a set of lines in order (1) to derive (from their C-values) either the conditions of the source or gf-values for the lines, or (2) to check previous assumptions about these quantities. For lines of equivalent width $W_\nu > 2\Delta\nu_D$, the data are the most useful only when the damping effects are known for each line. This information is not available for many elements of interest. The difficulty can be serious for $W_\nu \geqslant 4\Delta\nu_D$ and for sets of lines which originate from a wide range of energy levels.

For lines arising from similar levels, the optical collision diameters and Stark coefficients may be similar. Thus the same (but perhaps unknown) damping factor may roughly apply to all the lines. Some information about the source can be derived by matching the observed intensities with a theoretical curve of growth.* If the conditions of a spectroscopic source are well known, then the curve-of-growth can be used to evaluate the damping effects. In any case, this method of data reduction serves to systematize the information contained in a line spectrum.

*See Goldberg[36] et al., for many examples of solar curves of growth.

Considerable use may be made of the "forbidden regions" of Figure 18. These are the regions below the pure Doppler broadening curve and above the dashed line which is the limiting curve for large values of a.* If measured values of $\mathcal{J}$ and computed values of C conspire to place a data point in either of these regions, then it is a clear sign that the conditions of the source or the strength of the spectral line are not correctly understood. Conversely, if a source is well known, one may derive bounds on the gf-value for a line by observing what bounds are placed on C by the measured intensity. The lower the line intensity, the better is this method. For lines of equivalent width $W_\nu = \Delta\nu_D/2$, the admissible range of $\log_{10}$ C is about .045, and the gf-value can in principle be determined with 10% accuracy. Hinnov and Kohn[34] have applied a related method to f-value measurements on metallic lines emitted from flames. They find, for example, that the f-value for CrIλ4254 must be greater than 0.011. This result allows not only the Ostrovskiĭ and Penkin value of 0.15 but also Estabrook's value[103] of 0.084; the Huldt and Lagerqvist[104] result (0.00097) is ruled out.

In Chapter VI, we will describe absolute line intensity measurements for CrI and CrII. Since the shock tube theory also gives absolute abundances of these species, the curve of growth then reads to absolute gf-values by the means discussed above.

*This dashed line also represents the previous Equation (V.14) for the optically thin, or pure spontaneous emission, case. For a fixed value of C, an unlimited increase in a so broadens the line that it becomes optically thin in all frequencies. The corresponding diminution of $\tau'_\nu = CH(a,b)$ at the line center (b = 0) is illustrated in Table VII.

CHAPTER VI

RADIATION EXPERIMENTS ON NEUTRAL AND SINGLY IONIZED CHROMIUM

1. INTRODUCTION

This chapter describes the study of chromium spectra emitted from the gas behind the reflected shock. The emission was generated in a controlled manner by the addition of small partial pressures of chromium carbonyl to the neon carrier gas. Absolute line intensities were measured by the procedures of heterochromatic photometry, and the thermodynamic state of the radiating gas was computed by the methods of Chapter II. The radiative and thermal data were compared by means of the theory discussed in Chapter V. Absolute gf-values were measured for the lines of several CrI multiplets which have upper excitation potentials between 3.3 and 5.8 ev and wavelengths between 4500 and 5000 Å. Also, gf-values were found for the lines of two CrII multiplets in the save wavelength range.

Experimentally, the central problem has been to take calibrated photographs of the shock tube spectrum over a range of chromium abundance sufficiently low to avoid strong effects of self-absorption. The recording of faint spectral lines was made possible by a large aperture, time-resolving spectrograph designed by George Charatis[105] and briefly described here in Section 2. The calibration technique enabling the shock tube spectrograms to be reduced to relative line intensity was developed by Lowell Doherty[35] from the photometric methods of G.R. Har-

rison.[106] The present author has extended this technique to include the use of a primary radiation standard external to the shock tube. In Section 3, we describe the methods of image formation employed with the shock tube and the calibrating light sources. Section 4 discusses the problem of film calibration per se; i.e., finding the relations between the blackening of images and the light intensities responsible for the images.

In Section 5, we review some of the x-t photographic data for the chromium experiments. This material is treated here rather than in Chapter III because the present additive ($Cr(CO)_6$) is a much more effective perturber of the hydrodynamic variables than any of the additives previously discussed. We also discuss here the fast ionization-relaxation process observed behind the reflected shock. That this process does occur and rapidly leads to steady line intensities argues strongly for the assumption of thermal equilibrium in the final state. The various lines of CrI and CrII (and bands of CrO) recorded in survey spectra are given in Section 6. Sections 7 and 9 describe the data analysis and results of the quantitative line intensity measurements on CrI and CrII.

The set of gf-values given for CrI differs markedly from the set of relative values previously published by Hill and King.[46] The systematic increase of the discrepancy with excitation potential indicates a temperature error in the previous measurements (see Section 8). Additional evidence supporting our set of gf-values for CrI is drawn from studies of emission lines in laboratory sources and absorption lines in the solar

atmosphere. To our knowledge, the gf-values given for two multiplets of CrII are the first to be measured for this ion.

2. SPECTROGRAPH

Figure 19 shows the over-all arrangement used in recording the shock tube emission spectrum. During an experiment, the room is darkened except for two dim running lights, the spectrograph box is covered with a light-tight plate, and the camera is draped with black cloth. By means of the "external optics" the spectrograph views the gas through the back window of the tube, allowing x-t photographs to be taken through the unobstructed front window. The external optics will be described in Section 3, since they are arranged to satisfy certain requirements on the illumination of the slit and grating of the spectrograph. We also use this arrangement to take spectrograms of a carbon arc and a xenon flash lamp; these auxiliary light sources are discussed in Section 3.

With any source, the light which enters the spectrograph slit is rendered parallel by the collimating lens (34.5" f.l. achromat), diffracted at the reflection grating (30,000 lines/inch, Bausch and Lomb) and focused by the camera lens (f/5.6, 21" f.l. telephoto) onto the moving film inside the rotating drum housing. The reduction factor from slit to slit-image is about 1.7 and the dispersion of wavelength is 13 Å/mm in first order. Charatis discusses the construction and performance of the spectrograph in his dissertation.[105] A highly desirable feature of this instrument is its "speed"; the effective camera lens aperture

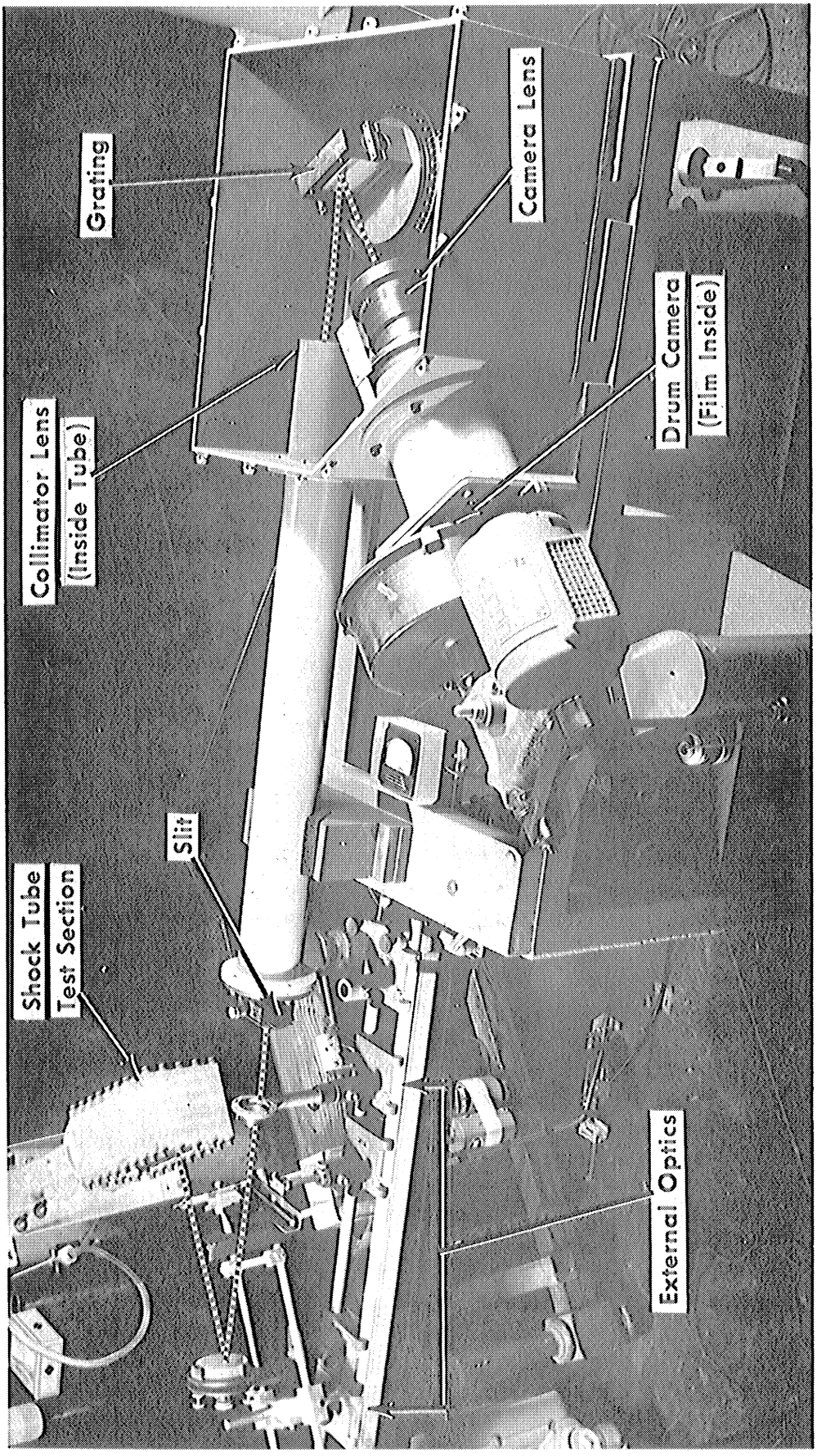

Figure 19. Time-resolving spectrograph viewing the shock tube test section.

defined by the ruled area of the grating is about f/7. The spectrograph was developed following a suggestion by Eugene Turner in 1956 that the instrument then in use (Jarrell-Ash 1.5 meter Ebert, f/19) would not be fast enough for the contemplated studies in the visible and near infrared. Charatis designed the new spectrograph to accomodate many of the Jarrell-Ash mechanical parts as well as a variety of optical elements. The focal curve of this particular camera lens is sufficiently smooth that one can achieve sharp focus on a flat film over any 500 Å interval between 4500 Å and 9000 Å.

Figure 20 shows a side view of the spectrograph cart. At the bottom right is a variable resistance bank of cone heaters for controlling the rotation speeds of the drum cameras. On the left of both shelves is another bank of resistors for controlling the current drawn by the carbon arc. The arc and the cameras are run from the University's 220 DC circuits. The box above the arc resistors houses an ammeter for reading the arc current (~ 11 amperes).

3. LIGHT SOURCES AND METHODS OF ILLUMINATION

To reduce the shock tube spectrograms to absolute line intensity requires the use of auxiliary light sources. We use (1) the anode crater of a carbon arc to expose the film to a known distribution of absolute intensity over the wavelength range of interest, and (2) a xenon flash lamp with a stepped-transmission filter to expose each wavelength region of the film to a known relative intensity distribution. This procedure

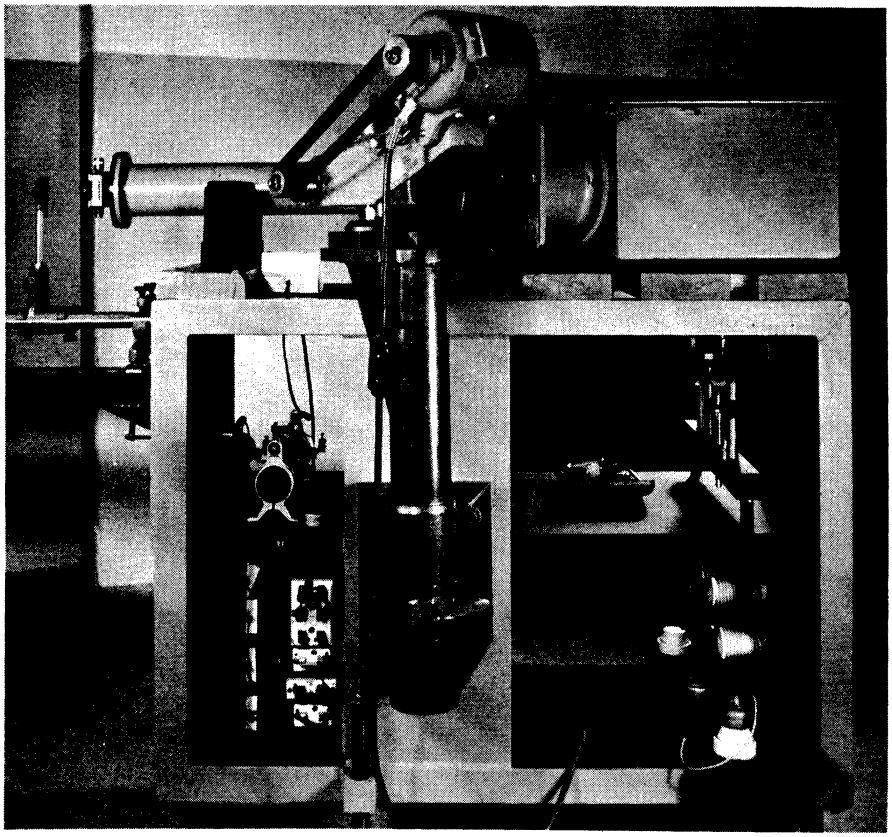

Figure 20. Spectrograph cart with camera mounting and 220 DC control circuits.

leads to the absolute intensities of spectral lines via their intensities relative to the carbon arc; i.e., we use the arc as a primary radiation standard.* This is allowed by the method of spectrograph illumination which will presently be described. The characteristics of the arc and flash lamp are discussed at the end of this section.

The external optics are shown in Figure 21 with the carbon arc in place of the shock tube test section. The arc anode is the 1/4" dia. horizontal electrode which is viewed end-on-end by the optical system. The first lens forms an enlarged image of the anode at the mask, so that only the rays from a 2 mm square in the center of the anode crater can pass into the spectrograph. The second lens forms an enlarged image of the mask on the grating inside the spectrograph, while rendering the illumination in the plane of the slit uniform over a circle which easily covers the maximum possible slit length (14 mm). The same system is used to record the shock tube spectra; i.e., the spectrograph sees only the light emitted through a 2 mm square patch at the boundary of the gas volume, all other light being excluded by the external mask.** Since this mask sharply defines the illuminated portion of the grating, the

*In Doherty's studies of HI, NeI, etc., he used the carbon arc primarily to find the variation of film sensitivity with wavelength. Doherty's primary standard was the Balmer line H_β whose absolute intensity he computed from the known f-value and the shock tube conditions.[35]

**To prevent significant scattering of light into the spectrograph, we also cover the back test section window with a black paper mask which has a dime-sized hole in it at the place of viewing. Two other devices which are commonly used are not shown in Figure 21. A mechanical shutter (duration 1/200 sec) is put in front of the slit to limit the arc exposure to one revolution of the drum camera. A sheet of heat-absorbing glass is put between the arc and the first lens (an achromat). The power dissipation at the arc is in excess of 500 watts, and the resulting heat flux would damage the lens. Since the glass has a definitely bluish tint, it is also put in the optical path during the shock tube exposures to avoid systematic errors in comparing the brightness of the two sources.

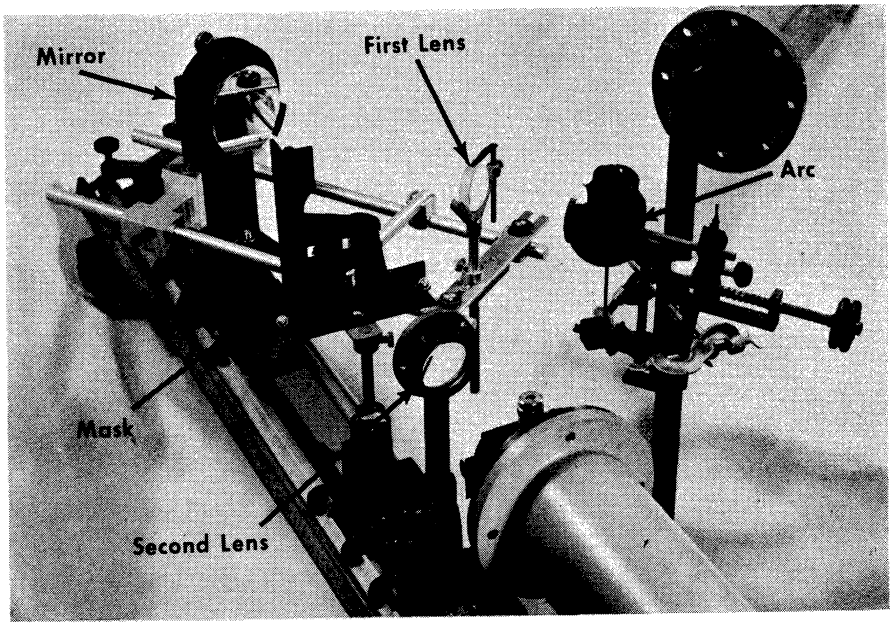

Figure 21. External optics for intensity measurement with time-resolving spectrograph. Carbon arc shown in place of test section.

spectrograph is used at the same f-stop (i.e., the same solid angle of collection by the camera lens) for both the arc and shock tube exposures. The uniform illumination of the slit insures that the luminous flux to the grating is proportional to the open area of the slit. Thus various slit dimensions may be used as needed, with full knowledge of their effects on the film exposure. The length and width of the slit must often be varied to get comparable exposures for the two very different light sources of interest.

Since a moving film is used with both the arc and the shock tube, the slit length is a factor in the exposure of these spectrograms. For any element of film area, the "potential exposure time" Δt is the product of the slit-image length (mm) and the "writing rate" of the drum camera (μsec/mm of film length). Whether or not Δt is also the actual exposure time depends on the duration of the light source. Suppose we set the spectrograph slit length at 3.4 mm and the writing rate of the drum camera at 20 μsec/mm. Because of the reduction factor of 1.7, the length of the slit-image is 2 mm, and Δt is 40 μsec. The resulting profiles of film exposure are illustrated in Figure 22 for three different durations of a pulsed light source. In case A, the source lasts only 10 μsec, and the film is exposed from 0 to 2.5 mm with a blurred snapshot of the slit. This is the sort of "flash" typically seen in a shock tube spectrogram when the zone of reflected shock luminosity rapidly transits the line of sight. In case B the source duration is equal to Δt, and the potential exposure time is taken full advantage of only at the 2 mm posi-

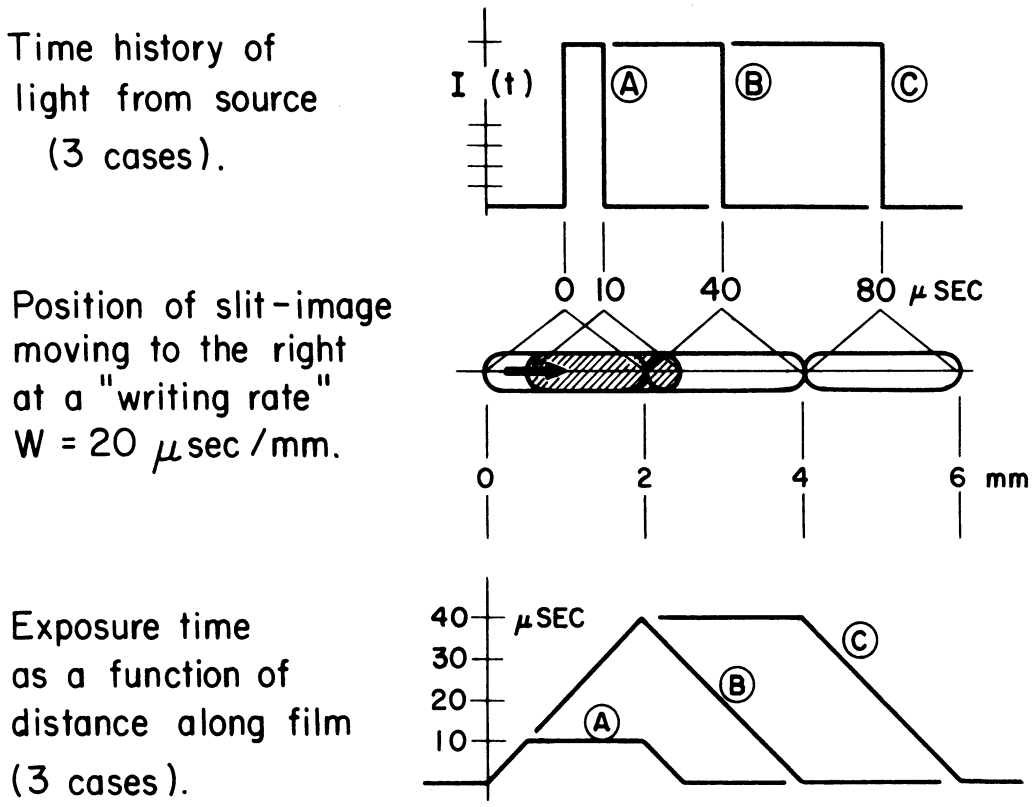

Figure 22. Effects on film exposure arising from duration of light source and relative motion between film and slit-image.

tion on the film. Case C is most generally characterized by saying that Δt is significantly less than the duration of the source, whence the actual exposure time is constant (and equal to Δt) over a significant fraction of the exposed portion of the film. The numbers given for this case in Figure 22 roughly describe the maximum slit length situation we use for spectrograms of the steady state behind reflected shock waves. Shorter slits are often used when the spectral lines are strong enough

to warrant shorter exposure times. One cannot go to much longer slits without spoiling the time resolution, since other light pulses precede and follow the steady pulse (~ 80 μsec in Figure 22) from the gas behind the reflected shock. The use of a $\Delta t \sim 40$ μsec leaves the film between 2 and 4 mm uncontaiminated by the light from the other gas volumes. The carbon arc spectrograms are an extreme case where the necessary exposure times (again ~ 40 μsec) are much less than the duration of the source. For both of these sources, then, the choice of slit length affects the exposure of the spectrograms in a well defined and easily calculated way.

The influence of slit <u>width</u> on film exposure depends on the character of the spectrum. For every wavelength of light, the spectrograph forms a slit-image which has an appreciable extension in the wavelength direction. Thus any given area of the film may be exposed to radiation lying within a "potential bandwidth" $\Delta\lambda$, namely the product of slit-image width (mm) and the dispersion of the instrument (Å/mm). The exposure of each area is proportional to the total radiant energy lying in the associated $\Delta\lambda$. The potential bandwidth increases with slit width, but the exposure increases only if there is radiant energy in the added wavelength interval. Thus the effect of varying the slit width depends on the smoothness of the spectrum near the wavelength of interest. For a source of continuum such as the carbon arc, the energy distribution is practically uniform over typical bandwidths (~ 2Å), and the exposure is therefore proportional to $\Delta\lambda$ to a very good approximation. Thus one

can control the exposure of the arc film by varying the width of the slit as well as its length.

Under the shock tube conditions of interest in this report, the emission spectrum consists primarily of lines which are simultaneously narrow and widely separated compared to the useful bandwidths $\Delta\lambda$. Thus, for all practical purposes, the bandwidth of light reaching a given film area may contain only the radiation belonging to one spectral line; further, the exposure over most of each observed "line" (i.e., slit image) arises from the integrated intensity of the line, rather than the wavelength distribution of intensity within the line. The latter point is illustrated in Figure 23 for the idealized case of a triangular emission line whose basewidth is $\delta(\mathring{A})$ and maximum specific intensity is i. The line is observed with a spectrograph whose slit-image width (again in $\mathring{A}$) is $\Delta\lambda > \delta$. Thus the film is exposed over a band of width $\Delta\lambda + \delta$ in the wavelength direction. Over the central portion of the image, the exposure is uniform and is proportional to the total energy in the line. With increasing slit width (larger $\Delta\lambda$) the width of the central portion grows linearly, but the exposure within it remains the same; there is a corresponding decrease, not in the absolute amount, but in the percentage of the image which is non-uniformly exposed. The profile of exposure becomes essentially rectangular, while the exposure itself is independent of slit width. The additional energy admitted to the spectrograph with a wide slit just goes into a correspondingly wide slit image of the same energy density.

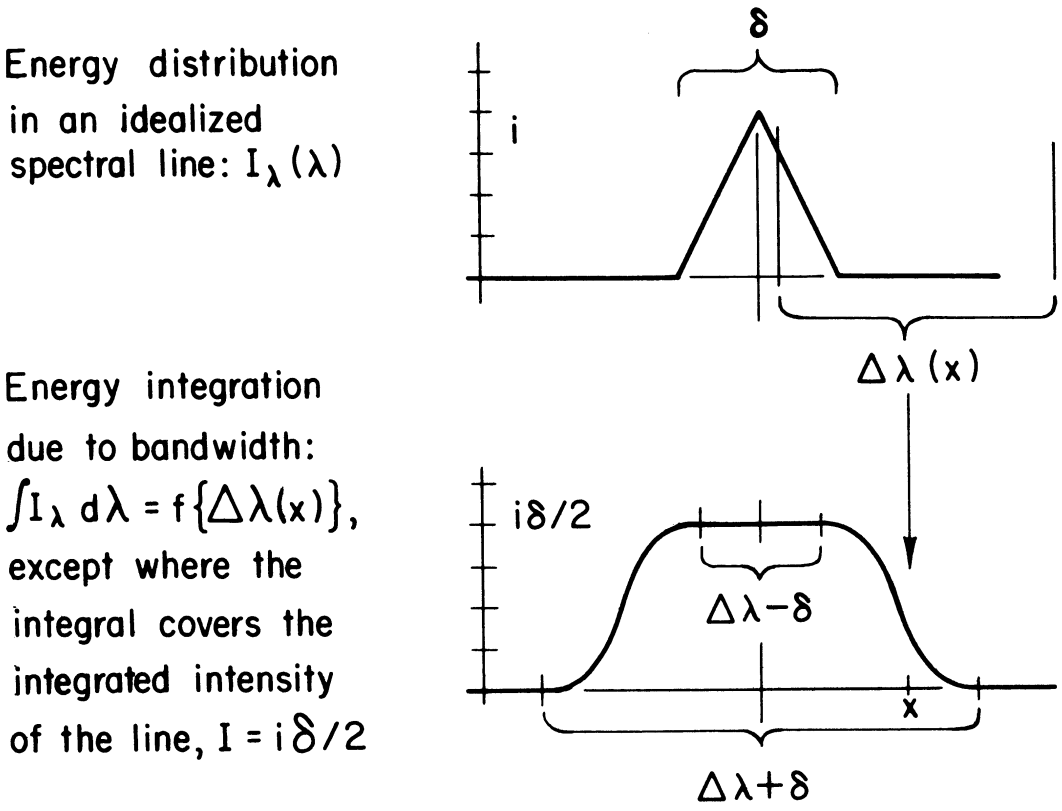

Figure 23. Effect of wavelength integration on observation of a spectral line.

The minimum practicable slit width is limited by what one might call "overall resolution," which is compounded of several factors such as the resolving power of the grating and the average grain size of the photographic emulsion. In performing intensity measurements of emission lines whose shapes can just barely be resolved, it is most advantageous to use a wide slit in order to observe the integrated intensity directly. Short of the intensity profile of the line, the integrated

intensity is, in terms of the radiative transfer theory, the most meaningfully measured quantity (Chapter V). In addition, the Eberhard effect changes the response of the photographic emulsion to light intensity in the vicinity of a steep intensity gradient such as the side of a narrow spectral line; a much more reliable measurement can be made near the center of a wide slit image. For these reasons, wide slits (100 to 500 microns) were used in recording the chromium lines emitted from the shock tube. A given spectrum was considered useful for integrated intensity measurements only if the lines of interest were recorded with the requisite shape, i.e., essentially rectangular profiles (of uniform width $\Delta\lambda$) jutting up from the zero intensity base-line of film. The role of the photographic emulsion will be discussed further in Section 4. The remainder of this section is concerned with our auxiliary light sources.

In addition to the carbon arc, we employ another source and a special filter to calibrate the response of the film to light intensity at each wavelength. A General Electric FT-230 xenon flash lamp* is mounted in front of the external mirror (see Figure 21) and all the intervening optics removed. A rhodium-on-quartz step filter is placed immediately in front of the spectrograph slit. Since the illumination of the slit by the lamp is uniform, and confined to a small solid angle,

*The power supply for the flash lamp discharge is a 2 μfarad capacitor (G.E. Pyranol) charged to 4 KV. The discharge is triggered by an ignition-coil spark across a three-element gap in series with the flash lamp. The resulting light pulse lasts about 100 μsec and has a half-intensity width of 30 μsec. The discharge is essentially critically damped due to its own resistance in both the lamp and the external control gap.

the graded intensity along any slit image is a faithful reproduction of the (known) step-wise variation of transmission by the filter. The film in the drum camera is held stationary for the recording of the flash lamp spectrum. Several such spectra are photographed on one film, the difference between them being the level of light intensity at the film. This is controlled by the choice of slit width for each exposure, since the flash lamp spectrum contains a strong continuum as well as xenon lines. By using a range of slit widths from 50 microns to 2 mm, one can vary the exposure in the continuum by a factor of 40. Another variability factor of about 16 arises from the range of transmission covered by the steps of the rhodium-on-quartz filter. In principle, one could utilize this combination of flash lamp and step filter to find the intensity of one source relative to another that was 600 times as bright. However, any such procedure would be subject to a large probable error because of either shot-to-shot fluctuations in the brightness of the lamp or (avoiding the fluctuation problem) inaccuracies in fitting together an intensity-sequence of many exposures to bridge the gap between the two sources. To avoid this problem in measuring the intensities of shock tube emission lines, we have found it necessary to use as bright a primary source* as possible, namely the anode crater of a carbon arc.

The carbon arc is very useful as a bright standard source because

*The well known tungsten filament lamp is not bright enough for this purpose. Its use would inevitably lead to large probable errors because of the vagaries of low intensity photographic photometry.

of the simplicity of operation and the reproducibility of high anode temperature. For currents just below the "hissing point," the end of the anode is a quiescent cap of luminosity which is much brighter than any other part of the discharge. Hissing ensues when the anode surface becomes hot enough to boil. At the hissing point, the current depends on electrode size and discharge geometry, but the condition of the anode is quite insensitive to these factors if the carbon is spectroscopically pure. The light emitted by the "almost hissing" anode has been investigated by many workers, the most recent being J. Euler[107] whose articles provide a good bibliography of the subject. Reviewing all of the available data, Euler concludes that the anode emission corresponds to the Planck function for $T = 3995 \pm 15°K$ multiplied by a wavelength-dependent emissivity (e.g., $\epsilon = 0.76$ at 5000 Å); we have used these conditions in computing the radiation distribution for our intensity calibration. In view of the correspondence between our arc and those described in the literature, we have not felt it necessary to make another standardization.

The arc lamp (Figure 21) has movable carriages for the electrodes so that a constant electrode separation may readily be maintained in spite of erosion by the discharge. In combination with the 1/4" anode rod, we use a thinner cathode rod (1/8" dia.); this reduces the tendency of the positive column to wander over the face of the anode, causing non-uniform heating and sporadic hissing. In preparing to expose the arc film, we start the arc with sufficient series resistance to limit

the current to about 6 amperes. The resistance is then slowly reduced as the electrodes warm up and assume a slightly tapered shape. Once the hissing point is above 10 amperes, the brightness of the arc increases markedly and the arc can be operated for several minutes with the current just below the hissing value. In this regime, the potential drop across the arc decreases asymptotically to about 50 volts with increasing current. The maximum hissing current usually lies between 10.7 and 11.5 amperes, and the film is exposed while the current is within 0.1 or 0.2 amperes of the maximum.* After the exposure, the arc is run briefly to recheck the hissing point appropriate to the exposure and to verify that no higher quiescent current could have been achieved by delaying the exposure. That the maximum current varies from one set of carbons to the next may be due to a variable "history" of the electrodes arising from manual operation of the arc; the used anode rods show slight variations in taper and crater area.

4. PHOTOGRAPHIC PHOTOMETRY

In Figure 24, we show examples of our calibration films in the wavelength region 4500-4900 Å. For the carbon arc (left) we have selected that portion of the film which shows the opening of the mechanical shutter as time increases upwards. For the xenon flash lamp (right) we show three exposures with the step filter in front of the slit (slit

*Doherty[35] has shown that the temperature error encountered with this small deficit of current is at most 30°K. We prefer to work slightly below the hissing point so that the arc does not start to hiss during the exposure and thus spoil the film.

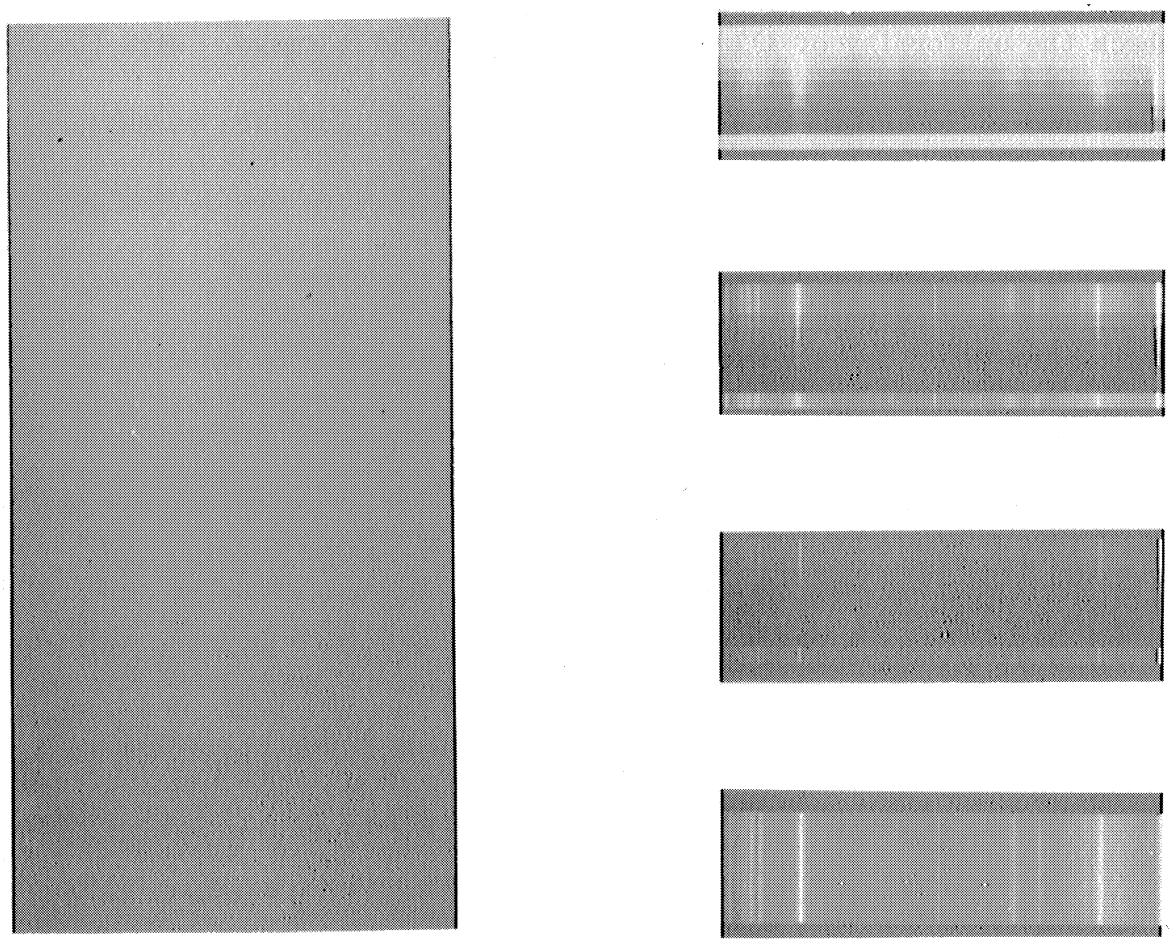

Figure 24. Calibration exposures for heterochromatic photometry, λ4550-λ4950. Carbon arc spectrum (left) recorded on moving film. Xenon flash-lamp spectra (right) recorded on stationary film with/without step filter at spectrograph slit.

width increasing upwards) and one exposure taken without the filter to check the uniformity of illumination along the slit image. With these two films the intensities of shock tube emission lines can be measured absolutely. Briefly the essentials of this procedure are as follows. Given some spectral line at a wavelength λ_o, the observable corresponding to its integrated intensity is the blackening of the film in the line image. Likewise, the blackening of the arc film at the λ_o position corresponds to the continuum emission of the arc in the neighborhood of the wavelength λ_o; this we presume known by the work of Euler and others. Thus we can compare the intensity of the line to the known intensity of the arc, given some intermediate calibration which relates blackening to intensity at the wavelength λ_o; this is provided by the set of flash lamp exposures with the step filter. Actually the quantitative response of an emulsion is primarily to <u>exposure</u> (ergs/cm^2) rather than intensity (e.g., ergs/cm^2-sec-sterad-Å), so that the above procedure measures relative <u>exposures</u> between the arc and the shock tube. The intensities are derived by taking into account the exposure time, solid angle, etc., appropriate to the spectra. Denoting the line and arc quantities by superscripts ℓ and a respectively, the integrated intensity of the spectral line may be written as

$$I^{\ell} = \int I_{\lambda}^{\ell} \, d\lambda = \frac{E^{\ell}}{E^{a}} \cdot \frac{I_{\lambda}^{a} \, \Delta\lambda^{a} \, \Delta t^{a}}{\Delta t^{\ell}} \, , \tag{VI.1}$$

where E^{ℓ}/E^{a} is the measured ratio of exposures and I_{λ} is the brightness of the arc at the line. The solid angle and grating efficiency do not appear here since the optical system is identical for both spectra.*

The quantitative measure of film blackening is photographic density, which is determined by the optical transmissivity of the processed film. If i_o is the light intensity under which the film is examined, and i is the intensity transmitted through an exposed area, then the absolute density** of this area is

$$D_o = \log_{10}(i_o/i) \tag{VI.2}$$

Some development of silver grains usually occurs in unexposed ("clear") portions of a film, so that the intensity transmitted there is $i_1 < i_o$. Correspondingly the relative density ("density above fog") of an exposed image is defined as

$$D_1 = \log_{10}(i_1/i)$$

The fog density ($\log_{10} i_o/i_1$) of a particular kind of film processed with a particular kind of developer varies with the following factors:

---

*For this and the calculation of $\Delta\lambda$ and Δt, we recall Section 3.

**This measure of transmission is commonly used with other semi-transparent objects besides film, e.g., our step filter which was specified by the manufacturer to cover a range of densities from 0.00 to 1.20 in equal steps. See Doherty's thesis for a discussion of variable density filters and, in particular, his measurements on the step filter currently in use.[35]

(1) age and concentration of developer solution,

(2) time and temperature of development,

(3) age of film and particular batch of emulsion used in its manufacture, and the

(4) temperature and humidity history of the film.

For an area of film exposed to light, the relative density depends (in addition to the above) on the following:

(5) wavelength of exposing light,

(6) exposure of the film area,

(7) duration of the exposure,

(8) degree of mixing by agitation during the development process, and

(9) time elapsed between exposure and development.

Since the shock tube experiments given rise to many spectral lines of different intensity, items 5 and 6 must be dealt with directly by some such means as our pair of calibration films (arc and flash lamp). For all practical purposes, it is necessary that the shock tube and calibration films be identical with respect to all the other items above (1-4, 7-9). The procedure described below enables us to use one pair of calibration films for six shock tube experiments while satisfying the identity criteria for all eight of the films in the group. These films (e.g., 103-D(2)) are consecutively cut off a 100 ft roll purchased from Eastman Kodak. They are all developed in identical developer solutions (D-19) at the same temperature (e.g., 20.0 ± 0.1°C), for the same time

(5 minutes), and after the same lapse of time following exposure (e.g., 1 hour). Much of the procedure is fairly obvious but, for the sake of completeness, we describe the details in an extended footnote.* We dis-

*The "spectroscopic films" made by Eastman Kodak have a clear celluloid base and can be bought with an anti-halation backing. Most of our work is done with the 103 emulsion (spectral classes D, F and O) which has both high sensitivity and good resolving power. In the wavelength region 4500-5000Å, we have found the 103-D(2) emulsion to be the most satisfactory. This type is slightly less sensitive than class O in the blue-green, but it has better aging and granularity qualities.

The rolls of film (35 mm x 100 ft) come sealed in airtight canisters which we store unopened in a refrigerator. At least a day prior to being put in use, a canister of film is transferred to the laboratory's temperature-controlled darkroom, so that the film will be warm when opened and not condense atmospheric mositure onto its surface. All eight films in a given "photometric group" are cut consecutively from the same roll so as to avoid the sensitivity variations from batch to batch which arise in manufacture of the emulsion.

For each of the eight films in a group, we use a one pint bottle of D-19 developer. The eight pints of developer are portioned out from a one gallon jug of solution which is thoroughly mixed beforehand. Development is done in a two-reel (1 pt.) Nikor tank with one reel empty and the other holding the film. We develop all films for 5 minutes, inverting the tank every 5 seconds to continually provide the film with fresh solution. Since the processing is done in the darkroom, the temperature of all solutions can be held constant to 0.1°C over each group of eight films and is usually between 20 and 25°C.

After the developer is poured out of the tank, the film is washed twice with distilled water to remove the anti-halation backing. The tank is filled with wash water and shaken vigorously. Most of the backing dissolves in the first wash which pours out looking like black ink; the second wash comes out almost clear.

We fix all the films with F-6 hypo solution. This is done in the Nikor tank for 10 minutes before the tank is opened. Then, after removing the film from the tank and reel, we fix for 5 more minutes in an open tub to remove any patches of emulsion left on the film edges.

The film is washed for an hour in running tap water and then rinsed with distilled water. During this rinse, we sponge both sides of the film with a wet wad of surgical cotton to remove any traces of anti-halation backing. The film is then hung up to dry for several hours and, when dry, is wrapped in soft tissue to protect the emulsion.

cuss here the necessity of comparable exposure times for the shock tube films and their calibrations. According to the "reciprocity law," the actual exposure time does not influence the response of an emulsion to light, and one expects the same density with half the exposure time and twice the intensity. Actually most emulsions demonstrate a "reciprocity failure" whereby short exposure times lead to a decreased sensitivity and, more generally, to a modified relation between exposure and density. Fortunately these changes take place slowly for exposure times less than a millisecond, and we make them negligible by restricting the duration of all exposures to the range 20-100 μsec.

We measure the photographic densities of films with a recording micro-densitometer. The transmission of small film areas is measured by means of a photomultiplier which sits in the image plane of a microscope. The film lies in the object plane and is illuminated from behind by a steady light source. The film is moved at a uniform rate perpendicular to the optic axis, and the photomultiplier signal is simultaneously recorded on moving paper. Such a tracing then represents the variation of photographic density along the particular direction in which the film is moved. Many densitometers employ DC amplification between the photomultiplier and recorder, and their reliability is very sensitive to amplifier stability. We have used two such instruments at the University (Departments of Astronomy and of Chemical Engineering) and have found it necessary to allow one or two hours of warm-up time to achieve stability. Once a steady state is reached, we trace all eight

films in a photometric group. Though this usually takes five or six hours, it is well worth the trouble since the subsequent reduction of the calibration traces is then applicable to all six shock tube films in the group. After each film is traced, we check the stability of the amplifier by recording its response to density standards such as 0% and 100% transmission and "clear film."

The arc and shock tube films are traced in the wavelength direction, i.e., across the 35 mm width. The arc tracing is done at three or four time locations to make sure that we avoid those times when the mechanical shutter, having been only partially open, constituted a stop in the optical system. With the 103-D(2) emulsion and $4500 < \lambda\ (\text{Å}) < 5000$, the arc density is practically constant over the width of the film. Prior to tracing the shock tube films, we examine them for uniformity of the spectra and mark the time locations (usually three or four) appropriate to the emission behind the first reflected shock. The films are then traced at all these locations to check the steadiness of the line intensity and to provide some statistics on the densities of the line images. The unexposed portions of both the arc and shock tube films are always traced over to check the level of "fog density." The net result of all these tracings is a set of density-vs.-wavelength profiles for the arc continuum and the shock tube line spectra. To convert these data into exposures and line intensities, it then remains only to find the density-exposure relations for the wavelengths of interest by means of the xenon flash lamp spectrograms (recall Figure 24).

For the emulsions we use, the characteristic curves vary sufficiently slowly with wavelength that they need only be determined every 100 Å. Thus we can find the curves for the region 4500-5000 Å by making at most four traces which more or less evenly cover the region. Beyond this, the only acceptability criterion for a particular wavelength position on the film is that it be free of emission lines for all values of slit width. For each chosen wavelength, we trace the exposures in the direction of film length (vertically in Figure 24). Within each picture we see the step-wise variation of density corresponding to the range of step-filter transmission. A portion of the characteristic curve can then be drawn by plotting the film density vs. the logarithm of exposure, i.e., light intensity transmitted by the filter. Another portion of the curve can be drawn for the next picture, since the level of exposure has been changed via a different choice of slit width. The portions of the curve so generated can all be blended into a single curve covering the entire density range of the film. This is done by sliding the portions together in the log (exposure) direction, the necessary condition for good photometry being that when the values of density match so also should the slopes of the curves.* By constructing the complete characteristic curve

*This condition is of particular interest in any system where the gross shifts of exposure are performed by a geometrical operation in the optical system, e.g., the variation of slit width in our case. In addition to uniformity of slit illimination, a good calibration further requires that, for all slit widths, none of the rays through the slit be lost from the slit image. Both the flash lamp and arc-shock tube systems were designed to satisfy these requirements. As a bonus, we found that the flash lamp brightness was reproducible to within 5%; when overlapping characteristic curves were matched as described in the text, the necessary shift in the log (exposure) scale was very nearly the logarithm of

for the wavelength λ_1, we are then able to reduce any two densities at λ_o to the corresponding relative exposures if $|\lambda_1-\lambda_o| \leqslant 50$ Å. In this way we find the exposure ratio between a shock tube emission lines and the carbon arc (E^l/E^a of Equation (VI.1)). The absolute integrated intensity of the line then follows from the geometrical factors of bandwidth and exposure time and the known brightness of the arc.

5. HYDRODYNAMIC OBSERVATIONS

In this section we discuss the x-t photographic data for the chromium experiments. When compared to the predictions of ideal theory, these data reveal informative similarities to and differences from the hydrodynamic situations discussed earlier in Chapter III. In accordance with the computations outlined in Chapter II, the $Cr(CO)_6$ additive is found to have a marked effect on the reflected shock velocity. Some of the spectroscopic results to be described later in this chapter are called upon to identify an ionization relaxation process behind the reflected shock. The relaxation time is found to have a systematic and plausible dependence on the computed electron pressure (or density) in the primary flow.

Figure 25 shows two typical x-t photographs of our $Cr(CO)_6$-in-neon experiments. For the left-hand picture, the primary shock speed gives $r_o = \rho_o U^2/p_o = 71.1$, the total initial pressure is $p_o = 1.022 \times 10^4$ dynes/cm^2 ("cgs"), and the initial fractional abundance of $Cr(CO)_6$ is η_o =

*the slit width ratio between the two exposures. Uniformity of slit illumination was verified in all cases by tracings of no-filter exposures (see bottom right of Figure 24).

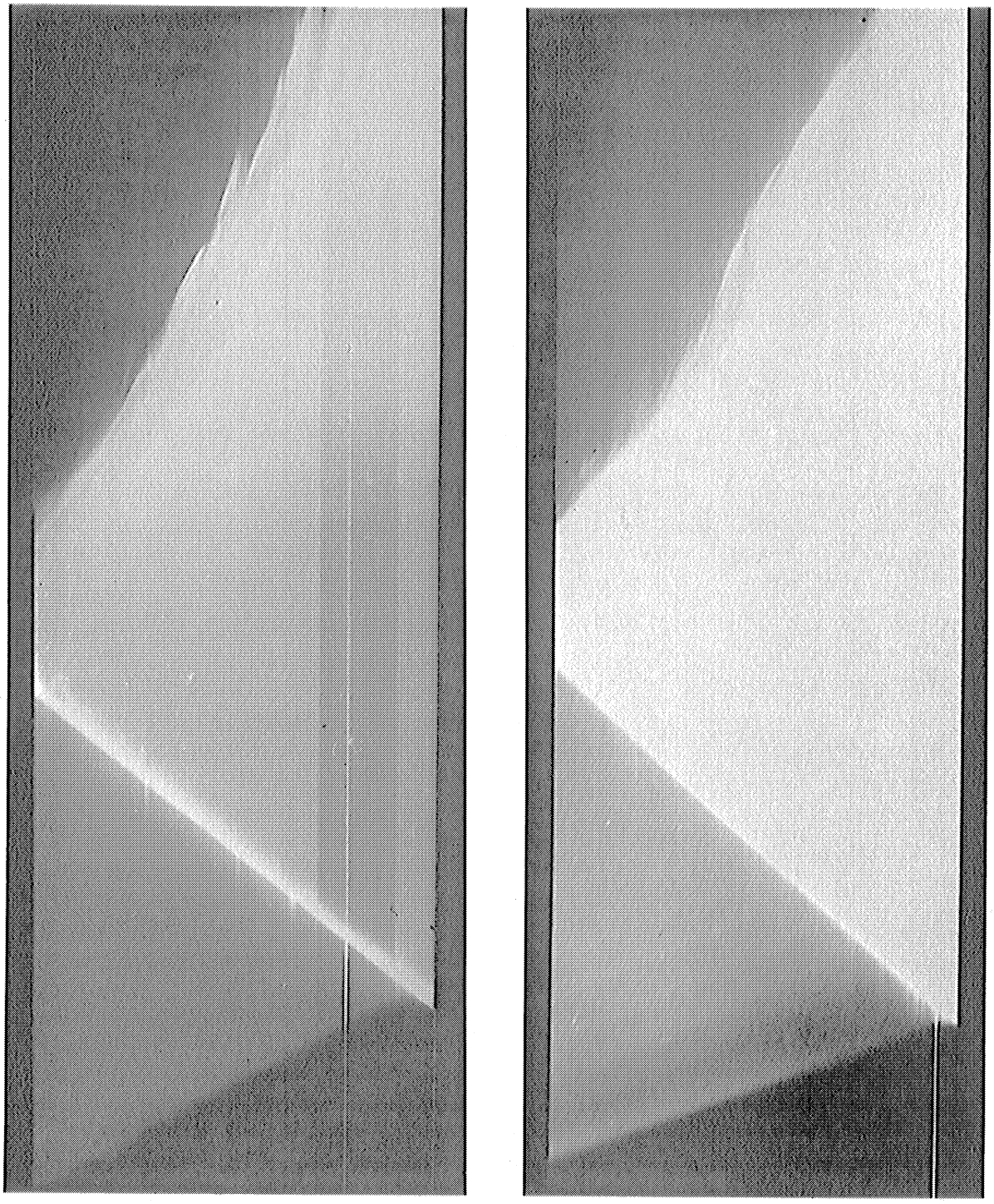

Figure 25. x-t photographs for chromium carbonyl in neon, fractional abundance ~ 0.03% (left) and 0.3% (right).

2.66×10^{-4}. This is what we will often call the "low abundance" case. By contrast, the right-hand picture is for a "high abundance," namely $\eta_o = 3.04 \times 10^{-3}$, while the other parameters have comparable values $r_o = 80.6$, $p_o = 1.034 \times 10^4$ cgs.* The test gases for these shots were premixed in the manner described in Section 3 of Chapter III. The x-t films were measured first to determine the primary shock velocity so that the conditions behind the reflected shock could be computed for the spectroscopic studies. Additional measurements were made of the reflected shock speed for comparison with theory. Finally we measured the "width" (in time) of the very intense band of luminosity at the reflected shock (left-hand of Figure 25); this luminosity is connected with ionization relaxation, and we will return to this topic at the end of the section.

A. According to the computations described in Chapter II, the carbonyl additive has a limited influence on the primary flow for the ranges of abundance and shock strength we have considered. Thus we expect that the primary shock strength will be the same function of driver gas pressure that one encounters without the carbonyl. This is borne out by the data we have collected in Figure 26 for the Michigan shock tube operated at initial pressures $p_o \sim 10^4$ cgs. All the experiments show

*Our division into low and high abundance cases stems from a number of evident differences between the two types of experiments. Of these, perhaps the most prominent is the high intensity of integrated light in the high abundance case, relative to the low; the aperture settings of the camera for the films in Figure 25 were f/4.5 and f/11, left and right respectively, and still a marked exposure discrepancy exists.

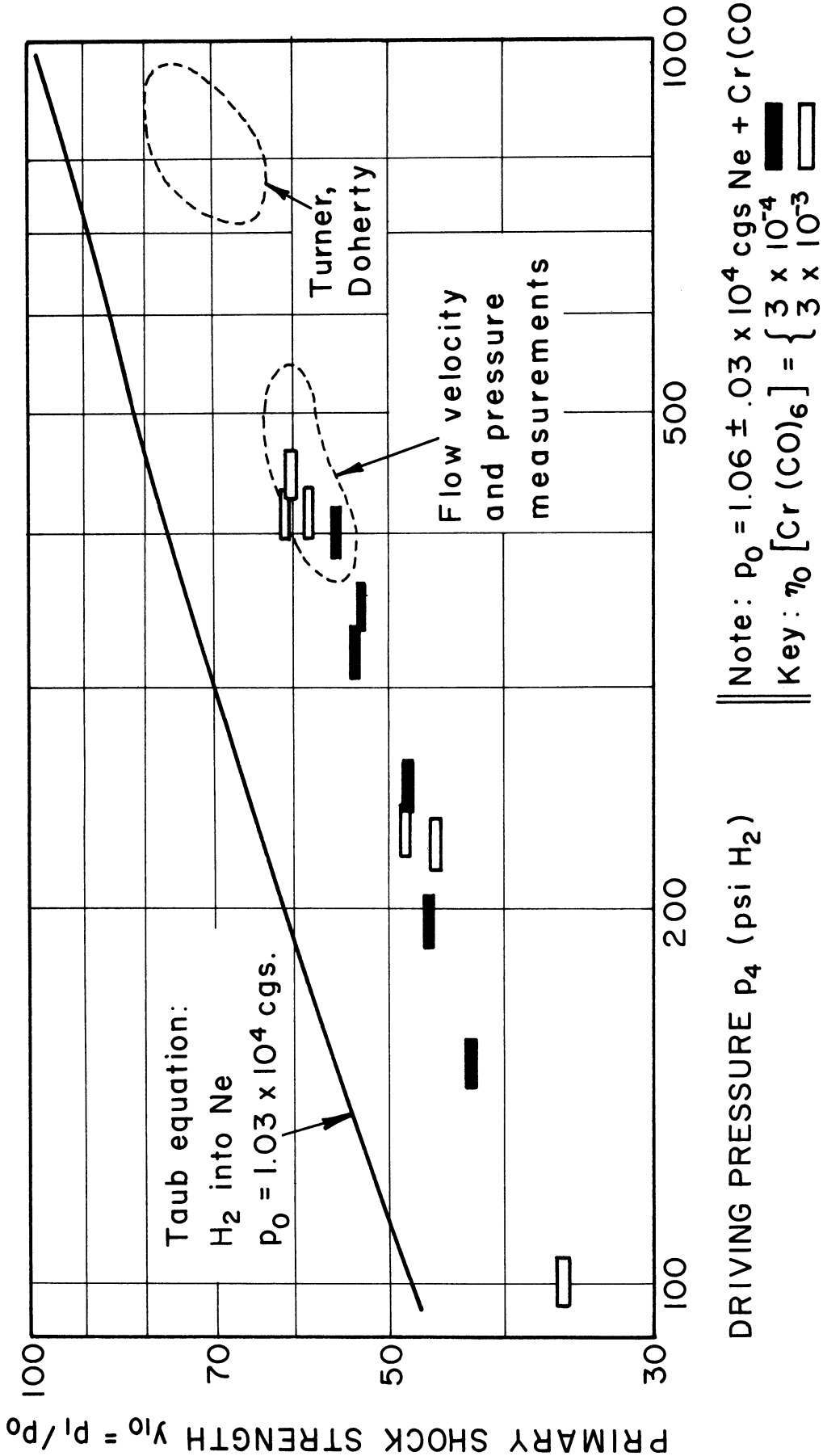

Figure 26. Primary shock strength vs. driver gas pressure, for the Michigan shock tube with $p_0 \sim 10^4$ cgs of neon.

~ 25% failure of shock strength relative to the Taub equation. There is no systematic difference between shots at the two abundance levels of carbonyl, or between these shots and those of Turner,[12] Doherty,[35] or this author (Chapter III) using different additives in the neon.

B. Such differences are clearly apparent, however, when one looks at the reflected shock speed data. Figure 27 shows both the theoretical curves and experimental points for the reflected shock speed ratio $U_{20} = V/U$ as a function of $1/r_0$. The carbonyl experiments behave quite differently from the others with less perturbing additives; moreover, the two levels of carbonyl abundance are easily distinguished from one another for $r_0 > 60$. The carbonyl experiments at low shock strength share the deficit of reflected shock speed common to the experiments we have discussed in Chapter III. With increasing shock strength, the new experiments tend to follow their appropriate theoretical curve. In this case, the effects of dissociation and ionization are apparently strong enough to dominate the shock reflection process, though some influence of viscosity remains to cause deviations from ideal theory. This "tendency toward agreement" for the two rather different levels of carbonyl abundance is reassuring as to the validity of our thermodynamic calculations. In particular, the marked decrease in U_{20} predicted for the high abundance case arises from a high density ratio x_{21} across the reflected shock. That we observe this decrease suggests that the corresponding suppression of T_2 (Figure 2, Chapter II) does indeed occur and can be expected to have a strong spectroscopic effect.

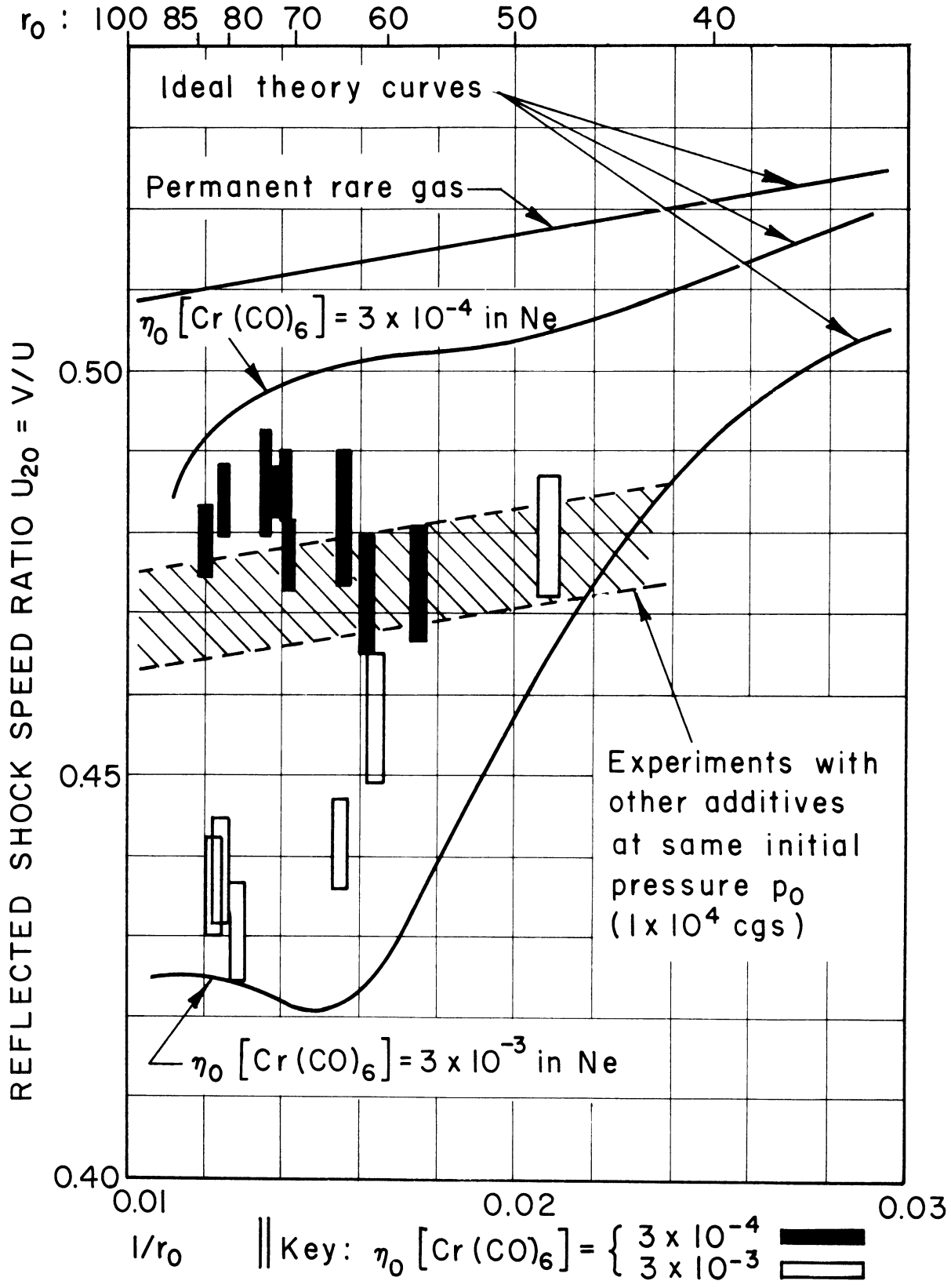

Figure 27. Reflected shock speed ratio vs. $1/r_o$.

C. We identified the ionization relaxation zone behind the reflected shock by means of time-resolved spectroscopy. For low abundance experiments, the spectra consistently showed an intense flash of neutral chromium (CrI) emission just prior to the establishment of steady line intensities behind the reflected shock.* The lines of singly ionized chromium (CrII) did not appear in the flash, though they were often strong in the later steady state. For CrI the ratio of intensities from flash to steady state was of the order to 10 to 20, while both these intensities were much greater than in the primary flow. We interpret the duration of the flash as the relaxation time for setting up the ionization equilibrium between CrI and CrII at the elevated temperature behind the reflected shock. First we will qualitatively discuss this process and its relation to others which have been observed; then we will discuss our data on the variation of the relaxation time with the flow parameters.

When the CrI and free electrons (clearly present in the primary flow) pass through the reflected shock, their translational equilibrium is much more rapidly established than is the ionization equilibrium $CrI \rightleftarrows CrII + e$. Thus there occurs a transitory phase in which the number density of CrI is

(1) roughly 2.5 times that in the primary flow, and

(2) many times greater than in the final "relaxed" state,

*This will be shown in Figure 31 of Section 6.

and the mean energy of exciting electrons is

(1) roughly 2.4 times that in the primary flow,

(2) comparable to the mean energy in the final state, and

(3) comparable to the maximum separation of adjacent energy levels in CrI.

During this phase, then, the lines of CrI can be very strong, owing both to the large fraction of the electron gas effective for excitation and the high abundance of CrI itself.

In contrast, most of the ionization relaxation times observed behind shock waves of comparable strength are associated with dark zones rather than highly luminous ones. The principal cause is that electrons are not generally available on the "input" side of the shock; in addition the first-excited-state energies of the atoms (usually the rare gases) are much higher above the ground state than in the case of CrI and are more comparable to the ionization potentials than they are to the mean electron energies of interest here (~ 1eV).*

For a summary of several ionization relaxation studies with shock waves, we refer the reader to the article by Alpher and White.[74] There is still considerable controversy regarding the details of such processes; however, most workers agree that the electron gas plays an essential role by virtue of the greater cross section for ionization by

*In the low abundance carbonyl experiments we often observe a "dark relaxation zone" behind the primary shock (see Figure 25). Here no free electrons exist in the test gas and the primary flow temperature is only about 0.4 eV. No systematic study was made of this case.

electron collisions than by any other pertinent means. Once a few electrons are created, they dominate the progress of the reaction through their production of more electrons versus their loss by recombination. The reaction is also influenced to some extent by modifications of the electron energy distribution arising from excitation and de-excitation of atoms and ions. Given sufficient time (the relaxation time τ) the electron chain reaction "goes critical"—i.e., the electron density becomes large enough to subsequently offset the losses—and the appropriate equilibrium is then rapidly established. It is clear that the magnitude of τ will depend strongly on the number of electrons initially provided and/or evolved early in the reaction. For example, Turner's experiments[12] with the dark relaxation zone in xenon (behind primary shocks of constant strength) showed that τ varied inversely with the ambient gas pressure p_o.

Proceeding in analogy with Turner's work, we have studied the variation of our "luminous relaxation time" behind the reflected shock as a function of the computed electron pressure p_{el} in the primary flow. Correspondingly we find that τ varies inversely as p_{el}. This can equally well be ascribed to the electron density n_{el}, since the primary flow temperature varies only over a narrow range (3640-4850°K). Our data are shown in Figure 28, where τ is plotted against the reciprocal of p_{el}. The measurement of τ was made on the x-t film for each experiment, and the computation of p_{el} was done from the measured primary shock speed and the ideal theory for chromium carbonyl in neon. The error flags on

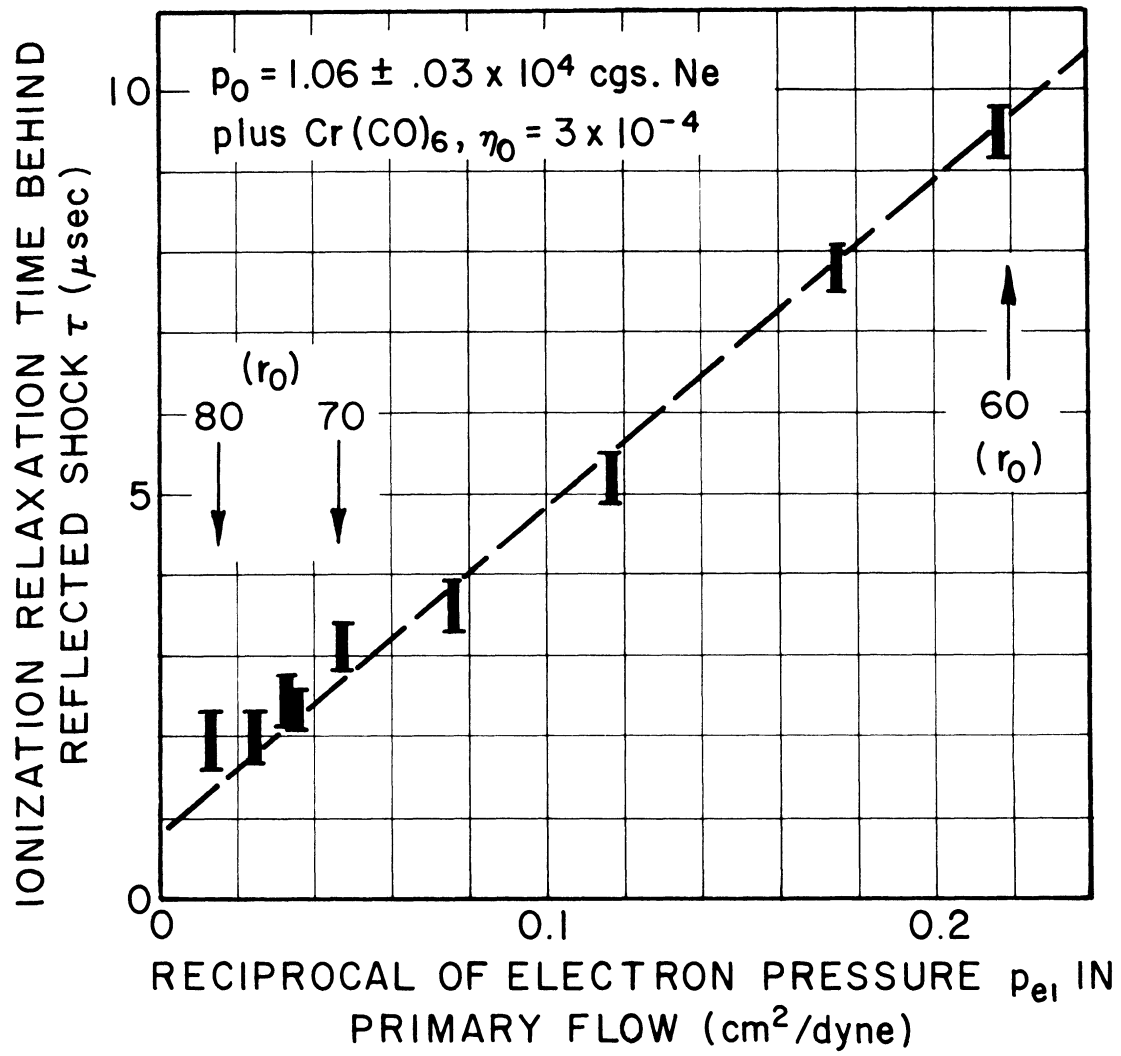

Figure 28. Dependence of ionization relaxation time behind reflected shock on electron pressure in primary flow.

τ reflect the uncertainty in locating the fuzzy trailing edge of the relaxation zone. The apparent value of τ on the x-t films was always corrected for the time extension (~ 1 μsec) of the x-t slit image. This limit on time resolution prevented our studying the fast relaxation process in high abundance experiments. All the data in Figure 28 are for the low abundance case.

The relation between τ and p_{e1} is not the only simple representation of the data. Many kinds of graphs were tried to find the most significant variable. Of these, η_{e1}, $\eta_{e1}/\sqrt{T_1}$, $\eta_{e1}\sqrt{T_1}$ and $p_{e1} = \eta_{e1}kT_1$ were equally acceptable for representation by a straight line. The magnitude of τ does not appear to offer any clear choice on dimensional grounds; e.g., for the electron density and pressure, one can compare $\tau = a/\eta_{e1}$ with $\tau = b/p_{e1}$, observing that $\tau \sim 5 \times 10^{-6}$ sec for $p_{e1} \sim 10$ cgs (and since $T_1 \sim 4000°K$, $\eta_{e1} \sim 1.8 \times 10^{13}/cm^3$). To satisfy the dimensions, we write $a = 1/\sigma_a v_e$ and $b = m_e v_e/2\sigma_b$, where σ is an ionization cross section and $v_e (\sim 1.5 \times 10^8$ cm/sec) is the electron velocity corresponding to the CrI ionization potential. With the above data we find

$$\sigma_a \sim 0.7 \times 10^{-16} \text{ cm}^2$$

$$\sigma_b \sim 14 \times 10^{-16} \text{ cm}^2 ,$$

both of which are conceivable cross sections for electrons at the ionization threshold. The relaxation process is doubtless much more complex than this analysis would pretend, and more data are needed to cover a wider range of conditions. To accomplish this, the most fruitful way would seem to be photoelectric observation of the spectral line intensities. The resulting improvement of time resolution would enable one to work at higher carbonyl abundance and thereby extend the range of electron pressure by one or two decades. It is also likely that a detailed intensity history for several multiplets of CrI and CrII would

shed considerable light on the details of the approach to equilibrium.

D. As well as being an interesting phenomenon in itself, the ionization relaxation of CrI is a welcome occurence for the spectroscopic work described in following sections. Since the steady line intensities behind the reflected shock are set up following a short non-equilibrium period, one is on much surer ground regarding the assumption of thermal equilibrium in the steady state. If the relaxation had not been observed, one would have to allow the possibility of an equilibration time longer than the spectroscopic observing time. The carbonyl abundance ($\eta_o \sim 3 \times 10^{-4}$) sufficient for rapid equilibration ($\tau \lesssim 10$ μsec) is also high enough to yield observable spectral lines, yet not so high as to cause serious self-absorption.

6. QUALITATIVE SPECTROSCOPIC OBSERVATIONS

Most of the wavelength range from 4200 to 7500 Å was surveyed with Charatis' time-resolving spectrograph[105] to determine what multiplets of CrI and CrII could be observed under various conditions. Here we will catalogue these lines as well as the bands of CrO that were seen. We feel that such a summary may be of interest to others contemplating similar experiments. No detailed correlation with abundance or gas conditions will be given here, since these variations gave rise primarily to differences in degree, rather than kind, in the emission spectra. In accord with the Saha equation, the lines of CrII were best brought out by low abundance ($\eta_o \sim 3 \times 10^{-4}$) and high temperature ($T_2 \sim 10{,}000°K$).

The primary flow emission spectrum consisted of the stronger lines of CrI and the bands of CrO.

At first we did not expect to observe the CrO bands on account of the low dissociation energy (~ 4eV) of this molecule. We were finally led to look for the bands because of a weak red luminosity appearing in x-t color photographs of the primary flow. (The integrated "color" of CrI and CrII emission ranged from greenish-blue to violet.) Table X lists the bandheads of CrO we recorded on 103-F film. We may refer to Ghosh and to Pearse and Gaydon[85] for fuller accounts of this spectrum.

TABLE X

OBSERVED BANDHEADS OF CrO

(Å)	Vibrational Quantum Numbers	
	Upper v'	Lower v''
5794.4	1	0
6051.6	0	0
6394.3	0	1
6451.5	1	2
6771.8	0	2

Not all the CrI and CrII lines seen in the shock tube will be listed. Instead we show the appropriate multiplets on energy level diagrams (Figures 29 and 30) which have been abstracted from the more complete diagrams prepared at this laboratory by Allen Ruess and George Charatis. The energy levels and the convention of multiplet numbers

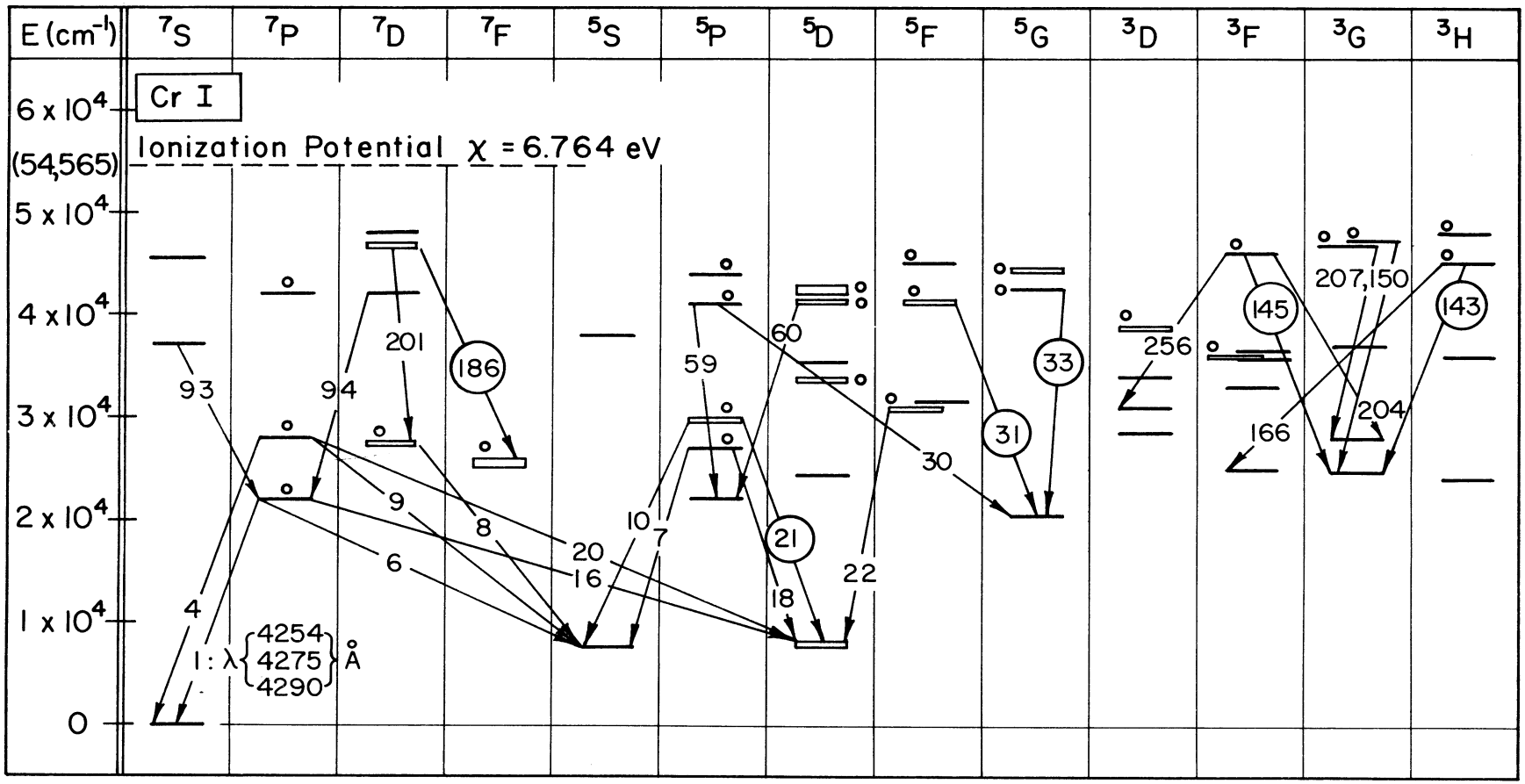

NOTES: (1) NOT ALL LEVELS AND TERMS SHOWN. (2) ODD PARITY DENOTED BY "O". (3) OBSERVED MULTIPLETS NUMBERED AS IN RMT. (4) LINES IN CIRCLED MULTIPLETS MEASURED FOR ABSOLUTE INTENSITY.

Figure 29. Energy levels and multiplets for neutral chromium.

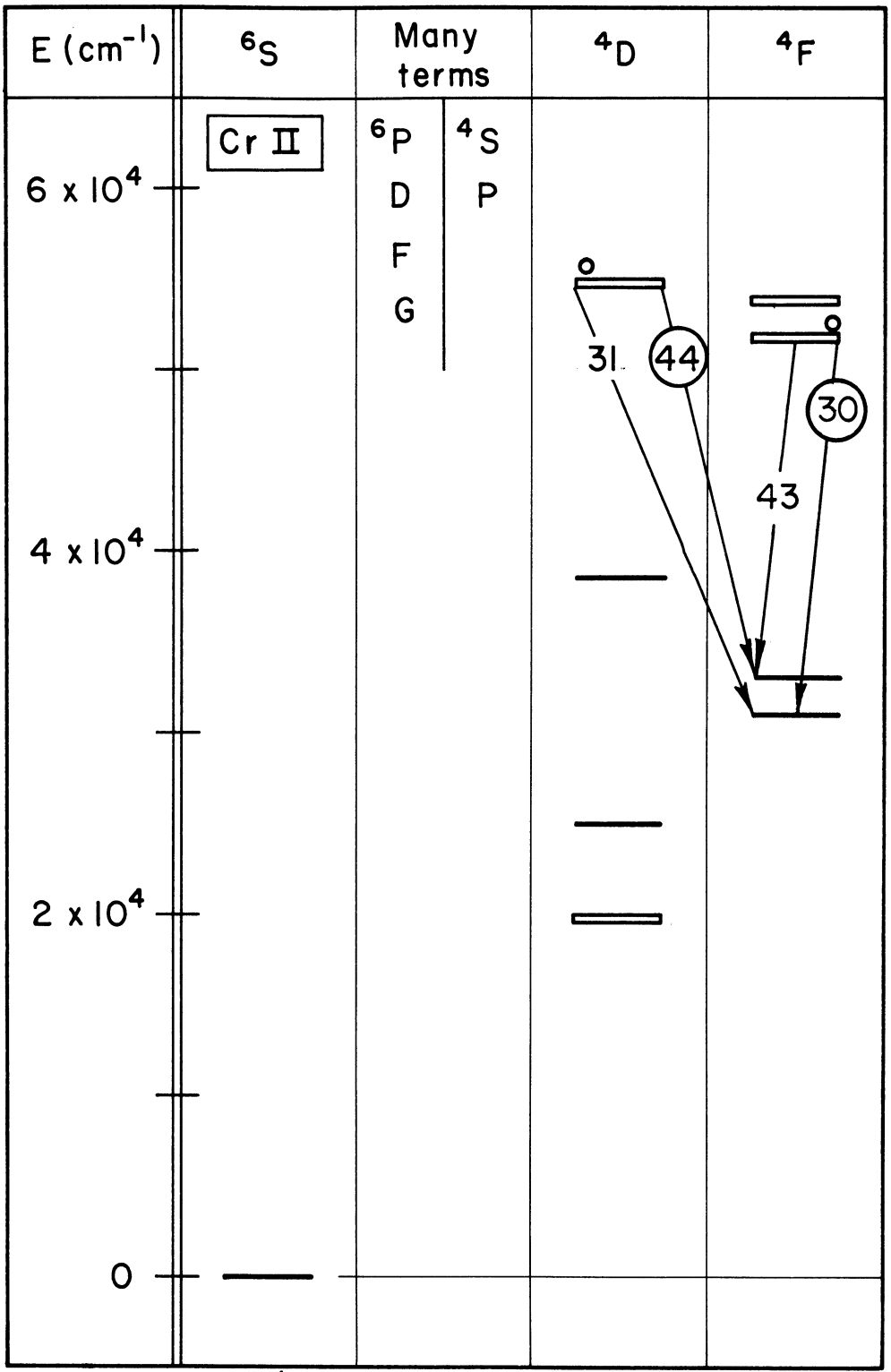

Figure 30. Some energy levels and multiplets for singly ionized chromium.

were taken from the compilations[53,108] by Charlotte Moore (Mrs. Sitterly). In her Revised Multiplet Table (RMT), each multiplet is further decomposed into its constituent lines. In the following sections we will list the lines (belonging to the circled multiplets on the diagrams) for which we have measured absolute intensities.

Figure 31 shows portions of two time-resolved shock tube spectra taken with the spectrograph viewing the tube perpendicularly at 2 cm from the end wall. A neon Geissler tube spectrum is also shown for wavelength comparison. For all three spectra the wavelength range is 4520-4950 Å, and the slit-image is about 3 Å wide. The shock tube experiments are alike in the low abundance of $Cr(CO)_6$($\eta_0 \sim 3 \times 10^{-4}$) but differ in the temperature T_2 behind the reflected shock ($\sim$ 7600,9600°K). At the higher temperature, the lines of CrII are brought out more strongly. These photographs also show the "flash" of CrI emission immediately behind the reflected shock, which was discussed in Section 5 in connection with ionization relaxation of CrI.*

*Two points should be brought out here regarding such flash spectra as appear in the photographs. From these one might erroneously conclude that (1) the flash duration was of the order of 30-50 μsec and (2) the flash was simply the primary flow emission occurring earlier in time at the place of viewing. As for the first possibility, the apparent duration is due to the length of the spectrograph slit or, more exactly, to the extension of the slit-image in the time direction of the film. (Recall Case A of Figure 22, Section 3 of this chapter.) In most cases, the duration measurements had to be made on the x-t films (with 1 μsec time resolution) once it was clear what x-t feature corresponded to the flash. This second point was easily cleared up by showing that the primary flow was not luminous enough to lay down the flash spectrum on the spectrograph film.

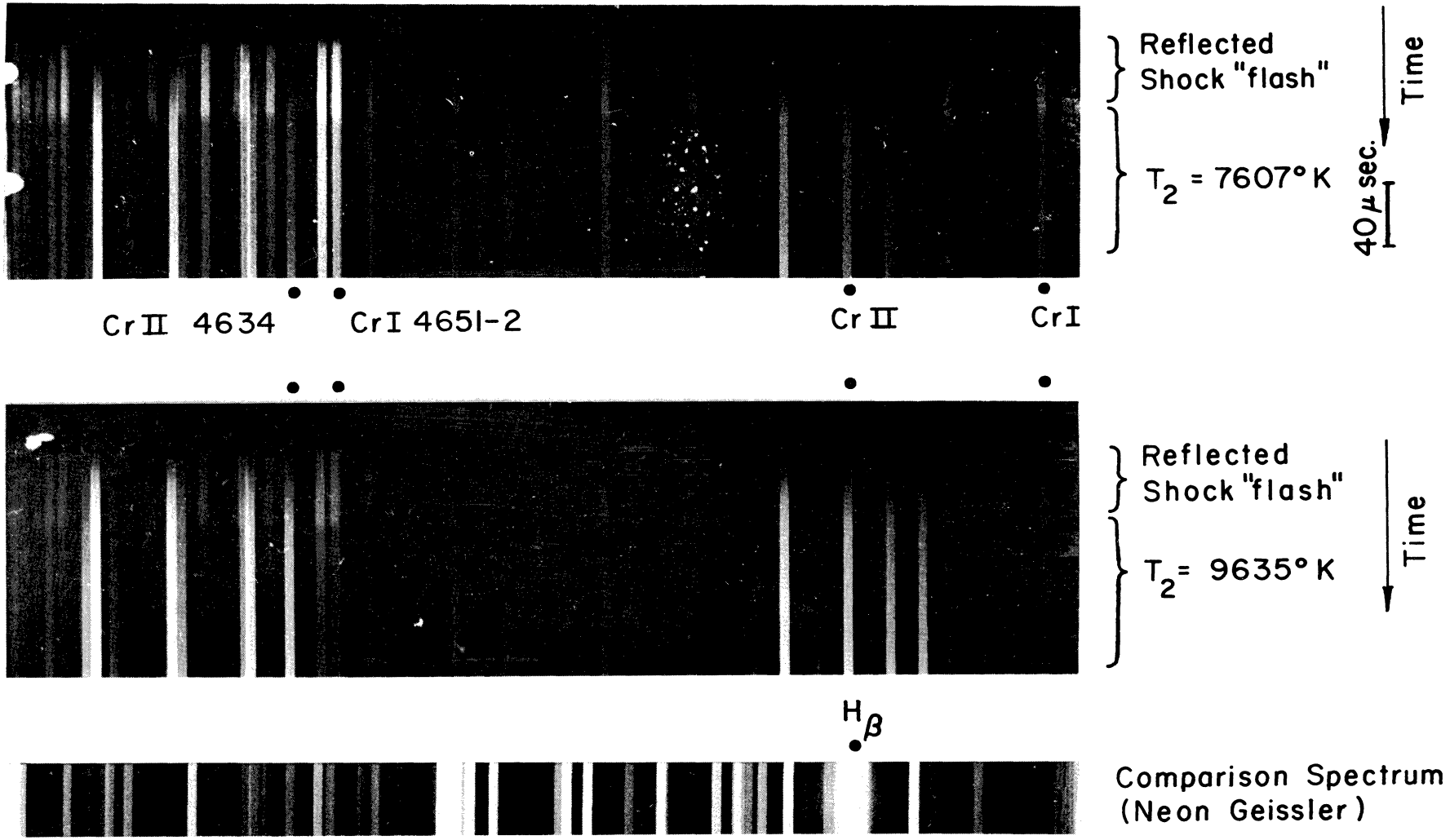

Figure 31. Time-resolved spectra (λ4520-4950 Å) for two chromium experiments. Both the "flash" and the steady emission behind the reflected shock are shown.

The steady spectra following the flash were the objects of study for line intensity measurements. Densitometer tracings across the middle of the steady spectra are shown in Figure 32 for the two shock tube spectra of Figure 31. These tracings are only qualitative and were used just to identify the lines and give a rough idea of comparative intensity. The quantitative tracings of these films were made with densitometer settings which emphasized the images of low photographic density. We have labeled a number of lines on the tracings and have also given the computed conditions in the two cases. The emphasis on CrII at the higher temperature is readily apparent. The flat-topped profiles of most of the lines are due to the width of the slit-image (~ 3 Å) and are good evidence that the heights of the profiles truly measure the integrated line intensities. (We recall here the discussion of $I = \int_0^\infty I_\lambda d\lambda$ in Section 3 of this chapter.)

7. MEASUREMENT OF INTENSITIES AND gf-VALUES FOR CrI

The quantitative measurements of line intensity to be discussed here and in Sections 8 and 9 were confined, for a number of reasons, to the range of variables considered in the latter part of the previous section, namely

wavelength: 4520-4950 Å

abundance: $\eta_o[Cr(CO)_6] = 3 \times 10^{-4}$

total initial pressure: $p_o \sim 1.03 \times 10^4$ cgs

temperature behind reflected shock: $T_2 = 7607\text{-}9635\,^\circ K.$

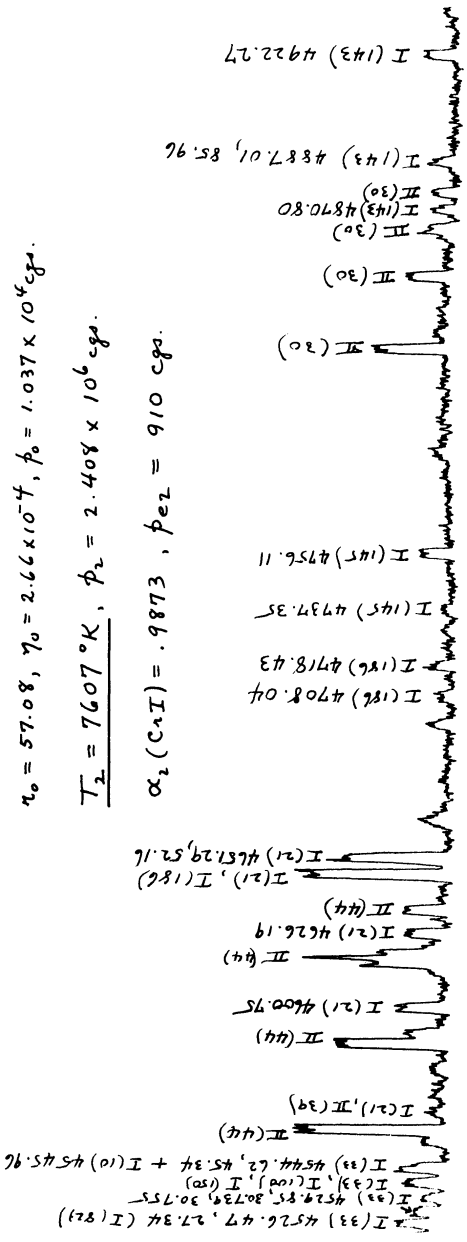

Figure 32. Qualitative tracings of steady spectra (λ4520-4950 Å) emitted from gas behind reflected shock in two chromium experiments.

We do not consider these restrictions to be as stringent as they might seem, since the experiments have yielded consistent absolute gf-values for twenty lines of CrI and eight lines of CrII.

The chosen range of wavelength arose from the original purpose of the chromium experiments, namely the verification of excitation temperature at a time when we suspected more serious errors in the shock tube state variables than now turn out to exist. (See Section 8.) Using Equations (V.14) and V.15), we determined the temperature T by measuring the integrated intensities I of spectral lines whose relative gf-values were presumed known from the experiments of Hill and King. Thus we chose this range as the one containing the largest number of measured and observable CrI lines free of contamination by unmeasured lines of CrI and CrII.*

The choice of abundance was made to insure that the lines were strong enough to be photographed with moderate time-resolution, while being weak enough to allow the assumption of optical thinness in most cases. Since these criteria have primarily to do with absolute abundance, the useful fractional abundance η_o is related to the total initial pressure p_o employed. p_o was chosen low enough to allow ease of operation of the shock tube while not so low as to cause serious hydrodynamic

*Unfortunately, the resonance lines of CrI (4250-4300 Å) could not be included in our quantitative work. Below 4400 Å, the focal curve of the spectrograph camera lens was not sufficiently flat to enable many lines to be photographed sharply at the same time. This is a particularly important consideration for quantitative measurements in the far blue and near ultra violet, owing to the "close packing" of lines in the spectrum.

effects arising from viscosity. Recalling Figure 26 (Section 5 of this chapter), we note that for $p_o \sim 10^4$ cgs, the maximum driver gas pressure required was only 400 psi of hydrogen. Also for this value of p_o, the experiments of Sections 7 and 8 of Chapter III show that one encounters only small errors in absolute pressure and kinetic temperature.

The range of temperature behind the reflected shock was also a compromise between two limits. For one, we preferred not to go to very high temperatures where the degree of CrI ionization would exceed 0.999. We could not go to much lower temperatures at this level of abundance, without so weakening the primary shock that its speed could not be measured with the x-t camera by means of flow luminosity.

The set of CrI lines for which we have measured the absolute gf-values is given in Table XI. This set contains twenty lines distributed over six multiplets (again numbered as in the RMT). The LS coupling designations and the energy levels are given for the upper and lower states of each line. Those lines surrounded by parentheses are double, i.e., they correspond to two overlapping transitions within the same multiplet.

Though we will presently discuss the details of our data analysis, we anticipate this somewhat to give the results of our gf-value measurements in Table XII, along with the previous results for the same lines.

The previous results given in the first column of Table XII were not originally to be found in this form; we compiled these absolute values from the set of <u>relative</u> values measured by Hill and King[46] to-

TABLE XI

MEASURED LINES OF CrI

Multiplet No. (RMT)	Wavelength λ(Å)	Lower		Upper	
		Term T_j	Energy $E_j(cm^{-1})$	Term T_i	Energy $E_i(cm^{-1})$
21	4600.752	a $^5D_3$	8095.2	y $^5P^o_3$	29825
21	4651.285	a $^5D_2$	7927.5	y $^5P^o_1$	29421
21	4652.158	a $^5D_3$	8095.2	y $^5P^o_2$	29585
31	4828.66	a $^5G_3$	20521	y $^5F^o_4$	41225
31	(4829.376)	a $^5G_{5,4}$	20524	y $^5F^o_{4,4}$	41225
31	4789.354	a $^5G_6$	20520	y $^5F^o_5$	41393
31	(4790.337)	a $^5G_{5,4}$	20524	y $^5F^o_{5,5}$	41393
33	4539.788	a $^5G_2$	20517	z $^5G^o_3$	42539
33	4540.502	a $^5G_3$	20521	z $^5G^o_3$	42539
33	4541.071	a $^5G_4$	20524	z $^5G^o_3$	42539
33	4544.619	a $^5G_2$	20517	z $^5G^o_2$	42515
33	4545.335	a $^5G_3$	20521	z $^5G^o_2$	42515
143	4870.796	a $^3G_3$	24834	z $^3H^o_4$	45359
143	4920.945	a $^3G_5$	25039	z $^3H^o_5$	45354
143	4922.267	a $^3G_5$	25039	z $^3H^o_6$	45349
145	4730.711	a $^3G_3$	24834	y $^3F^o_2$	45966
145	4737.350	a $^3G_4$	24898	y $^3F^o_3$	46000
145	4756.113	a $^3G_5$	25039	y $^3F^o_4$	46058
186	4708.040	z $^7F^o_5$	25549	f $^7D_4$	46783
186	4718.429	z $^7F^o_6$	25771	f $^7D_5$	46959

TABLE XII

CrI gf-VALUES

Previous Line Strengths (after Hill & King, Ostrovskiĭ & Penkin)*		Measured Line Strengths		Wavelength λ(Å)	Multiplet No. (RMT)
gf	gf(comb.)	gf	gf(comb.)		
0.321 Ar	0.321	0.29 ± .03	0.29 ± .03	4600.752	21
0.225 Ar 0.654 Ar	0.879	0.20 ± .02 0.60 ± .05	0.80 ± .07	4651.285 4652.158	21 21
0.31 (X) (3.87) Br	4.18	0.10 ± .01 1.0 ± .09	1.1 ± .1	4828.66 (4829.376)	31 31
4.69 (0.78) C	5.47	1.2 ± .17 0.20 ± .03	1.4 ± .2	4789.354 (4790.337)	31 31
3.69 D 9.93 D 3.24 C	16.9	0.74 ± .09 2.0 ± .23 0.65 ± .08	3.4 ± .4	4539.788 4540.502 4541.071	33 33 33
10.9 D 2.65 D	13.6	2.2 ± .24 0.50 ± .06	2.7 ± .3	4544.619 4545.335	33 33
19.5 C	19.5	3.9 ± .3	3.9 ± .3	4870.796	143
5.4 (X) 32.3 Br	37.7	1.1 ± .1 6.4 ± .5	7.5 ± .6	4920.945 4922.267	143 143
25.7 D	25.7	3.2 ± .4	3.2 ± .4	4730.711	145
32.6 D	32.6	4.1 ± .5	4.1 ± .5	4737.350	145
57.2 C	57.2	7.2 ± .8	7.2 ± .8	4756.113	145
50.4 D	50.4	4.5 ± .4	4.5 ± .4	4708.040	186
50.5 W	50.5	5.6 ± .5	5.6 ± .5	4718.429	186

*Calculated from set of HK relative values, using OP absolute value gf(CrI(1)λ4254) = 1.05.

gether with the absolute value gf = 1.05 given by Ostrovskiĭ and Penkin[101] for the resonance line, CrI (1)λ4254. Save for this absolute scale reference, we have thus focused our attention on Hill and King's measurements (hereinafter denoted by HK) since they are the most extensive in existence for CrI, covering 430 lines with a range of lower state E_j from 0 to 3.5 eV. A few of these lines were also measure absolutely by Ostrovskiĭ and Penkin (OP) and by Allen and Asaad,[109] but we will use only the OP resonance line strength for the present. We will defer further comparison of these latter results to Section 8.

The letters appended to the previous gf-values follow the notation of HK for indicating their reliability estimates on each of the relative values. In order, the symbols A, B, C, D and W roughly represent probable errors of 5, 10, 25, 50 and 100 percent. As we shall see, there must also be systematic errors in the HK values as large as 1000%. The two numbers followed by (X) were not given by HK and were estimated by us from relative arc intensities within multiplets as listed in the RMT.

The second column of previous results in Table XII, labeled gf(comb.), takes cognizance of our need to use slit images so wide as to (incidentially) lump together separate lines of the same multiplet lying within 1 or 2 Å of one another. For wavelengths in which the source is optically thin, a combination of such lines in the spectrograph is equivalent to a blend of lines in the source, with a total gf(comb.) equal to the sum of the individual gf-values. Of our twenty CrI lines, thirteen are such

blends and seven are pure.

These combined gf-values were used to interpret the intensity measurements described below. The resulting discrepancies with theory then led to our new values of gf(comb.) listed in the fourth column of Table XII. From these we derived new gf-values for the blended lines within multiplets (third column) by partitioning our gf(comb.) according to the ratios indicated in the previous work. Though the HK values appear to be affected by a temperature error, this last procedure is probably justified by the closeness of levels (and hence Boltzmann factors) within each multiplet.

Our measurements could have been extended to more lines were it not for overlapping between lines of different multiplets of CrI (and CrII). The choosing of clean lines was an involved business which we will only sketch briefly here in a footnote.* Most of the listed lines were definitely clean; three borderline cases will also be discussed.

The line intensity data for CrI were reduced in a manner appropriate

*An atlas of lines of CrI, CrII, CI, OI and NeI was compiled by the author from the finding list in the RMT. Each CrI line which appeared to be a likely candidate for intensity measurement was examined for possible contamination by other lines. If a given line L was neighbored by a member of some other CrI multiplet M, the spectrum was examined for all other members of M, and L was accepted only if the strongest lines of M were missing. For this purpose, both the HK relative values and the approximate RMT arc intensities were used. For example, the strong line CrI (21) λ4646.174 was rejected because of the adjacent line CrI (186) λ4646.808 and the appearance of other lines of (186) in the shock tube spectrum. Similar criteria were used for CrII. No lines of the other species listed above were observed.

to the theory of the curve of growth (Chapter V, Sections 5 and 6). We recall that such curves relate the integrated intensity I of a spectral line to the product of the gf-value and the abundance of atoms in the lower state E_j. The curves constitute a one-parameter family, the parameter being the damping ratio a which measures the relative broadening contributions by damping effects and the Doppler effect. The abscissa is $\log_{10} C$, where

$$C = \frac{\pi e^2 \ell n \left(1 - e^{-h\nu/kT}\right)}{mc\, Z\, \sqrt{\pi}\, \Delta\nu_D} g_j f_{ji} e^{-E_j/kT} \qquad \text{(VI.3)}$$

and the ordinate is $\mathcal{J}(C, a)$, where

$$\mathcal{J}(C, a) = I / 2 \Delta\nu_D B_\nu(T)$$

For each experiment, the measured quantities were the integrated line intensity I and the speed of the primary shock wave. In Sections 3 and 4 of this chapter, we have described the measurement of I by comparing the exposure of the line to the exposure of the carbon arc radiation standard. The calculation of temperature and abundance behind the reflected shock, as a function of primary shock speed, has been described in Chapter II. All the thermally dependent quantities were computed from this theory, namely the shock tube Planck function $B_\nu(T_2)$, the Doppler width $\Delta\nu_D$, the total number density n of neutral atoms, the CrI partition function Z, and the Boltzmann factor e^{-E_j/kT_2}. In order to have a definite starting place, the gf-values were assumed to be the values of

gf(comb.) compiled from the previous work (HK, OP).

Figure 33 shows a curve of growth representation of the line intensities in our lowest temperature experiment. The vertical error bars reflect our estimate of 10% for the photometric reliability. All the line intensities are such that $\mathcal{J}$ (C, a) $\leqslant 1$, so that the damping ratio is not a critical quantity. One observes agreement between theory and experiment for the multiplet (21) having the lowest excitation potential; however, the lines of higher potential lie well into a "forbidden region" of the graph. Whether one says that these lines fall below or to the right of the allowed curves depends on whether one assumes the errors to be in the measured intensity or in the previous gf-values. We will presently show that the latter is the case. The evidence against intensity errors is discussed in a footnote.*

By lumping together multiplets of roughly the same excitation energy, we have simulated curves of growth for each group. These "apparent" curves (dashed lines in Figure 33) are parallel to the theoretical curves $a = \infty$. This behavior is strongly suggestive of systematic errors in the previous gf-values, errors which increasingly overestimate the values

*The assumption of intensity errors raises more questions than it settles, primarily because of the (so to speak) random scattering of the lines over a wavelength region in which the film sensitivity and the appropriate Planck functions are smoothly and slowly varying. The best that one could do with the lines on Figure 33, for example, would be to elevate the center of the multiplet cluster (33, 143, 145, 186) from $\mathcal{J} = 0.25$ to $\mathcal{J} = 1.5$ by assuming that the carbon arc standard was actually six times brighter than computed. Beside straining one's credulity regarding the arc temperature, this would raise multiplet (31) somewhat above the curve $a = \infty$ and would throw multiplet (21) far into the upper "forbidden region."

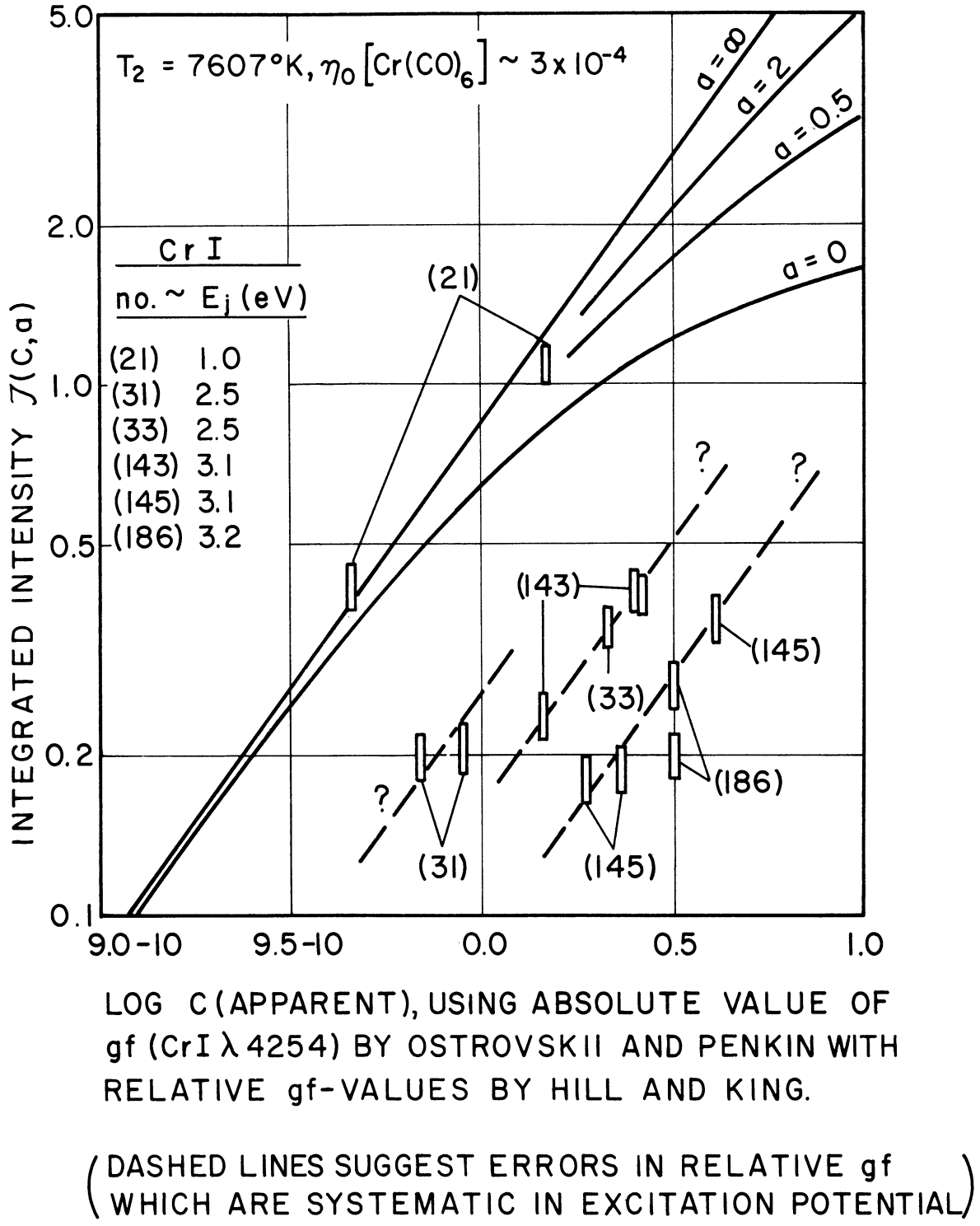

Figure 33. Curve of growth representation of several CrI multiplets measured in one experiment.

as the excitation energy increases. To correct the gf-values, one would simply find the subtrahend in $\log_{10} C$ required to shift the apparent curves to the left and into correspondence with the theoretical curve.

To verify this hypothesis, we have studied the curves of growth traced out by each multiplet as the shock tube conditions are varied over a set of six experiments. In describing these results we will continue to use the suspect gf-values (HK, OP) and will thus still speak of the curves and the C-values as "apparent." The new gf-values are derived from the shift in $\log_{10} C$ required to bring theory and experiment into agreement. One could just as well derive the gf-values by direct comparison of the measured $\mathcal{J}$ and the computed C/gf; we will illustrate this method in our treatment of CrII gf-values in Section 9.

The apparent curves of growth for the CrI lines belonging to different multiplets are shown in Figures 34, 35 and 36. For the most part, these graphs are self explanatory, and the approximate correction in $\log_{10}$ gf is shown in most cases.

Multiplets (21) and (143) are shown in Figure 34. As in all the CrI cases to follow, the upper right-hand data points for each line (or blend) are for the lowest temperature experiment, which we have already discussed. With increasing temperature, both the Planck function $B_\nu(T)$ and the degree of ionization α(CrI) increase, so that the points move down and to the left. For multiplet (143), both the line and the blend follow the same curve; the indicated gf-value correction amounts to a reduction by about a factor of five.

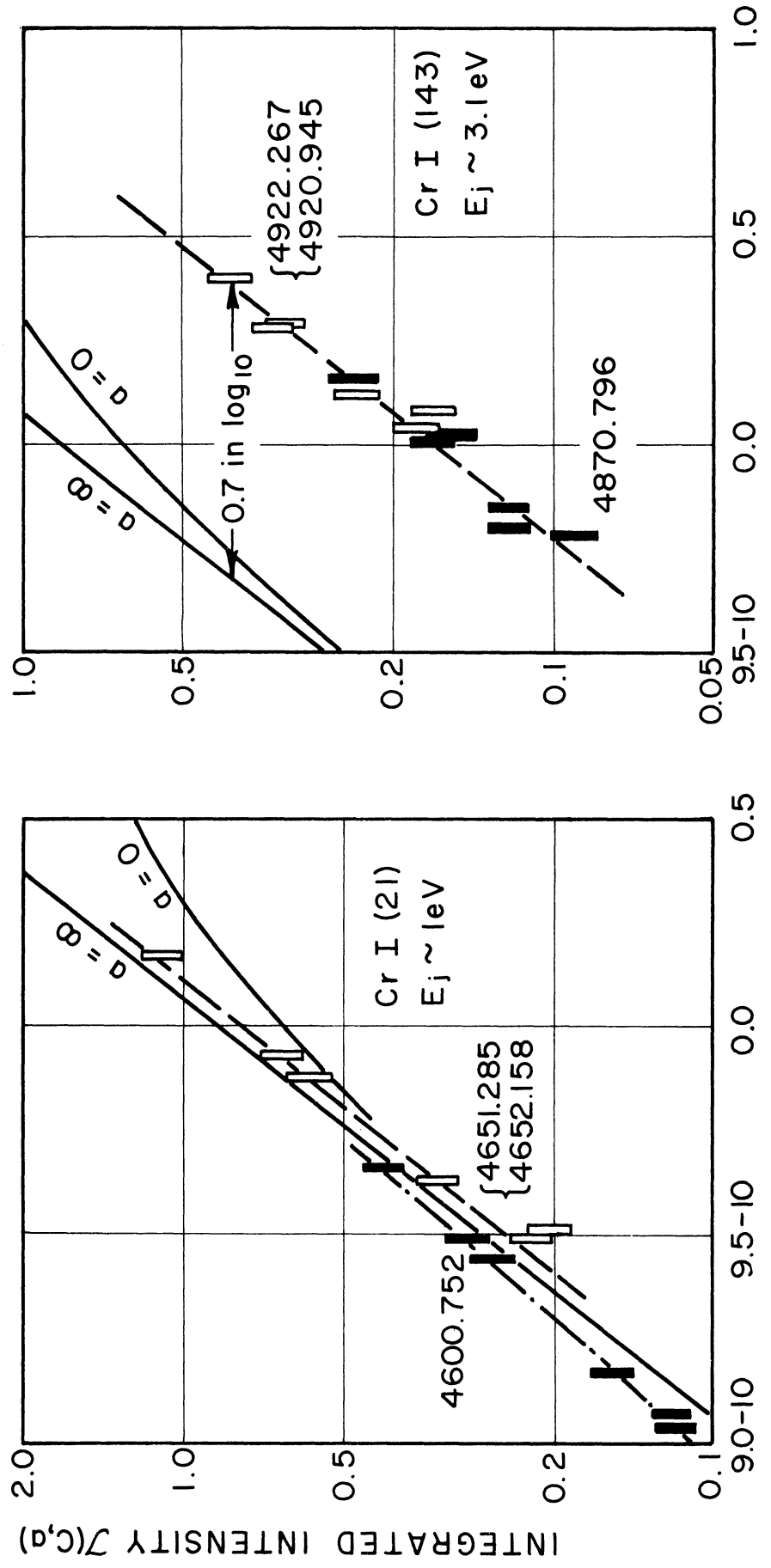

Figure 34. Apparent curves of growth for two CrI multiplets measured in six experiments (low and high excitation potential).

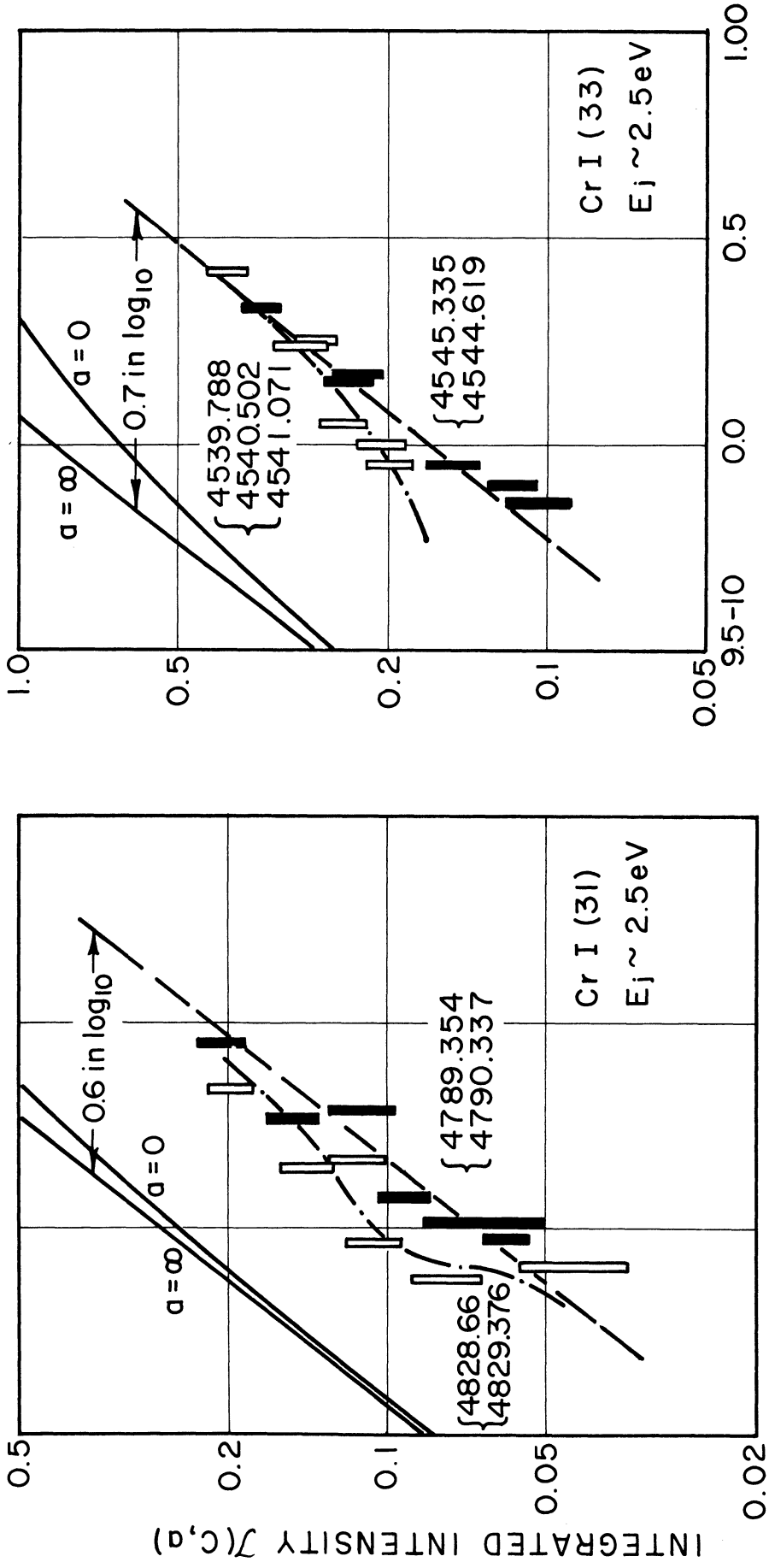

Figure 35. Apparent curves of growth for two CrI multiplets measured in six experiments (moderate excitation potential).

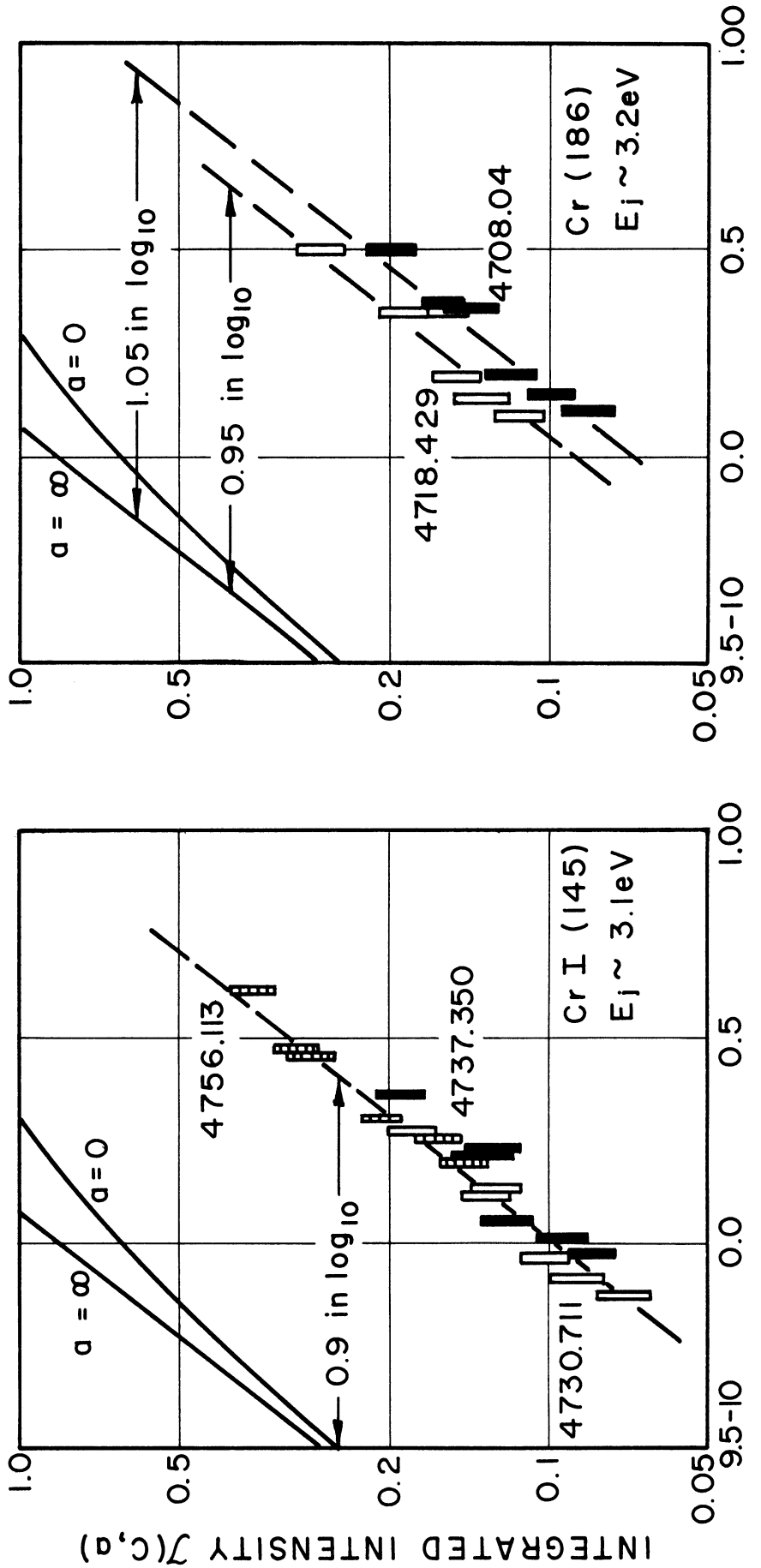

Figure 36. Apparent curves of growth for two CrI multiplets measured in six experiments (high excitation potential).

In multiplet (21), the blend (λ4651-2) traces out a curve which roughly agrees with theory, showing that its combined gf-value is essentially correct. Allowing for experimental error, we take the value -0.04 ± .04 as the small correction in $\log_{10}$ gf(comb.). The isolated line of this multiplet (λ4600.752) was suspected beforehand of possible contamination by seven lines of four other CrI multiplets (32, 171, 172, 210) and, indeed, shows evidence here of a slight additional intensity varying with the shock tube conditions. Though no individual members of any of these other multiplets was positively identified (in the photometric experiments) the possibility of a small total contribution to the line of interest cannot be ruled out. Resorting, then, to the previous argument that the HK relative values are probably satisfactory within each multiplet, we ascribe to this single line the same $\log_{10}$ gf correction given above for the blend.

Two multiplets (31, 33) of medium excitation energy are shown in Figure 35. All the measured "lines" are blends. Each multiplet contains a pure blend* which follows a curve parallel to the curve a = ∞. As expected, the intensities of the contaminated blends* are contributed to in ways which depend on the temperature. Again, the corrections in $\log_{10}$ gf were computed from the pure blends and then applied to all the blends.

*By a "pure blend" we mean a blend of lines belonging to the same multiplet. A "contaminated blend" contains some CrI line(s) of interest plus line(s) of CrII or some other multiplet of CrI.

Finally, Figure 36 shows the apparent curves of growth for pure lines in two multiplets (145, 186) of high excitation energy. The three lines of multiplet (145) follow the same curve over a factor of 5 in the intensity. In multiplet (186), the two lines follow curves which can just be distinguished from one another outside the experimental error. Since the gf-value corrections for each are therefore different (by 0.1 in $\log_{10}$ gf), one arrives at a ratio between the two which is not exactly the same as for the HK values. This circumstance does not seriously affect our previous and opposite assumption, since these lines belong to the two worst HK classes of probable error.

To recapitulate, we have used previously measured gf-values for CrI to systematize the line intensity data for the shock tube. The apparent curves of growth traced out by each line (or blend of lines) have been interpreted as remeasurements of the gf-values. The lines in question and the old and new gf-values are listed in Tables XI and XII.

8. DISCUSSION OF INTENSITIES AND gf-VALUES FOR CrI

We would like to emphasize at the outset that we assume the shock tube conditions to be very much as we have computed them from theory. Though this is implicit throughout Section 7, we restate it here because much of the following discussion is concerned with the role of temperature errors in the determination of gf-values and, in particular, the propagation of such errors in subsequent temperature measurements. Though we have not shown directly that the kinetic temperature and the

chromium excitation temperature are identical, the sum total of the indirect evidence is strongly in favor of this equality. This point is further discussed in Section 2 of Chapter VII.

The CrI line intensities have been studied by several workers, both in the solar atmosphere and in laboratory sources. From this work it is evident that the set of relative values measured by Hill and King[46] must be corrected in the manner shown by our experiments. This conclusion is very important for spectroscopic determinations of temperature using CrI as the thermometric element.

If line strengths could be reliably predicted from wave mechanics, the need for gf-value measurements would be greatly reduced. Thus the results of such measurements should be compared with theory wherever possible. We find that the relative strengths between a number lines and multiplets of CrI agree fairly well with the rules of LS coupling.

The reliability of our absolute gf-value scale is hard to assess. Very few measurements have been made of the lines we have studied. Even if these lines had been included in more of the earlier work, it is likely that the scatter (a factor of 10, over the best resonance line studies) would have allowed only an order of magnitude comparison. Where direct comparison of absolute values is possible, our gf-values for CrI are 3 to 5 times larger than the values found by other workers. There is as much or more to be said in favor of the shock tube results as there is for the previous experiments.

A. The strengths of the CrI Fraunhofer lines have recently been reviewed by Goldberg, Müller and Aller[36] in their study of elemental abundances in the solar atmosphere. They use a growth diagram to compare the observed absorption strengths with Hill and King's relative gf-values. They observe that "...the higher-excited lines suggest a curve of growth displaced by about a factor of 5 to the right of the curve of growth defined by the lines of lower excitation, and the points exhibit a large scatter." Thus the solar results are analogous to our example of an "apparent" curve of growth for shock tube emission lines (recall Figure 33). Moreover, the implied reduction of the higher-excited HK values by a factor of 5 is indeed the result we have obtained for multiplets (31, 33, 143) of CrI (Figures 34 and 35). The scatter of the solar results is also so large as to include our larger reduction factors (~ 10) for multiplets (145) and (186). Goldberg et al., further show that subsets of the HK values for CrI lead to an unlikely conclusion for the abundance of this element compared to the abundances of Ti I, V I, Mn I, Fe I, Co I and Ca I. Of this group of seven elements, CrI is the only one which shows a relation between the calculated solar abundance and the excitation potential of the lines used for the calculation.*

Systematic errors in Hill and King's values have been suspected for about six years due to the anomalously low excitation temperature implied

*Because of the considerable help given us by Dr. Müller in compiling a bibliography for CrI, we communicated our results to her in advance of publication. According to a preliminary analysis, she finds that the new CrI gf-values define a very good curve of growth for the sun. We understand that she is looking into the implications for the absolute solar abundance of chromium.

for CrI in arcs and in the sun. We unknowingly came upon this effect in the shock tube when we attempted to measure the gas temperature by means of the CrI line intensities. In this case the apparent temperature decrement was very striking compared to the previously observed anomalies, because the shock tube temperatures (7500-10,000°K) were roughly twice the temperatures involved in the solar and arc work. We will return to this general point after discussing an example of the shock tube results.

Figure 37 shows the intensity-energy diagram used to find the excitation temperature of CrI in a shock tube experiment. In accord with Equations (V.14) and (V.15) given in Chapter V for the optically thin case, we have plotted $I\lambda^3/gf$ vs. E_i, where I is the measured integrated intensity of a spectral line and E_i the energy of its upper level. The excitation temperature is then just the negative slope of the line (connecting the data points) multiplied by 5041°K. According to the set of relative gf-values by Hill and King, the dashed line gives an apparent temperature of 5170°K compared to 9270°K computed for the gas behind the reflected shock. Applying the correction in $\log_{10}$ gf given by us in Section 7, we arrive at the corrected excitation temperature of 9180°K which is within 1% of the computed value. This result is typical of all the CrI experiments.

That Hill and King's gf-values must be increasingly reduced with increasing excitation potential implies that the relative occupations of levels in the HK experiments were actually higher than assumed, in the same systematic manner. (We will elaborate on this in the next

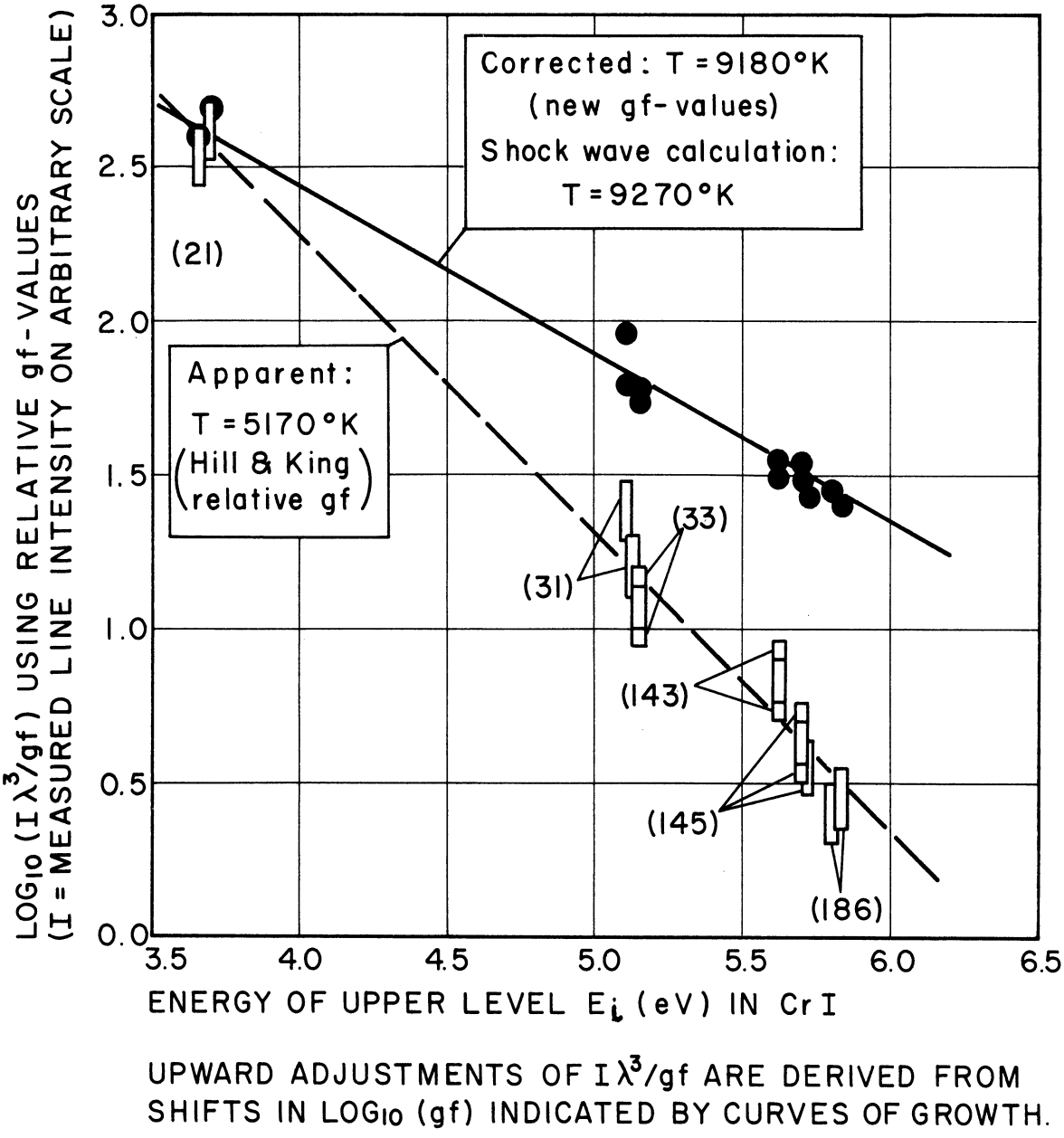

Figure 37. Relation between validity of temperature measurement and reliability of gf-values.

paragraph.) These experiments were performed in absorption, with chromium vapor in a graphite-tube electric furnace. According to the authors, the furnace temperature T_f was varied between 1370 and 3120°K to adjust the optical depth of different groups of lines. If one assumes a mean T_f(HK) = 2000°K, the new gf-values imply that the actual mean T_f was between 2200 and 2400°K. Though this 10% to 20% underestimate of T_f by Hill and King is hard to understand, the same conclusion is apparent from other studies of CrI. Similar errors in T_f of about 400 and 200°K, respectively, were suggested by the work of (1) Sandage and Hill (1951) on CrI absorption in the sun,[110] and (2) Allen and Asaad (1957) on CrI emission from an arc.[109] In analogy with the comparative studies among groups of elements in the sun, Allen and Asaad found that CrI was anomalous (with respect to FeI, CoI, MnI and NiI) in the low excitation temperature implied by Hill and King's relative gf-values.

Once a temperature error is made in determining a set of relative gf-values, this error propagates throughout all subsequent measurements of temperature which make use of these relative values. For the original measurement, let us assume that the temperature was actually θ_o while the assumed temperature was θ'_o. It is easily shown that the erroneous values (gf)' are related to the true values (gf) by the equation

$$(gf)' = (gf)\, e^{-E_i/\theta_o}\, e^{+E_i/\theta'_o} \qquad \text{(VI.4)}$$

If the (gf)' are then used to determine some other temperature, one will be led to a value θ_1' which is different than the true temperature θ_1 of the source under study. These new apparent and true temperatures are related to the original ones by

$$\frac{1}{\theta_0} + \frac{1}{\theta_1'} = \frac{1}{\theta_0'} + \frac{1}{\theta_1} \qquad \text{(VI.5)}$$

In the case of CrI, Hill and King's original measurements apparently fell into the category $\theta_0' < \theta_0$; hence all later temperature measurements using their relative gf-values resulted in $\theta_1' < \theta_1$. The magnitude of this defect increases with increasing θ_1/θ_0.*

It is important to note that diagrams such as Figure 37 do not enable one to recognize an original temperature error by virtue of any curvature in the plot; i.e., the propagation of error is such as to preserve the linear connection of the data points. When the graph is curved, one must suspect a non-Boltzmann distribution or appreciable optical depth either in the original gf-value work or in the source under study.

*Irrespective of "future temperature measurements," Equation (VI.4) points out the serious %-errors in gf-values which can arise from small %-errors in temperature, when the excitation energy is large compared to the thermal energy of the gas. Doherty[35] has found it necessary to consider this problem in his study of neon lines ($E_i \sim 15$ eV, $\theta \lesssim 1.5$ eV). In the present work on CrI, a 5% overestimate of temperature would have led to an underestimate of the gf-values by 10 to 30%. Even this level of error seems precluded by the kinetic temperature measurements of Section 7, Chapter III.

B. We now turn to the comparison of the measured gf-values for CrI with theoretical predictions. Just as in experimental work, there is a natural distinction between the subjects of relative and absolute gf-values computed from wave mechanics. The relative strengths of lines within a multiplet (and of multiplets within a transition array) can be computed from the angular dependence of the wave functions. Extensive tables of relative strengths in LS coupling have been computed by White and Eliason[111] (line strengths) and by Goldberg[112] and Rohrlich[113] (multiplet strengths). The absolute strength which one computes for a transition depends on the radial eigenfunctions and thus on one's knowledge of the potential field for the transition electron(s). Short of self-consistent field calculations, two methods are commonly used to solve this problem approximately. One is the Coulomb (or hydrogenic) approximation of Bates and Damgaard.[114] The other method is the f-sum rule, which is based on the Thomas-Kuhn sum rule for one-electron systems. We may refer to Condon and Shortley[32] and to Goldberg et al.,[36] for discussions of these methods* and their application.

*In the hydrogenic approximation, one compares the levels of interest with the ionization potential, in order empirically to transform the atom into a "pseudo-hydrogen" atom. The radial matrix elements are then given as functions of the effective radial quantum numbers for the levels. The f-sum rule bypasses any explicit consideration of the radial eigenfunctions and states that "...the sum of the f-values governing transitions from a single level of an atom to all other energy levels, both discrete and continuous, is equal to the number of jumping electrons."[36] The f-value for a single transition may be set equal to unity when (1) the transition is much more probable than any others into and out of the given level, and (2) the levels of interest differ primarily in the quantum state of a single electron outside a fixed core.

We will first compare the measured gf-values for the lines of three CrI multiplets with relative values computed in LS coupling by Goldberg et al.[36] The multiplets (33, 143, 145) belong to the same transition, $3d^54s$-$3d^54p$. Figure 38 shows the experimental values and the normalized theoretical values in the customary matrix form. Out of the 25 lines allowed in these multiplets, 10 are covered by our measurements. The theoretical relative values are fairly well borne out by experiments; the largest deviation is ~50% for the normalization employed. We also note that the sums of experimental gf-values for the $^5G^o_3$ and $^5G^o_2$ rows of CrI(33) are indeed in the ratio of 2J+1 (7 and 5, respectively) to within the experimental error.

The calculations of Goldberg et al., are actually more comprehensive than we have so far indicated. By means of the f-sum rule, they computed absolute gf-values for lines in 14 multiplets belonging to the $3d^54s$-$3d^54p$ transition array. The values of interest are compared graphically with our experimental results in Figure 39. The proximity of the points to the 45° dashed line reflects the extent of (relative) agreement previously noted for Figure 38. All the lines can be represented by saying that the f-sum rule underestimates the gf-values by a factor of 1.9 ± 1.0.

C. The final topic in this section is the comparison of our absolute CrI gf-values with previous experimental determinations. Very few of the lines we have measured have also been measured absolutely by other workers. The previous studies have dealt primarily with the resonance lines and the lines of low excitation energy ($E_j \lesssim 1$ eV).

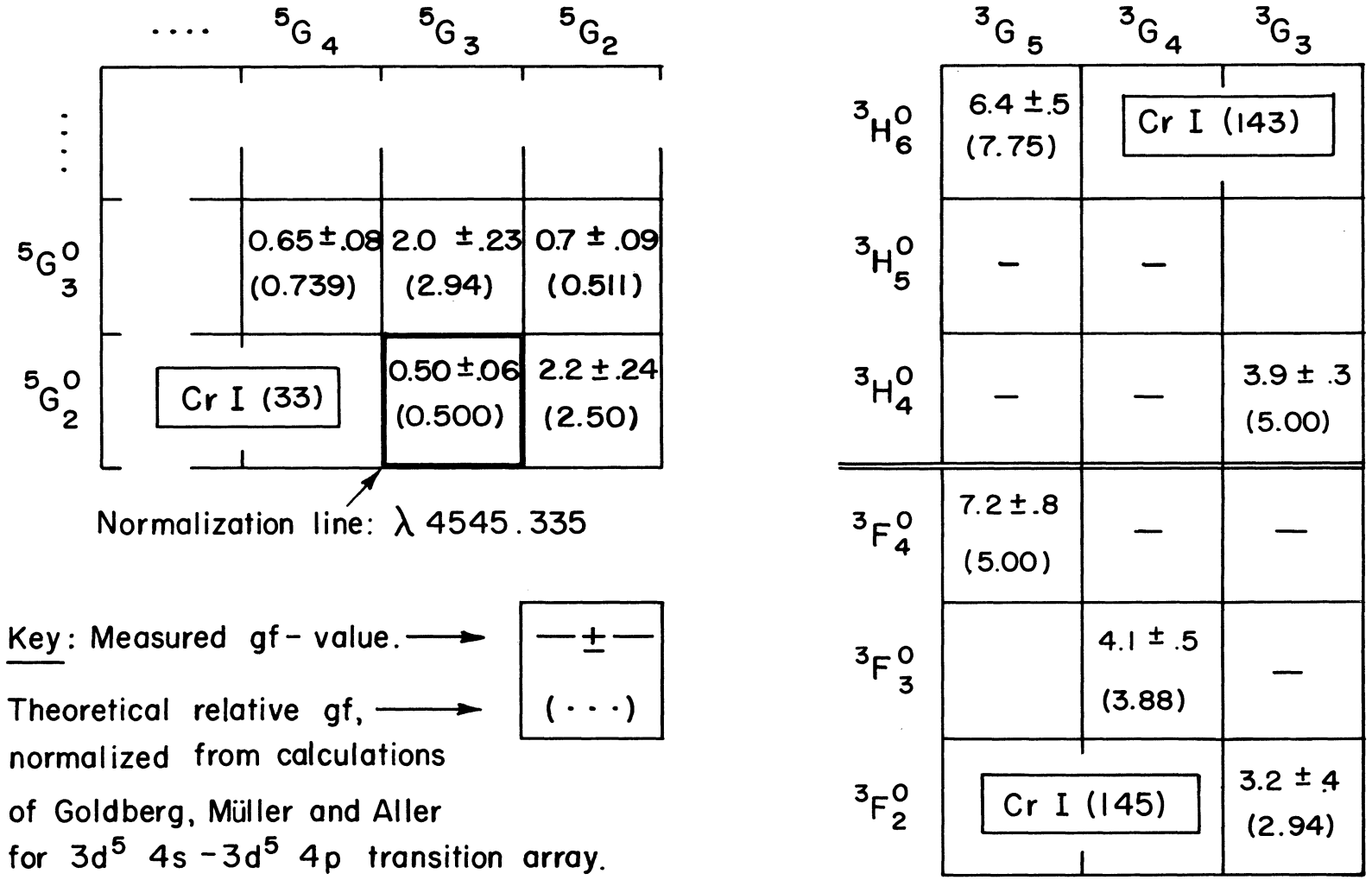

Figure 38. Comparison of experimental gf-values for CrI with normalized relative values computed in LS coupling.

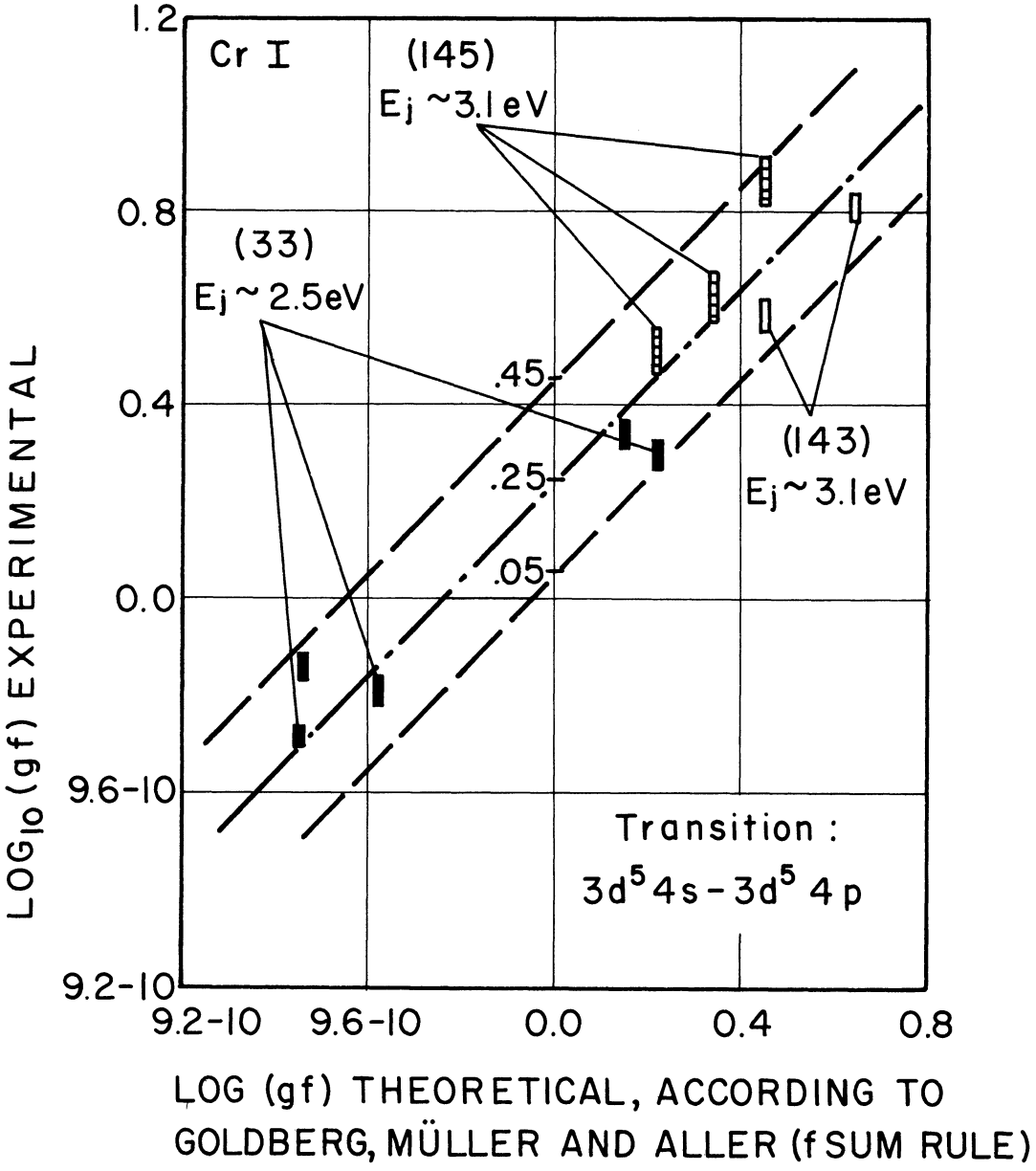

Figure 39. Comparison of theory and experiment for absolute gf-values of three CrI multiplets in the same transition array.

This emphasis on lower-lying transitions is due to the low temperatures in the sources employed, relative to the shock tube. Rather than extrapolating our results to the resonance lines, we will confine our comparisons to those lines which are common to both the past and present investigations. For the sake of completeness, it should be mentioned here that most of the CrI studies have been catalogued by Goldberg, Müller and Aller;[36] they conclude that the absolute gf-values for the resonance lines of CrI are still uncertain within an order of magnitude, even excluding those experiments which are now known to be faulty.

The comparison of gf-values in shown in Table XIII for two lines in one multiplet and one line in another. In addition to our work (Column "W"), two experimental sources are considered; some theoretical

TABLE XIII

COMPARISON OF ABSOLUTE gf-VALUES FOR CrI ACCORDING TO VARIOUS MEASUREMENTS AND CALCULATIONS

Lines of CrI		gf(Experimental)			gf(Theoretical)	
Mult.	λ(Å)	AA	OP	W	Σf	BD
(21)	4600.752	0.062	0.11	0.29 ± .03	-	0.89
(21)	4652.158	--	0.17	0.60 ± .05	-	1.8
(33)	4544.619	0.56	-	2.2 ± .24	1.4	0.09

estimates are also included. In the experimental section, "AA" denotes Allen and Asaad[109] and "OP" denotes Ostrovskiĭ and Penkin.[101] In the theoretical section, the single entry under "Σf" was computed by Goldberg

et al., and has already been discussed.* The column headed by "BD" gives the results we have computed by the method of Bates and Damgaard.

The measurements by Allen and Asaad were made on emission lines from an arc plasma whose temperature was about 4300°K. The arc electrodes were alloys of copper with small percentages of several other metals.

Using previously measured relative gf-values for each element, and assuming the plasma composition to be the same as the composition of the electrodes, Allen and Asaad established a relative gf-value scale covering all the metals. The absolute scale was then inferred by finding the factor which brought the relative scale into correspondence with a weighted mean of previous gf-value measurements on the various resonance lines.

Ostrovskiĭ and Penkin measured absolute gf-values for many low-lying lines of CrI by means of an interferometric absorption experiment, using the "hooks" method of Roshdestvensky.[115] We may also refer to Mitchell and Zemansky[33] for a discussion of this method. A vacuum furnace containing chromium vapor was used as one leg of an interferometer in Ostrovskiĭ and Penkin's work. The "anomalous dispersion" observed in the vicinity of an absorption line led to the product of the gf-value with the number density of atoms in the lower level of the line. The absolute gf-value was then computed from data on the vapor pressure of chromium as a function of temperature.

*The f-sum rule was not applied to CrI(21) since transitions of this type (d^4s^2-d^4sp) are known to be much weaker than indicated by $\Sigma f = 1$.

Our measured gf-values are about three to five times larger than indicated by the previous work. In view of the difficulties which arise in such studies, one can say that no line strength has been reliably determined until several independent methods yield consistent results. Rather than leaving this an entirely open question, however, we will make a few observations here on the methods so far employed for CrI.

It is difficult to judge the reliability of Allen and Asaad's absolute scale. These authors do not specify how the "weighted mean" of previous resonance line strengths was taken, while their bibliography of CrI strengths includes some values which are now known to be one or two orders of magnitude too low.[109] These early data were adversely affected by serious overestimates of the vapor pressure of chromium.

The reliability of Ostrovskii and Penkin's results depends directly on the chromium vapor pressure. If the data they used are borne out by future measurements, there can be little doubt that their absolute gf-value scale is correct. The temperature of their furnace is apparently well understood. Their relative gf-values[36,101] (resonance lines and lines of 1 eV excitation) demonstrate the excitation potential anomaly in Hill and King's relative values which now seems firmly established.

The absolute scale of our shock tube gf-values would be affected somewhat by at least two factors which we will discuss here. One is the vapor pressure data we have used for the absolute abundance of $Cr(CO)_6$ in the test gas, and the other is the high degree of ionization com-

puted for CrI behind the reflected shock. It is likely that the vapor pressures employed for $Cr(CO)_6$ are accurate to better than 5%, in view of (1) the agreement between our measurements and earlier work (Chapter III, Section 3), and (2) the control of ambient temperature during the mixing of $Cr(CO)_6$ with the neon carrier gas. As for errors in the small amount of CrI left after ionization, we have computed the effects of extra electron pressure due to impurities in the gas or the relaxation effects suggested by Doherty.[35] In Doherty's work at higher temperatures, electron pressures were observed to be ~20% above the computed values. If one allows excesses of this same order in the chromium experiments, α(CrI) is suppressed to the extent that the amount of CrI is increased by 15 to 20%. On these grounds it would not seem justified to reduce our absolute gf-value scale by more than 25%.

We will close this section by noting the disparity between experiment and theory shown by the Bates and Damgaard[114] values in Table XIII. Though the Coulomb approximation is often useful for light atoms, the results for CrI suggest that this theory can be very misleading for the heavier metals.

9. MEASUREMENT OF INTENSITIES AND gf-VALUES FOR CrII

To our knowledge, no previous measurement has been made of gf-values for CrII. We have therefore used the curve of growth in a direct manner to analyze the intensities of CrII lines emitted from the shock tube. Due to overlapping of lines from CrI, not all the observed CrII lines

could be reduced to absolute strength. A total of eight were measured, one in one multiplet (44), seven in another (30) with one double blend. The wavelengths, terms, energies and gf-values are given in Table XIV.

Each CrII line was measured in six experiments, in fact, the same low abundance experiments that were used to find the CrI gf-values given in Section 7. In every case, the value of $\mathcal{J}$ (C, a) was computed from the measured intensity and the shock tube Planck function, while the value of C/gf was computed from the appropriate thermal quantities. From $\mathcal{J}$ (C, a) the value of C was inferred via the theoretical curve of growth for a = ∞. The gf-value for each line was found by plotting C vs. C/gf for the six experiments. Examples of these graphs for two of the stronger CrII lines are shown in Figure 40. The vertical error bars again represent the 10% reliability of the photometric system.

In the absence of any data on the Stark coefficients for CrII, our use of the curve a = ∞ is perhaps open to objection. However there are good reasons for assuming that our damping ratios were large enough to permit the calculation of C from $\mathcal{J}$ (C, ∞). This evidence is discussed in a footnote.* Now that we have determined the gf-values with the

*Of the 42 cases treated (6 experiments x 6 lines + 1 blend) only seven had intensities such that $\mathcal{J} > 1$; for the two strongest cases, $\mathcal{J} \sim 1.6$. Even at this height on the growth diagram, the difference in $\log_{10}$ C is only 0.1 between the curves a = ∞ and a = 1. That the condition a = 1 could be achieved (or exceeded) is likely under the experimental conditions. Even the CrI resonance line (discussed in Section 6 of the last chapter) would have a~.06 due to quadratic Stark broadening by the electrons alone (p_{e2} = 3880 cgs, T_2 = 9635°K). For excited states of CrII in such an atmosphere, the total damping ratio could easily be larger by a factor of 100 or 1000. It should be noted that, since the Doppler width $\Delta\nu_D$ is roughly .03 Å, damping ratios as high as 5 or 10 would still leave the line shape undetected with a slit-image width of 3 Å. Finally, none

TABLE XIV

LINES OF Cr II MEASURED FOR ABSOLUTE INTENSITY

Multiplet No. (RMT)	Wavelength, (Å)	Lower		Upper		Measured Line Strengths, gf
		Term, T_j	Energy, $E_j(cm^{-1})$	Term, T_i	Energy, $E_i(cm^{-1})$	
44	4634.11	b $^4F_{3/2}$	32845	z $^4D^o_{1/2}$	54418	0.28 ± .04
30	4812.35	a $^4F_{7/2}$	31169	z $^4F^o_{9/2}$	51943	0.038 ± .005
30	4824.13	a $^4F_{9/2}$	31219	z $^4F^o_{9/2}$	51943	0.34 ± .05
30	4836.22	a $^4F_{5/2}$	31118	z $^4F^o_{7/2}$	51789	0.044 ± .006
30	4848.24	a $^4F_{7/2}$	31169	z $^4F^o_{7/2}$	51789	0.24 ± .03
30	4864.32	a $^4F_{5/2}$	31118	z $^4F^o_{5/2}$	51670	0.14 ± .02
30	4876.41	a $^4F_{3/2}$	31083	z $^4F^o_{3/2}$	51584	0.14 ± .02
30	4876.48	a $^4F_{7/2}$	31083	z $^4F^o_{5/2}$	51584	

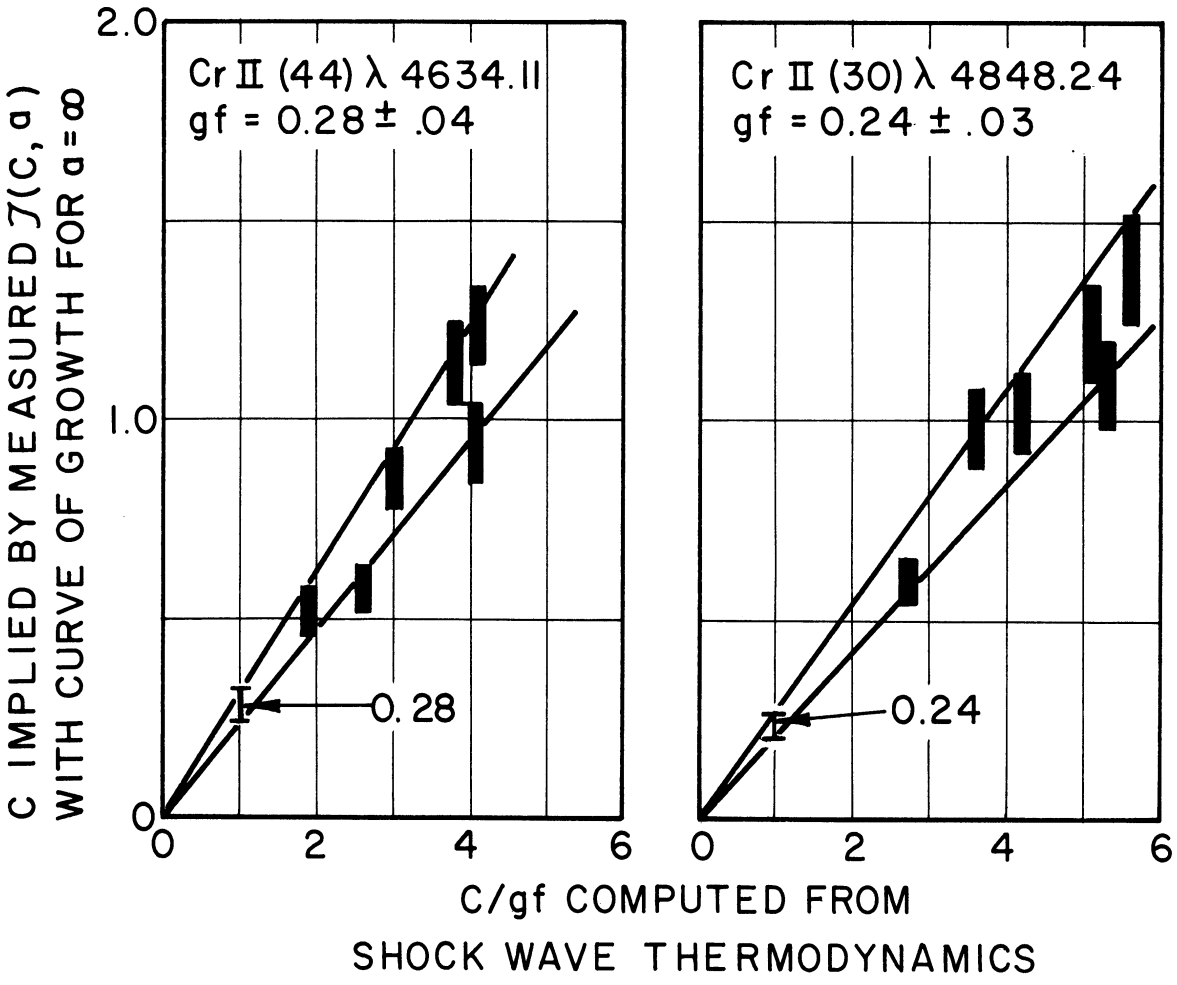

Figure 40. Two examples of graphical determination of gf-values for CrII.

linear portion of the curve of growth, it would be interesting to study the growth of line intensities for ionic abundances one or two decades higher.

We will close this section by comparing our gf-values for CrII (30) with LS coupling theory, though selection rules forbid this multiplet in a certain sense. The transition for CrII (30) may be written more fully as $3d^4(a^3F)4s(a^4F) - 3d^4(a^5D)4p(z^4F^o)$; i.e., the terms involved are built upon <u>different</u> terms of the parent ion.* Strict LS coupling forbids such transitions of one or more electrons outside a group to which they are not equivalent. (See the discussions in Chapter 9-11 of Condon and Shortley[32] and in the articles by Goldberg[112] and by Rohrlich.[113])

That CrII (30) is observed implies a partial breakdown of LS coupling, which is not too surprising in view of the existence of many intercombination multiplets (even between terms with the same parent ion). Nonetheless, the relative gf-values within CrII (30) agree very well with the relative strengths computed by White and Eliason[111] for LS coupling. Figure 41 shows this comparison in the usual JJ' matrix

---

of the graphs of C vs. C/gf showed curvature, within the experimental scatter. Such a curvature would have occurred if the lines had actually belonged to the non-linear curves of growth.

*Whether one really regards CrII(30) as a "forbidden" transition depends on how seriously one regards the parentage assigned for the $3d^4$ core. According to Condon and Shortley, there is some question about the exactness of the spin quantum number of the core, under the addition of anthing other than an s electron.

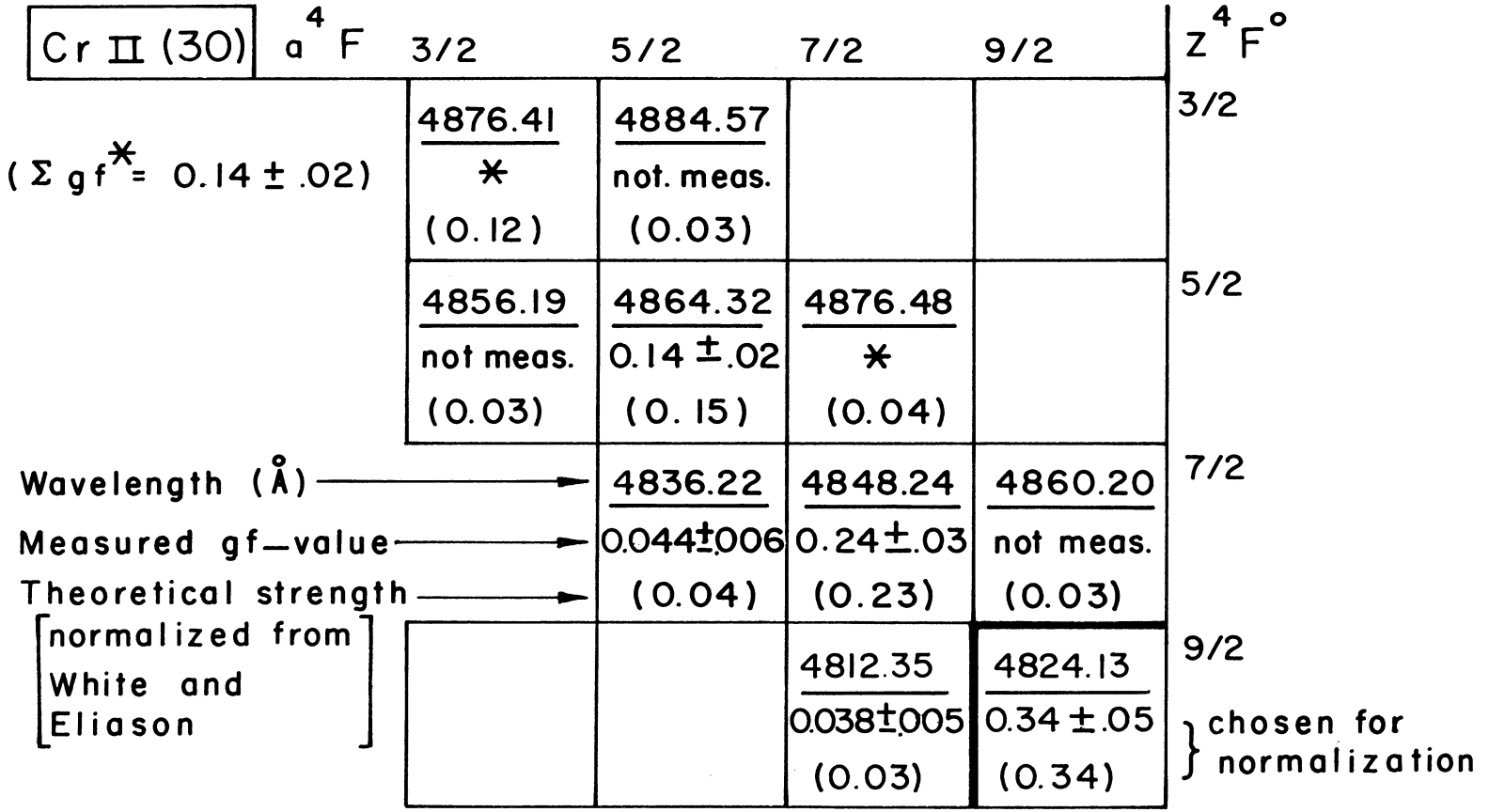

Figure 41. Comparison of measured gf-values for CrII (30) with theoretical relative strengths in LS coupling.

form.*

To summarize, we have found absolute gf-values for eight lines of CrII. These values are given in Table XIV. It is hoped that the gf-values we have measured for both CrI and CrII will be of some use in checking the Saha equation in other spectroscopic sources.

*Since the wavelength range covered by this multiplet is so small, the relative gf-values can be compared directly with the relative strengths. Generally, $(gf)_1(gf)_2 = (s_1/s_2)\lambda_2/\lambda_1$ within a multiplet. The strengths s are directly related to the matrix elements of the transition. (Recall Chapter V, Section 5.)

CHAPTER VII

SUMMARY OF THE PRESENT WORK AND CONSIDERATION OF FUTURE EXPERIMENTS

1. INTRODUCTION

In this dissertation, two regimes of luminosity in shock-heated gases have been considered. We have observed (1) the transient emission which arises from non-equilibrium processes, and (2) the steady emission from gases in thermal equilibrium. The principal aim has been to use the equilibrated gases as sources of light for quantitative spectroscopic measurements. Specifically, we have measured gf-values for a number of lines of neutral and singly ionized chromium, by observing the line intensities associated with the computed abundances and level populations of the atoms and ions. The several phases of this program will be summarized in Section 2. We will briefly review here the non-equilibrium studies, since they are for the most part incidental to the principal work. Two examples of transient emission were observed and studied semi-quantitatively.

A. In the chromium experiments, an intense spectrum of CrI was emitted by the gas immediately behind the reflected shock. The duration of this luminosity (< 10 μsec) varied inversely as the computed electron pressure in the primary flow. This behavior, and other observations given in Section 5 of Chapter VI, led us to conclude that the transient CrI emission was associated with ionization relaxation behind the reflected shock.

B. Strong emission by the C_2 molecule was observed when organic vapors were added to the shock tube gas. This phemonenon enabled direct photographs to be taken of the (otherwise non-luminous) shock fronts and boundary layers. These observations and their possible hydrodynamic applications are discussed in Section 5 of Chapter III. Experiments with methane showed that the C_2 molecule was rapidly synthesized in electronically excited states following the dissociation of methane behind shock fronts. In Chapter IV we have discussed the evidence for such processes and have advanced a supporting theory of a radiative and chemical-kinetic nature; similar experiments with other molecules are also proposed.

2. MEASUREMENT OF gf-VALUES FOR CrI AND CrII

We have measured the gf-values for a number of chromium lines by a direct method which consists, in essence, of dividing the absolute intensity of each emission line by the atomic population in the level responsible for the line. The success of this method indicates that the shock tube will be a valuable spectroscopic source in the future. On this basis, the comparitively sophisticated measurements to be proposed in Section 3 may be expected to come to the fore as more powerful techniques. However, many of the problems we have had to solve are common to any investigation of spectral line strength.

The chromium emission spectra were generated by the inclusion of small partial pressures of chromium carbonyl [$Cr(CO)_6$] in the neon

carrier gas. For the spectrograph employed, the lines of CrI and CrII were observed to have ample intensities for time-resolved spectroscopy. The lines had steady intensities for times of the order of 100 μsec behind the reflected shock. Since the neon carrier gas was only slightly ionized, the spectra were not confused by strong continuum emission. Thus it was clear that the work of Turner[12] and Doherty[35] (with the rare gases, hydrogen, carbon and oxygen) could be extended to chromium and, most likely, to any other metal for which gaseous compounds exist.

The abundance of chromium in the shock tube was controlled by means of the temperature dependence of the vapor pressure of chromium carbonyl. Since conflicting data had previously been published, we remeasured the carbonyl vapor pressure in the room temperature range and verified the results of Hieber and Romburg;[55] our data are given in Section 3 of Chapter III.

The thermodynamic effects of chromium carbonyl in the shock tube gas were computed by the iterative process described in Chapter II. The excitation and ionization of CrI, CI, OI and the excitation and dissociation of CO were found to cause significant reductions in the temperature of the gas behind the reflected shock, relative to the temperatures predicted for pure neon. For accurate calculations of these effects, it was necessary first to compute several thermodynamic functions for the species involved. Tables of these computations for

various atoms, ions and molecules are given in Appendix A. The dissociation of the carbonyl itself is discussed in Appendix B. The net result of this work was a complete set of thermodynamic predictions, for two levels of carbonyl abundance over a temperature range of 4000-11000°K behind the reflected shock. The computed states of the gas were then used in the spectroscopic experiments of Chapter VI, in order to find the abundances and level populations of CrI and CrII as functions of the primary shock speed.

For the spectroscopic program to succeed, it was essential to know whether or not the computed thermal states of the shock tube gas were actually achieved in the experiments. Several discrepancies with theory were observed in the experiments described in Section 6 of Chapter III. These, and similar measurements by other workers, related primarily to the velocities of the primary flow and the reflected shock as functions of the primary shock speed. These defects of ideal shock tube theory are now well known to arise from the viscosity of the gases and the consequent development of boundary layers on the shock tube walls.

Since the most important spectroscopic variables were the temperature and pressure of the gas, we initiated experiments designed to measure these quantities as directly as possible (Section 7 and 8 of Chapter III). The gas pressure was measured behind primary and reflected shocks by means of a quartz transducer. The kinetic temperatures on both sides of the reflected shock were computed from ob-

servations of flow velocity in both regions and of the reflected shock speed, the flow luminosity having been induced with caesium nitrate dust on a thread inside the flow channel. Though some deviations from ideal theory were also observed in this work, it was shown that the absolute pressure and the kinetic temperature of the gas near the end wall of the tube were very close to the theoretical values; i.e., the pressure was confirmed to within 5% and the kinetic temperature to within 2%, for the range of conditions appropriate to the spectroscopic experiments.

Given the agreement with theory for the kinetic temperature in the shock tube gas, it was then necessary to demonstrate that this temperature also described the degrees of ionization and the distributions of atoms over their excited states. We justified the assumption of complete thermal equilibrium in the chromium experiments on four grounds.

A. The observations of ionization relaxation for CrI behind the reflected shock showed that steady states of emission were established in times short compared to the total observing time.

B. Doherty's calculations for neon and hydrogen in the shock tube showed that only small deviations from thermal equilibrium would occur in a state of steady luminosity. This is due primarily to the number density of electrons capable of maintaining the equilibria via collision processes. The case of chromium was expected to be even more favorable, owing to the lower ionization potential and the much smaller

spacings between energy levels.

C. The reflected shock speed data given in Section 5, Chapter VI confirmed that, for the higher shock strengths, considerable amounts of translational energy were being taken up in internal degrees of freedom behind the reflected shock. This was taken only as a favorable sign, however, since the viscosity-induced defect in reflected shock speed was still strong enough to prevent a detailed comparison with theory.

D. In the spectroscopic work described in Chapter VI we observed that, for every line of CrI and CrII, the integrated intensity possessed the correct (linear) dependence on the abundances and level populations computed from the equilibrium equations.

The observations of the shock tube emission spectrum were made with the equipment and techniques described in Sections 2-4 of Chapter VI. Charatis' time-resolving spectrograph[105] was used to record the lines of CrI and CrII and the bands of CrO over most of the visible spectrum. The quantitative measurements on CrI and CrII were confined to the wavelength range 4500-5000 Å. These spectra were reduced to absolute line intensity via an extension of Doherty's photometric method[35] to include a primary radiation standard external to the shock tube. The standard source was a DC carbon arc operated after the manner of Euler[107] (and others) so as to emit a continuum of known brightness.

The absolute line intensities were reduced to absolute gf-values for the lines by combining the computed state of the gas with the radiative transfer theory discussed in Chapter V. The curve-of-growth diagram was used throughout the data reduction (Section 7 and 9 of Chapter VI) to provide a continual check on the importance of self-absorption. The gf-values were measured for twenty lines of CrI and eight lines of CrII. To our knowledge, no previous measurement has been made of CrII gf-values.

The relation of our CrI results to those found in previous work is discussed in Sections 7 and 8 of Chapter VI. Only three of the CrI lines we have studied have also been measured for absolute strength by other workers. For these lines, our gf-values are larger by factors of 4.5 and 3, respectively, than the values found by Allen and Asaad[109] and Ostrovskiĭ and Penkin.[101] Though there is reasonable doubt about the former work, the latter seems as internally consistent as ours. The factor of 3 disparity will apparently have to stand until more definitive measurements are made. Situations of this kind are commonly encountered in line strength studies, due to the difficulty of measuring the atomic populations.

The results we have found for twenty lines of CrI appear to constitute a significant remeasurement of the relative gf-value scale for this element. The original work by Hill and King[46] has been shown to contain a systematic overestimate of relative line strength with increasing excitation potential. This confirms the numerous sugges-

tions of a temperature error in the original work, which have arisen from studies of CrI spectra in the solar atmosphere and in laboratory sources. All the data now available indicate that Hill and King underestimated the temperature of their furnace by 10% to 20% in the chromium experiments. The resulting errors in level populations gave rise to tenfold overestimates for the gf-values of high-excitation lines, relative to the values for low-lying lines. It is hoped that the new set of CrI gf-values given here will be useful in future measurements of excitation temperature.

3. CONSIDERATION OF FUTURE EXPERIMENTS

Taken altogether, the spectroscopic work done on various elements in this laboratory has demonstrated a considerable flexibility of the shock tube as a spectroscopic source. It has proved possible to use neon as an inert carrier gas up to 10000°K and yet to generate strong NeI emission by raising the temperature to 12000 or 13000°K. A wide range of relative intensities between the spectra of CrI and CrII has been covered by variations of temperature and chromium abundance. The spectra of several elements of moderate ionization energy have been studied. Considerable Stark broadening of H_β has been observed for readily available ion densities.

The three dissertations derived from this work have included several quantitative measurements as well as many qualitative observations. The Stark broadening of H_β has been measured as a function of ion density

by Turner[12] and Doherty.[35] Absolute gf-values have been measured for a total of 96 atomic lines by Doherty (NeI, CI, OI, NI, AI) and this author (CrI, CrII). Semi-quantitative studies have been made by Turner of the second-order Stark broadening of rare gas lines (AI, KrI, XeI). The approach to equilibrium ionization behind shock waves has been studied by Turner (XeI, primary shocks) and this author (CrI, reflected shocks). This phenomenon of ionization relaxation has also been recognized in several other gases. The strong non-equilibrium radiation by C_2 and CN molecules has been studied to some extent by all three authors. In addition to the species listed so far, we have also generated the line spectra of XeII, SI, ClI, ClII, CuI and the band spectra of CO, CrO by putting the appropriate gases in the shock tube.

The success of this program indicates that the use of the shock tube should be further explored for the purposes of quantitative spectroscopy. Several other workers in this field have come to the same conclusion.* Thus it seems appropriate to consider the measurements and the techniques of measurement which might profitably be pursued in future work of this kind. We will first discuss some additional methods which could be applied to the experiments reported here.

*In the past few years, a number of interesting experiments on shock tube spectroscopy have been reported by workers in this country and in England, Germany and Russia. Much of this work has not been treated here since it does not bear directly on the experiments under discussion. For summaries of the omitted work, we refer the interested reader to References 15 and 16. The range of available temperatures has been extended to ~100,000°K by the development of electrically-driven shock tubes.

An obvious improvement in the accuracy and generality of the calculations would result from the use of digital computers. Some machine computations of shock transitions, including ionization, dissociation, etc., have been published in References 50 and 51. The necessary thermodynamic functions for atoms and molecules can also be computed by machine; in fact, a set of computed thermal functions covering most of the periodic table does not seem to be an unreasonable goal. Such results would find wide application in astrophysics and experimental gas dynamics.

The spectroscopic measurements can be made more definitive by the use of methods which can broadly be classed as absorption spectroscopy, in contrast to the exclusively emission spectroscopy we have done. For this one needs a source of continuous radiation which illuminates the shock tube gas during, say, the period of steady conditions behind the reflected shock. A number of important measurements can be made with different methods of observing the transmitted light. The three methods discussed below are applicable to the shock tube for determining gf-values and the temperature and electron density in the hot gas.

A. For the observation of an absorption line, the brightness of the external source must exceed the value of the Planck function $B_\nu(T)$ corresponding to the temperature of the shock tube gas. In this case, the integral of the intensity absorbed out of the continuum by the line is analogous to the integrated line intensity which one treats for emission spectra. The theory of the curve of growth goes through as before,

except that the Planck function entering into the ordinate of the diagram is now that of the external source rather than the $B_\nu(T)$ of the shock tube gas. This method has the advantage that the Planck function of interest can be measured directly.

B. The technique of line-reversal can be used to find the shock tube Planckfunction $B_\nu(T)$, if one has a time-dependent source whose brightness passes through the value of $B_\nu(T)$ during the time of interest. If the intensity of the source is, say, decreasing when this cross-over occurs, then one observes a reversal of the absorption spectrum into a spectrum showing emission lines on top of a weaker continuum. Thus the $B_\nu(T)$ for the shock tube is put in evidence by measurements of the source brightness at the time of reversal. The form of $B_\nu(T)$ can be checked by determining the reversal points of several spectral lines. A number of recent line-reversal studies with shock tubes have been summarized by Kolb and Griem.[16] We understand that Charatis[105] is undertaking reversal measurements on CrI and CrII.

C. If the shock tube gas is made to sit in one leg of an optical interferometer, one can measure electron densities and gf-values of spectral lines by means of the wavelength dependence of the refractive index of the gas. Alpher and White[74] have determined electron densities in shock-heated argon by measuring fringe shifts at two wavelengths for which the refractive index of neutral argon was known. We have discussed the interferometric method of measuring gf-values in Section 8 of Chapter VI. To our knowledge, no shock tube measurement has yet

been performed in this way. The method has the advantage of avoiding any measurement of emitted or absorbed energy, but shares with other methods the necessity of knowing the atomic populations.

A promising application of the shock tube is the measurement of gf-values. The shock tube provides the spectroscopist with such a range of temperature and abundance that the lines of many atoms and their ions can be studied. For quantitative measurements it is necessary to introduce the elements into the shock tube in the gas phase. This can be done for at least 50 elements by means of the volatile compounds which they form. We will mention a number of the less familiar examples here. The carbonyl compounds alone offer the possibility of studying eleven other metals besides chromium, including such seemingly unlikely ones as tungsten and osmium (see Appendix B). One can use volatile halide compounds (e.g., $GaCl_3$, SF_6, VCl_5) to generate the spectra of the halogens as well as the elements with which they are combined; other examples are boron, titanium, indium, silicon, and carbon. The hydrides afford the means of introducing into the shock tube gas such elements as germanium, boron, selenium, tellurium, silicon, phosphorous, arsenic and antimony. Volatile organic compounds are formed, for example, by lead and manganese; Turner[12] used copper acetyl acetonate to generate spectra of CuI. It is clear that various molecular band spectra can also be generated by these means and studied under conditions of thermal equilibrium.

The properties of many of the compounds we have discussed pose additional problems for the experimenter. Decomposition (by heat and water vapor) and toxicity are problems which can be avoided by careful technique. Knowing the abundance of the compounds in the shock tube gas is a problem of a different kind. The method we have used for $Cr(CO)_6$, namely the control of vapor pressure via temperature, would seem to be applicable in many cases. For this, however, one needs to have reliable vapor pressure data. We suggest that a considerable amount of remeasurement by modern methods could profitably be carried out on the physical properties of these unusual compounds.

In Section 6, Chapter V, we have discussed the importance of knowing the Stark coefficients for interpreting the integrated intensity of a self-absorbed emission line. Though there are practically no data available for the Stark effect in CrI and CrII, we were fortunately able to conduct and interpret the experiments of Chapter VI in the regime of low optical depth where the line shape is not very important. In other shock tube experiments, and particularly in other sources having relatively inflexible conditions, one can expect to have to deal directly with the effects of Stark broadening. For this reason, there is a need for quantitative Stark effect measurements on the lines of many elements. Aside from the interpretation of line intensity, the Stark coefficients are obviously important parameters for the theory of line broadening in plasmas and for the experimental determination of plasma conditions via the observed line shapes.

The great interest in gf-values arises from a desire to deduce from the observed intensities of spectral lines some information about the atomic abundances and the thermodynamic states in various light sources. The line strengths for boron and flourine will probably be useful quantities to know in future developments of reaction engines. In the branch of plasma physics devoted to thermonuclear research, the spectra of CII, CIII, OIII, etc., are commonly encountered. A knowledge of their gf-values would aid in determining their abundances, which are often crucial quantities in limiting the temperature of the plasma.

The need for line strengths is probably the greatest in astrophysics, particularly for the determination of elemental abundances. For example, there is currently some interest in relating the abundances of elements found in meteorites to the abundances in the stars. Since silicon is the reference element commonly used in meteoritic studies, whereas the solar reference element is hydrogen, the silicon-hydrogen ratio in the sun is an important quantity. According to the recent survey by Goldberg, Müller and Aller,[36] the abundance ratio of silicon to hydrogen in the solar atmosphere is uncertain within a factor of 6, due to the lack of reliable gf-values for the lines of SiI and SiII. It is generally believed that the determination of elemental abundances in the universe will be decisive in the field of evolutionary theories. We anticipate that the shock tube will prove to be of great value in determining the atomic constants which are needed in the studies we have discussed.

APPENDIX A

COMPUTED THERMODYNAMIC FUNCTIONS

This appendix consists of tables of the thermodynamic functions we have computed for NI, OI, CrI, CoI, NiI, MoI, WI, NeI, CsI, CI, HgI (and their ions) and N_2, CO. The temperature range of interest is 0-10000°K in most cases. The computations were performed in various ways by S.C.C. Ting and this author, using primarily the energy level data given in Charlotte Moore's compilations.[53] Specifically, we have computed the partition functions Z, the internal excitation functions f_E, f_V and the dissociation-ionization functions f(T) discussed in Section 4 of Chapter II. From this chapter, we recall the defining Equations (II.17, 21, 22, 23, 26, 30, 31) to avoid repetition here. For example, we have defined the ionization function f(T) in Equation (II.17) by the equilibrium condition (Saha equation) $\alpha/1-\alpha = f(T)/Pe$, where Pe is the electron pressure and α is the degree of ionization of the atom of interest. For the values of the ionization function given in the tables, we have used the notation f(T) = N(n) to represent $f(T) = N \times 10^n$. The ionization (or dissociation) energy is denoted throughout by χ.

Tables A.1 through A.11 are concerned primarily with the first ionization equilibira of the atoms listed (in order) above. For A.1 through A.7 (nitrogen-tungsten), the partition functions ZI, ZII and electronic excitation functions f_EI, f_EII were manually computed at 2500, 5000, 7500 and 10000°K. Since the shock tube work involved intermediate tem-

peratures, the computations were graphed for purposes of interpolation. The validity of this procedure was tested in several cases, and the accuracy of the graphical values was found to lie between 1% and 3%. These graphs were also used to find the intermediate values of ZI/ZII given in the tables. This ratio is generally such a slowly varying function of temperature that the check calculations showed agreement to better than 1%. Thus the ionization function f(T) is appropriately given to three figures in Tables A.1 - A.7.

Tables A.8 and A.9 give the results for neon and caesium, respectively. These are unusual cases due to the high (NeI) and low (CsI) ionization energies. Also, Z = 1 and f_E = 0 for NeI and CsII. In the case of neon, seven values of temperature between 5000 and 13000°K are considered. Since caesium is so much more readily ionized, we have covered the temperature range 500-8000°K in ten steps.

CI and HgI are treated in Tables A.10 and A.11, respectively. These results were computed by Ting on the IBM 704 at The University of Michigan Computing Center. Ting's tables were more extensive than indicated here and required about five minutes of running time on the computer for each element. Here we list the values for nine temperatures between 2000 and 10000°K. Table A.10 supplants (and confirms) the results we computed for CI in the manner of Tables A.1-A.7.

Finally, Table A.12 gives the vibrational excitation functions $f_V(T)$ and the dissociation function f(T) computed for N_2 and CO. The rigid rotator and harmonic oscillator approximation were used (as described in Chapter II) to cover the temperature range 2500-10000°K in ten steps.

TABLE A.1

$NI \rightleftharpoons NII + e^-$; $\chi(NI) = 117{,}345\ cm^{-1} = 168{,}800°K$

T°(K)	Z(NI)	f_E(NI)	Z(NII)	f_E(NII)	Z(I)/Z(II)	f(T) (cgs)
2500	4.00	~0	8.48	0.051	0.472	2.02 (-21)
3000					0.467	2.50 (-16)
4000					0.461	6.58 (-10)
5000	4.04	0.057	8.80	0.056	0.459	5.40 (-6)
6500					0.463	2.45 (-2)
7500	4.27	0.245	9.09	0.104	0.470	1.13 (0)
9000					0.486	7.49 (+1)
10000	4.72	0.452	9.42	0.149	0.501	5.98 (+2)

TABLE A.2

$OI \rightleftharpoons OII + e^-$; $\chi(OI) = 109{,}837\ cm^{-1} = 158{,}000°K$

T(°K)	Z(OI)	f_E(OI)	Z(OII)	f_E(OII)	Z(I)/Z(II)	f(T) (cgs)
2500	8.64	0.043	4.00	~0	2.16	3.26 (-20)
3000					2.17	1.93 (-15)
4000					2.20	2.09 (-9)
5000	8.87	0.048	4.00	0.009	2.22	9.76 (-6)
6500					2.24	2.76 (-2)
7500	9.11	0.096	4.06	0.078	2.24	1.01 (0)
9000					2.24	5.39 (+1)
10000	9.42	0.139	4.23	0.217	2.23	4.04 (+2)

TABLE A.3

$CrI \rightleftharpoons CrII + e^-$; $\chi(CrI) = 5465\ cm^{-1} = 78{,}492°K$

T°K	Z(CrI)	f_E(crI)	Z(crII)	f_E(CrII)	Z(I)/Z(II)	f(T) (cgs)
2500	7.30	0.165	6.02	0.027	1.21	3.83 (-6)
3000					1.30	1.05 (-3)
4000					1.40	1.47 (0)
5000	10.5	0.944	7.17	0.657	1.47	1.19 (+2)
6500					1.51	8.47 (+3)
7500	17.8	1.78	11.3	1.59	1.58	5.83 (+4)
9000					1.69	5.06 (+5)
10000	33.5	2.44	18.6	2.06	1.80	1.52 (+6)

TABLE A.4

$CoI \rightleftharpoons CoII + e^-$; $\chi(CoI) = 63438\ cm^{-1} = 91256°K$

T(°K)	Z(CoI)	f_E(CoI)	Z(CoII)	f_E(CoII)	Z(I)/Z(II)	f(T) (cgs)
2500	22.0	0.589	18.4	0.658	1.19	2.35 (-8)
3000					1.15	1.71 (-5)
4000					1.12	7.30 (-2)
5000	33.2	0.695	29.7	0.666	1.12	1.18 (+1)
6500					1.13	1.58 (+3)
7500	44.8	0.867	38.6	0.653	1.16	1.45 (+4)
9000					1.22	1.64 (+5)
10000	59.6	1.18	46.2	0.650	1.25	5.97 (+5)

TABLE A.5

$NiI \rightleftharpoons NiII + e^-$; $\chi(NiI) = 61579\ cm^{-1} = 88{,}581°K$

T(°K)	Z(NiI)	f_E(NiI)	Z(NiII)	f_E(NiII)	Z(I)/Z(II)	f(T) (cgs)
2500	24.6	0.366	7.79	0.283	3.16	2.67 (-8)
3000					3.13	1.59 (-5)
4000					3.02	5.26 (-2)
5000	30.5	0.288	10.7	0.696	2.87	8.41 (0)
6500					2.52	1.08 (+3)
7500	34.7	0.371	14.8	0.887	2.34	1.02 (+4)
9000					2.17	1.30 (+5)
10000	40.1	0.629	19.1	0.951	2.10	5.84 (+5)

TABLE A.6

$MoI \rightleftharpoons MoII + e^{-}$; $\chi(MoI) = 57260\ cm^{-1} = 82369°K$

T(°K)	Z(MoI)	f_E(moI)	Z(MoII)	f_E(MoII)	Z(I)/Z(II)	f(T) (cgs)
2500	7.04	0.044	6.03	0.039	1.17	8.15 (-7)
3000					1.16	3.31 (-4)
4000					1.16	6.52 (-1)
5000	8.83	0.901	7.63	0.922	1.16	6.88 (+1)
6500					1.17	6.02 (+3)
7500	16.5	2.13	13.7	1.90	1.20	4.57 (+4)
9000					1.27	4.02 (+5)
10000	33.1	2.65	24.8	2.19	1.33	1.30 (+6)

TABLE A.7

WI $\rightleftharpoons$ WII + e^- ; χ(WI) = 64400 cm^{-1} = 92640°K

T(°K)	Z(WI)	f_E(WI)	Z(WII)	f_E(WII)	Z(I)/Z(II)	f(T) (cgs)
2500	4.79	1.42	5.57	1.16	0.860	1.92 (-8)
3000					0.870	1.43 (-5)
4000					0.893	6.41 (-2)
5000	12.6	1.48	13.7	1.42	0.921	1.15 (+1)
6500					0.967	1.48 (+3)
7500	25.0	1.87	24.9	1.53	1.00	1.40 (+4)
9000					1.07	1.62 (+5)
10000	44.4	2.10	39.4	1.56	1.13	5.68 (+5)

TABLE A.8

$NeI \rightleftharpoons NeII + e^-$; $\chi(NeI) = 173{,}932\ cm^{-1} = 250{,}200°K$

$Z(NeI) = 1$, $f_E(NeI) = 0$, $Z(NeII) = 4 + 2e^{-1125/T}$

T(°K)	Z(NeII)	f_E(NeII)	f(T) (cgs)
5000	5.597	0.06419	1.224 (-12)
6500	5.682	0.05125	2.483 (-7)
7500	5.721	0.04514	4.306 (-5)
9000	5.765	0.03827	2.493 (-2)
10000	5.787	0.03474	5.249 (-1)
11500	5.814	0.03052	1.949 (+1)
13000	5.834	0.02721	3.271 (+2)

TABLE A.9

$CsI \rightleftharpoons CsII + e^-$; $\chi(CsI) = 31407\ cm^{-1} = 45179°K$

$Z(CsII) = 1$, $f_E(CsII) = 0$

T(°K)	Z(CsI)	f_E(CsI)	f(T) (cgs)
500	2.00	~0	9.89 (-34)
1000	2.00	~0	2.42 (-13)
1500	2.00	~0	2.36 (-6)
2000	2.00	0.010	9.07 (-3)
2500	2.01	0.041	1.41 (0)
3000	2.04	0.113	4.59 (+1)
4000	2.08	0.460	4.02 (+3)
5000	2.57	1.10	5.49 (+4)
6000	3.40	2.00	2.90 (+5)
8000	7.28	3.15	1.84 (+6)

TABLE A.10

$CI \rightleftharpoons CII + e^{-}$; $\chi(CI) = 90{,}878\ cm^{-1} = 130{,}730°K$

T(°K)	Z(CI)	f_E(CI)	Z(CII)	f_E(CII)	f(T) (cgs)
2000	8.814	0.0239	5.820	0.0302	3.226 (-21)
3000	8.911	0.0348	5.879	0.0202	2.577 (-11)
4000	9.033	0.0628	5.909	0.0152	2.825 (-6)
5000	9.192	0.0947	5.927	0.0123	3.356 (-3)
6000	9.377	0.1238	5.940	0.0109	4.060 (-1)
7000	9.576	0.1480	5.950	0.0113	1.316 (+1)
8000	9.780	0.1680	5.960	0.0145	1.861 (+2)
9000	9.985	0.1854	5.972	0.0212	1.506 (+3)
10000	10.191	0.2025	5.988	0.0319	8.232 (+3)

TABLE A.11

$Hg \rightleftharpoons HgII + e^-$; $\chi(HgI) = 84{,}184\ cm^{-1} = 121{,}100°K$

T(°K)	Z(HgI)	f_E(HgI)	Z(HgII)	f_E(HgII)	f(T) (cgs)
2000	1.000	0.0000	2.000	0.0000	1.204 (-18)
3000	1.000	0.0000	2.000	0.0000	1.934 (-9)
4000	1.000	0.0001	2.000	0.0001	9.588 (-5)
5000	1.000	0.0008	2.000	0.0011	7.140 (-2)
6000	1.001	0.0049	2.001	0.0053	6.380 (0)
7000	1.002	0.0178	2.004	0.0158	1.676 (+2)
8000	1.006	0.0495	2.011	0.0355	2.033 (+3)
9000	1.016	0.1175	2.023	0.0664	1.462 (+4)
10000	1.035	0.2500	2.041	0.1093	7.239 (+4)

TABLE A.12

	N_2		CO	
T(°K)	f_v	f(T)	f_v	f(T)
2500	0.469	2.22 (-8)	0.501	3.65 (-10)
3000	0.540	5.06 (-5)	0.572	2.36 (-6)
3500	0.592	1.32 (-2)	0.619	1.25 (-3)
4000	0.634	8.17 (-1)	0.661	1.44 (-1)
4500	0.670	2.14 (+1)	0.693	5.78 (0)
5000	0.697	2.89 (+2)	0.727	1.11 (+2)
6500	0.766	6.93 (+4)	0.780	5.39 (+4)
7500	0.797	8.32 (+5)	0.797	8.61 (+5)
9000	0.816	1.31 (+7)	0.828	1.96 (+7)
10000	0.838	5.39 (+7)	0.859	8.48 (+7)

APPENDIX B

THE DISSOCIATION EQUILIBRIUM FOR CHROMIUM CARBONYL

The reaction

$$Cr(CO)_6 \rightleftharpoons Cr + 6\,CO \tag{B.1}$$

goes completely to the right at temperatures far below those that one might expect from the stability of the compound at room temperature and the moderately high dissociation energy

$$\chi_{Cr(CO)_6} = 171 \text{ kilocalories/mole} = 86{,}100°K/\text{particle}. \tag{B.2}$$

A strong hint that this is the case is provided by the experimental observations* of chromium deposition from the carbonyl vapor at temperatures above 100°C.

The relative ease with which chromium carbonyl may be dissociated is due to the unusual form of the mass action law governing reaction (B.1). As before, we will represent the extent of the reaction by α, the fractional dissociation of the carbonyl. In any equilibrium state, the pressures of chromium and carbon monoxide are

$$p(Cr) = \alpha(Cr(CO)_6)\,p^o(Cr(CO)_6),$$

$$p(CO) = 6p(Cr),$$

*Volatile carbonyls and carbonyl hydrides are know to exist for at least twelve metals: Cr, Fe, Ni, Mo, Ru, W, Os, Co, Rh, Re, Ir, and Mn. Summaries of the carbonyl properties and references to the original literature are given in Vols. I and II of Sidgwick[116] and in the article by Mattern and Gill in Bailar's[117] compilation.

where p^o is the carbonyl pressure if no dissociation were to take place. The temperature is assumed to be so low that CO does not dissociate and Cr does not ionize. The equilibrium condition is then

$$\frac{\alpha^7}{1-\alpha} = \left(\frac{kT}{6p^o}\right)^6 \frac{Z_{Cr}\left(Z_{CO}\right)^6}{Z_{Cr(CO)_6}} e^{-\chi/kT} \qquad (B.3)$$

Neglecting the vibration of CO, this may be written as

$$\frac{\alpha^7}{1-\alpha} = \frac{1.24 \times 10^{32}\ T^{21}\ e^{-\chi/kT}}{(p^o)^6\ Z_{Cr(CO)_6}} \qquad (B.4)$$

We have computed the value of χ given in (B.2) and the partition function Z from thermochemical data* given in the recent literature. Sample values of the partition function are given in Table B.1.

The large number of states available to the carbonyl even at low temperature is due to its many allowed modes of vibration and the close packing of its rotational levels. Owing to the large moment of inertia of the molecule, the computed** rotational term constant is

*From their near-infrared absorption data, Hawkins, Mattraw, Sabol and Carpenter[118] have computed thermodynamic functions up to 600°K for chromium and molybdenum carbonyl. The internal partition function follows from the free energy (e.g., see Herzberg, Vol. II, Chapter V).[119] Sharifov and Rezukhina[120] have measured the heats of formation for the carbonyls of Cr, Mo and W. The dissociation energy then follows by an energy cycle. The other data required are the heats of formation for Cr vapor and CO, the internal heat content of the carbonyl (Hawkins et al.), and its heat of sublimation (see Section 3 of Chapter III).

**See Brockway, Ewens and Lister[121] for electron diffraction data on the internuclear distances in $Cr(CO)_6$.

$$B_{Cr(CO)_6} = 0.022 \text{ cm}^{-1},$$

which is about 1/100 of the values typical for such molecules as CO. The magnitudes of χ and Z might be expected to suppress the carbonyl dissociation significantly. These effects, however, are over-ridden at about 600°K by the temperature sensitivity in the numerator of Equation (B.4). This is illustrated in Table B.2. Z(700°K) was estimated by extrapolation of the data of Hawkins et al. The dissociation of $Cr(CO)_6$ is certainly complete at the higher temperatures of interest in this report (2000°K and above).

TABLE B.1

PARTITION FUNCTION FOR CHROMIUM CARBONYL

T	$Z_{Cr(CO)_6}$
100°K	1.02×10^5
298	8.36×10^9
600	1.85×10^{15}

TABLE B.2

DEGREE OF DISSOCIATION, $\alpha(Cr(CO)_6)$

T(°K)	$p^o[Cr(CO)_6]$	
	10^2 cgs	10^3 cgs
600	0.89	0.17
700	1.0	1.0

REFERENCES

1. Berthelot, M. and Vielle, P., Compt. Rend. 93. 18 (1881).

2. Mallard, E. and Le Chatelier, H. L., Compt. Rend. 93, 145 (1881).

3. Dixon, H. B., et al., Phil. Trans. Roy. Soc. A200, 315 (1903).

4. Lewis, Bernard and von Elbe, Guenther, Combustion, Flames and Explosions of Gases, Academic Press, Inc. (1951).

5. Vielle, P., Compt. Rend. 129, 1228 (1899).

6. Kobes, K., Zeit. Öst. Ing.-u-Arch. Vereines 62, 558 (1910).

7. Schardin, H., Phys. Zeit. 33, 60 (1932).

8. Courant, R. and Friedrichs, K. O., Supersonic Flow and Shock Waves, Interscience (1948).

9. Payman, W., Shepherd, W. F. C., et al., Proc. Roy. Soc. A120, 90 (1928); Proc. Roy. Soc. A132, 200)1931); Proc. Roy. Soc. A148, 604 (1935); Proc. Roy. Soc. A152, 418 (1935); Proc. Roy. Soc. A158, 348 (1937); Proc. Roy. Soc. A186, 293 (1946).

10. Toepler, A., Ann. der Physik und Chemie (Poggendorff) 5th series, 127, 556 (1866); 128, 126 (1866); 131, 33 (1867); 131, 180 (1867); 134, 194 (1868).

11. Muraour, H. and Michel-Levy, A., Compt. Rend. 198, 825, 1499, 1760, 2091 (1934).

12. Turner, Eugene B., "The Production of Very High Temperatures in the Shock Tube with an Application to the Study of Spectral Line Broadening", PhD Thesis and University of Michigan Engineering Research Institute Report No. 2189-2-T, AFOSR TN-56-150, ASTIA Document No. AD 86309 (May,1956).

13. Zel'dovich, Ia. B., J. Exptl. Theoret. Phys. (USSR) 32, 1126 (1957); Soviet Physics JETP 5, 919 (1957).

14. Glass, I. I. and Hall, J. G., Shock Tubes, University of Toronto Institute of Aerophysics Review No. 12 (May, 1958) and Section 18, Volume 6, Handbook of Supersonic Aerodynamics, Navord Report 1488 (December, 1959).

REFERENCES (Continued)

15. Laporte, O. and Wilkerson, T. D., J. Opt. Soc. Am. 50, 1293 (1960).

16. Kolb, Alan C. and Griem, Hans R., "High Temperature Shock Waves", Chapter 1, Atomic and Molecular Processes, D. R. Bates (ed.), Academic Press (1961).

17. Gouy, G. L., Ann. Chim. Phys. 18, 5 (1879).

18. White, H. E., Introduction to Atomic Spectra, McGraw-Hill (1934).

19. Voigt, W., Ber Münch Akad. Wiss., 603 (1912).

20. Reiche, F., Verh. d. D. Phys. Ges. 15, 3 (1913).

21. Weisskopf, V., Zeits. f. Physik 75, 287 (1932).

22. Michelson, A. A., Astrophys. J. 2, 251 (1895).

23. Lorentz, H. A., Koninklijke Akad. Wetenschappen Amsterdam, Versl., 14, 518, 577 (1905-6).

24. Ladenburg, R. and Reiche, F., Ann. d. Physik 42, 181 (1913).

25. Ladenburg, R. and Levy, S., Zeits f. Physik 65, 189 (1930).

26. Schütz, W., Zeits. f. Astrophysik 1, 300 (1930); Zeits. f. Physik 71, 301 (1931).

27. Minnaert, M. and Slob, C., Koninklijke Akad. Wetenschappen Amsterdam, 34, 542 (1931).

28. Füchtbauer, Chr. and Hofmann, W., Ann D. Physik 43, 96 (1914).

29. Senftleben, H., "Über die Zahl der Emissionszentren der in Flammen leuchtenden Metalldämpfe und die Beziehungen dieser Zahl zur Helligkeit der ausgesandten Spektrallinien", Breslauer Dissertation; Ann. d. Physik 47, 949 (1915).

30. Einstein, A., Physik. Zeits. 18, 121 (1917).

31. Ladenburg, R., Zeits. f. Physik 4, 451 (1921).

32. Condon, E. U. and Shortley, G. H., The Theory of Atomic Spectra, Cambridge University Press (1953).

REFERENCES (Continued)

33. Mitchell, A. C. G. and Zemansky, M. W., Resonance Radiation and Excited Atoms, MacMillan (1934).

34. Hinnov, Einar and Kohn, Hedwig, "Flame Spectroscopy", Technical Report No. 10, ONR and Dept. of Physics, Duke University (1954); Hinnov, Einar, J. Opt. Soc. Am. 47, 151 (1957); Hinnov, Einar and Kohn, Hedwig, J. Opt. Soc. Am. 47, 156 (1957).

35. Doherty, Lowell R., PhD Thesis and University of Michigan Research Institute Report, in preparation (1961).

36. Goldberg, Lec, Müller, Edith A., and Aller, Lawrence H., Astrophys. J., Supplement No. 45, V, 1-138 (1960).

37. Hollyer, Jr., R. N., Hunting, A. C., Laporte, Otto, Schwarcz, E. H., and Turner, E. B., Phys. Rev. 87, 911 (1952).

38. Hollyer, R. N., Hunting, A. C., Laporte, O., and Turner, E. B., Nature 171, 395 (1953).

39. Perry, R. W. and Kantrowitz, A., J. Appl. Phys. 22, 878 (1951); Resler, E. L., Lin, Shao-Chi, and Kantrowitz, Arthur, J. Appl. Phys. 23, 1390 (1952).

40. Shreffler, G. and Christian, R. H., J. Appl. Phys. 25, 324 (1954).

41. Fowler, R. G., et al., Phys. Rev. 82, 879 (1951); Phys. Rev. 87, 966 (1952); Phys. Rev. 88, 137 (1952).

42. Charatis, George and Wilkerson, Thomas D., Bull. Am. Phys. Soc. (Ser. II) 3, 292 (1958).

43. Doherty, L. R., Bull. Am. Phys. Soc. (Ser. II) 5, 131 (1960).

44. Hollyer, Jr., R. N., "A Study of Attenuation in the Shock Tube", PhD Thesis and University of Michigan Engineering Research Institute Report (July, 1953); J. Appl. Phys. 27, 254 (1956).

45. Griem, H. R., Kolb, A. C., and Shen, K. Y., Phys. Rev. 116, 4 (1959).

46. Hill, A. and King, R. B., J. Opt. Soc. Am. 41, 315 (1951).

47. Charatis, G. and Wilkerson, T. D., Phys. Fluids 2, 578 (1959).

REFERENCES (Continued)

48. Wilkerson, T. D., Bull. Am. Phys. Soc. (Ser. II) 5, 131 (1960).

49. Johnson, W. R., "The Interaction of Plane and Cylindrical Sound Waves with a Stationary Shock Wave", PhD Thesis and University of Michigan Research Institute Technical Report No. 2539-8-T (June, 1957); Johnson, W. R. and Laporte, Otto, Phys. Fluids 1, 82 (1958).

51. Alpher, R. A. and Greyber, H. D., Phys. Fluids 1, 160 (1958).

52. Turner, E. B., "Equilibrium Hydrodynamic Variables behind a Reflected Shock Wave in Hydrogen", Space Technology Laboratories Report TR-59-0000-00744 (June, 1959).

53. Moore, Charlotte E., Atomic Energy Levels, Vols. I-III, Nat. Bur. Stds. Circular 467 (1949-1958).

54. Christian, R. H. and Yarger, F. L., J. Chem. Phys. 23, 2042 (1955); Christian, R. H., Duff, R. E., and Yarger, F. L., J. Chem. Phys. 23, 2045 (1955).

55. Hieber, W. and Romberg, E., Zeit. für Anorg. u. Allgem. Chemie 221, 332 (1935).

56. Windsor, Manly M. and Blanchard, Arthur, J. Am. Chem. Soc. 56, 823 (1934).

57. Petschek, H. E., Phys. Rev. 84, 614 (1951).

58. Turner, E. B., "Radiation from a Strong Shock Front in Krypton", University of Michigan Engineering Research Institute Resport No. 2189-1-T (July, 1955); Reports Control No. OSR-TN-55-184.

59. Turner, E. B., Phys. Rev. 99, 633 (1955).

60. Rosa, R. J., Phys. Rev. 99, 633 (1955).

61. Charatis, G., Doherty, L. R., and Wilkerson, T. D., J. Chem. Phys. 27, 1415 (1957).

62. Chabai, Albert J., "Measurement of Wall Heat Transfer and of Transition to Turbulence during Hot Gas and Rarefaction Flows in a Shock Tube", PhD Thesis and Lehigh University Institute of Research Report No. 12 (September, 1958).

REFERENCES (Continued)

63. Duff, R. E., Phys. Fluids 1, 546 (1958).

64. Mark, H., "The Interaction of a Reflected Shock Wave with the Boundary Layer in a Shock Tube", AFOSR-TN-57-345, AD 132 418, and PhD Thesis, Cornell University (June, 1957); J. Aero. Sci. 24, 304 (1957).

65. Emrich, R. J. and Wheeler, Jr., D. B., Phys. Fluids 1, 14 (1958).

66. Glass, I. I., Martin, W., and Patterson, G. N., "A Theoretical and Experimental Study of the Shock Tube", University of Toronto Institute of Aerophysics Report No. 2 (November, 1953); Glass, I. I. and Patterson, G. N., J. Aero. Sci. 22, 73 (1955); Glass, I. I. and Martin, W. A., J. Appl. Phys. 26, 113 (1955).

67. Mack, J. E., "Density Measurement in Shock Tube Flow with the Chrono-Interferometer", PhD Thesis and Lehigh University Institute of Research Report No. 4, (1954); Curtis, C. W., Emrich, R. J., and Mack, J. E., Phys. Rev. 87, 913 (1952).

68. Mirels, H. and Braun, W. H., "Nonuniformities in Shock Tube Flow due to Unsteady-Boundary-Layer Action", NACA TN 4021 (1957).

69. Duff, R. E., Phys. Fluids 2, 207 (1959).

70. Amdur, I. and Mason, E. A., Phys. Fluids 1, 370 (1958).

71. Toennies, J. P., "An Investigation of the Dissociation Energies of Nitrogen and Carbon Monoxide and the Ionization of Argon with Reflected Shock Waves", PhD Thesis, Brown University (June, 1957); Toennies, J. P. and Greene, E. F., J. Chem. Phys. 26, 655 (1957).

72. White, Donald R., "Influence of Diaphragm Opening Time on Shock Tube Flows", General Electric Research Laboratory Report No. 58-RL-1999, Schenectady (1958); J. Fluid Mech. 4, 585 (1958).

73. Strehlow, R. A. and Cohen, A., J. Chem. Phys. 28, 983 (1958).

74. Alpher, Ralph A. and White, Donald R., Phys. Fluids 2, 162 (1959).

75. Kaegi, E. M., Warren, W. R., and Vitale, A. J., "Experimentation with the General Electric Six-Inch Shock Tunnel", Proceedings of the Second Shock Tube Symposium (March, 1958), sponsored by the Air Force Special Weapons Center, SWR-TM-58-3.

REFERENCES (Continued)

76. Herzberg, Gerhard, Molecular Spectra and Molecular Structure, I. Spectra of Diatomic Molecules, 2nd Edn., Van Nostrand (1950).

77. Van Vleck, J. H. and Sherman, A., Rev. Mod. Phys. 7, 167 (1935).

78. Voge, H. H., J. Chem. Phys. 4, 581 (1936).

79. Hammerling, P., Teare, J. D., and Kivel, B., Phys. Fluids 2, 422 (1959).

80. Harcourt, A. Vernon and Esson, William, Proc. Roy. Soc. of London 14, 470 (1865); Phil. Trans. Roy. Soc. of London 156, 193 (1866); Phil. Trans. Roy. Soc. of London 157, 117 (1867).

81. Laidler, Keith J., Chemical Kinetics, McGraw Hill (1950).

82. Glasstone, Samuel, Textbook of Physical Chemistry, 2nd Ed., Van Nostrand (1946).

83. Magnus, Wilhelm and Oberhettinger, Fritz, Formulas and Theorems for the Special Functions of Mathematical Physics, Chelsea (1949).

84. Fairbairn, A. R. and Gaydon, A. G., Nature 175, 253 (1955); Proc. Roy. Soc. A239, 464 (1957).

85. Pearse, R. W. B. and Gaydon, A. G., The Identification of Molecular Spectra, 2nd Ed., Wiley (1950).

86. Downie, A. R. and Barrow, R. F., Nature 160, 198 (1947).

87. Greene, E. F., J. Amer. Chem. Soc., 76, 2127 (1954).

88. Roth, W., J. Chem. Phys. 31, 720 (1959); Erratum, J. Chem. Phys. 31, 1683 (1959).

89. Unsöld, A., Physik der Sternatmosphären, Springer (1955).

90. Chandrasekhar, S., An Introduction to the Study of Stellar Structure, Dover (1957); Radiative Transfer, Dover (1960).

91. Aller, Lawrence H., Astrophysics, Ronald Press (1953).

92. Milne, E. A., "Thermodynamics of the Stars", Handbuch der Astrophysik, Band III, Erste Hälfte, Chapter 2, Springer (1930).

REFERENCES (Continued)

93. Cowan, R. D. and Dieke, G. H., Rev. Mod. Phys. 20, 418 (1948).

94. Margenau, Henry and Lewis, Marvin, Rev. Mod. Phys. 31, 569 (1959).

95. Allen, C. W., Astrophysical Quantities, University of London, The Athlone Press (1955).

96. Landolt-Börnstein, Zahlenwerte und Funktionen, Band I, Springer (1950).

97. Schwartzschild, K., Göttinger Nachrichten, p. 41 (1906).

98. Keck, James C., Camm, John C., Kivel, Bennett, and Wentink, Jr., Tunis, Annals of Physics 7, 1 (1959).

99. Penner, S. S. and Kavanagh, R. W., J. Opt. Soc. Am. 43, 385 (1953).

100. v. d. Held, E. M. F., Zeits. F. Physik 70, 508 (1931).

101. Ostrovskii, Yu. I., and Penkin, N. P., Optika i Spektrosk. 3, 193 (1957); Science Abstracts (Physics) 61, 455 (1958), No. 4865.

102. Schütz, W., Z. Physik 45, 30 (1927).

103. Estabrook, F. B., Astrophys. J. 115, 571 (1952).

104. Huldt, L. and Lagerqvist, A., J. Opt. Soc. Am. 42, 142 (1952).

105. Charatis, George, PhD Thesis and University of Michigan Research Institute Resport (to be published).

106. Harrison, G. R., J. Opt. Soc. Am. 19, 267 (1959); J. Opt. Soc. Am. 24, 59 (1934).

107. Euler, J., Ann. Physik (6) 11, 203 (1953); Ann. Physik (6) 14, 10 (1954).

108. Moore, Charlotte E., A Multiplet Table of Astrophysical Interest (Revised Edition), Nat. Bur. Stds. Technical Note 36 (November, 1959).

109. Allen, C. W. and Asaad, A. S., M. N. R. A. S. 117, 36 (1957).

110. Sandage, A. R. and Hill, A. J., Ap. J. 113, 525 (1951).

REFERENCES (Concluded)

111. White, H. E. and Eliason, A. Y., Phys. Rev. 44, 753 (1933).

112. Goldberg, L., Ap. J. 82, 1 (1935; Ap. J. 84, 11 (1936).

113. Rohrlich, F., Ap. J. 129, 441, 449 (1959).

114. Bates D. R. and Damgaard, A., Phil. Trans. Roy. Soc. of London A242, 101 (1949).

115. Roshdestvensky, D., Ann d. Physik 39, 307 (1912); Trans. Opt. Inst. Leningrad 2, (No. 13) (1921).

116. Sidgwick, N. V., The Chemical Elements and Their Compounds, Vol. I and II, The University of Oxford, The Clarendon Press (1950).

117. Bailar, J. C., Jr. (Ed), The Chemistry of the Coordination Compounds, Reinhold (1956), Article 16: "Metal Carbonyls and Nitrosyls," pp. 509-546, J. A. Mattern and Stanley Gill.

118. Hawkins, N. J., Mattraw, H. C., Sabol, W. W., and Carpenter, D. R., J. Chem. Phys. 23, 2422 (1955).

119. Herzberg, G., Molecular Spectra and Molecular Structure (Vol. II) Infrared and Raman Spectra of Polyatomic Molecules, Van Nostrand (1950).

120. Sharifov, K. A., and Rezukhina, T. N., Akad. Nauk Azerbaidzhan SSR, Ser. Fiz. 6, 53 (1953); Chemical Abstracts (ACS) 49, 2173b (1955).

121. Brockway, L. O., Ewens, R.V.G., and Lister, M. W., Trans Far. Soc. 34, 1350 (1938).

DISTRIBUTION LIST

(One copy unless otherwise noted)

Commander 3
AF Office of Scientific Research
Washington 25, D.C.
Attn: SRY

Commander 2
AF Research Division
Washington 25, D.C.
Attn: RRRTL

Commander 4
Wright Air Development Division
Wright-Patterson Air Force Base
Ohio
Attn: WWAD

Commander
AF Cambridge Research Laboratories
L. G. Hanscom Field
Bedford, Massachusetts
Attn: CRREL

Commander
Rome Air Development Center
Griffiss Air Force Base
Rome, New York
Attn: RCOIL-2

Commander 2
Detachment 1
Hq, AF Research Division
The Shell Building
Brussels, Belgium

P. O. Box AA
Wright-Patterson Air Force Base
Ohio

Aeronautical Research Laboratories
Building 450
Wright-Patterson Air Force Base
Ohio
Attn: Technical Library

Armed Services Technical Information Agency 10
Arlington Hall Station
Arlington 12, Virginia
Attn: TIPCR

Director of Research and Development
Headquarters, USAF
Washington 25, D.C.
Attn: AFDRD

Office of Naval Research
Department of the Navy
Washington 25, D.C.
Attn: Code 420

Director
Naval Research Laboratory
Washington 25, D.C.
Attn: Technical Information Officer

Director, Army Research Office
Department of the Army
Washington 25, D.C.
Attn: Scientific Information Branch

Chief, Physics Branch
Division of Research
U. S. Atomic Energy Commission
Washington 25, D.C.

U. S. Atomic Energy Commission
Technical Information Extension
P. O. Box 62
Oak Ridge, Tennessee

National Bureau of Standards Library
Room 203, Northwest Building
Washington 25, D.C.

Physics Program
National Science Foundation
Washington 25, D.C.

DISTRIBUTION LIST (Continued)

Director
Office of Ordnance Research
Box CM, Duke Station
Durham, North Carolina

Director, Department of Commerce
Office of Technical Services
Washington 25, D.C.

ARO, Inc.
Arnold Air Force Station
Tullahoma, Tennessee
Attn: AEDC Library

Commander
AF Flight Test Center
Edwards Air Force Base
California
Attn: FTOTL

Commander
AF Special Weapons Center
Kirtland Air Force Base
New Mexico
Attn: SWOI

Commander
AF Missile Development Center
Holloman Air Force Base
New Mexico
Attn: HDOI

Commander
Army Rocket & Guided Missile Agency
Redstone Arsenal, Alabama
Attn: ORDXR-OTL

Commandant
Air Force Institute of Technology
(AU) Library
MCLI-LIB, Building 125, Area B
Wright-Patterson Air Force Base
Ohio

Commander
Air Research and Development Command
Andrews Air Force Base
Washington 25, D.C.
Attn: RDR 2
Attn: RDRA
Attn: RDRB
Attn: RDRC
Attn: RDRS

Commanding General
U.S. Army Signal Corps Research
and Development Laboratory
Fort Monmouth, New Jersey
Attn: SIGFM/EL-RPO

National Aeronautics and Space
Administration 6
Washington 25, D.C.

Advanced Research Projects Agency
Washington 25, D.C.

RAND Corporation
1700 Main Street
Santa Monica, California

Chairman
Canadian Joint Staff
For DRB/DSIS
2450 Massachusetts Avenue, N.W.
Washington 25, D.C.

Professor Hannes Alfvén
Royal Institute of Technology
Stockholm, Sweden

Dr. H. J. Davis
Division/Section 3.2
National Bureau of Standards
Connecticut Avenue at
Van Ness Street, N.W.
Washington 25, D.C.

DISTRIBUTION LIST (Continued)

Professor L. H. Aller
The Observatory
The University of Michigan
Ann Arbor, Michigan

Dr. Ralph A. Alpher
General Electric Research Laboratory
Schenectady, New York

The Library
AVCO Research Laboratory
2385 Revere Beach Parkway
Everett 49, Massachusetts

Dr. W. L. Barr
Lawrence Radiation Laboratory
P. O. Box 808
Livermore, California

Dr. F. D. Bennett
EBL, Ballistics Research
Laboratories
Aberdeen, Maryland

Dr. Peter C. Bergmann
Physics Department
Syracuse University
Syracuse 10, New York

Dr. R. S. Berry
Chemistry Department
Yale University
New Haven, Connecticut

Dr. Daniel A. Bershader
Lockheed Missiles and Space Division
Palo Alto, California

Professor P.M.S. Blackett
Physics Department
Imperial College
Imperial Institute Road
London, S.W. 7, England

Professor Walker Bleakney
Palmer Physical Laboratory
Princeton University
Princeton, New Jersey

Dr. John N. Bradley
Department of Inorganic and
Physical Chemistry
University of Liverpool
Vine Street
Liverpool 7, England

Professor J. M. Burgers
Institute for Fluid Dynamics
University of Maryland
College Park, Maryland

La Bibliothèque
Centre de Formation en Aérodynamique
Expérimentale
72, Chaussée de Waterloo
Rhode-Saint-Genèse (Bruxelles),
Belgique

Dr. A. H. Chisnell
Mathematics Department
University of Manchester
Manchester, England

Dr. J. L. Climenhaga
Department of Physics
Victoria College
Victoria, B.C., Canada

Dr. F. H. Coensgen
Lawrence Radiation Laboratory
P. O. Box 808
Livermore, California

Dr. Lowell R. Doherty
Harvard College Observatory
60 Garden Street
Cambridge 38, Massachusetts

DISTRIBUTION LIST (Continued)

Professor R. W. Courant
Institute of Mathematics and
Mechanics
New York University
45 Fourth Street
University Heights
New York 53, New York

Dr. Russell E. Duff
P. O. Box 1663
Los Alamos, New Mexico

Dr. E. John Eastmond
Space Technology Laboratories, Inc.
P. O. Box 95004
Los Angeles 45, California

Professor B. Edlén
Physics Department
University of Lund
Lund, Sweden

Dr. Charles L. Eisen
Plasma Propulsion Laboratory
Republic Aviation Corporation
Farmingdale, New York

Professor Raymond J. Emrich
Physics Department
Lehigh University
Bethlehem, Pennsylvania

Dr. J. Evans
Upper Air Research Laboratory
Sacramento Peak, New Mexico

Dr. R. G. Fowler
Physics Department
University of Oklahoma
Norman, Oklahoma

Dr. Roger M. Gallet
National Bureau of Standards
Boulder, Colorado

Dr. W.R.S. Garton
Physics Department
Imperial College
Imperial Institute Road
London, S.W. 7, England

Dr. A. G. Gaydon
Chemical Engineering Department
Imperial College
Prince Consort Road
London, S.W. 7, England

Professor Irvine I. Glass
Institute of Aerophysics
University of Toronto
Toronto 5, Canada

Dr. Martin Gluckstein
Ethyl Corporation Research Laboratory
1600 W. Eight Mile Road
Detroit, Michigan

Professor Leo Goldberg
Harvard University
Cambridge 38, Massachusetts

Dr. Melvin B. Gottlieb
Plasma Physics Laboratory
Princeton University
Princeton, New Jersey

Dr. Edward F. Greene
Chemistry Department
Brown University
Providence 12, Rhode Island

Dr. J. Greenstein
Department of Astronomy
California Institute of Technology
Pasadena, California

Guggenheim Aeronautical Laboratory
California Institute of Technology
Pasadena, California

DISTRIBUTION LIST (Continued)

Dr. Hans Griem
Institute for Fluid Dynamics
University of Maryland
College Park, Maryland

Professor E. Gross
Physics Department
Syracuse University
Syracuse 10, New York

Dr. A. Hertzberg
Cornell Aeronautical Laboratory, Inc.
4455 Genesee Street
Buffalo 21, New York

Mr. Roy J. Heyman
The Martin Company
Denver Division
P. O. Box 179
Mail No. A-96
Fluid Dynamics Section
Denver 1, Colorado

Dr. Einar Hinnov
Plasma Physics Laboratory
Princeton University
Princeton, New Jersey

Dr. D. W. Holder
National Physical Laboratory
Teddington, Middlesex, England

Dr. Robert N. Hollyer
General Motors Technical Center
Warren, Michigan

Dr. Robert G. Jahn
California Institute of Technology
Pasadena, California

Dr. W. B. Johnson
Speedway Research Laboratory
Linde Company
1500 Polco Street
Indianapolis 24, Indiana

Dr. Walter R. Johnson
Physics Department
Notre Dame University
South Bend, Indiana

Dr. H. Jones
Mathematics Department
Imperial College
Exhibition Road
London, S.W. 7, England

Dr. Arthur Kantrowitz
AVCO Research Laboratory
2385 Revere Beach Parkway
Everett 49, Massachusetts

Dr. Karl G. Kessler
National Bureau of Standards
Connecticut Avenue at
Van Ness Street, N.W.
Washington 25,D.C.

Professor Robert B. King
Norman Bridge Laboratory of Physics
California Institute of Technology
Pasadena, California

Dr. Bennett Kivel
AVCO Research Laboratory
2385 Revere Beach Parkway
Everett 49, Massachusetts

Dr. Alan C. Kolb
Radiation Division, Code 7410
Naval Research Laboratory
Washington 25, D.C.

Dr. Toyoki Koga
University of Southern California
University Park
Los Angeles 7, California

Dr. James L. Lauer
Sun Oil Company
Marcus Hook, Pennsylvania

DISTRIBUTION LIST (Continued)

Dr. Wade M. Kornegay
Department of Chemistry and
Chemical Engineering
University of California
Berkeley 4, California

Dr. Lester Kraus
Physics Group
Convair-San Diego
San Diego, California

Dr. P. Kusch
Physics Department
Columbia University
New York 17, New York

Dr. Marshall Lapp
Division of Engineering
California Institute of Technology
Pasadena, California

Dr. R. Latham
Physics Department
Imperial College
Imperial Institute Road
London, S.W. 7, England

Dr. Shao-Chi Lin
AVCO Research Laboratory
2385 Revere Beach Parkway
Everett 49; Massachusetts

Professor Dr. W. Lochte-Holtgreven
Institut für Experimentalphysik der
Universität Kiel
Olshausenstrasse 40-60
Kiel, Germany

Dr. Roland E. Meyerott
Lockheed Missiles and Space Division
Palo Alto, California

Dr. W. Millar
AERE Harwell
Didcot, Berkshire, England

Dr. Emmet Lubke
Special Defense Products Department
General Electric Company
2900 Cambell Avenue
Schenectady 6, New York

Professor Sten Luthander
Division of Aeronautics
Royal Institute of Technology
Stockholm 70, Sweden

Mr. James MacLachlan
Sloane Physics Laboratory
Yale University
217 Prospect Street
New Haven, Connecticut

Professor H. Margenau
Physics Department
Yale University
New Haven, Connecticut

Dr. R.W.P. McWhirter
CTR Division, H. 7
AERE Harwell
Berkshire, England

Dr. Donald H. Menzel
Harvard College Observatory
60 Garden Street
Cambridge 38, Massachusetts

Dr. E. Montroll
Institute for Fluid Mechanics and
Applied Mathematics
University of Maryland
College Park, Maryland

Dr. Henry Nagamatsu
General Electric Research Laboratory
Schenectady, New York

Dr. S. S. Penner
California Institute of Technology
Pasadena, California

DISTRIBUTION LIST (Continued)

Mr. J. C. Muirhead
Chief Superindendent
Suffield Experimental Station
Ralston, Alberta, Canada

Dr. M. McChesney
Research Laboratory
A.E.I (Rugby)
Rugby, England

Dr. H. N. Olsen
Speedway Research Laboratory
Linde Company
1500 Polco Street
Indianapolis 24, Indiana

Dr. Donald Osterbrock
Washburn Observatory
University of Wisconsin
Madison 6, Wisconsin

Dr. J. Payne
Physics Department
Imperial College
Imperial Institute Road
London, S.W. 7, England

Dr. R. W. Perry
ARO, Inc.
Arnold Engineering Development Center
Tullahoma, Tennessee

Dr. Harry Petschek
AVCO Research Laboratory
2385 Revere Beach Parkway
Everett 49, Massachusetts

Professor E. L. Resler
Graduate School of Aeronautical
Engineering
Cornell University
Ithaca, New York

Dr. Mary F. Romig
Convair Scientific Research Laboratory
San Diego, California

Dr. Jacob Pomerantz
Hyperballistics Division
Room 4-172
U. S. Naval Ordnance Laboratory
White Oaks, Maryland

Dr. Walter Roth
Armour Research Foundation
10 West 35th Street
Chicago 16, Illinois

Professor M. Santangelo
Istituto di Fisica Sperimentale
dell'Università
Via Archirafi 36
Palermo, Sicillia

Dr. D. L. Schultz
National Physical Laboratory
Teddington, Middlesex, England

Dr. F. Schultz-Grunow
Institute for Fluid Dynamics
University of Maryland
College Park, Maryland

Dr. F. R. Scott
John Jay Hopkins Laboratory for
Pure and Applied Science
General Atomic Division of General
Dynamics Corporation
San Diego, California

Professor K. M. Siegel
Department of Electrical Engineering
The University of Michigan
Ann Arbor, Michigan

R. Simon
Institut d'Astrophysique de
l'Université de Liège
Cointe-Sclessin, Belgique

Dr. Zack I. Slawsky
U. S. Naval Ordnance Laboratory
Silver Spring 19, Maryland

DISTRIBUTION LIST (Continued)

Professor A. Slettebak
Perkins Observatory (OSU)
Delaware, Ohio

Dr. Graydon Synder
Poulter Laboratories
Stanford Research Institute
Menlo Park, California

Professor D. B. Spalding
Department of Mechanical Engineering
Imperial College of Science and Technology
Exhibition Road
London, S.W. 7, England

Dr. Edward A. Spiegel
Institute of Mathematical Sciences
New York University
New York, New York

Professor Lyman Spitzer
Department of Astronomy
Princeton University
Princeton, New Jersey

Dr. Niel Spokes
Chemistry Department
Yale University
New Haven, Connecticut

Dr. Roger Strehlow
IBL, Ballistics Research Laboratories
Aberdeen, Maryland

Mr. M. L. Streiff, Aerophysics Group
Via: Nancy Scholder,
Astronautics Library
Convair-Astronautics
San Diego, California

Dr. B. Strömgren
Yerkes Observatory
Williams Bay, Wisconsin

Dr. Otto Struve
Astronomy Department
University of California
Berkeley, California

Dr. Peter Thoneman
AERE, Harwell
Didcot, Berkshire, England

Dr. Eugene B. Turner
Aerospace Corporation
Los Angeles 45, California

The Library of the Observatory
The University of Michigan
Ann Arbor, Michigan

Dr. Anne Underhill
Dominion Astrophysical Observatory
Royal Oak, British Columbia, Canada

The Library
United Aircraft Corporation
400 Main Street
East Hartford, Connecticut

Professor Jacques Valensi
Institut de Mecanique des Fluides
1 Rue Honnarat
Marseille 3, France

Dr. B. Vodar
Laboratoire des Hautes Pressions
Place A. Briand
Bellevue, France

Dr. H. D. Weymann
University of Rochester
Rochester, New York

Dr. Donald R. White
General Electric Research Laboratory
Schnectady, New York

DISTRIBUTION LIST (Concluded)

Dr. Gordon W. Wares, CRZCH
Geophysics Research Directorate
Air Force Cambridge Research Center
Hanscom Field
Bedford, Massachusetts

Dr. Stewart Way
Westinghouse Research Laboratory
Churchill Borough
Pittsburgh 35, Pennsylvania

Dr. Peter P. Wegner
Jet Propulsion Laboratory
California Institute of Technology
Pasadena, California

Dr. E. P. Wheaton
Douglas Aircraft Company, Inc.
3000 Ocean Park Boulevard
Santa Monica, California

Dr. Yusuf A. Yoler
Gas Dynamics Laboratory
Boeing Airplane Company
Seattle 24, Washington

Dr. Wolfgang Wiese
National Bureau of Standards
Washington 25, D.C.

Dr. Per Gloersen
Missiles and Space Vehicles Dept.
General Electric Company
Philadelphia, Pennsylvania

Dr. G. B. Whitham
Institute of Mathematical Sciences
New York University
25 Waverley Place
New York 3, New York

Dr. W. A. Wildhack, Chief
Office of Basic Instrumentation
National Bureau of Standards
Washington 25, D.C.

Dr. Marshall Wrubel
Kirkwood Observatory
Indiana University
Bloomington, Indiana

Dr. Walter Wurster
Cornell Aeronautical Laboratory, Inc.
4455 Genesee Street
Buffalo 21, New York

Miss Brenda M. VerVaecke
Ballistic Missile Radiation
Analysis Center
Willow Run Laboratories
The University of Michigan
Ann Arbor, Michigan